

# High Frequency Earthquake Ground Motion Scaling in Southeastern Canada and Korea

Young-Soo Jeon, B.E., M.S.

A Dissertation Presented to the Faculty of the Graduate  
School of Saint Louis University in Partial  
Fulfillment of the Requirements for the  
Degree of Doctor of Philosophy

2004

# Abstract

Vertical and horizontal component velocity seismograms from the CNSN seismic network of southeastern Canada and from the KMA and KIGAM networks of Korea are used for this study of high frequency ground motion scaling. I analyzed a data set consisting of 4646 three component seismograms for southeastern Canada, distances  $< 400$  km, and 2701 three component waveforms for Korea, distances  $< 600$  km. I performed the regressions of Fourier velocity spectra and peak filtered ground velocities for southeastern Canada, the Korean peninsula, and inland Korea for different combinations of vertical and horizontal components.

The regression results for southeastern Canada are characterized by rapid decreases of amplitude at distance less than 40 km ( $r^{-1.3}$ ) and three segments of geometrical spreading at mid distance ranges (40 - 400 km). The associated model for the attenuation term can be expressed by  $Q(f) = 650f^{0.33}$ . The geometrical spreading functions for vertical, horizontal, and all component show same values at mid to long distance ranges, while there are some deviations at shorter distance ranges. Even if the spectral parameters of  $\kappa = 0.01$  sec, and stress drop of 200 bars are selected to predict the theoretical excitation spectra, the Brune (1970) model does not fit the excitation spectra for events with moment magnitude greater than 4. The earthquakes in this region may have a distribution of stress drops rather than a single universal stress drop.

The regression results for Korea are parameterized by  $Q(f) = 330 f^{0.40}$  and

typical geometrical spreading for both Korean peninsula and inland Korea. The Korean wave propagation study results indicate a more moderate near source amplitude decay at short distance ranges (less than 40 km) than seen in southeastern Canada. The oceanic events do not introduce any bias in determining the wave propagation functional. A  $\kappa = 0.005$  sec, and stress drop of 200 bars for Korean peninsula and  $\kappa = 0.005$  sec, and stress drop of 300 bars for inland Korea are selected for spectral parameterizations. A simple modification of the two-corner model of Atkinson (1993a) yields better fit to Korean excitations in the high frequency ranges compare to those of Brune (1970) model which showed the lack of fit at moderate size magnitude events.

COMMITTEE IN CHARGE OF CANDIDACY:

Professor Robert B. Herrmann,

Chairperson and Advisor

Assistant Professor Keith Koper

Assistant Professor Lupei Zhu

## Acknowledgements

I would like to thank my parents for supporting me and giving me their unconditional love through many years of study. I thank my advisor, Dr. Robert B. Herrmann, for his systematic instruction, support and tolerance throughout this work. I thank Dr. Keith Koper and Dr. Lupei Zhu for critically reviewing this dissertation. I thank Eric Haug for providing and maintaining the excellent computer environment used for this research. I also thank my former advisor, Dr. Kyung-Duk, Min, Professor of Yonsei University and vice President of Yonsei University for his unconditional attention to me and my work. I really appreciate my friends in Korea and colleagues at Saint Louis University for their assistance with finishing this work and for their friendship. Finally, I thank my wife for her patience and love.

# Table of Contents

<b>List of Tables</b> .....	<b>vi</b>
-----------------------------	-----------

<b>List of Figures</b> .....	<b>vii</b>
------------------------------	------------

## **CHAPTER 1: Introduction**

1.1	Importance of high frequency ground motion . . . . .	1
1.2	Southeastern Canada . . . . .	3
1.2.1	Ground motion of Southeastern Canada . . . . .	5
1.2.2	Saguenay earthquake . . . . .	7
1.2.3	S-wave attenuation in southeastern Canada . . . . .	9
1.2.4	Objective of study in southeastern Canada . . . . .	11
1.3	Korea . . . . .	14
1.3.1	Previous earthquake studies in Korea . . . . .	15
1.3.2	Objective of study in Korea . . . . .	17

## **CHAPTER 2: Data processing and modeling**

2.1	Data preparation . . . . .	19
2.1.1	Initial data preparation . . . . .	19
2.1.2	Filtered time series . . . . .	21
2.1.3	Random Vibration Theory . . . . .	22
2.1.4	Fourier amplitude spectra . . . . .	25
2.2	Regression . . . . .	26
2.2.1	Regression method . . . . .	26
2.2.2	Coda waves . . . . .	29
2.2.3	Implementing Coda normalization method . . . . .	32
2.2.4	Implementing general regression . . . . .	34
2.3	Ground motion models . . . . .	37
2.3.1	Earthquake dislocation and stress drop . . . . .	37
2.3.2	Stochastic modeling . . . . .	39
2.3.3	Two corner model . . . . .	42
2.3.4	Finite fault model . . . . .	44

## **CHAPTER 3: Ground motion scaling in southeastern Canada**

3.1	Data set . . . . .	47
3.1.1	CNSN network . . . . .	47
3.1.2	Data set and study area . . . . .	50
3.2	Data processing . . . . .	51

3.2.1	Coda Shape . . . . .	51
3.2.2	Regression of Fourier velocity spectra . . . . .	55
3.2.3	Duration . . . . .	61
3.2.4	Regression of peak filtered velocity . . . . .	68
3.3	Parameterization . . . . .	73
3.3.1	Propagation parameters . . . . .	77
3.3.2	Modeling Fourier velocity spectra . . . . .	79
3.3.3	Parameterization of Fourier velocity spectra . . . . .	80
3.3.4	Parameterization of peak filtered velocity . . . . .	83
3.3.5	Wave propagation comparisons: Atkinson and Boore (1995) model . . . . .	89
3.4	Site . . . . .	94
3.5	Excitation . . . . .	95
3.5.1	Source model parameters of Atkinson and Boore . . . . .	98
3.5.2	Source excitation comparisons . . . . .	102
3.6	Summary . . . . .	104

**CHAPTER 4: Ground motion scaling in Korea**

4.1	Data set . . . . .	109
4.1.1	Korean network . . . . .	109
4.1.2	Study area . . . . .	109
4.1.3	Coda Shape . . . . .	115
4.2	Regression and parameterization of Fourier velocity spectra . . .	118
4.3	Duration . . . . .	128
4.4	Regression and parameterization of peak filtered velocity . . . .	131
4.4.1	Site . . . . .	143
4.4.2	Excitation . . . . .	144
4.5	Inland regression . . . . .	146
4.5.1	Regression of peak filtered velocity . . . . .	146
4.5.2	Proposed Korean model . . . . .	158
4.5.3	F-test . . . . .	165
4.6	Summary . . . . .	166

**CHAPTER 5: Conclusions**

5.1	Results . . . . .	169
5.2	Final remarks . . . . .	172

**Bibliography . . . . .175**

**Vita Auctoris . . . . .184**

# List of Tables

<p>Table 1.1: <math>Q_{Lg}^{-1}</math>, <math>Q_p^{-1}</math>, and <math>Q_s^{-1}</math> relations in Korea from previous studies. SSK<sup>†</sup>, SKP<sup>†</sup>, and SK<sup>†</sup> are acronyms of Southeastern south Korean, Southeastern part of Korean Peninsula, and South Korea. . . . .</p>	17
<p>Table 2.1: Earthquake source model of Brune (1970, 1971). <math>r/\beta</math> is the decay time, <math>f r/R</math> is a factor to take into account spherical spreading, <math>t' = t - R/\beta</math>. <math>\langle R_{\theta\phi} \rangle</math> is the <i>rms</i> average of the radiation pattern, <math>r</math> is the radius of an equivalent circular dislocation surface, <math>R</math> is the distance, <math>F(\epsilon) = \{[2 - 2\epsilon][1 - \cos(1.21 \epsilon \omega / \alpha)] + \epsilon^2\}^{1/2}</math>, <math>\epsilon</math> is the fraction of stress drop, and <math>\alpha = 2.21 \beta/r</math> . . . . .</p>	38
<p>Table 3.1: List of stations for the Broad Band Canadian National Seismograph Network. CNS in the top panel is an acronym for Canadian National Seismograph. STN code represents the station code, Lat, Lon, and Elev each denote latitude, longitude, and elevation. . . . .</p>	48
<p>Table 3.2: List of stations for the Extremely Short Period Canadian National Seismograph Network. CNS in the top panel is an acronym for Canadian National Seismograph. STN code represents the station code, Lat, Lon, and Elev each denote latitude, longitude, and elevation. . . . .</p>	49
<p>Table 3.3: List of stations for the rest of Canadian National Seismograph Network used for this study. ESPDialup represents Extremely short period Dial up CNSN (EHZ) station. POLARIS indicates the Broadband POLARIS Canadian stations. VBBCNSN is Very Broadband CNSN (BH*) stations. HBB/VBB means that the station is either High Broadband CNSN (HH*) or Very Broadband CNSN (BH*). . . . .</p>	49
<p>Table 3.4: Attenuation functional at 1.0, 2.0, 3.0, and 4.0 Hz for Fourier velocity spectra. The columns give values of frequency (first and sixth columns), hypocentral distance (second and seventh columns), attenuation <math>D(r, f)</math> at a reference distance of 40 km (third and eighth columns), associated error bar (fourth and ninth columns) and number of observations (fifth and tenth columns). . . . .</p>	62

Table 3.5: Attenuation functional at 6.0, 8.0, 10.0, and 12.0 Hz for Fourier velocity spectra. The columns give values of frequency (first and sixth columns), hypocentral distance (second and seventh columns), attenuation $D(r, f)$ at a reference distance of 40 km (third and eighth columns), associated error bar (fourth and ninth columns) and number of observations (fifth and tenth columns). . . . .	63
Table 3.6: Attenuation functional at 14.0 and 16.0 Hz for Fourier velocity spectra. The columns give values of frequency (first and sixth columns), hypocentral distance (second and seventh columns), attenuation $D(r, f)$ at a reference distance of 40 km (third and eighth columns), associated error bar (fourth and ninth columns) and number of observations (fifth and tenth columns). . . . .	64
Table 3.7: Number of observations in regressions of band-passed filtered velocity and Fourier velocity. . . . .	64
Table 3.8: Durations as a function of distance and frequencies from 1 to 16 Hz. . . . .	68
Table 3.9: Measured durations from band-passed filtered for southeastern Canada. Hor, Ver, and All are acronyms of horizontal, vertical, and combined data set. . . . .	69
Table 3.10: Attenuation functional at 1.0, 2.0, 3.0, and 4.0 Hz for band passed filtered. The columns give values of frequency (first and sixth columns), hypocentral distance (second and seventh columns), attenuation $D(r, f)$ at a reference distance of 40 km (third and eighth columns), associated error bar (fourth and ninth columns) and number of observations (fifth and tenth columns). . . . .	74
Table 3.11: Attenuation functional at 6.0, 8.0, 10.0, and 12.0 Hz for band-pass filtered. The columns give values of frequency (first and sixth columns), hypocentral distance (second and seventh columns), attenuation $D(r, f)$ at a reference distance of 40 km (third and eighth columns), associated error bar (fourth and ninth columns) and number of observations (fifth and tenth columns). . . . .	75

Table 3.12: Attenuation functional at 14.0 and 16.0 Hz for bandpass filtered. The columns give values of frequency (first and sixth columns), hypocentral distance (second and seventh columns), attenuation $D(r, f)$ at a reference distance of 40 km (third and eighth columns), associated error bar (fourth and ninth columns) and number of observations (fifth and tenth columns). . . . .	76
Table 4.1: List of stations for the KMA and KIGAM Digital Stations. STN code represents the station code, Lat, Lon, and Elev each denote latitude, longitude, and elevation. Epi, SS-1, STS-1, and STS-2 each denote accelerometer, short period (1 Hz) velocity sensor, broadband sensor and broadband sensor. . . . .	110
Table 4.2: List of stations for the KMA and KIGAM Digital Stations. STN code represents the station code, Lat, Lon, and Elev each denote latitude, longitude, and elevation. Epi, SS-1, STS-1, and STS-2 each denote accelerometer, short period (1 Hz) velocity sensor, broadband sensor and broadband sensor. . . . .	111
Table 4.3: KMA and KIGAM digital station sensors. . . . .	115
Table 4.4: Attenuation functional at 0.25, 0.5, 1.0, and 2.0 Hz for Fourier velocity spectra. The columns give values of frequency (first and sixth columns), hypocentral distance (second and seventh columns), attenuation $D(r, f)$ at a reference distance of 40 km (third and eighth columns), associated error bar (fourth and ninth columns) and number of observations (fifth and tenth columns). . . . .	125
Table 4.5: Attenuation functional at 3.0, 4.0, 6.0, and 8.0 Hz for Fourier velocity spectra. The columns give values of frequency (first and sixth columns), hypocentral distance (second and seventh columns), attenuation $D(r, f)$ at a reference distance of 40 km (third and eighth columns), associated error bar (fourth and ninth columns) and number of observations (fifth and tenth columns). . . . .	126
Table 4.6: Attenuation functional at 10.0, 12.0, 14.0 and 16.0 Hz for Fourier velocity spectra. The columns give values of frequency (first and sixth columns), hypocentral distance (second and seventh columns), attenuation $D(r, f)$ at a reference distance of 40 km (third and eighth columns), associated error bar (fourth and ninth columns) and number of observations (fifth and tenth columns). . .	127

Table 4.7: Number of observations in regression of filtered velocity and Fourier velocity. . . . .	128
Table 4.8: Durations as a function of distance and frequencies from 0.25 to 16 Hz for the three component data set. . . . .	132
Table 4.9: Measured durations from band-passed filtered for Korea. Hor, Ver, and All are acronyms for horizontal, vertical, and combined data set. . . . .	135
Table 4.10: Attenuation functional at 0.25, 0.5, 1.0, and 2.0 Hz for band passed filtered. The columns give values of frequency (first and sixth columns), hypocentral distance (second and seventh columns), attenuation $D(r, f)$ at a reference distance of 40 km (third and eighth columns), associated error bar (fourth and ninth columns) and number of observations (fifth and tenth columns). . . . .	140
Table 4.11: Attenuation functional at 3.0, 4.0, 6.0, and 8.0 Hz for band-pass filtered. The columns give values of frequency (first and sixth columns), hypocentral distance (second and seventh columns), attenuation $D(r, f)$ at a reference distance of 40 km (third and eighth columns), associated error bar (fourth and ninth columns) and number of observations (fifth and tenth columns). . . . .	141
Table 4.12: Attenuation functional at 10.0, 12.0, 14.0, and 16.0 Hz for bandpass filtered. The columns give values of frequency (first and sixth columns), hypocentral distance (second and seventh columns), attenuation $D(r, f)$ at a reference distance of 40 km (third and eighth columns), associated error bar (fourth and ninth columns) and number of observations (fifth and tenth columns). . . . .	142
Table 4.13: Measured durations from band-passed filtered for inland Korea. . . . .	154
Table 4.14: Lat $\ddagger$ and Lon $\ddagger$ denote latitude and longitude. Thick bold $M_W$ denotes inland events. Details of source parameters of Korea are at <a href="http://www.eas.slu.edu/People/RBHerrmann/KOREA.2003">http://www.eas.slu.edu/People/RBHerrmann/KOREA.2003</a> . . . .	158
Table 4.15: $F$ test results obtained from the variances (second and third column) of Korean events with known $M_W$ . Value at the sixth column denotes the range of percentiles of $F$ distributions. . . . .	166

Table 4.16:  $F$  test results obtained from the variances of Southeastern Canada events with known  $M_W$ . Value at the sixth column denotes the range of percentiles of  $F$  distributions. . . . . 167

Table 5.1: Propagation parameters of all, horizontal and vertical component for southeastern Canada and Korea. . . . . 171

# List of Figures

Figure 3.1: Map of epicenters (stars) and stations (triangles) for the study area. . . . .	50
Figure 3.2: Map of seismograph stations and epicenters in Western Quebec, Eastern Ontario. The epicenters are marked by the stars and the stations are represented by the station code. . . . .	51
Figure 3.3: Map of seismograph stations and epicenters in the Charlevoix - Kamouraska, Quebec. The epicenters are marked by the stars and the stations are represented by the station code. . . . .	52
Figure 3.4: Map shows the seismograph stations and epicenters located upper right corner of Quebec. . . . .	53
Figure 3.5: Source-receiver hypocentral distance distribution of observed stations for the data recorded along the seismic network. . . . .	54
Figure 3.6: Shape of the 1.0 Hz normalized seismic coda as a function of lapse time from earthquake origin time. The black lines denote the initial part before the P-wave arrival, light gray lines are the signal between P and S-wave arrivals, gray lines are the coda-normalized <i>RMS</i> average between the S-wave arrival and the dark gray segment of the curves start at $2t_s$ . Gray triangles represent the peak values and circles denote normalized peak amplitudes. . . . .	56
Figure 3.7: Shape of the 6.0 Hz normalized seismic coda as a function of lapse time from earthquake origin time. The black lines denote the initial part before the P-wave arrival, light gray lines are the signal between P and S-wave arrivals, gray lines are the coda-normalized <i>RMS</i> average between the S-wave arrival and the dark gray segment of the curves start at $2t_s$ . Gray triangles represent the peak values and circles denote normalized peak amplitudes. . . . .	57
Figure 3.8: Regression analysis for 2.0 and 4.0 Hz. Top, coda estimate of $D(r)$ using coda normalization technique. Middle, coda and regression propagation functionals. Bottom, final residuals of the regression analysis. . . . .	58
Figure 3.9: Regression analysis for 8.0 and 12.0 Hz. Top, coda estimate of $D(r)$ using coda normalization technique. Middle, coda and regression propagation functionals. Bottom, final residuals of the regression analysis. . . . .	59

Figure 3.10: The reduced attenuation functional $D(r, f)$ obtained from the regression on the Fourier velocity spectra at the frequencies of 1.0, 2.0, 3.0, 4.0, 6.0, 8.0, 10.0, 12.0, 14.0, and 16.0 Hz for southeastern Canada. . . . .	60
Figure 3.11: Durations at 1.0, 2.0, 4.0 and 6.0 Hz obtained for southeastern Canada. Rounded gray circles indicate individual duration estimates and thick solid lines denote the duration measured using by a median value method. . . . .	66
Figure 3.12: Durations at 8.0, 10.0, 14.0, and 16.0 Hz. Rounded gray circles indicate individual duration estimates and thick solid lines represent measured durations. . . . .	67
Figure 3.13: Regression analysis for 2.0 and 4.0 Hz. Top, coda estimate of $D(r)$ using coda normalization technique. Middle, coda and regression propagation functionals. Bottom, final residuals of the regression analysis. . . . .	70
Figure 3.14: Regression analysis for 8.0 and 12.0 Hz. Top, coda estimate of $D(r)$ using coda normalization technique. Middle, coda and regression propagation functionals. Bottom, final residuals of the regression analysis. . . . .	71
Figure 3.15: The reduced attenuation functional $D(r, f)$ at the frequencies of 1.0, 2.0, 3.0, 4.0, 6.0, 8.0, 10.0, 12.0, 14.0, and 16.0 Hz for southeastern Canada. . . . .	72
Figure 3.16: (a) The reduced attenuation functional $D(r, f)$ obtained from the regression on the Fourier velocity spectra at the frequencies of 1.0, 2.0, 3.0, 4.0, 6.0, 8.0, 10.0, 12.0, 14.0, and 16.0 Hz for southeastern Canada; (b) The residuals of the model fit to the Fourier velocity spectra $D(r, f)$ for the frequency range of 1 - 16 Hz. . . . .	82
Figure 3.17: Horizontal component (top panel) and vertical component (bottom panel) reduced attenuation functional $D(r, f)$ obtained from the regression on the Fourier velocity spectra from 1.0, to 16.0 Hz for the southeastern Canada. . . . .	84
Figure 3.18: (a) Three component reduced attenuation functional $D(r, f)$ at the frequencies of 1.0, 2.0, 3.0, 4.0, 6.0, 8.0, 10.0, 12.0, 14.0, and 16.0 Hz for southeastern Canada; (b) The residuals of the model fit to the band pass $D(r, f)$ from 1 to 16 Hz. . . . .	86

Figure 3.19:(a) Horizontal component reduced attenuation functional $D(r, f)$ from bandpass-filtered velocities of 1.0, 2.0, 3.0, 4.0, 6.0, 8.0, 10.0, 12.0, 14.0, and 16.0 Hz for southeastern Canada; (b) The residuals of the model fit to the band pass $D(r, f)$ . . . . .	87
Figure 3.20:(a) Vertical component reduced attenuation functional $D(r, f)$ obtained from the regression on the bandpass-filtered velocities of 1.0, 2.0, 3.0, 4.0, 6.0, 8.0, 10.0, 12.0, 14.0, and 16.0 Hz for southeastern Canada; (b) The residuals of the model fit to the band pass $D(r, f)$ for the frequency range of 1 - 16 Hz. . . . .	88
Figure 3.21:(a) The $D(r, f)$ obtained from the regression on the bandpass-filtered velocities for southeastern Canada. The black lines in the background are the theoretical $D(r, f)$ of Atkinson and Boore (1995) model parameters; (b) The residuals of the model fit to the band pass $D(r, f)$ from 1 to 16 Hz. . . . .	90
Figure 3.22:(a) Horizontal component $D(r, f)$ of the bandpassed filtered velocities on southeastern Canada and theoretical $D(r, f)$ of Atkinson and Boore (1995) model (black lines in the background); (b) The residuals of the model fit to the band pass $D(r, f)$ from 1 to 16 Hz. . . . .	91
Figure 3.23:(a) Vertical component $D(r, f)$ of the bandpass-filtered velocities for southeastern Canada. Atkinson and Boore (1995) model parameters used for theoretical $D(r, f)$ ; (b) The residuals of the model fit to the band pass $D(r, f)$ from 1 to 16 Hz. . . . .	92
Figure 3.24:Inverted site amplifications of southeastern Canada in peak amplitudes. a and b are Z and H component site terms of ground motion while c and d are H and Z component site terms of ground motion. . . . .	96
Figure 3.25:Inverted filtered ground velocity excitation terms for the earthquake events recorded by three-component velocity seismograms plotted on a linear frequency scale. Thin black lines are the inverted excitation and thick gray lines are model based prediction for southeastern Canada. . . . .	99
Figure 3.26:Band passed filtered velocity excitation (thin black lines) and model based prediction (thick gray lines) for the southeastern Canada. The thin black line linked by thin long-dashed line is the observed excitation of Au Sable Forks earthquake and the thin black lines linked by thick short-dashed lines are the excitations of $M_w = 4.3, 4.4,$ and $4.5$ events. . . . .	101

Figure 3.27: The residuals of the model fit to the band pass $E(f)$ for the stochastic point source model as a function of frequency range from 1 to 16 Hz for southeastern Canada. . . . .	102
Figure 3.28: Modified residuals of the model fit to the band pass $E(f)$ for the the stochastic point source model as a function of frequency range from 1 to 16 Hz for southeastern Canada. Individual stress drops (100, 200, 300, 400, and 500 bars) are applied to stochastic model to reduce the residuals. . . . .	103
Figure 4.1: Map shows the epicenters and station locations for whole KMA and KIGAM data-set. The earthquake epicenters are marked by black stars, the big stars indicate the epicenters of known moment magnitudes, and stations are denoted by black triangles. . . .	112
Figure 4.2: Map shows the epicenters and station locations for inland KMA and KIGAM data-set. The earthquake epicenters are marked by black stars, the big stars indicate the epicenters of known moment magnitudes, and stations are denoted by black triangles. . . .	113
Figure 4.3: Distance coverage for KMA and KIGAM stations. The observation distances for each station that containing horizontal and vertical component should cover a wide distance range and overlap with other stations to reduce the tradeoff possibility between the excitation and propagation term. . . . .	114
Figure 4.4: Shape of the 0.5 Hz normalized seismic coda as a function of lapse time from earthquake origin time. The black lines denote the initial part before the P-wave arrival, light gray lines are the signal between P and S-wave arrivals, gray lines are the <i>RMS</i> average between the S-wave arrival and the dark gray segment of the curves start at $2t_s$ . Gray triangles represent the peak values and circles denote normalized peak amplitudes. . . . .	116
Figure 4.5: Shape of the 1.0 Hz normalized seismic coda as a function of lapse time from earthquake origin time. The black lines denote the initial part before the P-wave arrival, light gray lines are the signal between P and S-wave arrivals, gray lines are the <i>RMS</i> average between the S-wave arrival and the dark gray segment of the curves start at $2t_s$ . Gray triangles represent the peak values and circles denote normalized peak amplitudes. . . . .	117
Figure 4.6: Regression analysis for 1.0 and 3.0 Hz. Top, coda estimate of $D(r)$ using coda normalization technique. Middle, coda and regression propagation functionals (open circles linked by thin black lines). Bottom, final residuals of the regression analysis. . . . .	119

Figure 4.7: Regression analysis for 4.0 and 10.0 Hz. Top, coda estimate of  $D(r)$  using coda normalization technique. Middle, coda and regression propagation functionals (open circles linked by thin black lines). Bottom, final residuals of the regression analysis. . . . . 120

Figure 4.8: (a) Three component reduced attenuation functional  $D(r, f)$  obtained from the regression of the Fourier amplitudes at the frequencies of 0.25, 0.5, 1.0, 2.0, 3.0, 4.0, 6.0, 8.0, 10.0, 12.0, 14.0, and 16.0 Hz. The black lines at the background are the theoretical  $D(r, f)$ . (b) The residuals of the model fit to the Fourier velocity spectra  $D(r, f)$  for the frequency range of 0.25 - 16 Hz. . . . . 122

Figure 4.9: Horizontal component (top panel) and vertical component (bottom panel) reduced attenuation functional  $D(r, f)$  obtained from the regression on the Fourier amplitudes from 0.25 to 16.0 Hz for Korea. The black lines at the background are the theoretical  $D(r, f)$ . The presentation of this plot is to emphasize the departure from  $r^{-1}$  spreading. . . . . 123

Figure 4.10: Durations at 0.5, 1.0, 2.0 and 4.0 Hz obtained for Korea. Rounded gray circles denote individual duration estimates. Thick solid lines represent the duration computed using a median value method. . . . . 129

Figure 4.11: Durations at 6.0, 10.0, 12.0, and 16.0 Hz obtained for Korea. Rounded gray circles denote individual duration estimates. Thick solid lines represent the duration computed using a median value method. . . . . 130

Figure 4.12: Regression analysis for 1.0 and 3.0 Hz. Top, coda estimate of  $D(r)$  using coda normalization technique. Middle, coda and regression propagation functionals (open circles linked by thin black lines). Bottom, final residuals of the regression analysis. . . . . 133

Figure 4.13: Regression analysis for 4.0 and 10.0 Hz. Top, coda estimate of  $D(r)$  using coda normalization technique. Middle, coda and regression propagation functionals (open circles linked by thin black lines). Bottom, final residuals of the regression analysis. . . . . 134

Figure 4.14: (a) Three component reduced attenuation functional  $D(r, f)$  obtained from the regression on the bandpass-filtered velocities from 0.25 to 16.0 Hz for Korea. The presentation of this plot is to emphasize the departure from  $r^{-1}$  spreading. The black lines in the background are the theoretical  $D(r, f)$ . The horizontal dashed line represents  $r^{-1}$  trend; (b) The residuals of the model fit to the band pass  $D(r, f)$  from 0.25 to 16 Hz. . . . . 136

Figure 4.15:(a) Horizontal component reduced attenuation functional $D(r, f)$ obtained from the regression on the bandpass-filtered velocities of 0.25, 0.5, 1.0, 2.0, 3.0, 4.0, 6.0, 8.0, 10.0, 12.0, 14.0, and 16.0 Hz for Korea. The reference distance at 40 km was used to normalize the $D(r, f)$ ; (b) The residuals of the model fit to the band pass $D(r, f)$ for the frequency range of 0.25 - 16 Hz. . . . .	138
Figure 4.16:(a) Vertical component reduced attenuation functional $D(r, f)$ obtained from the regression on the bandpass-filtered velocities of 0.25, 0.5, 1.0, 2.0, 3.0, 4.0, 6.0, 8.0, 10.0, 12.0, 14.0, and 16.0 Hz for Korea; (b) The residuals of the model fit to the band pass $D(r, f)$ for the frequency range of 0.25 - 16 Hz. . . . .	139
Figure 4.17:Inverted site amplifications of Korea. Each line denotes single stations. a and b are Z and H component site terms of ground motion while c and d are H and Z component site terms of ground motion. . . . .	143
Figure 4.18:Inverted filtered ground velocity excitation terms for the earthquake events recorded by three-component velocity seismograms plotted on a log scale for Korea. The thin black lines linked by thick short and long dash lines are the excitations of known moment magnitudes. . . . .	145
Figure 4.19:Source-receiver hypocentral distance distribution of observed stations for the data recorded along the seismic network. . . . .	147
Figure 4.20:Regression analysis for 1.0 and 3.0 Hz. Top, coda estimate of $D(r)$ using coda normalization technique. Middle, coda and regression propagation functionals. Bottom, final residuals of the regression analysis. . . . .	148
Figure 4.21:Regression analysis for 4.0 and 10.0 Hz. Top, coda estimate of $D(r)$ using coda normalization technique. Middle, coda and regression propagation functionals. Bottom, final residuals of the regression analysis. . . . .	149
Figure 4.22:Three component reduced attenuation functional $D(r, f)$ from band passed-filtered velocities at the frequencies from 0.25 to 16.0 Hz for inland Korea. The black lines in the background are the theoretical $D(r, f)$ ; (b) The residuals of the model fit to the band passed $D(r, f)$ for the frequency range of 0.25 - 16 Hz. . . . .	150

Figure 4.23:Horizontal component (top panel) and vertical component (bottom panel) reduced attenuation functional $D(r, f)$ obtained from the regression on the band passed filtered spectra from 0.25 to 16.0 Hz for the inland Korea. The black lines in the background are the theoretical $D(r, f)$ . . . . .	152
Figure 4.24:Durations at 1.0, 3.0, 4.0, 8.0, 10.0, and 14.0 Hz obtained for inland Korea. Rounded gray circles indicate individual duration estimates and thick solid lines is the duration measured using by a median value method. . . . .	153
Figure 4.25:Inverted site amplifications of inland Korea in peak amplitudes. a and b are Z and H component site terms of ground motion while c and d are H and Z component site terms of ground motion. .	154
Figure 4.26:Inverted filtered ground velocity excitation terms for the earthquake events recorded by three-component velocity seismograms plotted on a linear frequency scale. Thin black lines are the inverted excitation and thick gray lines are model based prediction for inland Korea. . . . .	156
Figure 4.27:The residuals of the model fit to the band pass $E(f)$ for the stochastic point source model as a function of frequency range of 1 - 16 Hz for inland events of Korea. . . . .	157
Figure 4.28:Modified residuals of the model fit to the band pass $E(f)$ for the stochastic point source model as a function of frequency range of 1 - 16 Hz for oceanic events. . . . .	157
Figure 4.29:Proposed model for Korea source spectral amplitudes as a function of frequencies for seismic moments 4 - 6 (thick short dashed lines) compared with corresponding two-corner model of Atkinson (1993a) on a log scale (solid lines) . . . . .	161
Figure 4.30:Comparison of the stochastic model of Boore (1983), thick short dashed lines, and empirical two-corner model of Atkinson (1993a) solid lines. Comparisons are made for seismic moments of 4, 5, 6, and 7. . . . .	162
Figure 4.31:Inverted filtered ground velocity excitation terms for the earthquake events recorded by three-component velocity seismograms plotted on a log scale. The thin black lines linked by thick short and long dash lines are the excitations of known moment magnitudes. . . . .	163

Figure 4.32: Excitation of peak filtered velocity for the combined vertical and horizontal data sets in linear scale of frequency range. Thin black lines are the inverted excitation and Thick gray curve is the prediction of suggested model. . . . . 164

# Chapter 1

## Introduction

### 1.1 Importance of high frequency ground motion

One of the most important issues in earthquake ground motion studies is the separation of the original source signal from other effects that distort the observed signal during wave propagation from the earthquake to the seismic station recording the signal. The observed ground motion generated by earthquakes is complicated because it is affected by source, travel path, and local site conditions. Travel path effects describing wave propagation through the medium of the earth are geometrical spreading, attenuation that causes frequency dependent reduction of the amplitude and phase shifts, and scattering effects which yield complicated superpositions of wavelets with different paths. Site effects are the result of reverberation in shallow sedimentary layers that raise frequency dependent amplification (Scherbaum, 1996), shallow crustal rocks and surface topography effects. If the effect of the wave propagation (travel path and site conditions) is well known, then one can constrain the physical process of the source in terms of earthquake size, depth, stress drop, rupture process, and fault geometry. The specification of ground motion parameters for the source, propagation, and site term is one of the most important problems in earthquake engineering and seismic hazard studies.

An important contribution of earthquake seismology to human society is

the evaluation of seismic hazard. In order to mitigate that threat, earthquake-resistant design is developed to produce a structure or facility withstanding a certain level of shaking without excessive damage. Defining the expected level of shaking is a difficult but important problem in earthquake engineering. After successfully quantifying those parameters, one integrates them with the historical earthquake catalog to produce a numerical estimation of seismic hazard for a certain region.

Seismic hazard may be analyzed either deterministically or probabilistically. Deterministic Seismic Hazard Analysis (DSHA) involves the development of a particular seismic scenario that is used later for ground motion hazard evaluation. The four step process of DSHA (Reiter, 1990) is to identify and characterize all earthquake sources which may produce significant ground motion in a site, to choose the shortest distance from the source zone to the site of interest to select the controlling earthquake in terms of size and distance from the site, and finally to define the hazard in terms of the ground motions produced at the site controlling event. DSHA evaluation is based upon the worst-case ground motions and applied to structures such as nuclear power plants and large dams. It does not necessarily consider the likelihood of occurrence of the controlling earthquake.

The DSHA used in the early years of geotechnical earthquake engineering was later replaced by Probabilistic Seismic Hazard Analysis (PSHA) that considers uncertainties in the earthquake size, earthquake location, ground motion parameter prediction, and rate of recurrence of earthquakes. PSHA

is developed in the following order: identify and characterize the earthquake sources in terms of the probability distribution of potential rupture locations; characterize the temporal distribution of earthquake recurrence; define the ground motion produced at the site by the earthquakes of any possible size occurring at any possible point in each source zone; combine the uncertainties to obtain the probability. PSHA requires the assumption that the recurrence law obtained from past seismicity is appropriate for the prediction of future seismicity (Kramer, 1996).

The objective of this work is to derive absolute ground motion scaling relations for Southeastern Canada and Korea for ultimate use in seismic hazard analysis. Korea and Southeastern Canada are similar in the nature of the modern seismic data sets, the low levels of seismicity, and the age of geological structures. So, I am also interested in comparing the ground motion scaling between these two regions.

## **1.2 Southeastern Canada**

Eastern North America (ENA) is a typical intra-plate region with low to moderate seismic activity. ENA encompasses southeastern Canada and northeastern United States. Although this region consists of stable lithospheric plates, damage from future events could affect human society. Large and damaging earthquakes have occurred in the past and will inevitably occur in the future. About 300 earthquakes occur in eastern Canada each year. Within this number, about four will exceed magnitude 4, thirty will be greater than

magnitude 3, and about fifteen additional events will be reported felt. Normally, a decade will include three events greater than magnitude 5 generally the threshold of damage. Instrumental recordings have identified earthquakes occurring at depths varying from the surface to 30 km.

The cause of earthquakes in eastern Canada is not well understood. Unlike plate boundary regions where the rate and size of seismic activity are directly correlated with plate interaction, eastern Canada is part of the stable interior of the North American Plate. Seismic activity in areas like these seems to be related to the regional stress fields, with the earthquakes concentrated in regions of crustal weakness ([http://www.seismo.nrcan.gc.ca/historic\\_eq/eastcan\\_e.html](http://www.seismo.nrcan.gc.ca/historic_eq/eastcan_e.html)).

Earthquakes are normally classified as inter-plate and intra-plate earthquakes. The inter-plate earthquakes occur along or parallel to the major plate boundaries with a large slip rate. Thrust fault along subduction zones and strike-slip earthquakes of the transform faults are typical of the inter-plate earthquakes. Intra-plate earthquakes refer to those which occur clearly within a plate.

The generating mechanisms of the intra-plate earthquakes are not clearly identified. Sykes (1978) insisted that earthquakes occur along old zones of crustal weakness such as sutures or rifts which are reactivated by the current stress field in the plates. Johnston and Kanter (1990) found that stable continental regions which have undergone extension since the Cretaceous are likely to experience more earthquakes than other ancient regions. Zoback et al.

(1989) mentioned that numerous intra-plate stress observations are compressional in stable eastern North America and have nearly uniform orientations of the maximum compressive stress. Zoback (1992) later indicated that the mid-plate stress fields are modulated by some local perturbations related with specific geologic or tectonic features such as lithospheric flexure and lateral density contrasts that give rise to buoyancy forces.

The earthquakes in the Northeastern United States and southeastern Canada occur in the region of high stress along unhealed fault zones of late Paleozoic or younger age (Sbar and Sykes, 1973). Adams and Basham (1989) divided southeastern Canada seismicity into four seismic zones and argued that most earthquakes were associated with the reactivation of a late Protozoic to Paleozoic rift system along the St. Lawrence and Ottawa rivers.

### **1.2.1 Ground motion of Southeastern Canada**

Predicting ground motion for future earthquakes in eastern North America (ENA) are based on the stochastic model (Atkinson, 1984; Atkinson and Boore, 1990) which has its origin in the work of Hanks and McGuire (1981). The Brune (1970) source model, with a stress parameter of about 100 bars, has provided accurate estimates of average ground motions when used with a stochastic model (Hanks and McGuire, 1981; Boore, 1983; Boore et. al., 1992) for western united states (WUS). The application of the Brune (1970) source model to ENA was justified using a few moderate (M 4 to 5) ENA events (Atkinson, 1984; 1989) and teleseismic data of larger historical earthquakes

(Somerville et al., 1987). But, the 1988 Saguenay earthquake at Quebec (M 5.8) raised questions concerning the application of the underlying source model for larger earthquakes and the appropriateness of the ENA source spectra (Atkinson and Boore, 1995). Boatwright and Choy (1992) showed that the teleseismic spectra of large intraplate events appears to have two corner frequencies instead of the single corner of the Brune model. Their high frequency level is equivalent to a Brune stress parameter of about 500 bars, but the level at intermediate to low frequencies (less than 1 Hz) is matched by a stress parameter of less than 100 bars (Boore and Atkinson, 1992).

The large discrepancy between the California and ENA high-frequency source levels at large magnitudes may be a result of real differences in stress released during large events (Atkinson and Silva, 1997). It has been suggested that stress drops are related to the repeat time of large events, such that infrequent large events on well-healed fault zones might be characterized by higher stress, perhaps due to a greater density of strong asperities (e.g., Kanamori and Anderson, 1975; Kanamori and Allen, 1986).

Ground motions in eastern North America are enriched in high frequency energy relative to those from California earthquakes with similar magnitudes and distances (Atkinson and Boore, 1990). This is largely due to quantified differences in crustal anelastic attenuation. Shi et al. (1996) indicated that lower  $Q$  values are associated with younger ages of orogenic movement and that high  $Q$  values are associated with older ages of tectonic activity. It may be that ENA crustal conditions, which are characterized by high horizontal compres-

sive stresses and long earthquake repeat times, lead to patches of particularly high stress on the rupture surface in some cases (Atkinson, 1993a) or they may lead to unusual rupture geometries (Haddon, 1992).

The results of recent studies of ground motion in southeastern Canada and northeastern United States indicate that source spectra for ENA earthquakes greater than magnitude 4 differ from the Brune 100 bar model (Atkinson, 1993a), and that the attenuation of spectral amplitudes is disturbed by the transition from direct-wave to Lg-wave spreading, postcritical reflections from internal crustal interfaces, and the Moho discontinuity in the distance range from about 60 to 120 km. A trilinear form for the geometrical spreading is suggested (Atkinson and Mereu, 1992) and the duration increases with distance in a complex shape (Atkinson, 1993b).

### **1.2.2 Saguenay earthquake**

The Saguenay earthquake is very important because this earthquake raised argument that the application of Brune (1970) model is not appropriate to the ENA source model. This earthquake (short period magnitude,  $m_N = 6.5$  or moment magnitude,  $M_W = 5.8$ ) that occurred near Chicoutimi ( $48^{\circ}12' N$ ,  $71^{\circ}18' W$ ), Province of Quebec, Canada, on November 25, 1988, at about 23:46 (GMT) is the largest earthquake in eastern North America since 1942 (Boore and Atkinson, 1992). This event differs from other events because of its depth (28 km rather than 5 to 15 km), the rarity of earthquakes in the source region, and the large high frequency spectral level of the radiation at the source.

The source spectra of the foreshock ( $m_N = 4.8$ ) and aftershock ( $m_N = 4.1$ ) are matched well by Brune's single source model with a 65 bar stress drop and moderate seismic moments, while the spectrum of the mainshock differs from the conventional spectral shape and requires a stress parameter of 500 bars and higher seismic moments. The Brune model overestimates spectral amplitudes near 1 Hz by a factor of 2. The high frequency radiation of the main shock is inconsistent with other intraplate earthquakes. One of the issues raised by this earthquake is whether the observed mainshock should influence the prediction of future ground motions and earthquake resistant design. The focal depth study of foreshock (28 km) and aftershock (30 km) indicates that the high stress parameter for the mainshock is not the sole factor controlling the observed signal parameters (Boore and Atkinson, 1992). Fletcher et al. (1984) found that the maximum stress drop increases with depth and the large stress drop of 500 bars might not be possible for shallower sources.

The failure of a single corner frequency model to predict the source spectra of the Saguenay earthquake required consideration of more complex spectral models to improve the accuracy of prediction. Atkinson (1990) suggested and applied the use of two corner frequencies for larger ENA earthquakes to reconcile the observed depletion of intermediate frequencies. This suggestion is consistent with theoretical concepts of Joyner (1984), Boatwright (1988) and Boatwright and Choy (1992). The lower frequency corner may be related to overall fault rupture characteristics and the higher corner reflects on the breaking of the highest stress asperities on the fault surface. The specifica-

tion of higher frequency corner is difficult unless it is related to the physical characteristics of certain local area or tectonic regimes (Boore and Atkinson, 1992).

The frequency dependent  $Q(f) = 755 f^{0.52}$  for the S wave found through the study of Saguenay earthquake is very different from that of other areas such as western North America. The amplitude decrease with distance, from Quebec to the Adirondacks, is less than for paths to eastern Maine. This is because the waves propagating to western Maine are attenuated more than waves in a SW direction (Hough et. al., 1989). The difference in apparent attenuation may be due to the actual difference anelastic and structural properties in the tectonic provinces or to anisotropy induced by the structural grain under given condition of azimuthally nonuniform distribution of data (Boore and Atkinson, 1992).

### **1.2.3 S-wave attenuation in southeastern Canada**

The shear-wave phases are of engineering interest, since their amplitudes are typically about five times larger than the P-wave amplitudes (Atkinson and Mereu, 1992). The shear-wave energy is carried by the direct-S wave at distances less than approximately 60 km (Burger et al., 1987). At regional distances (200 to 1000 km) the dominant phase is the  $Lg$  phase, comprised of multiple postcritical reflections of  $S$  waves trapped within the crustal wave guide (Kennett, 1986). The  $S_n$  phase is also significant at regional distances, particularly for frequencies above 5 Hz (Shin and Herrmann, 1987).

The validity of assuming a simple underlying shape for the attenuation curve, with specific geometric spreading coefficient values of 1.0 and 0.5 for near-source and regional distances, respectively, has recently been called into question. The wave propagation studies of Burger et al. (1987) and Ou and Herrmann (1990) indicate that the expected shape of amplitude decay for simple layered crustal models is complex. Layering in the crust causes direct-wave amplitudes to decay more steeply than  $R^{-1}$  where  $R$  is the hypocentral distance. Then, as the direct arrivals are joined by postcritical reflections off the Moho and intracrustal discontinuities, there may be distance ranges where amplitudes actually increase with distance, between approximately 50 and 200 km. Beyond 200 km, geometric attenuation of the spectra may be significantly greater than  $R^{-0.5}$ , depending on the nature of the crust-mantle transition (Burger et al., 1987; Bowman and Kennett, 1991). A sharp velocity contrast traps energy within the crustal waveguide, while a positive gradient may increase amplitudes at shorter distances. Further complexity may be introduced by crustal heterogeneity, which causes significant perturbations of travel paths and erratic, indeterminate amplitude variations (Ojo and Mereu, 1986).

Atkinson and Mereu (1992) indicated that the attenuation curve of southeastern Canada showed that the amplitudes decay slightly more rapidly than  $1/R$  ( $R^{-1.1}$ ) at distances less than 70 km. Between 70 to 130 km, where the direct wave is joined by  $S_mS$ , spectral amplitudes are approximately constant. Beyond 130 km, corresponding to the  $Lg$  phase, amplitudes decay at a rate consistent with  $R^{-0.5}$  and  $Q(f) = 670f^{0.33}$ . These results support the hypothesis

of Burger et al. (1987) that postcritical reflections from the Moho discontinuity play an important role in determining the shape of the attenuation curve. However, the influence of  $S_{mS}$  is subtle, allowing the shape to be approximated by simple functional forms.

#### **1.2.4 Objective of study in southeastern Canada**

Since ground motion model proposed for southeastern Canada or ENA relies on an empirical model of attenuation including the stochastic method, its relation becomes the basis for current USGS probabilistic seismic hazard maps for the eastern United States. My first purpose is to study the wave propagation and excitation spectra in southeastern Canada and then critically review and compare with the previous study results. The area ranges from  $40^{\circ}$  to  $60^{\circ}$  in latitude and from  $85^{\circ}$  to  $65^{\circ}$  in longitude (degrees west).

A study of high frequency ground motion scaling in Eastern North America (ENA) can be compared with previous studies of Ou and Herrmann (1990), EPRI (1993), Atkinson and Somerville (1994), Atkinson and Boore (1995, 1997, and 1998) and Toro et al. (1997). Those studies used different techniques in which the propagation of motions through the Earth's crust is modeled, but the outcomes were all similar in describing the ENA crustal structure given the same source description.

The most controversial issue for the development of reliable ground motion relations for ENA is the accurate specification of the earthquake source spectrum for future earthquakes (Atkinson and Boore, 1998). Earthquake

source parameters such as focal mechanism, depth, and seismic moment not only contribute to the understanding ground motions for a region, but also provide useful information for understanding seismotectonic setting and in estimating future seismic hazards. Previously determined source mechanisms for ENA earthquakes were mostly obtained by using P-wave first-motion data from a sparse distribution of seismic stations. Analog data with inadequate station coverage may result in less precisely constrained solutions. The sparse distribution of seismic stations and the lack of standardized recordings with high dynamic range in ENA made it difficult to determine source parameters through waveform modeling for most events until recently (Du et al., 2003).

One of the major difficulties in defining ground motion relations for ENA is that the strong ground motion data set is not large enough to derive reliable models for ground motion processes directly from empirical data. On the contrary, California has sufficient numbers of strong motion data to develop ground motion relations for engineering applications. Thus the question of the underlying shape of the source spectrum and its scaling with earthquake magnitude has considerable consequences for earthquake engineering in ENA.

Haddon (1996) proposed an approach to the ENA ground motion problem as following:

”Reliable estimates of strong ground motions for future large earthquakes in the region must be based on either empirical *S*-wave data from large earthquakes in other, analogous regions or on theoretical extrapolations, based on reliable interpretation of empirical data from small and moderate earthquakes

that have previously occurred in the region”.

The current seismic hazard analyses of southeastern Canada rely on Atkinson and Boore’s (1995, 1998) ground motion studies. But, these studies have used older data sets with a sparse distribution of seismic stations, which may have resulted in poorly constrained models. Recent broadband data, modern 3-component short period and broadband digital seismographs of the Canadian National Seismographic networks (CNSN), provides improved coverage for small regional earthquakes in this region as well as wider frequency bands than used in previous studies.

The 2002 update of the National Seismic Hazard Maps weight five ground motion scaling relations instead of the two used in the 1996 maps. Two of these rely on the same empirically based geometrical spreading relation proposed by Atkinson and Mereu (1992). Since the Atkinson and Mereu (1992) paper, additional three component ground motion data has become available from southeastern Canada. The Atkinson and Mereu (1992) processing techniques focused primarily on the Fourier spectra and somewhat on duration. My study differs from previous studies in the region because of separate regressions over Fourier velocity spectra and peak filtered ground velocities and the determination of a distant dependent duration consistent with these two data sets. The regional wave propagation results have greater distance ranges than previous research results because of the use of a dense data set and a broad network coverage. I will divide the data set into horizontal and vertical components and perform separate regressions. Because horizontal component

ground motions are of most engineering interest, comparing horizontal, vertical, and all component ground motion is very important for earthquake hazard study.

### **1.3 Korea**

The Korean peninsula, a part of the North China Block or Sino-Korean Craton, lies between Japanese island arcs and China proper (Lee et al., 2003). It represents a denuded remnant of deformed basement rocks, sedimentary successions, granitic intrusions, and volcanics. The peninsula has a long history of basin formation and crustal deformation. It contains major Precambrian Massifs of Nangrim, Kyonggi, and Youngnam massifs. Imjingang Belt, a narrow suture zone recording high-grade metamorphic events in the late Permian-early Triassic (Cho et al., 1995; Ree et al., 1996) separated the Nangrim and Kyonggi massifs. Okchon Fold Belt separated the Kyonggi and Youngnam massifs, but the stratigraphy of the Okchon Group is poorly understood. On the northeast, the Okchon Basin initiated as an intraplate rift prior to the Late Proterozoic is bounded by the Taebaeksan Basin. The Taebaeksan Basin is composed of the Chosun Supergroup (Cambro-Ordovician) and Pyongan Supergroup (Carboniferous-Triassic). At the southeastern part of the peninsula, The Cretaceous Kyongsang Basin comprises gently eastward-dipping successions (Chang, 1975; Choi, 1985; Rhee et al., 1998). A Tertiary sequence deposited at the southeastern peninsula, Pohang Basin, is associated with back-arc opening in the East Sea, or Sea of Japan (Chough et al., 1990; Yoon and

Chough, 1995). The pre-Mesozoic geologic history of Korean Peninsula is not known well because of the lack of information on timing of basin initiation, sedimentation, and deformation.

The compressive stresses from collisions of the Eurasian plate with the surrounding Indian, Pacific, and Ryuku plates trigger earthquakes in the Korean peninsula (Lee et al., 2003). About 40 - 50 earthquakes occur in mainland Korea and its surrounding peninsula annually. Earthquake local magnitudes are normally less than 5. Though May 29, 2004 (10:14:26 GMT time)  $M_W = 5.1$  earthquake in the East Sea ( $36^{\circ} 67' N$ ,  $129^{\circ} 94' E$ ) indicates that Korea is not safe from the risk of damaging earthquakes offshore. Historically, the 1936 Ssanggyesa earthquake of magnitude 5.1 is the largest earthquake from 1905 to 1945 (Lee and Jung, 1980). Focal mechanism studies of this earthquake indicates a thrust fault with a considerable strike-slip component on the north-northeast-trending plane (Shimazaki, 1984) which is similar to the orientation of surrounding faults. The principal stress direction may be the east-west, but the existing inhomogeneities of the crustal rocks should be considered because of the deviation of the stress direction. The focal mechanisms of larger earthquakes may be thrust faults with the mix of strike-slip components (Lee et al., 2003).

### **1.3.1 Previous earthquake studies in Korea**

Wave propagation (or attenuation) in Korea has been studied by Chung and Sato (2001), Kim et al. (2002), and Chung and Lee (2003). Kim et al. (1999)

first measured  $Q^{-1}$  for P waves using only 10 earthquakes in southeastern Korea (Kyungsang Basin). Chung and Sato (2001) later obtained  $Q_p^{-1}$  and  $Q_s^{-1}$  values for the same region using local seismic data. Kim et al. (2002) expanded the study area for South Korea (or Southern Korea) and got different  $Q^{-1}$  values compared to the previous results. Chung and Lee (2003) later reported the high-frequency  $Q_{Lg}^{-1}$  in the crust of South Korea. Previous studies of  $Q$  values in Korea are summarized in Table 1.1 where Lg  $Q$ , P  $Q$ , and S  $Q$  each denoted by  $Q_{Lg}$ ,  $Q_p$ , and  $Q_s$ . Recent work improved results, but these studies have limitations because of epicenter locations and the number of waveforms used by the researchers. The inconsistent  $Q$  values may arise because of the trade-off of inversion parameters, specific forward models, different seismic phases, and different paths used for those study areas.

A proper Earth structure study is important because it ultimately provides earthquake epicenter and origin time required for estimation of wave propagation through the local and regional earth structures. Song and Lee (2001) and Yoo and Lee (2001) recently studied about the structure of the Korean peninsula using travel-time data of 29 local earthquakes from 1991 to 1998 and receiver functions of teleseismic events at Taejon (TJN) station in the southern part of Korean peninsula. Their results indicates a Moho depth of about 30 to 33 km and crustal P- and S-wave velocities of 5.8 - 6.3 km/sec and 3.3 - 3.6 km/sec respectively and a  $P_n$  of 7.8 - 7.9 km/sec velocity.

Authors	Region	Frequency range	Result
Chung and Sato (2001)	SSK†	1.5-24 Hz	$Q_p^{-1} = 0.009 f^{-1.05}$
Chung and Sato (2001)	SSK†	1.5-24 Hz	$Q_s^{-1} = 0.004 f^{-0.70}$
Kim et al. (2002)	SKP†	0.2-20 Hz	$Q(f) = 383.3 f^{0.406}$
Chung and Lee (2003)	SK†	1.5-24 Hz	$Q_{Lg}^{-1} = 0.0018 f^{-0.54}$

Table 1.1:  $Q_{Lg}^{-1}$ ,  $Q_p^{-1}$ , and  $Q_s^{-1}$  relations in Korea from previous studies. SSK†, SKP†, and SK† are acronyms of Southeastern south Korean, Southeastern part of Korean Peninsula, and South Korea.

### 1.3.2 Objective of study in Korea

My second purpose is to study the high frequency ground motion in Korea and compare the model parameters with those of southeastern Canada primarily because of a similar crustal age. The Korea study area ranges from  $33^{\circ}$  to  $43^{\circ}$  in latitude and from  $124^{\circ}$  to  $131^{\circ}$  in longitude (degrees east). The Korean modern seismic network rapidly expanded throughout the country since the late 1990's. It was installed because of the necessity of assessing the safety of the nuclear power plants in light of the hazards of the Kobe earthquake. The Korea Meteorological Administration (KMA) and Korea Institute of Geology, Mining and Materials (KIGAM) installed short and long period seismometers throughout the country since the late 1990's. An earthquake hazard study has been strongly requested by Korean government because of the dense population and man-made structures such as high-rise buildings, massive industrial facilities, and underground complexes.

A Korean ground motion study is important because its purpose is to min-

imize the damage and to protect people from the risk of the earthquakes. For this reason, an estimate of the seismic risk of the earthquake source characteristics and wave propagation is crucial. Although the earthquake hazard study for Korea is in its beginning stage, this study of the high frequency wave propagation and excitation spectra in Korea has a significant advantage over the previous studies (Chung and Sato, 2001; Kim et al., 2002; Chung and Lee, 2003) because of the separate regressions over Fourier velocity spectra, peak filtered ground velocities, the determination of a distant dependent duration sets, and absolute calibration of ground motions.

## Chapter 2

### Data processing and modeling

#### 2.1 Data preparation

##### 2.1.1 Initial data preparation

The first step in the data preparation is the collection of seismograms. The data were obtained from two different sources. The first network is CNSN network of Canada and the second is from combined KMA and KIGAM network in Korea. The seismograph network (CNSN) of the Geological Survey of Canada can detect all events exceeding magnitude 3 in eastern Canada and all events greater than magnitude 2.5 in densely monitored areas. The data are available through an autodrm ([http://www.seismo.nrcan.gc.ca/nwfa/events/index\\_e.php](http://www.seismo.nrcan.gc.ca/nwfa/events/index_e.php)) with waveforms and responses returned in the SEED format. The data are selected on the basis of signal to noise and corrected for instrument response to ground velocity in units of  $m/sec$  in the 0.2 - 40.0 Hz band.

The KMA and KIGAM seismic networks can detect all events exceeding local magnitude 1.0 in South Korea. The digital data series are given in the form of mini-SEED file format which are corrected for instrument response to form ground velocity in units of  $m/sec$  in the frequency band of 0.005 - 25.0 Hz. The instrument response was given in the pole-zero response system that consists of multiplying the constant in the normalized response by the calibration factor. The calibration factor in turn is constructed from the A/D sensitivity and

the actual sensor gain. Careful correction for instrument response is critical to this study since I will attempt to study the absolute scaling of ground motion generated by the source.

Once the digital data series are corrected for instrument response, the resulting time series represents the actual ground motion (velocity) in the pass-band. Ground motions are of interest to engineers in different ways. Lower frequencies are important for use with large structures such as bridges and tall buildings while high frequencies are important for small structures, stiff structures and geotechnical studies (Malagnini, 1999).

The selected waveforms must have P and S waves with high *signal/noise* ratio. P and S waves arrival times ( $t_p, t_s$ ) are picked for every waveform to provide a quick check on the assumed hypocentral distance through the difference in P and S wave arrival times ( $t_s - t_p$ ). Analysis of S-wave motion required picking the time of beginning of the S wave. In general, the hypocentral distance,  $x$ , is easily estimated on the basis of an assumed  $v_p/v_s$  ratio and crustal  $v_p$  as

$$t_s - t_p = x(1/v_s - 1/v_p) = t_p v_p (1/v_s - 1/v_p) t_p (v_p/v_s - 1) \quad (2.1)$$

$$t_p = \frac{t_s - t_p}{v_p/v_s - 1} = \frac{t_s - t_p}{0.732} \approx 1.37(t_s - t_p) \quad (2.2)$$

$$x \approx v_p \times 1.37(t_s - t_p) \approx 8.2(t_s - t_p) \quad (2.3)$$

where  $x$  is the travel distance,  $t_p = x/v_p$ ,  $t_s = x/v_s$ ,  $v_p/v_s = \sqrt{3}$ , if  $v_p = 6\text{km/sec}$  in

the crust. The constant 8.2 could be larger if the time signals measured are  $P_n$  and  $S_n$  rather than the crustal  $P_g$  and  $S_g$ . Normally,  $x = 8.0 \times (t_s - t_p)$  is good for most crustal events except at larger distances. As a check on the phases and the location, I compare the epicentral distance with the  $t_s - t_p$  time.

## 2.1.2 Filtered time series

Each waveform is filtered around a center frequency,  $f_c$ , using an 8-pole highpass causal Butterworth filter with corner frequency at  $f_c/\sqrt{2}$  Hz, followed by an 8-pole lowpass Butterworth filter with corner frequency at  $\sqrt{2}f_c$  Hz. The center frequencies used are 1, 2, 3, 4, 6, 8, 10, 12, 14, and 16 Hz and sometimes 0.25, 0.3 and 0.5 Hz if there is low frequency signal.

The filtered seismogram is squared and integrated from the onset of the S-wave to the time when the integral reaches a plateau where integrated velocity square is normalized to unity. The duration of the significant part of the seismogram,  $T$ , is defined as the time window bracketing the 5 % - 75 % of the integrated squared velocity. If the signal consists of a single isolated pulse, then the duration would be the 0 % - 100 % window.

Parseval's equality is used to relate the time-domain integral of the square of a time series to the frequency-domain integral of the square of its Fourier amplitude spectrum:

$$\int_{-\infty}^{+\infty} |a(t)|^2 dt = \int_{-\infty}^{+\infty} |A(f)|^2 df \quad (2.4)$$

The root mean square (*RMS*) values of a windowed time series is defined by

following relation:

$$a_{rms} = \sqrt{\frac{\int_{-\infty}^{+\infty} |a(t)|^2 dt}{T}} \approx \sqrt{\frac{\int_{-\infty}^{+\infty} |A(f)|^2 df}{T}} \quad (2.5)$$

Equation 2.5 will be used with the results of Random Vibration Theory (*RVT*) and  $\approx$  sign is used to take into account the distortion of the seismic spectrum due to the time domain windowing.

If the amplitude spectrum of the time series is nonzero within a certain frequency window (between  $f_1$  and  $f_2$ ) because of band pass filtering, then

$$\sqrt{\frac{\int_0^T |a(t)|^2 dt}{T}} \approx \sqrt{\frac{2 \int_{f_2}^{f_1} |A(f)|^2 df}{T}} \quad (2.6)$$

### 2.1.3 Random Vibration Theory

*RVT*, a tool to estimate the peak motion ( $a_{max}$ ) that only depends on duration and spectral shape, is used to connect the peak value of a time series to the *RMS* average of its Fourier amplitude spectrum through duration. Boore (1983) applied the *RVT* of Cartwright and Longuet-Higgins (1956), (CLH), to the seismological problem of estimating response spectra and peak velocity and acceleration for earthquakes.

The expected peak motion is related to the root mean square (*RMS*) value ( $a_{rms}$ ) by

$$a_{max} = \eta_{max} a_{rms} \quad (2.7)$$

where

$$\eta_{max} = \int_{-\infty}^{+\infty} \eta \frac{d}{d\eta} (1 - q(\eta))^N d\eta \quad (2.8)$$

and  $N$  is the number of maxima to be exceeded,  $\eta$  is the variable which represent the heights of a maxima (velocity or acceleration) and  $q(\eta)$  is the cumulative probability of  $\eta$  exceeding a given value (CLH 5.1). Both  $N$  and  $q(\eta)$  are functions of the spectral shape. Equation 2.8 is solved numerically and  $a_{max}$  is estimated by following sequences.

From Parseval's theorem,  $a_{rms}$  is given by

$$a_{rms} = \left(\frac{m_0}{T}\right)^{1/2} \quad (2.9)$$

where the  $k$ 'th moment is defined as

$$m_k = \frac{1}{\pi} \int_0^{\infty} \omega_k |A(\omega)|^2 d\omega, \quad (2.10)$$

$\omega_k$  is the  $2\pi f^k$ , and  $A(\omega)$  is the amplitude spectrum of the source term. The signal spectrum, which is a function of distance and frequency is used to compute the 0'th ( $m_0$ ), 2'nd ( $m_2$ ), and 4'th ( $m_4$ ) spectral moments that are used to define  $\eta_{max}$ . In general,  $T$  is the signal duration.

$\eta_{max}$  be calculated by following sequences. Boore (1983) expanded the integrand of the integral binomial series and integrated term by term as

$$\eta_{max} = \sqrt{\frac{\pi}{2}} \sum_{l=1}^N (-1)^{l+1} \frac{C_l^N}{\sqrt{l}} \xi^l \quad (2.11)$$

where  $C_l^N$  is binomial coefficients  $\frac{N!}{l!(N-l)!}$ .  $\xi$  is a measure of the bandwidth of the spectrum,

$$\xi = \frac{m_2}{(m_0 m_4)^{1/2}} \quad (2.12)$$

where  $m_0$ ,  $m_2$  and  $m_4$  are the zeroth, second and fourth moments of the energy density spectrum, respectively.

CLH (1956) derived the following asymptotic expression for large value  $N$

$$\eta_{max} = [2 \ln(N)]^{1/2} + \gamma/[2 \ln(N)]^{1/2} \quad (2.13)$$

where  $\gamma = 0.5772\dots$ (Euler's constant). This equation is a good approximation to equation 2.11, even for small values of  $N$ . Equation 2.14 is the first term of the asymptotic expansion of equation 2.13 (the error is about 10 per cent for  $N$  is 20 when the second term is ignored). This equation is based on the assumption of a stationary time series with uncorrected peaks, an assumption that is not strictly true in acceleration

$$\frac{a_{max}}{a_{rms}} = 2 \ln(N)^{1/2} \quad (2.14)$$

where

$$N = 2 \tilde{f} T \quad (2.15)$$

and  $\tilde{f}$  is the predominant frequency of the motion.

Finally equation 2.15 is used to estimate  $N$ . In equation 2.11,  $N$  is the number of extrema, and the appropriate frequency is

$$\tilde{f} = \frac{1}{2\pi}(m_4/m_2)^{1/2}. \quad (2.16)$$

For the asymptotic form (equation 2.13),  $N$  is the number of zero crossings given by equation 2.15 with

$$\tilde{f} = \frac{1}{2\pi}(m_2/m_0)^{1/2}. \quad (2.17)$$

In overall,  $a_{rms}$ ,  $N$ , and  $T$  must be estimated regardless of the equations used. The above equations shows that the relation between maximum amplitude ( $a_{max}$ ) and *RMS* amplitude ( $a_{rms}$ ) depends only on moments of the ground motion spectrum after choosing the proper duration  $T$ . The signal duration enters into the peak motion estimation in two ways: the estimate of the *RMS* value and in the definition of  $\eta_{max}$ . The duration helps to model the propagation and excitation terms of time domain observations more accurately (Ortega, 2000).

#### **2.1.4 Fourier amplitude spectra**

The signal over the same time window (5 % - 75 %) is Fourier transformed. The observed peak of the filtered seismogram is compared to the peak value computed via *RVT* to check if the duration chosen is properly evaluated in each case. The geometric mean of *RMS* spectrum in the filter pass band is used for the observed spectral amplitude at each frequency range. The pass

band is the  $(f_1, f_2)$  frequency window where  $f_1 = f_c/\sqrt{2}$ , and  $f_2 = \sqrt{2}f_c$ .

## 2.2 Regression

### 2.2.1 Regression method

In general the maximum amplitude is the multiplicative effect of source, path and site in a linear expression:

$$A(r, f) = Src(f) \cdot D(r, f) \cdot Site(f) \quad (2.18)$$

where  $f$  is the observed frequency,  $r$  is the hypocentral distance. Equation 2.19 is now modified to emphasize observations. The logarithm of the observed ground motion parameter is a combined effect of excitation, propagation and site:

$$PEAK_{i,j}(r, f) = E_i(r_{ref}, f) + S_j(f) + D(r, f) \quad (2.19)$$

where  $i$  is the source index ( $1 \leq i \leq I$ ),  $r_{ref}$  is the reference distance,  $j$  is the site index ( $1 \leq j \leq J$ ),  $E_i(r_{ref}, f)$  is the excitation term estimated at the reference distance and  $S_j(f)$  represents the site term. The term excitation is used since the regression only defines the scaling of observed ground motions and says nothing directly about the seismic source. The true separation of those terms requires assumptions about the propagation of the signal to the first observation point.

A piecewise linear function (Anderson and Lei, 1994; Harmsen, 1997; Yazd, 1993) was used to represent the distance dependence of observed motion,  $D(r, f)$ ,

at a fixed frequency,  $f_c$ :

$$D(r, f_c) = \sum_{k=1}^n L_k(r) D_k \quad (2.20)$$

where  $n$  is the number of nodes,  $L_k(r)$  is a linear interpolation function defined as

$$L_k(r) = \begin{cases} \frac{r-r_{k-1}}{r_k-r_{k-1}} & : \text{if } r_{k-1} \leq r \leq r_k \text{ and } 2 \leq k \leq n \\ \frac{r_{k+1}-r}{r_{k+1}-r_k} & : \text{if } r_k \leq r \leq r_{k+1} \text{ and } 1 \leq k \leq n-1 \\ 0 & : \text{otherwise} \end{cases}$$

and  $D_k \equiv D(r_k, f)$  are node values; the  $n$  coefficients  $D(r_k, f)$  are determined by the inversion of each sampling frequency (Malagnini *et al.*, 2000). The node values used are 10, 20, 30, 40, 50, 75, 90, 105, 120, 135, 150, 175, 200, 250, 300, 400, 500, 600, 700, 800, 900 and 1000 km. The Canadian study encompasses the 1000 km distance range while the Korean study covers a 600 km distance range. I prefer to use a large number of nodes,  $n$ , so that the regression can fit any curvature in the actual distance dependence.

The ground motion regression model is now written as

$$PEAK = \log A_{i,j}(r, f) = E_i(r_{ref}, f) + S_j(f) + \sum_{k=1}^n L_k(r) D_k. \quad (2.21)$$

For the forward problem, the value of  $D(r_0)$ ,  $r_k \leq r_0 \leq r_{k+1}$ , is computed by linearly interpolating between the values of  $D(r_k)$  and  $D(r_{k+1})$  which are located at  $r_k$  and  $r_{k+1}$ .

Observations satisfying this form of equation at a given frequency can be combined into a single matrix relationship if I define a vector of unknown pa-

rameters that contains the source excitation values, followed by the site amplification values, and then the values that I use to parameterize the geometrical spreading. The matrix equation constructed is solved by a least squares inversion using singular value decomposition (SVD) algorithm (Lawson and Hanson, 1974) with a damped regression after the following constraints are used to reduce the number of degrees of freedom of the system to permit a stable inversion:

- $D(r_{ref}) = 0$ , where  $r_{ref} = 40$  km. The reference distance chosen should be large enough to reduce the effect of source depth error on the hypocentral distance and shorter than the distance at which the first Moho arrivals are expected.
- $\sum S_j(f) = 0$  for selected data channels. If the geologic site characteristics are known, the constraint  $S_{rock}(f) = 0$  could be used.
- A smoothing constraint is applied to the  $D(r)$  by setting weighted finite-difference approximations for the derivative of  $D_k(r, f)$  with respect to distance to zero ( $D_{k-1} - 2D_k + D_{k+1} = 0$ ) which is only a linearity constraint if the  $r_l$  is evenly spaced in which case it approximates a zero second derivative (Malagnini *et al.*, 2000).

Given the level of motion  $E_i(r_{ref}, f)$  at  $r_{ref} = 40$  km, the  $D(r, f)$  propagates that motion to the desired distance,  $r$ , and the site term adjusts that motion to a particular physical location.

## 2.2.2 Coda waves

Coda waves are the continuous wavetrains in the tail portion of seismogram. Aki (1969) noticed that early portions of seismograms are composed of waves which propagate from the source and decrease with amplitude with increasing propagation distance, while the coda had similar amplitudes and spectral content at all stations independent of epicentral distance. The coda wave is caused by the incoherent scattering from the random heterogeneity in the earth's lithosphere. Coda waves are dominated by scattered surface waves at frequencies less than 10 Hz while higher frequency coda waves are composed of scattered body waves (Fehler and Sato, 2003).

The coda  $Q$ ,  $Q_c$ , varies with frequency, lapse time interval used in the observation, and tectonic region.  $Q_c^{-1}$  is generally lower in tectonically active regions and higher in stable regions, roughly  $10^{-2}$  at 1 Hz and decreases to about  $10^{-3}$  at 20 Hz (Fehler and Sato, 2003).

At epicentral distances less than 100 km and at times greater than two times the  $S$  wave travel time, the spectrum of coda waves is the same at all nearby recording stations for an earthquake (Tsumura, 1967) and the power spectra of coda waves decays same manner at a station for all events within a given region (Rautian and Khalturin, 1978). The coda decay shape is independent of earthquake magnitudes less than 6, and coda amplitude differs with local geology at a recording site.

The coda normalization technique was applied to remove the effects of in-

strument response, unknown source, and site effects and to isolate the attenuation in the mid- and lower-crust (Aki, 1980; Frankel et al., 1990). This technique is based upon the "single-station" method proposed by Aki (1980) who applied this method to several earthquakes observed at different distances from a single station. For this study, his method extended to use several stations.

To understand the coda normalization technique, I assume that the spectral amplitude  $A_s(r, \omega)$  of the  $S$  or  $Lg$  wave observed at a station is represented by

$$A_s(r, \omega) = R_{\theta\phi} I(\omega) S(\omega) G(\omega) R^{-\gamma} e^{-\omega R/2Q\beta} \quad (2.22)$$

where  $\omega$  is the angular frequency,  $2\pi f$ ,  $R$  is the hypocentral distance,  $R_{\theta\phi}$  is the radiation pattern, and  $\beta$  is the average  $S$  wave velocity.  $I(\omega)$ ,  $S(\omega)$ ,  $G(\omega)$  each represent the instrument gain, the source excitation, the site amplification, and  $\gamma$  is the the exponent of geometrical spreading. The  $Q$  is the effective  $Q$  of the crust and  $R_{\theta\phi}$  of  $Lg$  waves would denote some composite radiation pattern of the rays with various take off angles which contribute to this regional phase.

The narrow band passed amplitude coda wave  $A_c(\omega_c, t_s)$  can be parameterized as

$$A_c(\omega_c, t_s) = I(\omega_c) S(\omega_c) G(\omega_c) C(\omega_c, t_s) \quad (2.23)$$

where  $C(\omega_c, t_s)$  is the coda envelope shape showing the spectral amplitude decay with  $t_s$ , the S-wave travel time, at some time after the origin time and  $\omega_c$  is the center frequency of band-pass filter. The seismic coda is homogeneous

in space for  $t_s$  greater than twice the  $S$ -wave time. The levels at different stations are assumed to be due to the site response and instrument gain difference (Frankel et al., 1990).

If the amplitude of the  $S$  or  $Lg$  wave amplitude is divided by that of coda wave envelope, the instrument response, source spectrum, and perhaps site response divide out. The resulting ratio is

$$\frac{A_s(r, \omega)}{A_c(\omega, t_s)} = \frac{R_{\theta\phi} R^{-\gamma} e^{-\omega R/2Q\beta}}{C(\omega, t_s)} \quad (2.24)$$

For a linear system, this removes the frequency dependent instrument gain, source excitation and site amplification effects. Therefore, normalized  $S$  wave amplitudes from different stations and earthquakes for a certain region can be combined on a single plot for a given frequency range. The amplitude decay with distance, attenuation, is interpreted as a function of  $Q$  and geometrical spreading,  $\gamma$ .

The radiation pattern effects, a major source of scatter in the plots of coda normalization amplitudes, are not removed with this method. The major problem using the method is that the recordings from close stations do not continue long enough to record coda waves corresponding to lapse times which are twice the direct wave travel times (Frankel et al, 1990). To mitigate that problem, I used as much as long a time series as possible.

### 2.2.3 Implementing Coda normalization method

The peak S-wave arrival amplitude,  $A_s(r, f)$  and the RMS coda wave level,  $A_c(f, t_s)$ , at a reference time  $t_s$  is used to compute the ratio:

$$A_{reduced}(r, f) = \frac{A_s(r, f)}{A_c(f, t_s)} \quad (2.25)$$

which can be modeled as

$$\log[A_{reduced}(r, f)] = D(r, f) - C(f, t_s) \quad (2.26)$$

where  $C(f, t_s)$  is coda envelope shape that describes the decay of the coda spectral amplitude with lapsed time on the seismogram. Relative values of  $C(f, t_s)$  for each frequencies at the same time  $t_s$  show the effect of scattering and anelastic attenuation of the coda spectrum. By forcing  $D(r_{ref}, f) = 0$ , I can fix the amplitude offset caused by  $C(f, t_s)$ . The chosen reference distance,  $r_{ref} = 40$  km, should be far enough so that the effect of error in the source depth does not affect the hypocentral distance and less than the expected super-critically reflected crustal arrivals that complicates the motion, to eventually prevent inter-regional comparisons.

Combining equation 2.20 and 2.26, the logarithm of each reduced amplitude  $A_{reduced}(r, f)$  at a particular frequency can be written as

$$\log[A_{reduced}(r, f)] = L_k(r) \cdot D_k + L_{k+1}(r) \cdot D_{k+1} - C(f, t_s) \quad (2.27)$$

and equation 2.27 can be replaced by defining  $A_i(r) = \log[A_{reduced}(r, f)]$

$$A_i(r) = p \cdot D_j + (1 - p) \cdot D_{j+1} - C(f, t_s). \quad (2.28)$$

The problems for  $r_k \leq r \leq r_{k+1}$  becomes

$$A_{(n+m+1) \times 1} = G_{(n+m+1) \times (m)} \cdot M_{(m) \times 1}, \quad (2.29)$$

and in matrix form,

$$\begin{array}{c} \left| \begin{array}{c} A_1 \\ A_2 \\ \vdots \\ \vdots \\ A_n \\ \dots \\ 0 \\ \vdots \\ \vdots \\ \vdots \\ \vdots \\ 0 \\ \dots \\ 0 \end{array} \right| = \left| \begin{array}{cccccc} 0 & p & 1-p & 0 & \dots & 0 \\ p & 1-p & 0 & 0 & \dots & 0 \\ \vdots & & \vdots & & & \vdots \\ \vdots & & \vdots & & & \vdots \\ 0 & 0 & p & 1-p & \dots & 0 \\ \dots & & & & & \\ \hline -2w & w & 0 & 0 & \dots & 0 \\ w & -2w & w & 0 & \dots & 0 \\ \vdots & & \ddots & & & \vdots \\ \vdots & & \vdots & \ddots & & \vdots \\ \vdots & & \vdots & & \ddots & \vdots \\ \vdots & & \vdots & & \vdots & \ddots \\ 0 & 0 & 0 & \dots & w & -2w \\ \dots & & & & & \\ \hline 0 & 0 & w_{ref} & 0 & \dots & 0 \end{array} \right| \times \left| \begin{array}{c} D_1 \\ \vdots \\ \vdots \\ D_2 \\ \vdots \\ \vdots \\ D_3 \\ \vdots \\ \vdots \\ D_{m-1} \\ \vdots \\ \vdots \\ D_m \end{array} \right|$$

where dotted lines are inserted to separate the section of the rows related to observations from the rows enforcing the regression constraints. The bottom row is added to force the attenuation functional to be zero at the reference distance so as to eliminate the term  $C(f, t_s)$  from the equation above.  $w$  is the weighting factor that forces the constraints more effectively. Through this procedure, the normalized amplitudes yield an initial  $D(r, f)$  that an independent, unbiased estimate of the true  $D(r, f)$ .

## 2.2.4 Implementing general regression

The general regression for peak filtered motion or Fourier velocity is similar to the previous one for the reduced amplitudes in the coda normalization method. The linear equation used for the observed amplitude at a distance  $r_k \leq r \leq r_{k+1}$  is

$$\log A_l(f) = E_i(f) + p \cdot D_k(f) + (1 - p) \cdot D_{k+1}(f) + S_j(f) \quad (2.30)$$

and for  $r_k \leq r_0 \leq r_{k+1}$ :

$$p \equiv \frac{r_{k+1} - r_0}{r_{k+1} - r_k} \quad (2.31)$$

where  $l$  is the number of observation replacing  $ij$ ,  $1 \leq l \leq n$ ,

$i$  is the number of earthquakes,  $1 \leq i \leq ne$ ,

$k$  is the number of distance terms,  $1 \leq k \leq m$ , and

$j$  is the number of sites,  $1 \leq j \leq ns$ .

The matrix form is represented as:

$$A_{(n+m+1) \times 1} = B_{(n+m+1) \times (ne+m+ns)} \cdot M_{(ne+m+ns) \times 1} \quad (2.32)$$

where  $A_l$  is the logarithm of the observed processed peak values of the filtered time histories or Fourier spectra. Rows are added to enforce the regression constraint. In the following matrix, the rows above the first dotted lines relate to the data, the row between first and second dotted lines refers to the constraint to the site terms, the row between second and third dotted lines applied to the

smoothing of the attenuation term, and the last row is used to force the reference distance at the propagation functional to be zero. The general regression is performed by the least-squares algorithm. The form of the linear system equation is

	Source terms	Distance terms	Site terms
$\begin{pmatrix} A_1 \\ A_2 \\ \vdots \\ \vdots \\ A_n \\ \dots \\ 0 \\ \dots \\ 0 \\ \vdots \\ \vdots \\ \vdots \\ \vdots \\ 0 \\ \dots \\ 0 \end{pmatrix}$	$= \begin{pmatrix} 1 & 0 & \dots & 0 \\ 0 & 1 & \dots & 0 \\ \vdots & \vdots & & \vdots \\ \vdots & \vdots & & \vdots \\ 0 & 0 & \dots & 1 \\ \dots & \dots & \dots & \dots \\ 0 & 0 & \dots & 0 \\ \dots & \dots & \dots & \dots \\ 0 & 0 & \dots & 0 \\ \vdots & \vdots & & \vdots \\ 0 & 0 & \dots & 0 \\ \dots & \dots & \dots & \dots \\ 0 & 0 & \dots & 0 \end{pmatrix}$	$\begin{pmatrix} 0 & p & 1-p & \dots & 0 \\ p & 1-p & 0 & \dots & 0 \\ \vdots & \vdots & \ddots & & \vdots \\ \vdots & \vdots & & \ddots & \vdots \\ 0 & 0 & p & \dots & 0 \\ \dots & \dots & \dots & \dots & \dots \\ 0 & 0 & 0 & \dots & 0 \\ \dots & \dots & \dots & \dots & \dots \\ -2w & w & 0 & \dots & 0 \\ w & -2w & w & \dots & 0 \\ \vdots & \vdots & \ddots & & \vdots \\ \vdots & \vdots & & \ddots & \vdots \\ \vdots & \vdots & & & \ddots & \vdots \\ 0 & 0 & \dots & w & -2w \\ \dots & \dots & \dots & \dots & \dots \\ 0 & w_{ref} & 0 & \dots & 0 \end{pmatrix}$	$\begin{pmatrix} 1 & 0 & \dots & 0 \\ 0 & 1 & \dots & 0 \\ \vdots & \vdots & & \vdots \\ \vdots & \vdots & & \vdots \\ 0 & 0 & \dots & 1 \\ \dots & \dots & \dots & \dots \\ u & u & \dots & u \\ \dots & \dots & \dots & \dots \\ 0 & 0 & \dots & 0 \\ \vdots & \vdots & & \vdots \\ 0 & 0 & \dots & 0 \\ \dots & \dots & \dots & \dots \\ 0 & 0 & \dots & 0 \end{pmatrix}$
		$\times \begin{pmatrix} SRC_1 \\ SRC_2 \\ SRC_3 \\ \vdots \\ SRC_{ne} \\ \dots \\ D_1 \\ D_2 \\ D_3 \\ \vdots \\ \vdots \\ D_m \\ \dots \\ SITE_1 \\ SITE_2 \\ SITE_3 \\ \vdots \\ SITE_{ns} \end{pmatrix}$	

## 2.3 Ground motion models

### 2.3.1 Earthquake dislocation and stress drop

Brune (1970, 1971) modeled an earthquake dislocation as the approximation of a tangential stress pulse applied to the dislocation surface. In this case the displacement is perpendicular to the dislocation surface. He assumed that the pulse is applied uniformly over the fault surface and fault propagation effects are neglected. The stress pulse generates a shear wave which propagates from the dislocation surfaces.

The initial time function is directly related to the effective stress and represented by the following boundary conditions

$$\sigma(x, t) = \sigma H(t - x/\beta) \quad (2.33)$$

where  $H(t)$  is the Heaviside unit step function ( $H(t) = 1, t > 0$  and  $H(t) = 0, t < 0$ ),  $\sigma$  is the effective shear stress, and  $\beta$  is the shear wave velocity. The tangential displacement of the fault surface,  $u$ , corresponding to equation 2.33, is then

$$u = (\sigma/\mu)\beta t \quad t > 0 \quad (2.34)$$

where  $\mu$  is the rigidity and  $\sigma = \mu\partial u/\partial x$ . The particle displacement is given by equation 2.34 for an observation point near the center of the dislocation surface.

The spectrum of equation 2.34 is

	near-field term	far-field term
Displacement $u(t)$	$H(t)(\sigma/\mu) \beta \tau (1 - e^{-t/\tau})$	$H(t') \frac{f r \sigma \beta}{R \mu} t' e^{-\alpha t'}$
Amplitude Spectrum $\Omega(\omega)$	$\frac{\sigma \beta}{\mu \omega (\omega^2 + \tau^{-2})^{1/2}}$	$\frac{\langle R_{\theta\phi} \rangle \sigma \beta r F(\epsilon)}{\mu R (\omega^2 + \alpha^2)}$

Table 2.1: Earthquake source model of Brune (1970, 1971).  $r/\beta$  is the decay time,  $f r/R$  is a factor to take into account spherical spreading,  $t' = t - R/\beta$ .  $\langle R_{\theta\phi} \rangle$  is the *rms* average of the radiation pattern,  $r$  is the radius of an equivalent circular dislocation surface,  $R$  is the distance,  $F(\epsilon) = \{[2 - 2\epsilon][1 - \cos(1.21 \epsilon \omega / \alpha)] + \epsilon^2\}^{1/2}$ ,  $\epsilon$  is the fraction of stress drop, and  $\alpha = 2.21 \beta/r$

$$\Omega(\omega) = \int_0^\infty \frac{\sigma \beta t e^{-i\omega t}}{\mu} dt = \frac{-\sigma \beta}{\omega^2 \mu}. \quad (2.35)$$

This model describes the initial near-field radiation. However, the faulting process stops. The function  $\tau(1 - e^{-t/\tau}) \approx r/\beta$  for  $t \leq \tau$ ,  $\tau$  is the order of the dimension of the fault divided by the shear-wave velocity, can be used to represent the effect of applying a step change in stress and yet permits the near-field movement to stop. The far-field measured signal is the first derivative of the near-field signal.

Table 2.1 shows the earthquake source model ( $\omega$  square model) of Brune (1970, 1971). The Brune model permits an estimation of the stress parameter,  $\sigma$ , from observed spectra. He further showed how the moment is related to the stress drop and fault radius.

### 2.3.2 Stochastic modeling

Equations for predicting ground motion as a function of magnitude and distance can be determined empirically or model based. Empirical methods require many earthquakes having various earthquake size and observation distance to perform a reliable regression. While, model based predictions apply parametric models to represent excitation of source, duration and propagation using in a stochastic simulation of ground motion.

Keiiti Aki's early work (1966, 1967) on the shape and scaling of source spectra and seismic moment has been applied to predict high frequency ground motions. McGuire and Hanks (1980) combined seismic models of the spectral amplitude of ground motion with the concept that high frequency motions are random to predict *RMS* values.

Boore (1983) generated and extended the work of McGuire and Hanks (1980) to simulate time series by assuming the high frequency ground motion at a particular distance and site condition is distributed with random phase over a time duration related to earthquake size. Herrmann (1985) added the effect of propagation distance duration. A stochastic, instead of a deterministic, description of the source and path is often referred to as the stochastic model or stochastic method. The essence of the stochastic method is that the spectrum of the ground motion is usually encapsulated into simple equations. Frequency domain source spectrum scaling models are often described as a function of seismic moment or moment magnitude. This simple one parameter scaling

model provides a good fit to many aspects of high frequency ground motion.

The observed signal spectrum is formulated as:

$$a(\omega) = CM_0S(\omega, \omega_c)P(\omega, \omega_m)\frac{e^{-\omega R/2Q\beta}}{R} \quad (2.36)$$

where  $C$  is a constant,  $M_0$  is the seismic moment which is introduced by Aki (1966),  $P(\omega, \omega_m)$  is a high cut filter, and  $\frac{e^{-\omega R/2Q\beta}}{R}$  is the path term. Usually just one form of the source spectrum scaling is used for a given region. For the simple model given above, the corner frequency ( $f_c = \omega_c/2\pi$ ) is a function of seismic moment  $M_0$ . The source spectrum  $S(\omega, \omega_c)$  has its origin from Aki (1967) and Brune (1970, 1971)

$$S(\omega, \omega_c) = \frac{\omega^2}{1 + (\omega/\omega_c)^2} \quad (2.37)$$

where  $S(\omega, \omega_c)$  is the  $\omega$ -squared model. These parameters in turn can be related to the stress drop ( $\Delta\sigma$ ), a parameter controlling the strength of high frequency radiation, of a simple model of the fault (Brune, 1970, 1971) by the following equation

$$f_c = 4.9 \times 10^6 \beta (\Delta\sigma/M_0)^{1/3}. \quad (2.38)$$

Successful applications of the stochastic simulation was performed using 15 Hz cutoff frequency ( $f_m$ ) and  $\Delta\sigma = 100$  bars (Boore, 1983). This model fit all essential aspects of high frequency ground motion for earthquakes over a large magnitude range for western United States and would be valuable in the

Central and Eastern United States where earthquakes are of moderate size. The stochastic method does not include any phase effects due to the propagating rupture and to the wave propagation enroute to the site (including local site response). The differences between the various components of motion and different wave types are ignored. Fault-normal effects, phase differences over horizontal distances and directivity are not captured by the simulated motions. A common complaint often expressed is that most of the models based on the stochastic method are fundamentally a point-source model that excludes the near and intermediate field terms. This is not a concern if the frequencies are high enough ( $> 1$  Hz) that the far field terms dominate the spectrum, even if the site is near the fault. Using the closest distance to faulting (e.g., 1 km: from the source to site distance) as a measure of distance may help capture much of the near fault effect (Boore, 2003).

Atkinson (1993a) proposed an empirical source spectrum with two corner frequencies to describe the low to middle frequencies ( $\sim 0.1 - 2.0$  Hz) correctly for earthquakes in Eastern North America. This two-corner point-source model was applied later to develop stochastic ground motion for eastern North America. Atkinson and Silva (1997) and Beresnev and Atkinson (1997, 1998, and 1999) showed that the spectral shape of the stochastic finite-fault model provided a better fit to the observed spectra and accurate ground motion parameters for other study regions.

### 2.3.3 Two corner model

The stochastic point source model has been successful in characterizing high frequency (1 - 10 Hz) ground motions as finite-duration bandlimited Gaussian noise with an underlying amplitude spectrum at large distances represented by a simple source and propagation processes. Because this method is independent of the fault orientation and calculated over a whole sphere (Beresnev and Atkinson, 2002), the relative slips on simple faults may be similar (Atkinson and Beresnev, 1997). The point-source model does not fit observations well for the near-source observations from large earthquakes. That effect includes rupture propagation, directivity, source-receiver geometry and influences the amplitudes, frequency content, and duration of ground motion (Beresnev and Atkinson, 2002).

Boatwright and Choy (1992) argued that the teleseismic spectra of large intraplate events generally depart from the Brune model and most intraplate earthquakes may have two corner frequencies. Atkinson (1993a) introduced two-corner Brune spectra for the earthquake source spectrum  $E(M_0, f)$  for the horizontal component of ground motion in Eastern North America. This is an empirical representation instead of a theoretical model. The dramatic reduction of spectral amplitudes at intermediate frequencies (about 0.1 - 1 Hz) relative to Brune (1970) model is the most important feature of equation 2.39. The input parameters for ground motion predictions are similar to the stochastic model except for the following source term:

$$E(M_0, f) = C (2\pi f)^2 M_0 \left[ \frac{1 - \epsilon}{1 + (f/f_A)^2} + \frac{\epsilon}{1 + (f/f_B)^2} \right], \quad (2.39)$$

where  $C = \frac{R_p F V}{4\pi\rho\beta^3 R}$ ,  $R = 1$  km,  $R_p =$  average radiation pattern (0.55),  $F =$  free-surface amplification (2.0),  $V =$  partition onto two horizontal components (0.71),  $\rho =$  crustal density ( $2.8$  g/cm<sup>3</sup>), and  $\beta =$  shear-wave velocity ( $3.8$  km/sec).  $\epsilon$ ,  $f_A$ , and  $f_B$  are functions of seismic moment for  $4 \leq M \leq 7$  by

$$\log \epsilon = 2.52 - 0.637 M \quad (2.40)$$

$$\log f_A = 2.41 - 0.533 M \quad (2.41)$$

$$\log f_B = 1.43 - 0.188 M. \quad (2.42)$$

The lower corner frequency ( $f_A$ ) is  $1/2T$  where  $T$  is the source duration (Boatwright and Choy, 1992) while the upper corner frequency ( $f_B$ ) is determined from the source terms of the regression result.  $\epsilon$  is the value determined from the source terms in order to reduce the average misfit of equation 2.39 after lower and upper corner frequency are defined from previous relations (Atkinson and Silva, 1997).

Equation 2.39 was derived from 22 eastern North America earthquakes with  $4 \leq M < 7$  from several sources which cover the frequency range from 1 to 10 Hz. This equation matches both spectral amplitudes and corner frequencies. One of the most important aspects of equation 2.39 is the reduction

of spectral amplitudes at intermediate frequencies relative to the Brune model. Figure 1 of Atkinson and Boore (1995) compares the Brune 100 bar model to the empirical two-corner model. The two-corner model has a sag in spectral amplitudes near 1 Hz. The two-corner model was constrained by data from the Saguenay ( $M_W$  5.8) and Nahanni ( $M_W$  6.8) earthquakes (Atkinson and Boore, 1995).

The parameters determined for California source scaling modeling are  $\log f_A = 2.181 - 0.496 M$ ,  $\log f_B = 1.778 - 0.302 M$ , and  $\log \epsilon = 2.764 - 0.623 M$ . The higher  $f_B$  and  $\epsilon$  of *ENA* compared to California were required to fit the large spectral level of high frequencies (Atkinson and Silva, 1997).

### **2.3.4 Finite fault model**

The point source model has weakness in characterizing the ground motion features of large earthquakes, e. g., their long duration and the dependence of amplitudes and duration on the azimuth to the observation point, source and directivity (Beresnev and Atkinson, 2002). For larger events, the spectrum becomes complicated and stress drop becomes non-unique depending how it is measured. The source spectra can be modeled using concepts such as fractional stress drop, variable slip, dominant asperities or barriers, strong directivity effects, etc. (Atkinson and Beresnev, 1997). The finite fault model was developed to overcome the weakness of the point source model.

The first assumption of this method is that a large earthquake is composed of independent events occurring on independently rupturing subfaults.

A methodology that combines the finite source modeling technique (Hartzell, 1978) and the stochastic point source model has been developed by Silva et al. (1990), Silva and Stark (1992), and Schneider et al. (1993) to accommodate the effect of large finite source. In this model, the stochastic point source ground motions replace the empirical Green's function. The finite source model discretizes a rectangular fault into numbers of subfaults. In this case, each subfault is treated as a single point source. Factors such as location of the subevents within each fault (Hartzell, 1978) and subevent rise times are applied to generate the heterogeneity of the source process. Random slip values are signed to each asperity to give relative weights to form nonuniform slip (Atkinson and Silva, 1997). The rupture starts from a hypocentral point on the fault and propagates radially from it. The rupture triggers sub-faults as it passes those faults. The propagating fields from all subevents are delayed and added together geometrically at the observation point (Beresnev and Atkinson, 2002). Rupture velocity and radiation patterns also added the random components in each subfaults (Atkinson and Silva, 1997). The finite fault source model affects the duration, directivity of ground motions, and the shape of the spectra of seismic waves. The difference in spectral shape for a small magnitude event is not significant between the finite-fault method and point source models. A detailed description of this method is given by at Atkinson and Silva (1997). The 1989 Loma Prieta (Schneider et al., 1993) and 1987 Whittier Narrows earthquakes (Abrahamson et al., 1990) are used to test the validity of the finite fault stochastic model and found no apparent misfit in simulating the

ground motion of those earthquakes.

## Chapter 3

# Ground motion scaling in southeastern Canada

### 3.1 Data set

#### 3.1.1 CNSN network

The Canadian National Seismograph Network (CNSN) has about 100 high-gain seismographs, and about 60 low-gain accelerographs. The high-gain instruments are used to record weak ground motion from small local earthquakes and distant sites, while the low-gain instruments are used to record the strong ground shaking of larger earthquakes near the sites ([http://www.seismo.nrcan.gc.ca/cnsn/index\\_e.php](http://www.seismo.nrcan.gc.ca/cnsn/index_e.php)).

The strong motion seismograph triggers when the ground shaking exceeds  $0.25 - 1\%g$  and stops when the ground shaking returns to an imperceptible level. The Geological Survey of Canada (GSC) operates more than 30 strong motion instruments in British Columbia, 18 instruments radiating out from the Charlevoix zone in eastern Canada and other regions require to monitor strong motion ([http://www.seismo.nrcan.gc.ca/cnsn/sm-net\\_e.php](http://www.seismo.nrcan.gc.ca/cnsn/sm-net_e.php)).

The high-gain seismographs are installed in quiet sites, far from human made noise such as trains, vehicle traffic, mines, waves generated by oceans and lakes, and wind shaking the trees. They consist of two types of instruments: three-component broad band instruments recording a wide frequency band (typically from 0.03 Hz to 10 Hz), and vertical component short period in-

<b>Broad Band CNS Network</b>				
STN code (BH*)	Lat	Lon	Elev (km)	Station location
A11	47.2425	-70.1978	0.061	ST-ROCH-DES-AULNAIES, Quebec
A16	47.4706	-70.0064	0.015	RIVIERE OUELLE, Quebec
A21	47.7036	-69.6897	0.046	ST-ANDRE, Quebec
A54	47.4567	-70.4125	0.381	MISERE, Quebec
A61	47.6930	-70.0900	0.358	SAINTE MATHILDE, Quebec
A64	47.8264	-69.8922	0.137	SAINT-SIMEON, Quebec
FCC	58.7616	-94.0866	0.039	FORT CHURCHILL, Manitoba
FNB	58.8904	-123.0097	0.618	FORT NELSON, British Columbia
FNBB	58.8904	-123.0097	0.618	FORT NELSON, British Columbia
GAC	45.7033	-75.4783	0.062	GLEN ALMOND, Quebec
GGN	45.1184	-66.8421	0.006	ST. GEORGE, New Brunswick
ICQ	49.5217	-67.2719	0.058	ISLETS-CARIBOU, Quebec
KAP	49.4504	-82.5079	0.210	KAPUSKASING, Ontario
KAPO	49.4504	-82.5079	0.210	KAPUSKASING, Ontario
KGN	44.2272	-76.4934	0.089	KINGSTON, Ontario
KGNO	44.2272	-76.4934	0.089	KINGSTON, Ontario
LMN	45.8520	-64.8060	0.363	CALEDONIA MTN., New Brunswick
LMQ	47.5483	-70.3267	0.419	LA MALBAIE, Quebec
MNT	45.5025	-73.6231	0.112	MONTREAL, Quebec
OTT	45.3942	-75.7167	0.077	OTTAWA, Ontario
SAD	44.7694	-79.1417	0.243	SADOWA, Ontario
SADO	44.7694	-79.1417	0.243	SADOWA, Ontario
SCH	54.8319	-66.8336	0.501	SECHELT, British Columbia
SCHQ	54.8319	-66.8336	0.501	SECHELT, British Columbia
ULM	50.2499	-95.8750	0.281	LAC DU BONNET, Manitoba
VLD	48.1124	-77.4536	0.093	VAL D'OR, Quebec
VLDQ	48.1124	-77.4536	0.093	VAL D'OR, Quebec
YK5	62.4822	-114.4843	0.205	YELLOWKNIFE, Northwest Territories
YKW5	62.4822	-114.4843	0.205	YELLOWKNIFE, Northwest Territories

Table 3.1: List of stations for the Broad Band Canadian National Seismograph Network. CNS in the top panel is an acronym for Canadian National Seismograph. STN code represents the station code, Lat, Lon, and Elev each denote latitude, longitude, and elevation.

struments which record continuously at a higher sample rate (100 sample/second).

The broad band instruments provide high frequency data for local earthquakes as well as longer period energy associated with large and more distant earthquakes (<http://www.seismo.nrcan.gc.ca/cnsn/seis-net.e.php>).

The stations used in this study are mainly from the Eastern Canada network and a few stations from Arctic Canada network. The Arctic Canadian stations provide data only for moderate earthquakes. Tables 3.1, 3.2, and 3.3 are the descriptions for the Canadian National Seismograph Network used for this study (<http://www.seismo.nrcan.gc.ca/cnsn/can-list.e.php>).

<b>Extremely Short Period CNS Network</b>				
STN code (EHZ)	Lat	Lon	Elev (km)	Station location
CNQ	49.3022	-68.0744	0.200	COTE-NORD, Quebec
CRL	46.0375	-77.3801	0.168	CHALK RIVER, Ontario
CRLO	46.0375	-77.3801	0.168	CHALK RIVER, Ontario
DAQ	47.9644	-71.2425	0.939	LAC DARAN, Quebec
DPQ	46.6804	-72.7774	0.167	ST-JEAN-DES-PILES, Quebec
EEO	46.6411	-79.0733	0.398	ELDEE, Ontario
GRQ	46.6067	-75.8600	0.290	GRAND-REMOUS, Quebec
GSQ	48.9142	-67.1106	0.398	GROSSES-ROCHES, Quebec
GTO	49.7455	-86.9610	0.350	GERALDTON, Ontario
LG4	53.6269	-74.0972	0.168	LAGRANDE4, Quebec
LG4Q	53.6269	-74.0972	0.168	LAGRANDE4, Quebec
MOQ	45.3120	-72.2541	0.841	MONT-ORFORD, Quebec
SMQ	50.2225	-66.7025	0.344	STE-MARGUERITE, Ontario
SOL	50.0213	-92.0812	0.373	SIOUX LOOKOUT, Ontario
SOLO	50.0213	-92.0812	0.373	SIOUX LOOKOUT, Ontario
TBO	48.6473	-89.4083	0.468	THUNDER, Ontario
TRQ	46.2222	-74.5556	0.853	MONT-TREMBLANT, Ontario
WBO	45.0003	-75.2750	0.085	WILLIAMSBURG, Ontario

Table 3.2: List of stations for the Extremely Short Period Canadian National Seismograph Network. CNS in the top panel is an acronym for Canadian National Seismograph. STN code represents the station code, Lat, Lon, and Elev each denote latitude, longitude, and elevation.

<b>Other Canadian National Seismograph Network</b>					
STN code	Lat	Lon	Elev (km)	CNSN	Station location
EFO	43.0917	-79.3117	0.168	ESPDialup	EFFINGHAM, Ontario
KUQ	58.1090	-68.4113	0.054	ESPDialup	EFFINGHAM, Ontario
QCQ	46.7789	-71.2758	0.091	ESPDialup	QUEBEC, Quebec
PKR	43.9639	-79.0708	0.197	POLARIS	PICKERING, Ontario
PKRO	43.9639	-79.0708	0.197	POLARIS	PICKERING, Ontario
FRB	63.7467	-68.5467	0.018	VBBCNSN	IQALUIT, Northwest Territories
DRL	49.2560	-57.5042	0.238	VBBCNSN	DEER LAKE, Newfoundland
DRLN	49.2560	-57.5042	0.238	VBBCNSN	DEER LAKE, Newfoundland
YK2	62.425	-114.605	0.180	VBBCNSN	YELLOWKNIFE, Northwest Territories
YKW2	62.425	-114.605	0.180	VBBCNSN	YELLOWKNIFE, Northwest Territories
YK4	62.492	-114.742	0.200	VBBCNSN	YELLOWKNIFE, Northwest Territories
YKW4	62.492	-114.742	0.200	VBBCNSN	YELLOWKNIFE, Northwest Territories
YK3	62.5616	-114.6099	0.200	HBB/VBB	YELLOWKNIFE, Northwest Territories
YKW3	62.5616	-114.6099	0.200	HBB/VBB	YELLOWKNIFE, Northwest Territories

Table 3.3: List of stations for the rest of Canadian National Seismograph Network used for this study. ESPDialup represents Extremely short period Dialup CNSN (EHZ) station. POLARIS indicates the Broadband POLARIS Canadian stations. VBBCNSN is Very Broadband CNSN (BH\*) stations. HBB/VBB means that the station is either High Broadband CNSN (HH\*) or Very Broadband CNSN (BH\*).

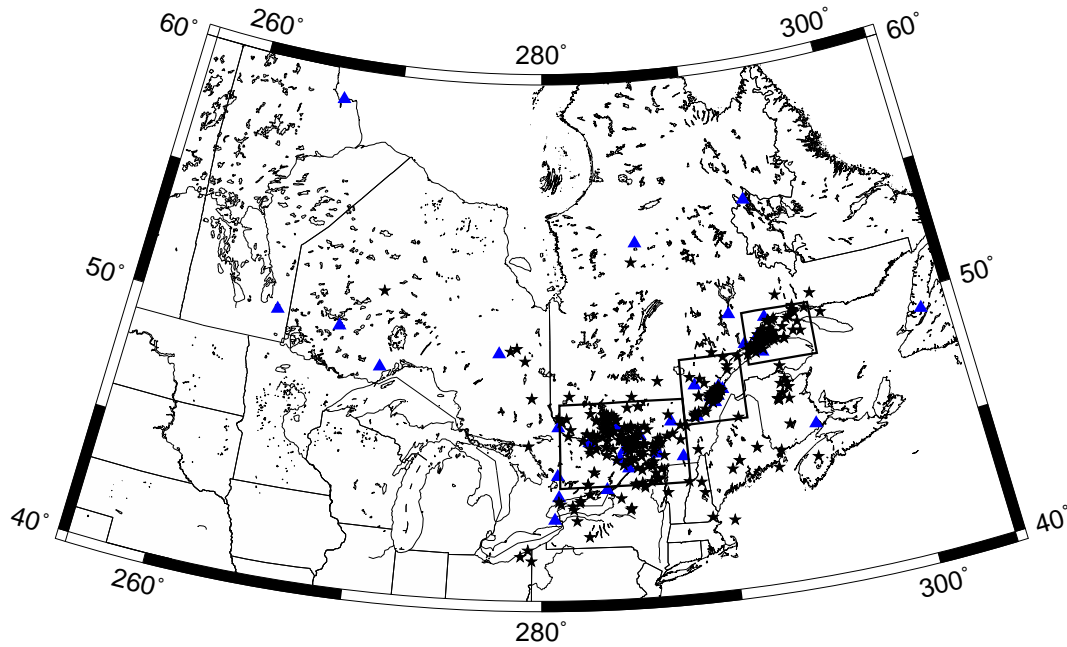


Figure 3.1: Map of epicenters (stars) and stations (triangles) for the study area.

### 3.1.2 Data set and study area

The study area ranges from  $40^{\circ}$  to  $60^{\circ}$  in latitude and from  $85^{\circ}$  to  $65^{\circ}$  in longitude (degrees west). Figure 3.1 is the map of the epicenters of the events and stations of the CNSN network providing the waveform data set for Canadian study. Figures 3.2, 3.3, and 3.4 are the detailed maps for the insets shown in Figure 3.1.

The data set used in this study consists of 394 earthquakes and 4646 waveforms recorded from 1993 to 2004. For every waveform, the first arrivals of P and S waves were picked to measure hypocentral distance between source and receiver. Figure 3.5 shows the vertical component distance coverage for CNSN stations. The observation distances for each station must cover a broad distance range and overlap with other stations to avoid the trade off of the site

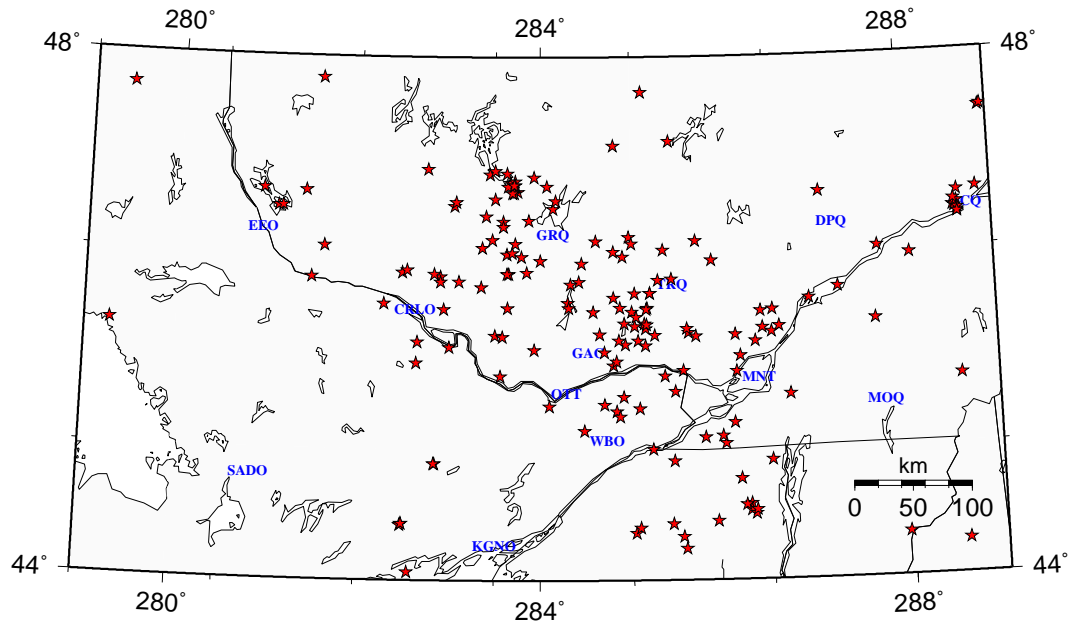


Figure 3.2: Map of seismograph stations and epicenters in Western Quebec, Eastern Ontario. The epicenters are marked by the stars and the stations are represented by the station code.

and propagation terms in the regression.

## 3.2 Data processing

### 3.2.1 Coda Shape

Figures 3.6 and Figures 3.7 illustrate the decay shape of the normalized coda as a function of time. Every peak value is normalized to the value of the coda at a reference level. The coda-normalized *RMS* average over a 256 point running window is computed for each time series and plotted with time. The black lines denote the initial part before the P-wave arrival which is regarded as the background noise of the seismic signal, light gray lines are the signal between P and S-wave arrivals, gray lines represent the coda-normalized *RMS* average between the S-wave arrival. The dark gray lines are signal in the sta-

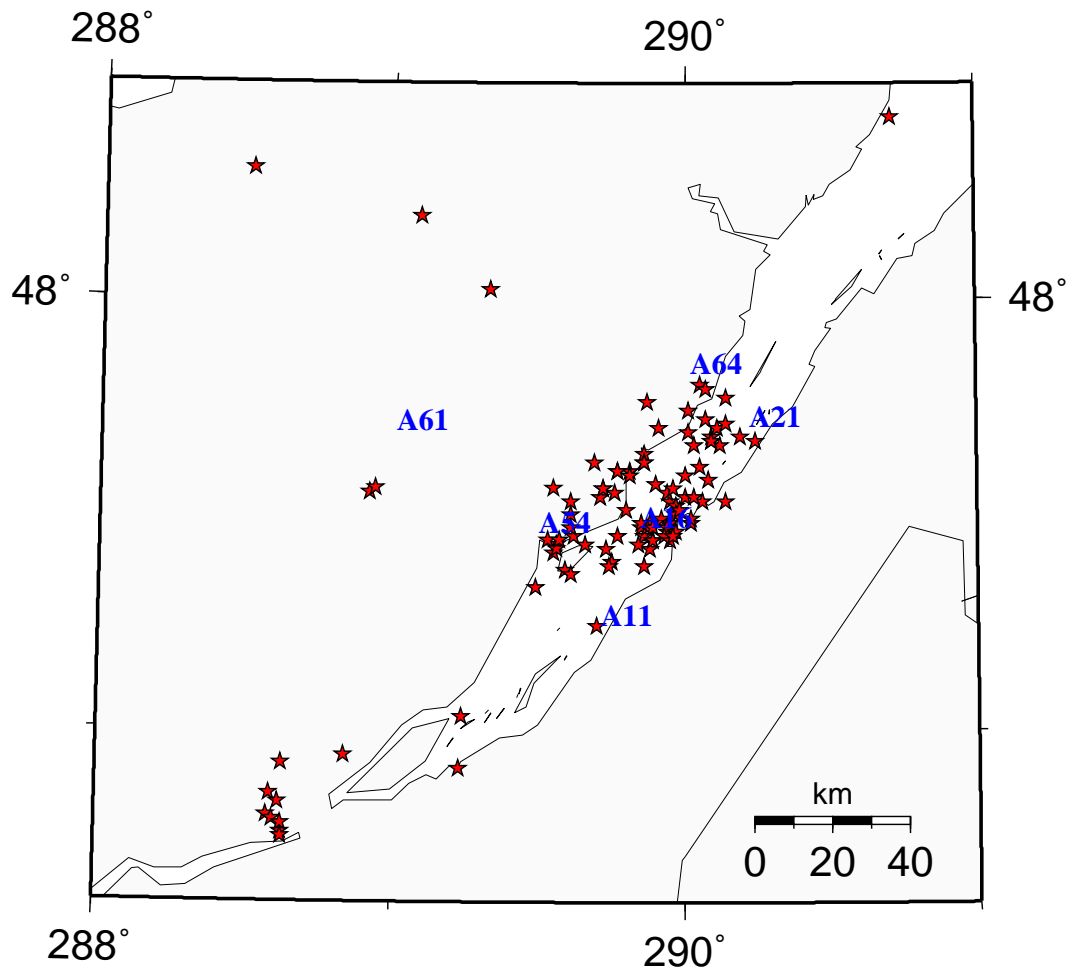


Figure 3.3: Map of seismograph stations and epicenters in the Charlevoix - Kamouraska, Quebec. The epicenters are marked by the stars and the stations are represented by the station code.

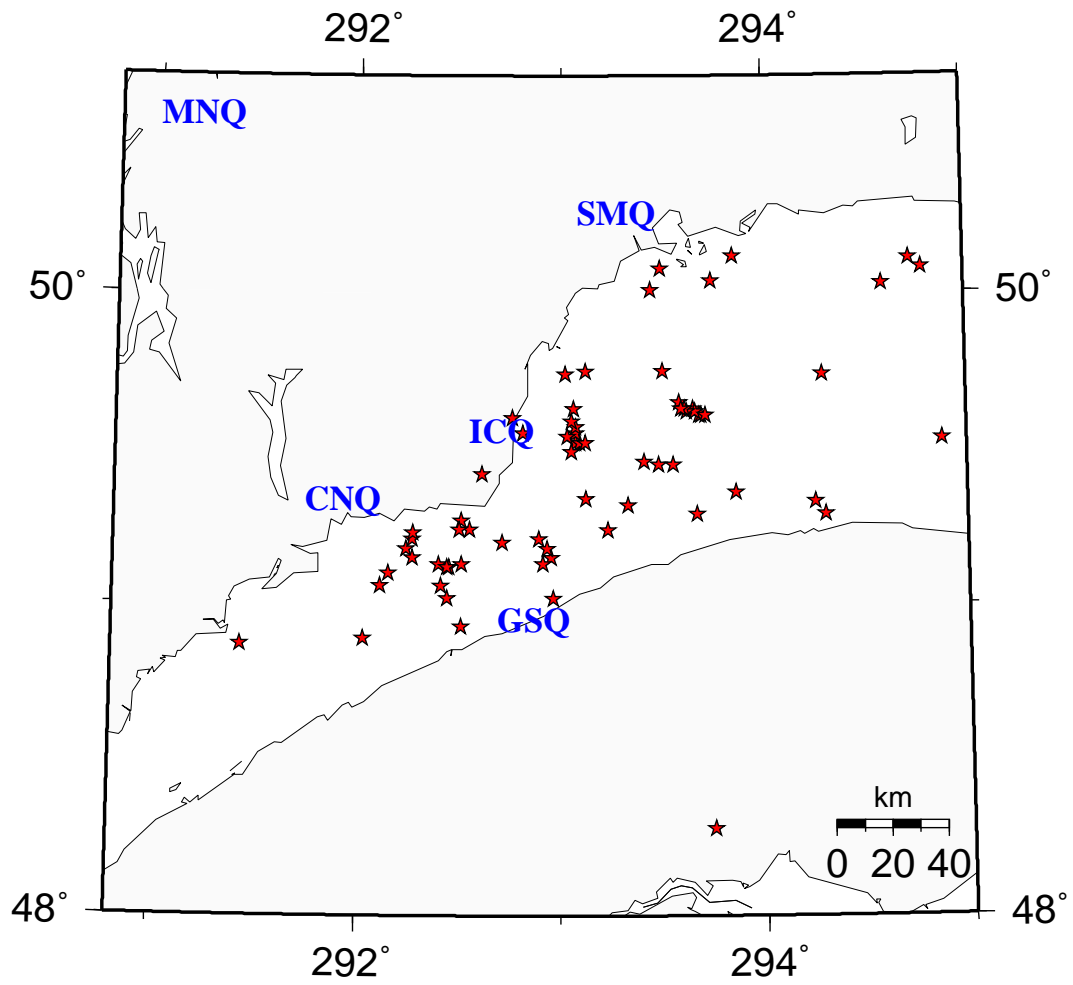


Figure 3.4: Map shows the seismograph stations and epicenters located upper right corner of Quebec.

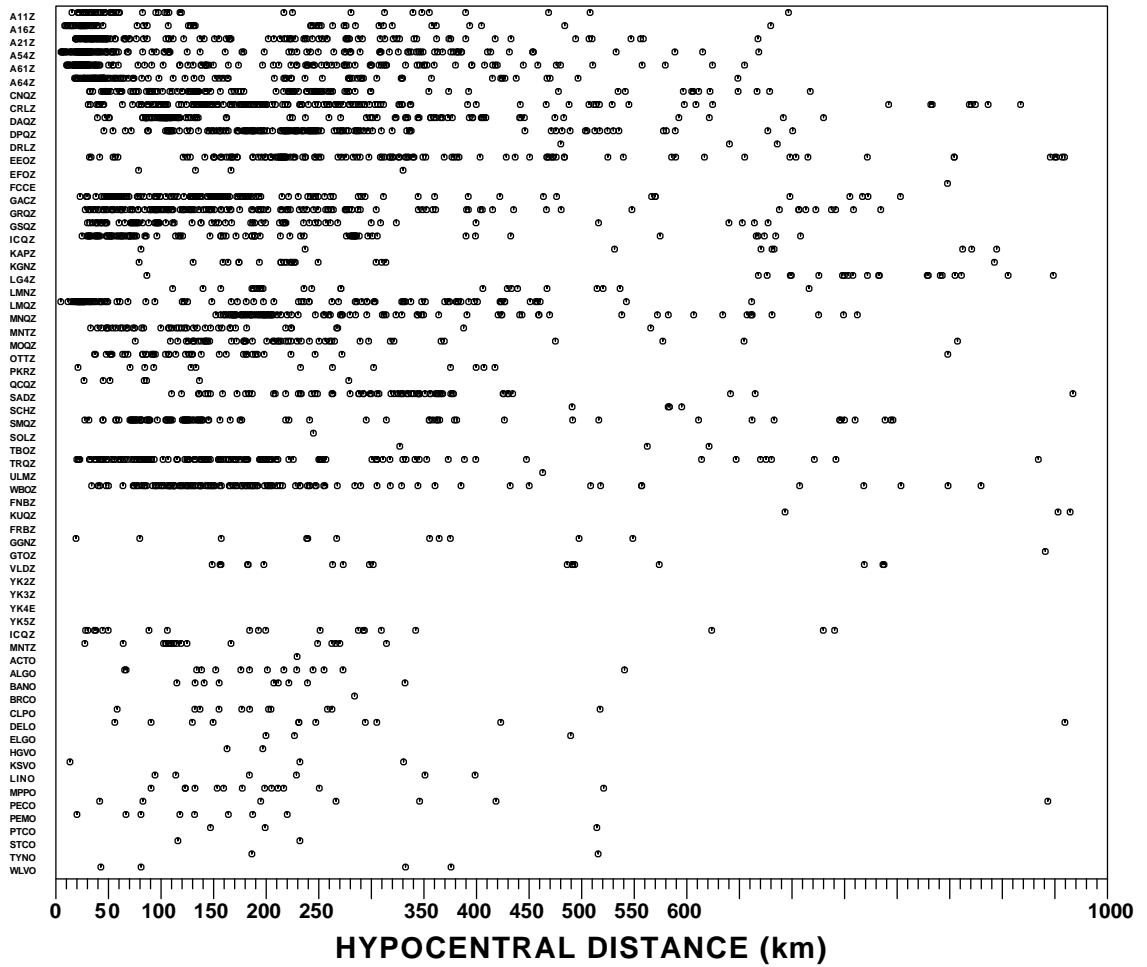


Figure 3.5: Source-receiver hypocentral distance distribution of observed stations for the data recorded along the seismic network.

ble coda which start at  $2t_s$ . The heavy gray line is the empirically determined coda shape function. The symbols denote the peak amplitude (gray triangles) value and the normalized peak amplitude (circles) used to provide an initial estimate of  $D(r)$ . The distribution of the normalized amplitudes is well defined and shows a consistent shape even some outliers exist.

### 3.2.2 Regression of Fourier velocity spectra

Figures 3.8 and 3.9 shows typical examples of the regression analysis at filter frequencies of 2.0, 4.0, 8.0, and 12.0 Hz on the Fourier velocity spectra. Top panels show the coda propagation term estimated by the coda normalization technique. The coda and regression propagation functionals in the mid-panels show similar trends for the Fourier velocity spectra data set at short and mid distance ranges. The slope of regression propagation functionals at large distance ranges are lower than those of coda propagation functionals because band-passed  $S$  wave regression propagation functionals do not contain propagation functionals of  $L_g$  waves which are dominant at large distance range. The estimates of the standard errors of the  $D(r, f)$  are about 0.1  $\log_{10}$  units from 1 - 16 Hz. Fourier velocity spectra residuals at the bottom maintain a uniform distribution for the entire distance range, meaning that the residuals are independent of distance.

Figure 3.10 shows the three component distance scaling of the  $D(r)$  term at the ten different frequencies for a regression on the Fourier velocity spectra. The figure is corrected for an  $r^{-1}$  hypocentral distance trend to emphasize

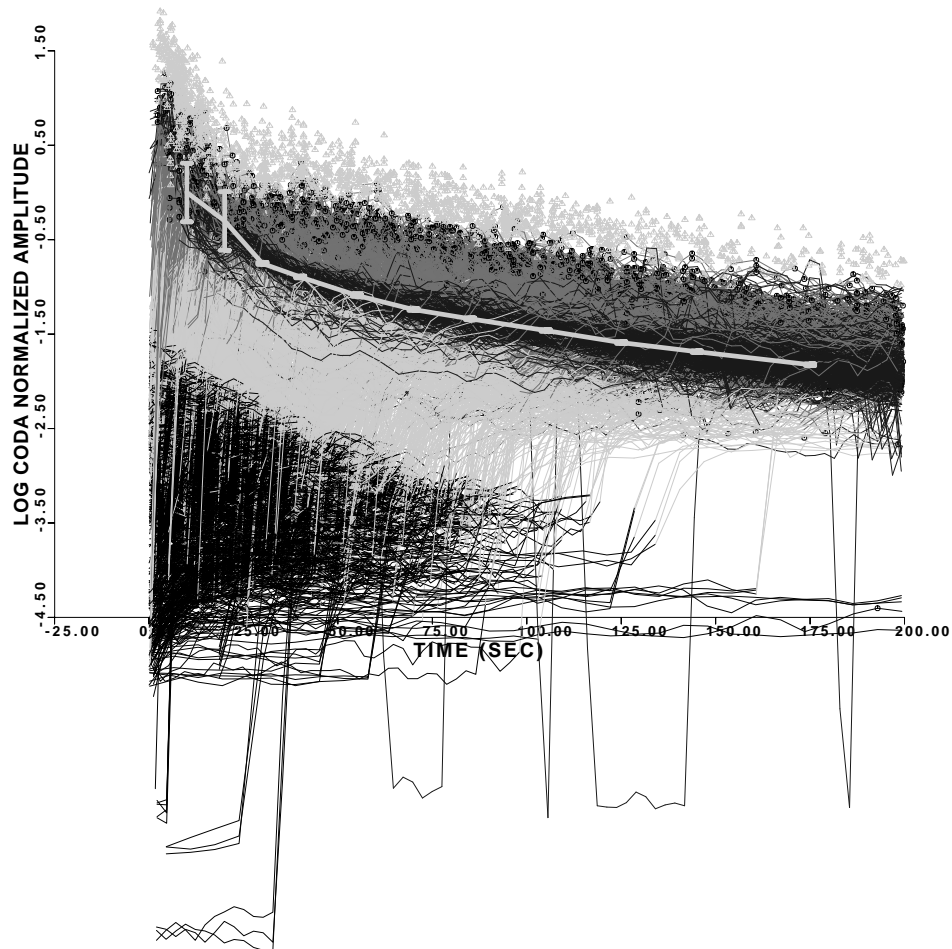


Figure 3.6: Shape of the 1.0 Hz normalized seismic coda as a function of lapse time from earthquake origin time. The black lines denote the initial part before the P-wave arrival, light gray lines are the signal between P and S-wave arrivals, gray lines are the coda-normalized *RMS* average between the S-wave arrival and the dark gray segment of the curves start at  $2t_s$ . Gray triangles represent the peak values and circles denote normalized peak amplitudes.

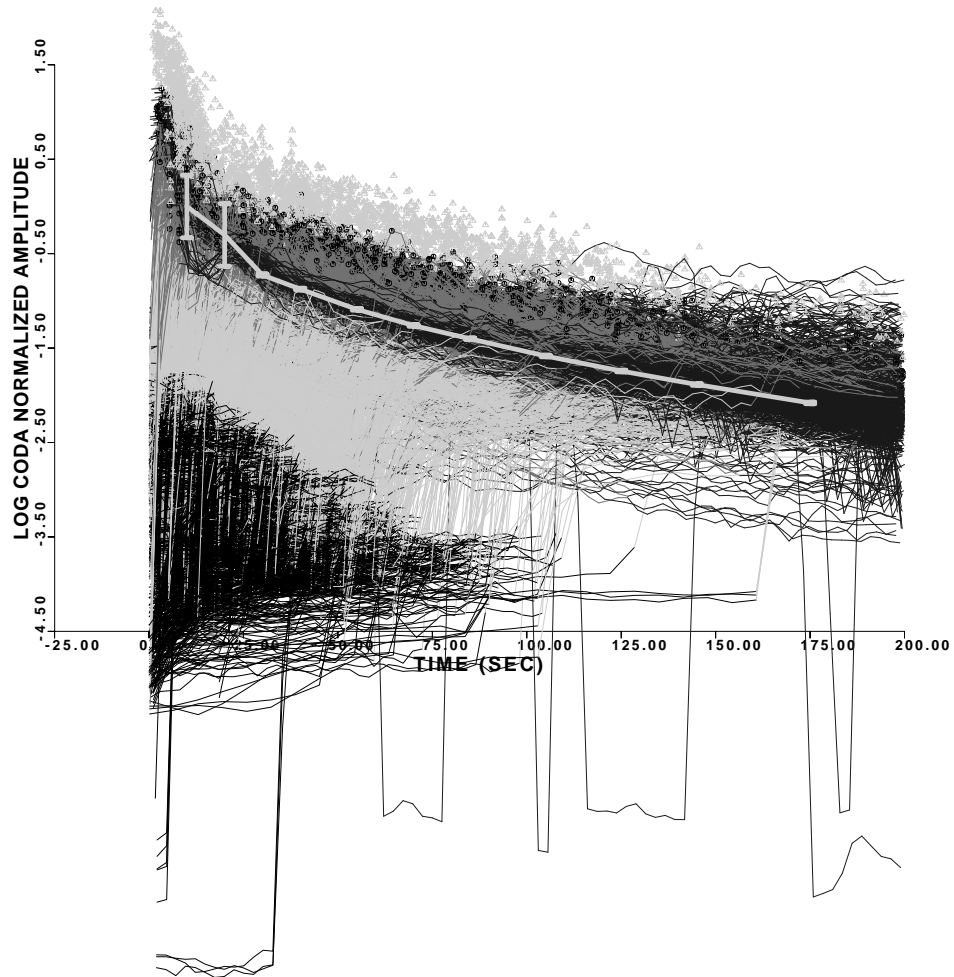


Figure 3.7: Shape of the 6.0 Hz normalized seismic coda as a function of lapse time from earthquake origin time. The black lines denote the initial part before the P-wave arrival, light gray lines are the signal between P and S-wave arrivals, gray lines are the coda-normalized *RMS* average between the S-wave arrival and the dark gray segment of the curves start at  $2t_s$ . Gray triangles represent the peak values and circles denote normalized peak amplitudes.

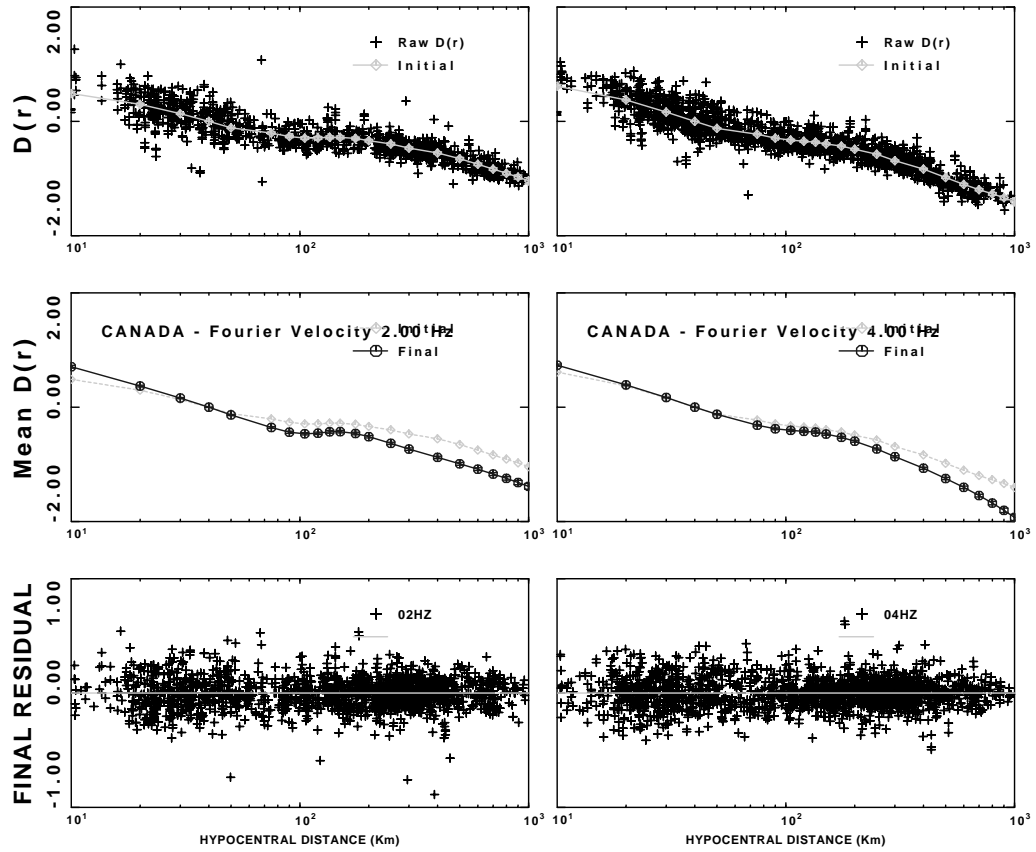


Figure 3.8: Regression analysis for 2.0 and 4.0 Hz. Top, coda estimate of  $D(r)$  using coda normalization technique. Middle, coda and regression propagation functionals. Bottom, final residuals of the regression analysis.

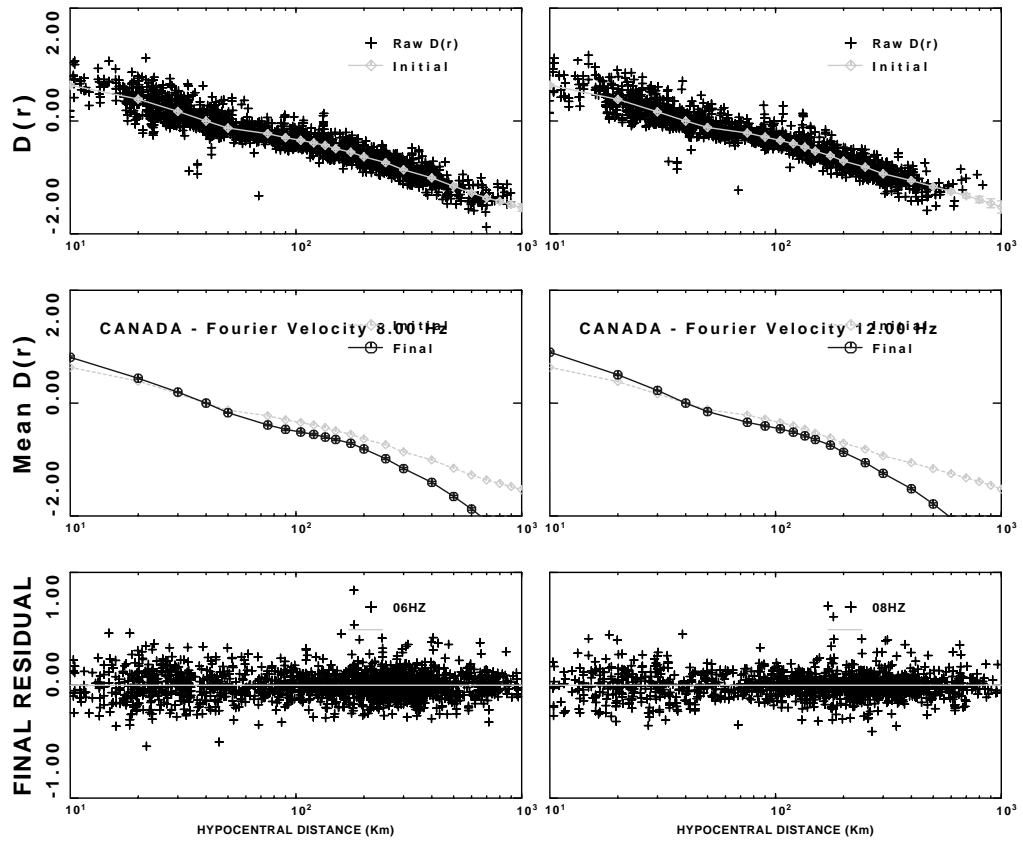


Figure 3.9: Regression analysis for 8.0 and 12.0 Hz. Top, coda estimate of  $D(r)$  using coda normalization technique. Middle, coda and regression propagation functionals. Bottom, final residuals of the regression analysis.

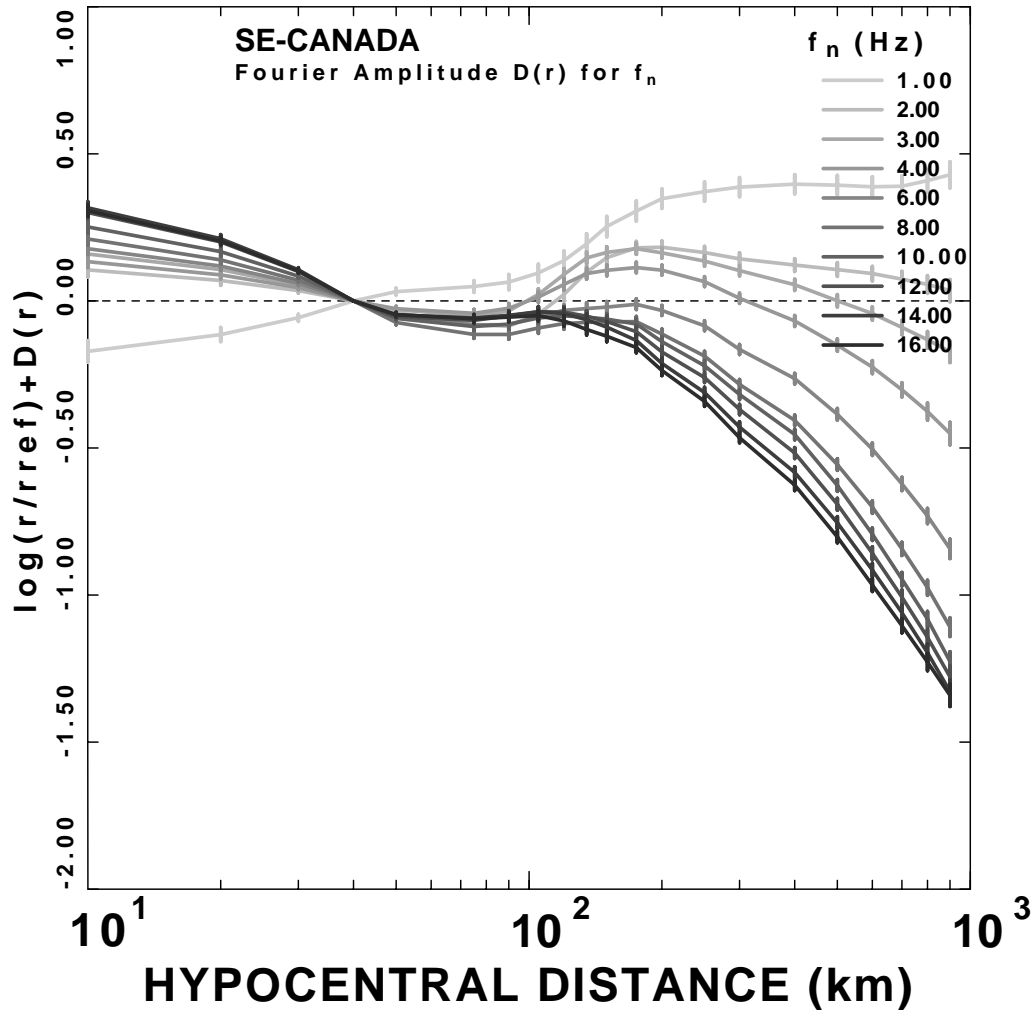


Figure 3.10: The reduced attenuation functional  $D(r, f)$  obtained from the regression on the Fourier velocity spectra at the frequencies of 1.0, 2.0, 3.0, 4.0, 6.0, 8.0, 10.0, 12.0, 14.0, and 16.0 Hz for southeastern Canada.

departure of high frequency spectra scaling with distance from  $r^{-1}$  spreading. The reference distance at 40 km was used to normalize the  $D(r, f)$  and the horizontal dashed line represents  $r^{-1}$  trend. The 1 Hz signal at short distance range in the top panel shows a different propagation shape compared to the rest of the  $D(r, f)$ . It may be that the 1 Hz signal is affected by noise that impairs the duration estimation.

Tables 3.4, 3.5, and 3.6 show the numerical results of the regression on the regional attenuation functional for Fourier velocity spectra. They give the corresponding value of  $D(r)$  for each frequency and distance as well as number of observation contributing to each node and error bars. Table 3.7 shows the number of waveforms used for the regressions. The Fourier domain waveforms number less than 50% of time domain waveforms due to the automatic rejection by the program if the waveforms have low signal to noise ratio.

### 3.2.3 Duration

Predicting peak time-domain amplitudes using  $RVT$  assumes stationary time series while the time series of seismology are not stationary. Boore (1983) demonstrated that  $RVT$  gave good predictions of peak motion from time-domain simulation, but encountered difficulties predicting the peak response of long period, lightly damped oscillators (Boore and Joyner, 1984).

The problem lies in using time-domain durations in two places: in determining  $N$  and in calculating  $a_{rms}$ . The number of extrema,  $N$ , that might produce the peak motion is given by a characteristic frequency ( $\approx f$ ), given by ratios of spectral moments (Boore, 1983), of the motion times the duration of quasi-stationary shaking and the duration of shaking is taken to be the source of duration.

Herrmann (1985) indicated that the simple duration used by Boore (1983) has limitation because real earthquake signals are controlled by the source duration in the beginning, and later increasingly controlled by propagation

Southeastern Canada Fourier velocity spectra $D(r)$									
f (Hz)	r (km)	$D(r, f)$	$\sigma$	Nobs	f (Hz)	r (km)	$D(r, f)$	$\sigma$	Nobs
1.0	10	0.431	0.364E-01	8.970	2.0	10	0.708	0.247E-01	25.24
1.0	20	0.187	0.243E-01	41.22	2.0	20	0.371	0.165E-01	124.4
1.0	30	0.068	0.121E-01	58.90	2.0	30	0.160	0.824E-02	152.1
1.0	40	0.000	0.146E-05	37.85	2.0	40	0.000	0.146E-05	97.13
1.0	50	-0.065	0.117E-01	50.63	2.0	50	-0.136	0.946E-02	99.21
1.0	75	-0.224	0.200E-01	31.61	2.0	75	-0.354	0.153E-01	51.02
1.0	90	-0.288	0.261E-01	31.53	2.0	90	-0.438	0.190E-01	45.65
1.0	105	-0.324	0.303E-01	33.00	2.0	105	-0.464	0.210E-01	50.86
1.0	120	-0.340	0.330E-01	27.56	2.0	120	-0.455	0.225E-01	33.24
1.0	135	-0.334	0.345E-01	26.95	2.0	135	-0.430	0.230E-01	50.20
1.0	150	-0.321	0.347E-01	30.92	2.0	150	-0.427	0.227E-01	58.55
1.0	175	-0.335	0.342E-01	42.85	2.0	175	-0.460	0.220E-01	73.46
1.0	200	-0.351	0.334E-01	42.13	2.0	200	-0.516	0.213E-01	109.2
1.0	250	-0.424	0.328E-01	62.20	2.0	250	-0.631	0.207E-01	184.1
1.0	300	-0.488	0.326E-01	91.95	2.0	300	-0.732	0.208E-01	230.6
1.0	400	-0.603	0.328E-01	85.52	2.0	400	-0.878	0.217E-01	177.3
1.0	500	-0.703	0.334E-01	34.05	2.0	500	-0.990	0.233E-01	64.31
1.0	600	-0.788	0.340E-01	45.13	2.0	600	-1.083	0.247E-01	49.53
1.0	700	-0.853	0.352E-01	51.56	2.0	700	-1.169	0.265E-01	52.26
1.0	800	-0.892	0.382E-01	23.27	2.0	800	-1.245	0.302E-01	18.29
1.0	900	-0.923	0.447E-01	16.19	2.0	900	-1.317	0.381E-01	12.89
1.0	1000	-0.950	0.564E-01	4.920	2.0	1000	-1.383	0.519E-01	3.400
3.0	10	0.762	0.216E-01	35.70	4.0	10	0.736	0.209E-01	41.87
3.0	20	0.408	0.144E-01	153.1	4.0	20	0.390	0.139E-01	169.9
3.0	30	0.178	0.720E-02	176.2	4.0	30	0.170	0.695E-02	167.3
3.0	40	0.000	0.141E-05	112.7	4.0	40	0.000	0.135E-05	95.22
3.0	50	-0.126	0.878E-02	112.5	4.0	50	-0.123	0.842E-02	102.2
3.0	75	-0.324	0.140E-01	72.02	4.0	75	-0.315	0.136E-01	69.41
3.0	90	-0.386	0.172E-01	54.33	4.0	90	-0.377	0.167E-01	44.23
3.0	105	-0.397	0.190E-01	60.83	4.0	105	-0.406	0.182E-01	67.95
3.0	120	-0.387	0.200E-01	50.75	4.0	120	-0.421	0.191E-01	58.38
3.0	135	-0.382	0.201E-01	66.90	4.0	135	-0.435	0.192E-01	69.05
3.0	150	-0.409	0.195E-01	70.78	4.0	150	-0.470	0.188E-01	69.96
3.0	175	-0.463	0.188E-01	82.24	4.0	175	-0.527	0.181E-01	84.14
3.0	200	-0.535	0.180E-01	130.4	4.0	200	-0.594	0.173E-01	139.8
3.0	250	-0.660	0.175E-01	217.0	4.0	250	-0.730	0.169E-01	233.7
3.0	300	-0.772	0.178E-01	261.7	4.0	300	-0.866	0.175E-01	260.2
3.0	400	-0.945	0.191E-01	182.3	4.0	400	-1.068	0.188E-01	166.7
3.0	500	-1.096	0.210E-01	61.20	4.0	500	-1.247	0.206E-01	60.05
3.0	600	-1.219	0.225E-01	44.95	4.0	600	-1.401	0.223E-01	44.18
3.0	700	-1.333	0.242E-01	46.33	4.0	700	-1.545	0.244E-01	39.15
3.0	800	-1.433	0.281E-01	15.91	4.0	800	-1.677	0.291E-01	17.59
3.0	900	-1.525	0.365E-01	14.05	4.0	900	-1.803	0.385E-01	10.37
3.0	1000	-1.615	0.509E-01	3.160	4.0	1000	-1.927	0.534E-01	2.530

Table 3.4: Attenuation functional at 1.0, 2.0, 3.0, and 4.0 Hz for Fourier velocity spectra. The columns give values of frequency (first and sixth columns), hypocentral distance (second and seventh columns), attenuation  $D(r, f)$  at a reference distance of 40 km (third and eighth columns), associated error bar (fourth and ninth columns) and number of observations (fifth and tenth columns).

Southeastern Canada Fourier velocity spectra $D(r)$									
f (Hz)	r (km)	$D(r, f)$	$\sigma$	Nobs	f (Hz)	r (km)	$D(r, f)$	$\sigma$	Nobs
6.0	10	0.780	0.203E-01	44.73	8.0	10	0.813	0.210E-01	46.97
6.0	20	0.420	0.136E-01	162.9	8.0	20	0.441	0.140E-01	148.8
6.0	30	0.184	0.678E-02	147.2	8.0	30	0.195	0.699E-02	123.7
6.0	40	0.000	0.129E-05	78.65	8.0	40	0.000	0.126E-05	65.71
6.0	50	-0.146	0.821E-02	92.27	8.0	50	-0.170	0.825E-02	74.55
6.0	75	-0.354	0.132E-01	64.57	8.0	75	-0.387	0.133E-01	65.55
6.0	90	-0.433	0.164E-01	52.87	8.0	90	-0.466	0.164E-01	59.58
6.0	105	-0.471	0.183E-01	62.72	8.0	105	-0.511	0.182E-01	65.07
6.0	120	-0.509	0.194E-01	56.67	8.0	120	-0.554	0.193E-01	54.16
6.0	135	-0.554	0.197E-01	55.74	8.0	135	-0.601	0.195E-01	48.56
6.0	150	-0.595	0.191E-01	69.12	8.0	150	-0.645	0.189E-01	62.16
6.0	175	-0.652	0.182E-01	99.22	8.0	175	-0.711	0.179E-01	88.99
6.0	200	-0.731	0.174E-01	149.0	8.0	200	-0.811	0.170E-01	141.4
6.0	250	-0.880	0.169E-01	238.2	8.0	250	-0.983	0.166E-01	237.6
6.0	300	-1.040	0.172E-01	263.4	8.0	300	-1.159	0.171E-01	266.5
6.0	400	-1.264	0.183E-01	166.0	8.0	400	-1.406	0.182E-01	175.2
6.0	500	-1.482	0.199E-01	61.76	8.0	500	-1.653	0.197E-01	66.80
6.0	600	-1.680	0.213E-01	46.34	8.0	600	-1.877	0.210E-01	50.68
6.0	700	-1.865	0.229E-01	48.23	8.0	700	-2.086	0.225E-01	55.29
6.0	800	-2.032	0.262E-01	21.40	8.0	800	-2.276	0.256E-01	22.09
6.0	900	-2.195	0.331E-01	13.43	8.0	900	-2.461	0.317E-01	13.27
6.0	1000	-2.355	0.452E-01	4.410	8.0	1000	-2.644	0.427E-01	5.270
10.0	10	0.854	0.212E-01	44.81	12.0	10	0.903	0.208E-01	41.38
10.0	20	0.469	0.142E-01	132.5	12.0	20	0.502	0.139E-01	105.0
10.0	30	0.209	0.708E-02	110.6	12.0	30	0.225	0.693E-02	78.56
10.0	40	0.000	0.127E-05	65.34	12.0	40	0.000	0.117E-05	47.63
10.0	50	-0.156	0.835E-02	63.27	12.0	50	-0.150	0.785E-02	61.45
10.0	75	-0.360	0.134E-01	62.92	12.0	75	-0.339	0.128E-01	54.29
10.0	90	-0.431	0.166E-01	53.94	12.0	90	-0.403	0.159E-01	48.99
10.0	105	-0.477	0.183E-01	70.81	12.0	105	-0.456	0.177E-01	67.74
10.0	120	-0.528	0.195E-01	53.33	12.0	120	-0.515	0.188E-01	53.17
10.0	135	-0.583	0.197E-01	48.58	12.0	135	-0.580	0.192E-01	50.71
10.0	150	-0.636	0.191E-01	70.59	12.0	150	-0.644	0.189E-01	63.92
10.0	175	-0.719	0.183E-01	94.29	12.0	175	-0.745	0.183E-01	78.71
10.0	200	-0.837	0.175E-01	135.4	12.0	200	-0.872	0.176E-01	108.1
10.0	250	-1.016	0.171E-01	237.6	12.0	250	-1.056	0.172E-01	197.3
10.0	300	-1.193	0.174E-01	264.0	12.0	300	-1.244	0.176E-01	204.6
10.0	400	-1.454	0.184E-01	184.5	12.0	400	-1.517	0.187E-01	139.6
10.0	500	-1.724	0.200E-01	69.80	12.0	500	-1.788	0.204E-01	51.43
10.0	600	-1.969	0.214E-01	52.78	12.0	600	-2.034	0.223E-01	38.59
10.0	700	-2.189	0.232E-01	51.21	12.0	700	-2.250	0.249E-01	31.01
10.0	800	-2.383	0.267E-01	23.39	12.0	800	-2.445	0.296E-01	14.41
10.0	900	-2.578	0.336E-01	14.45	12.0	900	-2.630	0.379E-01	7.730
10.0	1000	-2.774	0.453E-01	4.910	12.0	1000	-2.809	0.505E-01	2.480

Table 3.5: Attenuation functional at 6.0, 8.0, 10.0, and 12.0 Hz for Fourier velocity spectra. The columns give values of frequency (first and sixth columns), hypocentral distance (second and seventh columns), attenuation  $D(r, f)$  at a reference distance of 40 km (third and eighth columns), associated error bar (fourth and ninth columns) and number of observations (fifth and tenth columns).

<b>Southeastern Canada Fourier velocity spectra <math>D(r)</math></b>									
f (Hz)	r (km)	$D(r, f)$	$\sigma$	Nobs	f (Hz)	r (km)	$D(r, f)$	$\sigma$	Nobs
14.0	10	0.919	0.209E-01	37.28	16.0	10	0.909	0.204E-01	34.28
14.0	20	0.513	0.140E-01	92.30	16.0	20	0.505	0.136E-01	90.47
14.0	30	0.231	0.698E-02	65.84	16.0	30	0.227	0.681E-02	68.18
14.0	40	0.000	0.119E-05	54.74	16.0	40	0.000	0.117E-05	53.62
14.0	50	-0.144	0.791E-02	70.09	16.0	50	-0.143	0.782E-02	78.48
14.0	75	-0.331	0.129E-01	57.01	16.0	75	-0.334	0.128E-01	72.44
14.0	90	-0.401	0.160E-01	51.16	16.0	90	-0.407	0.160E-01	61.04
14.0	105	-0.456	0.179E-01	65.77	16.0	105	-0.469	0.177E-01	72.69
14.0	120	-0.520	0.190E-01	55.80	16.0	120	-0.545	0.186E-01	60.69
14.0	135	-0.592	0.194E-01	55.76	16.0	135	-0.625	0.188E-01	64.20
14.0	150	-0.663	0.192E-01	65.06	16.0	150	-0.694	0.186E-01	67.45
14.0	175	-0.775	0.187E-01	81.93	16.0	175	-0.799	0.182E-01	87.41
14.0	200	-0.911	0.181E-01	109.3	16.0	200	-0.935	0.177E-01	107.8
14.0	250	-1.107	0.177E-01	186.3	16.0	250	-1.137	0.173E-01	195.3
14.0	300	-1.304	0.180E-01	207.6	16.0	300	-1.340	0.175E-01	212.2
14.0	400	-1.583	0.191E-01	145.5	16.0	400	-1.626	0.186E-01	142.8
14.0	500	-1.851	0.208E-01	48.88	16.0	500	-1.899	0.203E-01	44.30
14.0	600	-2.091	0.227E-01	37.65	16.0	600	-2.142	0.220E-01	35.72
14.0	700	-2.303	0.255E-01	31.71	16.0	700	-2.347	0.244E-01	31.23
14.0	800	-2.497	0.308E-01	13.62	16.0	800	-2.529	0.293E-01	13.36
14.0	900	-2.680	0.400E-01	5.410	16.0	900	-2.693	0.378E-01	4.960
14.0	1000	-2.856	0.537E-01	1.230	16.0	1000	-2.847	0.506E-01	2.270

Table 3.6: Attenuation functional at 14.0 and 16.0 Hz for Fourier velocity spectra. The columns give values of frequency (first and sixth columns), hypocentral distance (second and seventh columns), attenuation  $D(r, f)$  at a reference distance of 40 km (third and eighth columns), associated error bar (fourth and ninth columns) and number of observations (fifth and tenth columns).

<b>Number of observations</b>		
Frequency	Peak velocity	Fourier velocity
01	2919	902
02	4433	1786
03	4608	2048
04	4635	2037
06	4654	2022
08	4646	1961
10	4636	1932
12	3709	1570
14	3699	1563
16	3688	1624

Table 3.7: Number of observations in regressions of band-passed filtered velocity and Fourier velocity.

through the earth. The *RVT* predictions depend on the assumed signal duration,  $T_s + T(r)$ , where  $T_s$  is the source contribution and  $T(r)$  is the distance dependent wave propagation contribution to total duration.

I modeled the distance dependence duration ( $T$ ) as a piecewise linear function of distance:

$$T = \sum_{l=1}^L T_l N_l(r) \quad (3.1)$$

where  $N$  is the distance nodes, and  $T_l$  is the duration estimated.  $T(r = 0 \text{ km})$  is used to the constraint for small earthquakes.

The importance of duration increases for larger events because the source duration may be comparable or larger than the propagation effect on duration. For smaller earthquakes at large distances, the effect of the increase of duration with propagation overwhelms the effect of source duration, so that the peak motions depend more upon a single parameter, magnitude, than upon two parameters, magnitude and stress drop.

The fits to the duration are shown in Figures 3.11 and 3.12, which also show the measured duration at 1.0, 2.0, 4.0, 6.0, 8.0, 10.0, 12.0, 14.0, and 16.0 Hz, an  $L_1$  norm optimization is applied to estimate the distance dependent duration. The individual duration estimates (gray circles) show much scatter in the lower frequency range of 1.0 - 2.0 Hz, while the scatter is less at higher frequencies.

Table 3.8 lists a simple frequency independent duration functional as a function of distance for vertical and horizontal data sets of southeastern Canada

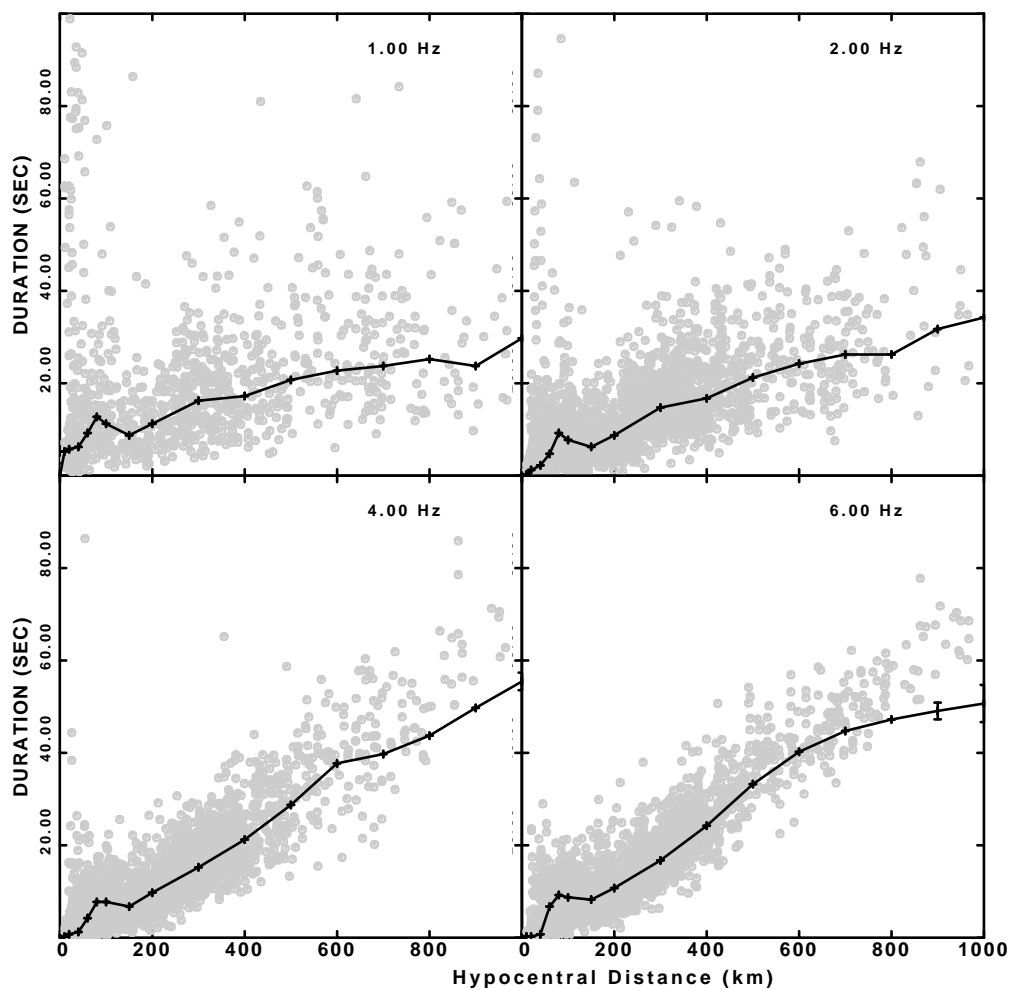


Figure 3.11: Durations at 1.0, 2.0, 4.0 and 6.0 Hz obtained for southeastern Canada. Rounded gray circles indicate individual duration estimates and thick solid lines denote the duration measured using by a median value method.

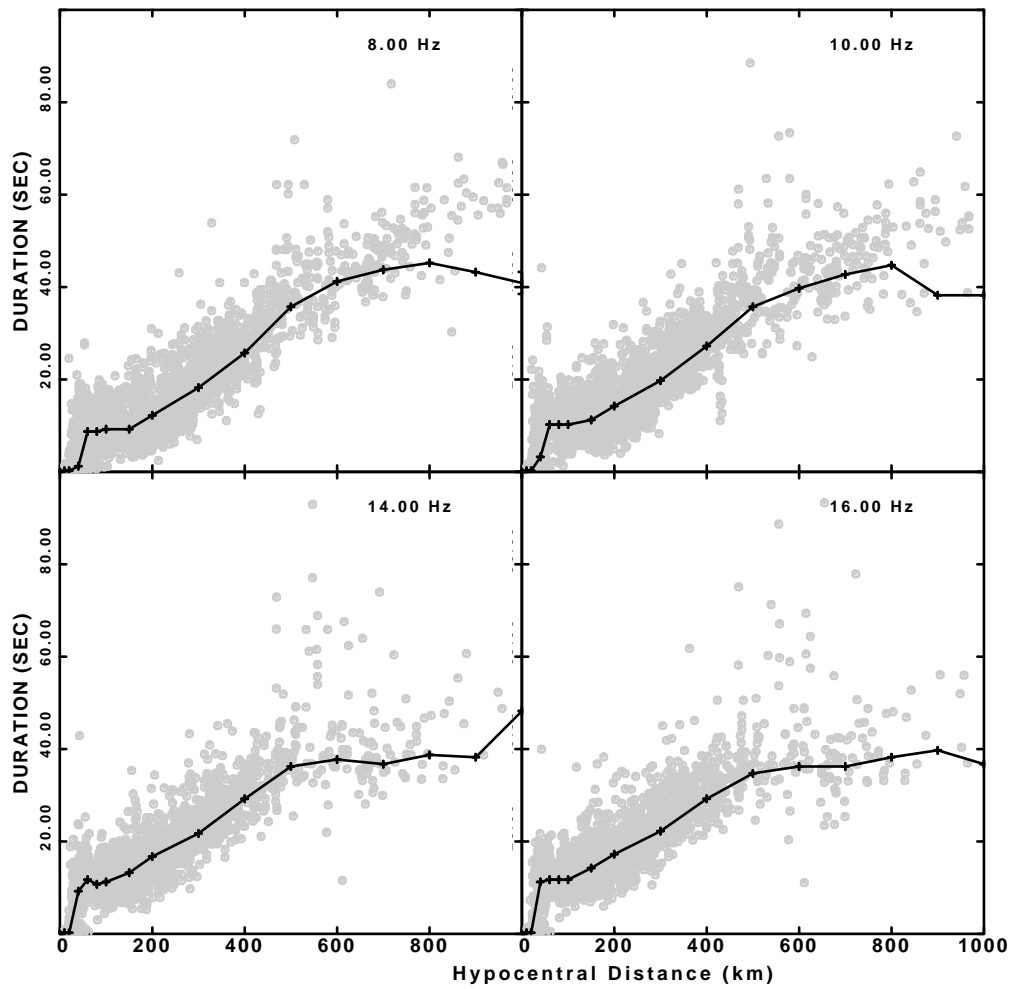


Figure 3.12: Durations at 8.0, 10.0, 14.0, and 16.0 Hz. Rounded gray circles indicate individual duration estimates and thick solid lines represent measured durations.

<b>Durations for different frequencies (Hz)</b>										
Distance (km)	01 Hz (sec)	02 Hz (sec)	03 Hz (sec)	04 Hz (sec)	06 Hz (sec)	08 Hz (sec)	10 Hz (sec)	12 Hz (sec)	14 Hz (sec)	16 Hz (sec)
0.000	0.000	0.000	0.000	0.000	0.000	0.000	0.000	0.000	0.000	0.000
10.000	5.250	0.250	0.250	0.250	0.250	0.250	0.250	0.250	0.250	0.250
20.000	5.750	1.250	0.750	0.750	0.250	0.250	0.250	0.250	0.250	0.250
40.000	6.250	2.250	1.750	1.250	0.750	1.250	3.250	6.250	9.250	11.250
60.000	9.250	4.750	4.250	4.250	6.750	8.750	10.250	10.750	11.750	11.750
80.000	12.750	9.250	8.250	7.750	9.250	8.750	10.250	10.250	10.750	11.750
100.000	11.250	7.750	7.250	7.750	8.750	9.250	10.250	10.250	11.250	11.750
150.000	8.750	6.250	6.250	6.750	8.250	9.250	11.250	11.750	13.250	14.250
200.000	11.250	8.750	8.750	9.750	10.750	12.250	14.250	15.250	16.750	17.250
300.000	16.250	14.750	15.250	15.250	16.750	18.250	19.750	20.750	21.750	22.250
400.000	17.250	16.750	19.250	21.250	24.250	25.750	27.250	28.250	29.250	29.250
500.000	20.750	21.250	24.250	28.750	33.250	35.750	35.750	36.250	36.250	34.750
600.000	22.750	24.250	30.250	37.750	40.250	41.250	39.750	38.750	37.750	36.250
700.000	23.750	26.250	31.750	39.750	44.750	43.750	42.750	39.750	36.750	36.250
800.000	25.250	26.250	36.249	43.750	47.250	45.250	44.750	40.750	38.750	38.250
900.000	23.750	31.750	29.751	49.750	49.089	43.250	38.250	38.750	38.250	39.750
1000.000	29.750	34.250	47.750	55.477	50.707	40.915	38.250	36.250	48.250	36.750

Table 3.8: Durations as a function of distance and frequencies from 1 to 16 Hz.

from 1 to 16 Hz. Table 3.9 lists measured frequency independent durations as a function of distance for vertical, horizontal, and combined data sets for south-eastern Canada for band-passed filtered.

### 3.2.4 Regression of peak filtered velocity

Figures 3.13 and 3.14 are typical examples of the regression analysis results for the band pass filtered spectra data for 2.0, 4.0, 8.0, and 12.0 Hz. The top panels illustrate the coda propagation term estimated from the coda normalization technique. The coda and regression propagation functional in the mid-panels show good agreement for the band pass filtered spectra data set at that distance range. The estimates of the standard errors of the  $D(r, f)$  are about  $0.2 \log_{10}$  units from 1 - 16 Hz. The regression residual plots on the bottom panels are used to see whether the distance nodes were appropriate to determine proper  $D(r)$ . Band-pass filtered regression results have more data points

<b>Measured durations</b>			
Distance (km)	All (sec)	Hor (sec)	Ver (sec)
0.00	0.0	0.0	0.0
10.00	0.8	0.9	0.6
20.00	1.0	0.9	1.0
40.00	3.6	5.2	3.4
60.00	8.2	9.1	7.4
80.00	9.9	10.3	9.3
100.00	9.6	10.9	9.2
150.00	9.6	10.8	9.1
200.00	12.5	13.2	12.1
300.00	18.1	18.1	17.8
400.00	23.9	23.7	23.8
500.00	30.7	30.3	31.6
600.00	34.9	34.8	35.2
700.00	36.5	33.5	36.9
800.00	38.6	34.1	38.8
900.00	38.2	-	39.6
1000.0	41.8	-	-

Table 3.9: Measured durations from band-passed filtered for southeastern Canada. Hor, Ver, and All are acronyms of horizontal, vertical, and combined data set.

than those of Fourier velocity spectra regressions.

Figure 3.15 shows the three component distance scaling of the peak filtered velocity  $D(r, f)$  term at the frequencies of 1.0, 2.0, 3.0, 4.0, 6.0, 8.0, 10.0, 12.0, 14.0, and 16.0 Hz for southeastern Canada. The  $D(r, f)$  values are corrected for an  $r^{-1}$  trend to emphasize the departure from  $r^{-1}$  spreading. The  $D(r, f)$  around 150 km shows an increase of the amplitude. Burger et al. (1987) indicated that post-critical reflections from the Moho and intra-crustal discontinuities increase the amplitude of the attenuation curve in the distance range of about 60 to 150 km, while the direct  $S$ -wave dominates the attenuation curve less than about 60 km in the eastern United States. This may be one of the characteristic of ENA crustal condition.

Tables 3.10, 3.11, and 3.12 give the numerical results of the regression on the regional attenuation functional for study region. They give the correspond-

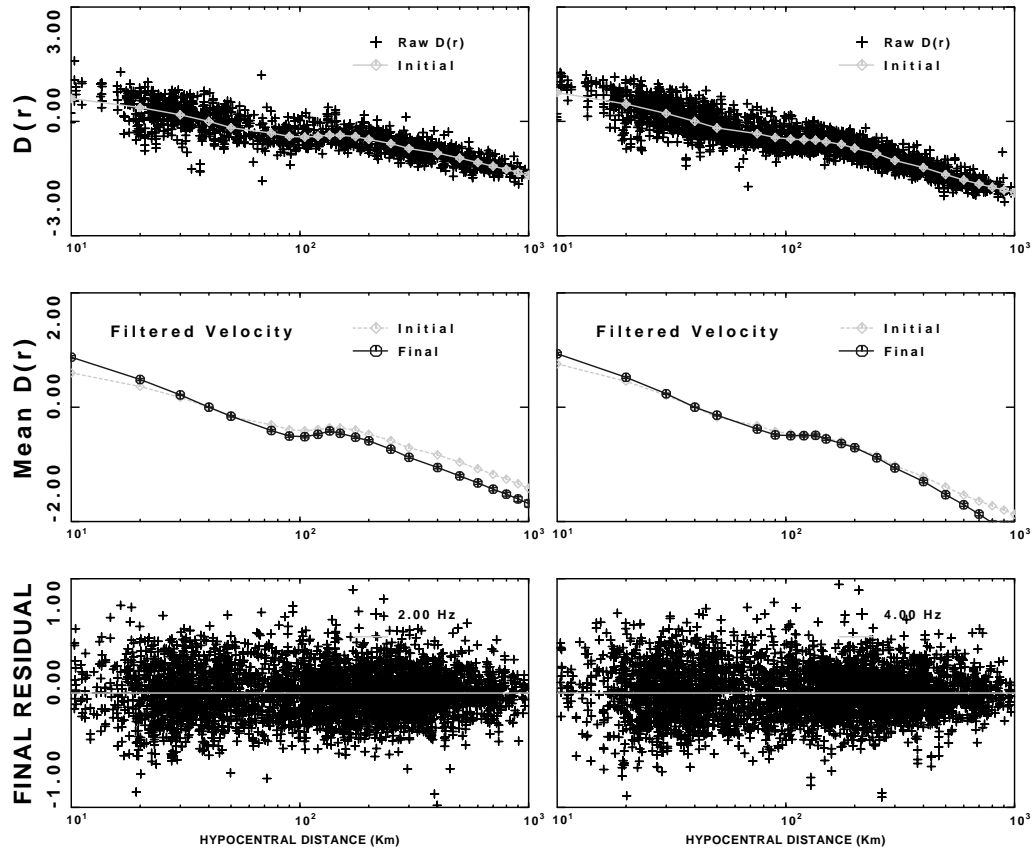


Figure 3.13: Regression analysis for 2.0 and 4.0 Hz. Top, coda estimate of  $D(r)$  using coda normalization technique. Middle, coda and regression propagation functionals. Bottom, final residuals of the regression analysis.

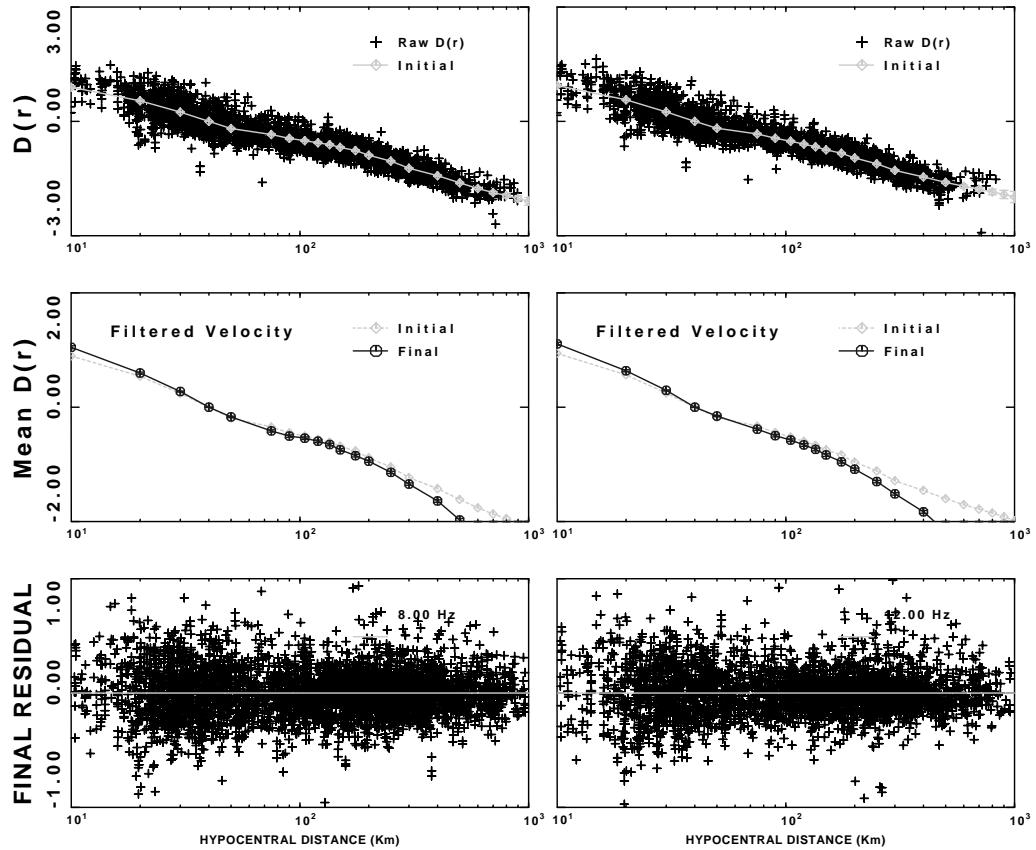


Figure 3.14: Regression analysis for 8.0 and 12.0 Hz. Top, coda estimate of  $D(r)$  using coda normalization technique. Middle, coda and regression propagation functionals. Bottom, final residuals of the regression analysis.

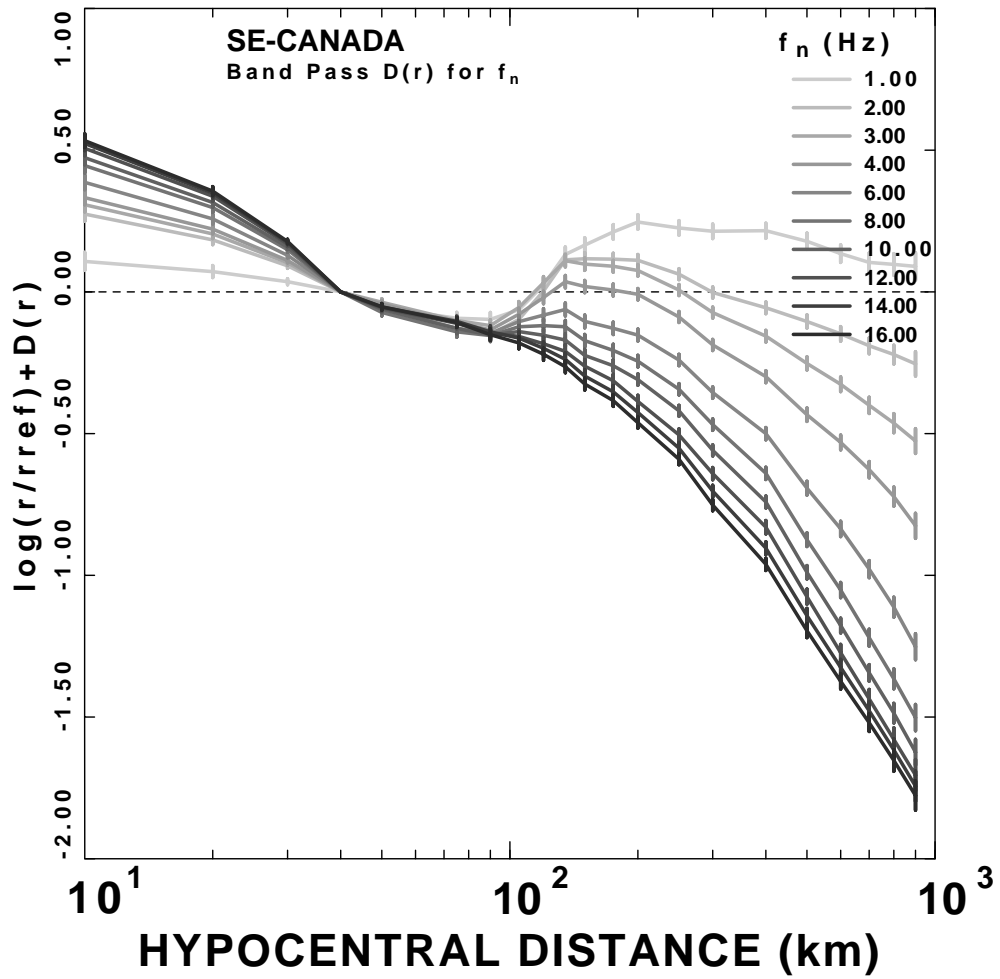


Figure 3.15: The reduced attenuation functional  $D(r, f)$  at the frequencies of 1.0, 2.0, 3.0, 4.0, 6.0, 8.0, 10.0, 12.0, 14.0, and 16.0 Hz for southeastern Canada.

ing value of  $D(r)$  for each frequency and distance as well as the number of observations contributing to each node.

### 3.3 Parameterization

Parameterization is required to model the regression results with a simple model that reduces the observations into a few parameters. This is essential for creating a forward ground motion prediction model using the interpretations of the regression terms as given by equation (3.5, 3.6, and 3.7). First, the Fourier velocity spectra  $D(r, f)$  are modeled using equation 3.6 by specifying  $g(r)$  and  $Q(f)$ . The  $Q(f)$  and  $g(r)$  are used with the  $T(r, f)$  to make  $RVT$  predictions of the filtered peak time domain  $D(r, f)$ . The parameters for formulating the  $D(r, f)$  of Fourier velocity spectra and filtered peak time domain should consistent with each others to validate that model parameters selected are well documented.

The second step is the parameterization of  $E(r, f)$  term for small earthquakes using equation 3.5. The predicted  $E(r, f)$  term depends on the already determined  $Q(f)$ ,  $g(r)$  and network average site effect (equation 3.8). The corner frequency,  $f_c$ , of equation 3.9 does not effect the excitation spectra shape because the  $f_c$  are much greater than the observations for small earthquakes. This step serves to define an average *kappa*.

Finally, I focus on absolute scaling of ground motion by predicting the observed  $E(r, f)$  for larger events with known moment magnitude greater than 4.0, but not large enough that the excitation is insensitive to stress drop at the

Southeastern Canada Filtered velocity spectra $D(r)$									
f (Hz)	r (km)	$D(r, f)$	$\sigma$	Nobs	f (Hz)	r (km)	$D(r, f)$	$\sigma$	Nobs
1.0	10	0.710	0.318E-01	42.16	2.0	10	0.877	0.258E-01	66.42
1.0	20	0.373	0.212E-01	199.1	2.0	20	0.485	0.172E-01	284.7
1.0	30	0.161	0.106E-01	266.6	2.0	30	0.217	0.861E-02	384.0
1.0	40	0.000	0.241E-05	174.2	2.0	40	0.000	0.230E-05	255.1
1.0	50	-0.152	0.138E-01	190.1	2.0	50	-0.157	0.122E-01	262.5
1.0	75	-0.366	0.212E-01	119.8	2.0	75	-0.408	0.181E-01	184.3
1.0	90	-0.449	0.247E-01	102.5	2.0	90	-0.503	0.207E-01	139.8
1.0	105	-0.482	0.258E-01	123.8	2.0	105	-0.516	0.213E-01	174.5
1.0	120	-0.453	0.265E-01	105.8	2.0	120	-0.474	0.219E-01	148.6
1.0	135	-0.396	0.265E-01	123.9	2.0	135	-0.415	0.218E-01	166.4
1.0	150	-0.409	0.261E-01	138.8	2.0	150	-0.457	0.215E-01	174.6
1.0	175	-0.429	0.256E-01	171.3	2.0	175	-0.525	0.210E-01	210.3
1.0	200	-0.452	0.256E-01	165.4	2.0	200	-0.587	0.203E-01	290.0
1.0	250	-0.570	0.258E-01	182.3	2.0	250	-0.733	0.195E-01	416.6
1.0	300	-0.661	0.259E-01	236.7	2.0	300	-0.877	0.196E-01	468.4
1.0	400	-0.784	0.266E-01	208.5	2.0	400	-1.056	0.209E-01	363.1
1.0	500	-0.918	0.286E-01	120.6	2.0	500	-1.201	0.232E-01	167.7
1.0	600	-1.041	0.310E-01	79.49	2.0	600	-1.324	0.258E-01	95.25
1.0	700	-1.139	0.336E-01	77.90	2.0	700	-1.433	0.284E-01	86.86
1.0	800	-1.204	0.382E-01	36.78	2.0	800	-1.522	0.332E-01	40.22
1.0	900	-1.262	0.481E-01	22.80	2.0	900	-1.606	0.431E-01	23.41
1.0	1000	-1.315	0.678E-01	7.300	2.0	1000	-1.683	0.624E-01	7.300
3.0	10	0.910	0.253E-01	69.64	4.0	10	0.935	0.254E-01	70.42
3.0	20	0.506	0.169E-01	303.7	4.0	20	0.523	0.169E-01	30.12
3.0	30	0.228	0.844E-02	414.1	4.0	30	0.236	0.846E-02	418.6
3.0	40	0.000	0.234E-05	277.7	4.0	40	0.000	0.237E-05	283.7
3.0	50	-0.133	0.123E-01	275.1	4.0	50	-0.139	0.124E-01	277.1
3.0	75	-0.374	0.182E-01	187.9	4.0	75	-0.382	0.182E-01	190.1
3.0	90	-0.471	0.207E-01	144.6	4.0	90	-0.486	0.208E-01	146.2
3.0	105	-0.474	0.213E-01	179.6	4.0	105	-0.498	0.215E-01	180.9
3.0	120	-0.445	0.219E-01	150.2	4.0	120	-0.497	0.221E-01	150.5
3.0	135	-0.418	0.219E-01	167.3	4.0	135	-0.492	0.220E-01	167.3
3.0	150	-0.476	0.216E-01	176.9	4.0	150	-0.555	0.217E-01	176.9
3.0	175	-0.550	0.210E-01	214.9	4.0	175	-0.634	0.212E-01	215.6
3.0	200	-0.623	0.202E-01	303.8	4.0	200	-0.707	0.203E-01	307.7
3.0	250	-0.789	0.194E-01	441.0	4.0	250	-0.884	0.195E-01	444.3
3.0	300	-0.948	0.195E-01	487.6	4.0	300	-1.062	0.196E-01	489.8
3.0	400	-1.156	0.209E-01	369.1	4.0	400	-1.299	0.211E-01	369.2
3.0	500	-1.349	0.234E-01	168.7	4.0	500	-1.530	0.236E-01	168.5
3.0	600	-1.502	0.260E-01	95.25	4.0	600	-1.707	0.262E-01	95.25
3.0	700	-1.643	0.287E-01	86.86	4.0	700	-1.870	0.289E-01	86.86
3.0	800	-1.764	0.336E-01	40.22	4.0	800	-2.023	0.339E-01	40.22
3.0	900	-1.878	0.438E-01	23.41	4.0	900	-2.177	0.442E-01	23.41
3.0	1000	-1.988	0.635E-01	7.300	4.0	1000	-2.330	0.641E-01	7.300

Table 3.10: Attenuation functional at 1.0, 2.0, 3.0, and 4.0 Hz for band passed filtered. The columns give values of frequency (first and sixth columns), hypocentral distance (second and seventh columns), attenuation  $D(r, f)$  at a reference distance of 40 km (third and eighth columns), associated error bar (fourth and ninth columns) and number of observations (fifth and tenth columns).

Southeastern Canada filtered velocity spectra $D(r)$									
f (Hz)	r (km)	$D(r, f)$	$\sigma$	Nobs	f (Hz)	r (km)	$D(r, f)$	$\sigma$	Nobs
6.0	10	0.989	0.263E-01	71.27	8.0	10	1.048	0.260E-01	71.27
6.0	20	0.559	0.175E-01	305.2	8.0	20	0.599	0.173E-01	303.4
6.0	30	0.254	0.875E-02	424.0	8.0	30	0.274	0.865E-02	423.7
6.0	40	0.000	0.246E-05	284.4	8.0	40	0.000	0.243E-05	282.8
6.0	50	-0.156	0.129E-01	279.0	8.0	50	-0.169	0.127E-01	277.8
6.0	75	-0.401	0.189E-01	190.1	8.0	75	-0.414	0.187E-01	190.3
6.0	90	-0.498	0.216E-01	145.8	8.0	90	-0.506	0.214E-01	146.8
6.0	105	-0.524	0.223E-01	180.3	8.0	105	-0.542	0.220E-01	180.9
6.0	120	-0.559	0.229E-01	151.5	8.0	120	-0.596	0.226E-01	151.5
6.0	135	-0.590	0.229E-01	167.4	8.0	135	-0.651	0.226E-01	167.4
6.0	150	-0.678	0.226E-01	176.7	8.0	150	-0.746	0.223E-01	177.2
6.0	175	-0.769	0.220E-01	216.6	8.0	175	-0.847	0.217E-01	217.1
6.0	200	-0.851	0.211E-01	309.5	8.0	200	-0.943	0.208E-01	310.2
6.0	250	-1.036	0.203E-01	445.7	8.0	250	-1.139	0.200E-01	446.8
6.0	300	-1.230	0.204E-01	491.1	8.0	300	-1.343	0.201E-01	490.5
6.0	400	-1.500	0.219E-01	369.8	8.0	400	-1.640	0.216E-01	369.8
6.0	500	-1.789	0.245E-01	168.7	8.0	500	-1.971	0.242E-01	168.3
6.0	600	-2.012	0.272E-01	96.03	8.0	600	-2.228	0.270E-01	95.42
6.0	700	-2.221	0.301E-01	86.86	8.0	700	-2.463	0.300E-01	85.01
6.0	800	-2.413	0.352E-01	40.22	8.0	800	-2.666	0.354E-01	39.17
6.0	900	-2.604	0.459E-01	23.41	8.0	900	-2.854	0.466E-01	21.19
6.0	1000	-2.793	0.666E-01	7.300	8.0	1000	-3.037	0.675E-01	6.430
10.0	10	1.076	0.253E-01	71.24	12.0	10	1.109	0.263E-01	66.74
10.0	20	0.617	0.169E-01	304.1	12.0	20	0.639	0.176E-01	272.4
10.0	30	0.283	0.844E-02	426.7	12.0	30	0.294	0.878E-02	386.0
10.0	40	0.000	0.237E-05	285.6	12.0	40	0.000	0.236E-05	262.3
10.0	50	-0.158	0.124E-01	276.4	12.0	50	-0.153	0.126E-01	247.8
10.0	75	-0.402	0.183E-01	190.2	12.0	75	-0.384	0.188E-01	171.5
10.0	90	-0.504	0.209E-01	146.9	12.0	90	-0.497	0.218E-01	132.6
10.0	105	-0.559	0.215E-01	180.9	12.0	105	-0.576	0.227E-01	153.8
10.0	120	-0.630	0.221E-01	151.5	12.0	120	-0.660	0.235E-01	123.7
10.0	135	-0.698	0.221E-01	167.4	12.0	135	-0.738	0.235E-01	142.7
10.0	150	-0.798	0.218E-01	177.2	12.0	150	-0.836	0.232E-01	143.0
10.0	175	-0.901	0.212E-01	217.1	12.0	175	-0.954	0.227E-01	164.3
10.0	200	-1.008	0.203E-01	310.5	12.0	200	-1.085	0.218E-01	235.4
10.0	250	-1.215	0.196E-01	443.8	12.0	250	-1.300	0.212E-01	337.9
10.0	300	-1.434	0.197E-01	488.4	12.0	300	-1.516	0.219E-01	336.5
10.0	400	-1.741	0.211E-01	368.4	12.0	400	-1.830	0.238E-01	243.8
10.0	500	-2.086	0.237E-01	166.3	12.0	500	-2.172	0.267E-01	108.7
10.0	600	-2.353	0.264E-01	92.69	12.0	600	-2.449	0.299E-01	64.02
10.0	700	-2.587	0.294E-01	79.91	12.0	700	-2.679	0.338E-01	53.56
10.0	800	-2.787	0.347E-01	39.17	12.0	800	-2.880	0.412E-01	23.60
10.0	900	-2.976	0.455E-01	21.78	12.0	900	-3.057	0.553E-01	11.62
10.0	1000	-3.162	0.659E-01	6.840	12.0	1000	-3.220	0.785E-01	4.070

Table 3.11: Attenuation functional at 6.0, 8.0, 10.0, and 12.0 Hz for band-pass filtered. The columns give values of frequency (first and sixth columns), hypocentral distance (second and seventh columns), attenuation  $D(r, f)$  at a reference distance of 40 km (third and eighth columns), associated error bar (fourth and ninth columns) and number of observations (fifth and tenth columns).

<b>Southeastern Canada filtered velocity spectra <math>D(r)</math></b>									
f (Hz)	r (km)	$D(r, f)$	$\sigma$	Nobs	f (Hz)	r (km)	$D(r, f)$	$\sigma$	Nobs
14.0	10	1.126	0.252E-01	66.74	16.0	10	1.136	0.241E-01	66.74
14.0	20	0.650	0.168E-01	272.1	16.0	20	0.657	0.160E-01	271.6
14.0	30	0.300	0.841E-02	385.1	16.0	30	0.303	0.802E-02	386.1
14.0	40	0.000	0.226E-05	262.6	16.0	40	0.000	0.216E-05	262.4
14.0	50	-0.150	0.121E-01	247.6	16.0	50	-0.149	0.115E-01	249.2
14.0	75	-0.377	0.180E-01	171.5	16.0	75	-0.381	0.172E-01	171.7
14.0	90	-0.493	0.209E-01	132.6	16.0	90	-0.503	0.199E-01	132.6
14.0	105	-0.582	0.218E-01	153.8	16.0	105	-0.599	0.208E-01	153.8
14.0	120	-0.676	0.225E-01	123.7	16.0	120	-0.697	0.214E-01	123.7
14.0	135	-0.766	0.225E-01	142.7	16.0	135	-0.792	0.215E-01	142.7
14.0	150	-0.871	0.223E-01	143.0	16.0	150	-0.899	0.212E-01	142.3
14.0	175	-0.993	0.217E-01	164.3	16.0	175	-1.024	0.207E-01	164.1
14.0	200	-1.124	0.209E-01	235.9	16.0	200	-1.160	0.199E-01	235.8
14.0	250	-1.347	0.204E-01	336.5	16.0	250	-1.386	0.194E-01	335.6
14.0	300	-1.578	0.211E-01	334.0	16.0	300	-1.627	0.201E-01	334.2
14.0	400	-1.904	0.229E-01	242.4	16.0	400	-1.961	0.218E-01	243.5
14.0	500	-2.239	0.256E-01	107.3	16.0	500	-2.292	0.246E-01	100.9
14.0	600	-2.501	0.287E-01	63.16	16.0	600	-2.550	0.275E-01	58.96
14.0	700	-2.721	0.325E-01	53.43	16.0	700	-2.763	0.310E-01	53.11
14.0	800	-2.917	0.399E-01	21.74	16.0	800	-2.954	0.382E-01	22.02
14.0	900	-3.096	0.535E-01	11.62	16.0	900	-3.129	0.515E-01	10.35
14.0	1000	-3.264	0.758E-01	4.070	16.0	1000	-3.293	0.732E-01	3.540

Table 3.12: Attenuation functional at 14.0 and 16.0 Hz for bandpass filtered. The columns give values of frequency (first and sixth columns), hypocentral distance (second and seventh columns), attenuation  $D(r, f)$  at a reference distance of 40 km (third and eighth columns), associated error bar (fourth and ninth columns) and number of observations (fifth and tenth columns).

lower frequency range. This step is also useful to check if the chosen  $g(r)$  is correct to the first observation from the source. If all of the premises are met, then I can state that I have the appropriate model parameters that can be used later for extrapolating vertical and horizontal motions of larger events if their source scaling be specified.

### 3.3.1 Propagation parameters

As indicated in the previous section, the  $D(r, f)$  term is a function of geometrical spreading  $g(r)$  and attenuation  $Q(f)$ . The simple forward model can be presented as a combination of those parameters.

$Q$  is a parameter which describes the filtering of high-frequency wave from the seismic signals as they propagate through the medium (wave-guide).  $Q$  for seismic waves may be independent of frequency at low frequency ranges (0.001 to 1.0 Hz), while it depends on frequency and increases with frequency at higher frequencies (Lay and Wallace, 1995). Short-period waves are sensitive to the lateral heterogeneities of the shallow part of the earth's crust. As the waves travel longer, they encounter more variety of heterogeneities (Singh and Herrmann, 1983).  $Q$  also varies laterally within the earth and may be a proxy for crustal temperature heterogeneity. Normally heat flow is higher in tectonically active region where attenuation is greater than colder regions. Mitchell (1995) also indicated that factors such as temperature, fluid content, partial melt of solid-state dislocation motion in the crust or upper mantle affect the parameter  $Q$ . The intrinsic  $Q$  values determined for the crust and

upper mantle play an important role in understanding the tectonic evolution of regions.

In mathematics, the loss of energy per cycle is presented by  $Q^{-1}$ :

$$\frac{1}{Q} = \frac{\Delta E}{2\pi E_{max}} \quad (3.2)$$

where  $\Delta E$  is the amount of energy lost per cycle and  $E_{max}$  is the maximum amount of elastic energy contained in a cycle. The distance decay of wave amplitudes can be described by  $e^{-\gamma x}$ , where  $\gamma$  is the attenuation coefficient. It is related to the  $Q$  factor by  $\gamma = \pi f / \beta Q$ , where  $f$  is the frequency and  $\beta$  is S-wave velocity.

$Q(f)$  is represented by the relation

$$Q(f) = Q_0(f/f_0)^\eta \quad (3.3)$$

where  $f_0 = 1.0$  Hz and  $\eta$  is the frequency dependent exponent that controls the separation of frequencies. If  $\eta$  is 0,  $Q$  is constant and the spatial attenuation at different frequencies varies strongly, with low frequencies attenuated less than high frequencies. If  $\eta$  is equal to 1,  $Q(f)$  is strongly frequency dependent and the spatial attenuation at different frequencies is same. Figure 13 of Singh and Herrmann (1983) shows a brief summary of  $\eta$  determinations of continental United States. The  $\eta$  values between 0.3 - 0.4 are calculated for northeastern United States, 0.1 to 0.3 for the central and southeastern United States, and an  $\eta$  of 0.4 to 0.6 in the western United States. Mitchell (1981) reported an  $\eta$

value between 0.3 to 0.5 for eastern United States and Aki and Chouet (1975) obtained  $\eta$  of 0.6 to 0.8 for central California.

### 3.3.2 Modeling Fourier velocity spectra

The predicted Fourier velocity spectra at a frequency  $f$  for a hypocentral distance  $r$  is

$$A(r, f) = S(f, \mathbf{M}_W) g(r) e^{-\pi f r / Q(f)\beta} V(f) e^{-\pi f \kappa} \quad (3.4)$$

where  $A(r, f)$  denotes the Fourier velocity spectrum,  $S(f, \mathbf{M}_W)$  be the Fourier velocity spectrum at a distance of 1 km,  $\mathbf{M}_W$  is the moment magnitude,  $g(r)$  is the geometrical spreading function relative to 1 km, and  $Q(f)$  is the frequency dependent quality factor which is taken to be  $Q_0 (f/1.0 \text{ Hz})^\eta$  and  $\beta$  is the shear-wave propagation velocity. The combination of  $V(f)$  and  $\kappa$  characterizes the site response.

Comparison of this simple prediction model to the regression terms (equation 2.19 and 2.20) shows the following correspondence for the excitation, propagation, and site terms:

$$10^E = S(f, \mathbf{M}_W) g(r_{ref}) e^{-\pi f r_{ref} / Q(f)\beta} \overline{V(f) e^{-\pi \kappa f}} \quad , \quad (3.5)$$

at  $r = r_{ref}$ ,

$$10^D = \frac{g(r) e^{-\pi f r / Q(f)\beta}}{g(r_{ref}) e^{-\pi f r_{ref} / Q(f)\beta}} \quad , \quad (3.6)$$

and

$$10^{S_i} = \frac{V(f) e^{-\pi\kappa f}}{\overline{V(f) e^{-\pi\kappa f}}} \quad , \quad (3.7)$$

where  $\overline{V(f) e^{-\pi\kappa f}}$  is the network average site effect. Because the geologic site characteristics are not known much, I define an effective  $\kappa$ ,  $\kappa_{eff}$ , for the composite effect of network average site amplification,  $V(f)$ , and  $\kappa$  by the following relation

$$e^{-\pi f \kappa_{eff}} = \overline{V(f) e^{-\pi\kappa f}}. \quad (3.8)$$

Note that as  $f \rightarrow 0$ , both sides of the equation approach 1.0. But, there may be a constant multiplier in previous equation when only a limited range of frequencies is used where some site amplification is.

### 3.3.3 Parameterization of Fourier velocity spectra

In this study, I performed three regressions of vertical, horizontal, and all component data. Figure 3.16 shows the three component distance scaling of the  $D(r, f)$  term at the ten different frequencies for regression on the Fourier velocity spectra. The presentation emphasizes departure (scattering, deviation) of high frequency spectra with distance from  $r^{-1}$  spreading. The black lines in the background are the theoretical  $D(r, f)$ . The reference distance at 40 km was used to normalize the  $D(r, f)$  and the horizontal dashed line represents  $r^{-1}$  trend. The 1 Hz signal at short distance range in the top panel shows different propagation shape compared to the rest of the  $D(r)$  frequency ranges. 1 Hz signal may be affected by noise more that affects the duration estimation. The

lower panel shows the Fourier velocity spectra  $D(r)$  residuals, the deviation between observed and predicted  $D(r, f)$  of the distance range. The residuals of fit are small for the all hypocentral distance ranges except for the higher frequency ranges distance greater than 300 km. I can not reduced the residuals at larger distances using a simple parameterization. This may be related to the observation of Shin and Herrmann (1987) that the high frequencies are dominated by  $S_n$  and the low frequencies by  $L_g$  at larger distances.

The parameters used are  $Q(f) = 650f^{0.33}$  and

$$g(r) = \begin{cases} r^{-1.3} & r < 40 \text{ km} \\ r^{-1.2} & 40 < r < 70 \text{ km} \\ r^{-0.0} & 70 < r < 100 \text{ km} \\ r^{-0.2} & 100 < r < 400 \text{ km} \\ r^{-0.5} & r > 400 \text{ km}. \end{cases}$$

Figure 3.17 shows the horizontal component (top panel) and vertical component (bottom panel) reduced attenuation functional  $D(r, f)$  obtained from the regression on the Fourier velocity spectra of 1.0, 2.0, 3.0, 4.0, 6.0, 8.0, 10.0, 12.0, 14.0, and 16.0 Hz for the southeastern Canada. The  $D(r, f)$  obtained from the regression of vertical and horizontal component data sets. An  $r^{-1.0}$  is required to fit the distance range (10 - 40 km) for horizontal component and the vertical component distance scaling. This  $g(r)$  is different from that of time domain result and may be due to the smaller number of observations used for the estimation for the  $D(r, f)$ . The parameters for vertical and horizontal component data sets are  $Q(f) = 650f^{0.33}$  and

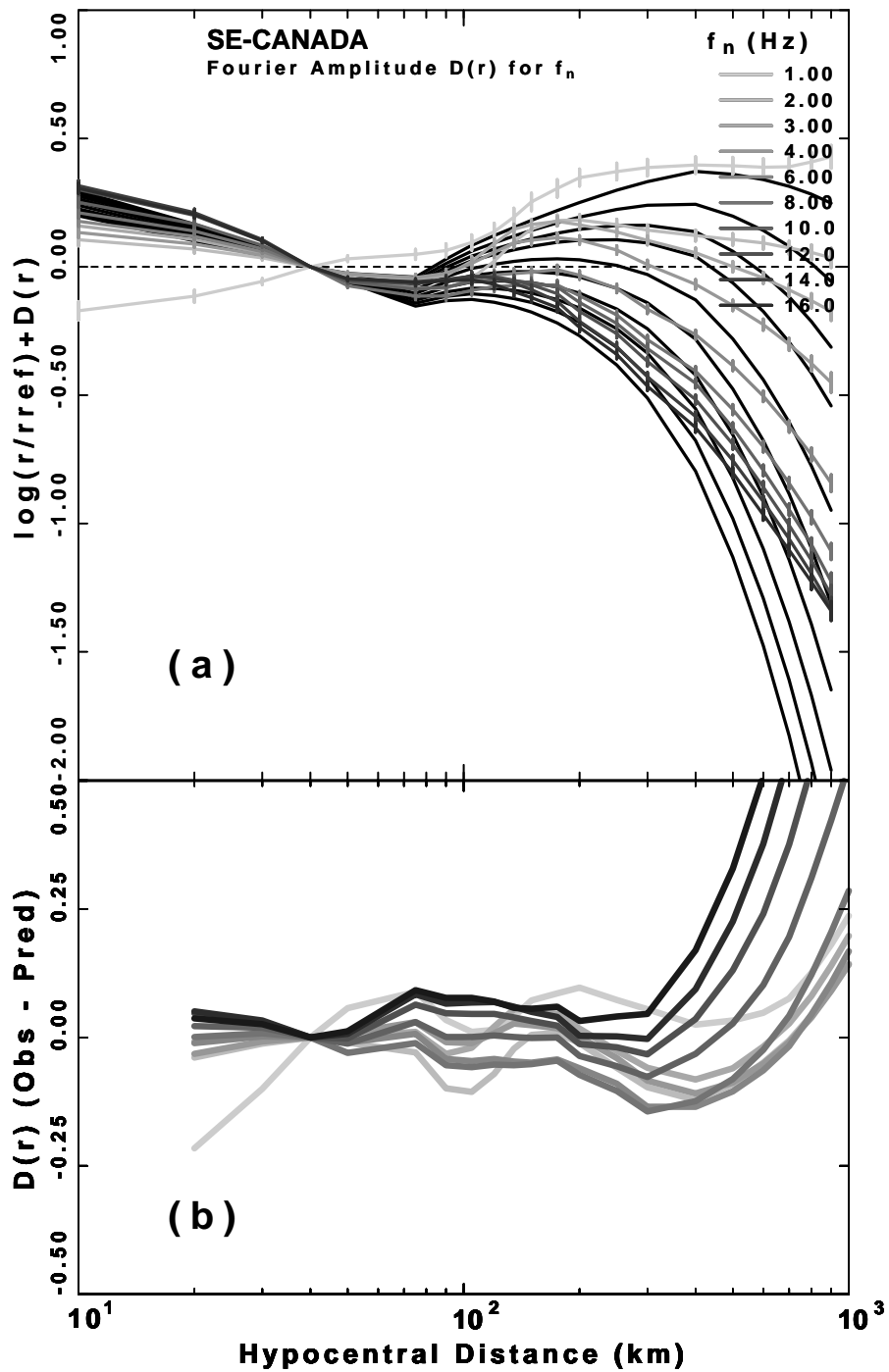


Figure 3.16: (a) The reduced attenuation functional  $D(r, f)$  obtained from the regression on the Fourier velocity spectra at the frequencies of 1.0, 2.0, 3.0, 4.0, 6.0, 8.0, 10.0, 12.0, 14.0, and 16.0 Hz for southeastern Canada; (b) The residuals of the model fit to the Fourier velocity spectra  $D(r, f)$  for the frequency range of 1 - 16 Hz.

$$g(r) = \begin{cases} r^{-1.0} & r < 60 \text{ km} \\ r^{-0.0} & 60 < r < 80 \text{ km} \\ r^{-0.2} & 80 < r < 400 \text{ km} \\ r^{-0.5} & r > 400 \text{ km}. \end{cases}$$

### 3.3.4 Parameterization of peak filtered velocity

Figure 3.18 shows the three component distance scaling of the peak filtered velocity  $D(r, f)$  term at ten different frequency ranges for the southeastern Canada. The presented  $D(r, f)$  values are corrected for an  $r^{-1.0}$  trend to emphasize departure from simple  $r^{-1.0}$  spreading. The reference distance at 40 km was used to normalize the  $D(r, f)$ . The horizontal dashed line represents  $r^{-1}$  trend. The regression results are plotted in gray shades and the theoretical predictions as solid black curves. The residuals of fit are small out to 400 km, but increase in a manner that is not simply related to frequency dependence at larger distances.

I used  $Q_0 = 650$ ,  $\eta = 0.33$ , and

$$g(r) = \begin{cases} r^{-1.3} & r < 40 \text{ km} \\ r^{-1.0} & 40 < r < 60 \text{ km} \\ r^{-0.0} & 60 < r < 80 \text{ km} \\ r^{-0.2} & 80 < r < 400 \text{ km} \\ r^{-0.5} & r > 400 \text{ km} \end{cases}$$

for propagation parameters for peak filtered velocity data set. These model parameters are first defined by fitting Fourier velocity  $D(r, f)$  and tested again by using the duration of Table 3.9 with  $RVT$  to match the time domain  $D(r, f)$ . I used time domain results because I want to model time domain data. The  $Q(f)$  trades off with  $g(r)$  because of the limited frequency range and finite distance.

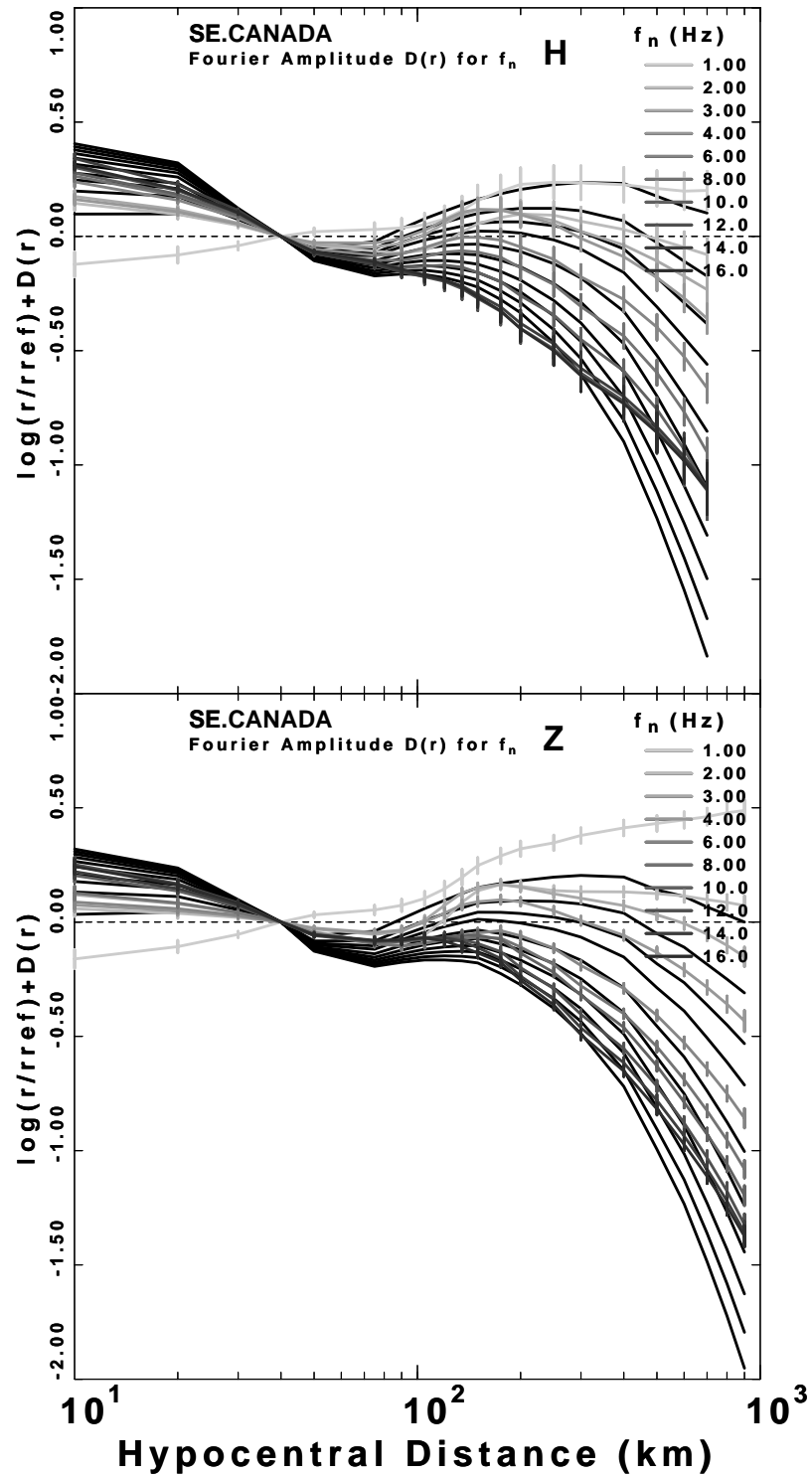


Figure 3.17: Horizontal component (top panel) and vertical component (bottom panel) reduced attenuation functional  $D(r, f)$  obtained from the regression on the Fourier velocity spectra from 1.0, to 16.0 Hz for the southeastern Canada.

Furthermore,  $Q(f)$  is closely related to the signal bursts within the duration window. Therefore, the  $Q(f)$  determined is not unique and is not directly related to  $Q(f)$  values estimated from other parts of the seismic waveform ( $Q_c$ ,  $Q_P$ , and  $Q_{Lg}$ ).

Figure 3.19 shows horizontal component distance scaling of the  $D(r, f)$  terms of the peak filtered velocities on southeastern Canada. The residuals of fit are greater than that of Figure 3.18 in overall distance range, especially at frequency range greater than 12 Hz. Figure 3.20 shows vertical component distance scaling of the  $D(r, f)$  terms for the regression on southeastern Canada. The residuals of fit is similar to that of Figure 3.18 in overall distance range. I used different geometrical spreading  $g(r)$  at a short distance range and separate durations for each component. An  $r^{-1.3}$  is required to fit the distance range for horizontal component while  $r^{-1.0}$  is used to fit the vertical component distance scaling. Table 3.9 shows the duration used for each parameterization.

For Horizontal component:  $Q_0 = 650$ ,  $\eta = 0.33$ , and

$$g(r) = \begin{cases} r^{-1.3} & r < 40 \text{ km} \\ r^{-1.2} & 40 < r < 60 \text{ km} \\ r^{-0.0} & 60 < r < 80 \text{ km} \\ r^{-0.2} & 80 < r < 400 \text{ km} \\ r^{-0.5} & r > 400 \text{ km} \end{cases}$$

for Vertical component:  $Q_0 = 650$ ,  $\eta = 0.33$ , and

$$g(r) = \begin{cases} r^{-1.0} & r < 40 \text{ km} \\ r^{-1.2} & 40 < r < 60 \text{ km} \\ r^{-0.0} & 60 < r < 80 \text{ km} \\ r^{-0.2} & 80 < r < 400 \text{ km} \\ r^{-0.5} & r > 400 \text{ km}. \end{cases}$$

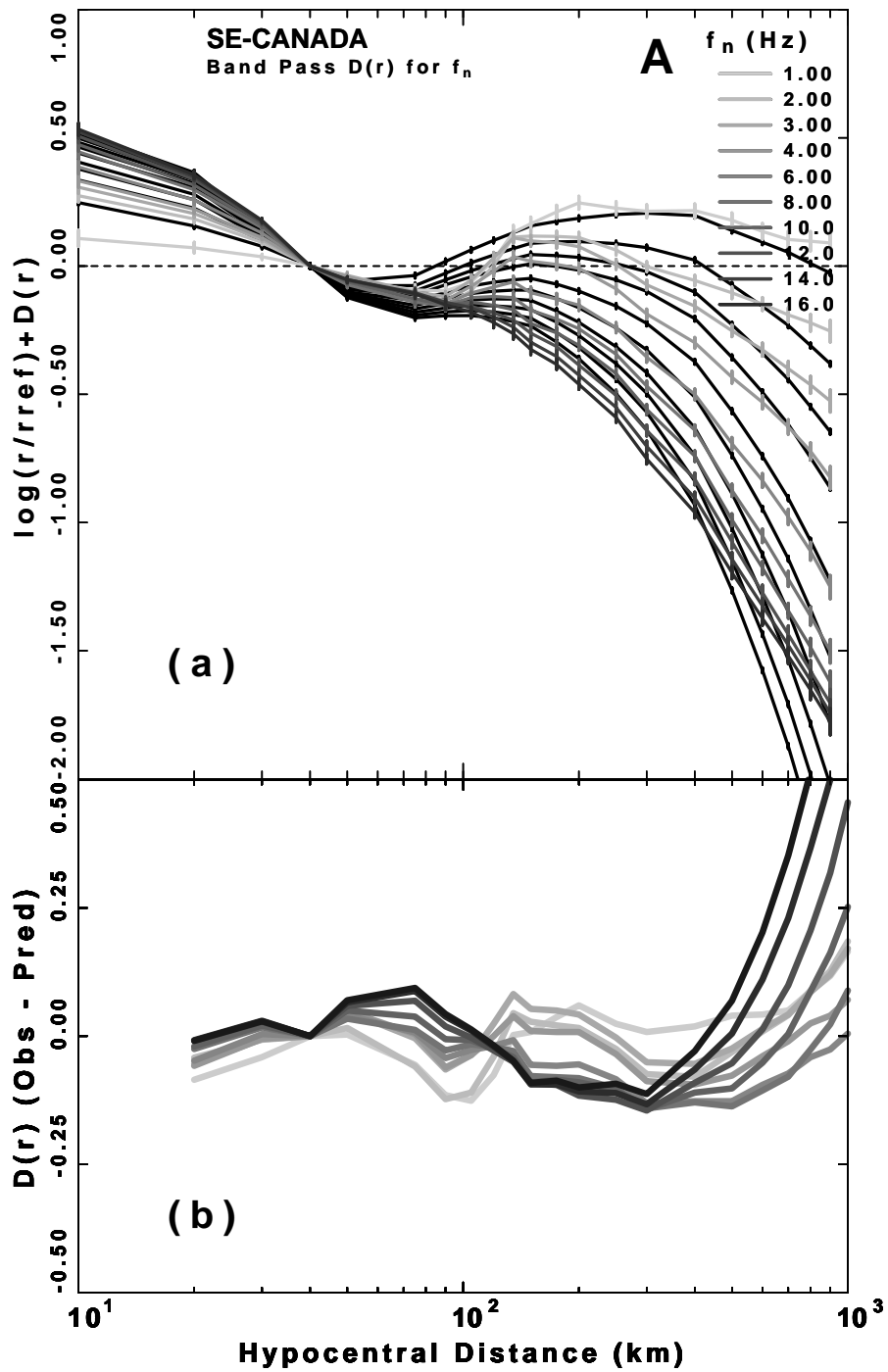


Figure 3.18: (a) Three component reduced attenuation functional  $D(r, f)$  at the frequencies of 1.0, 2.0, 3.0, 4.0, 6.0, 8.0, 10.0, 12.0, 14.0, and 16.0 Hz for southeastern Canada; (b) The residuals of the model fit to the band pass  $D(r, f)$  from 1 to 16 Hz.

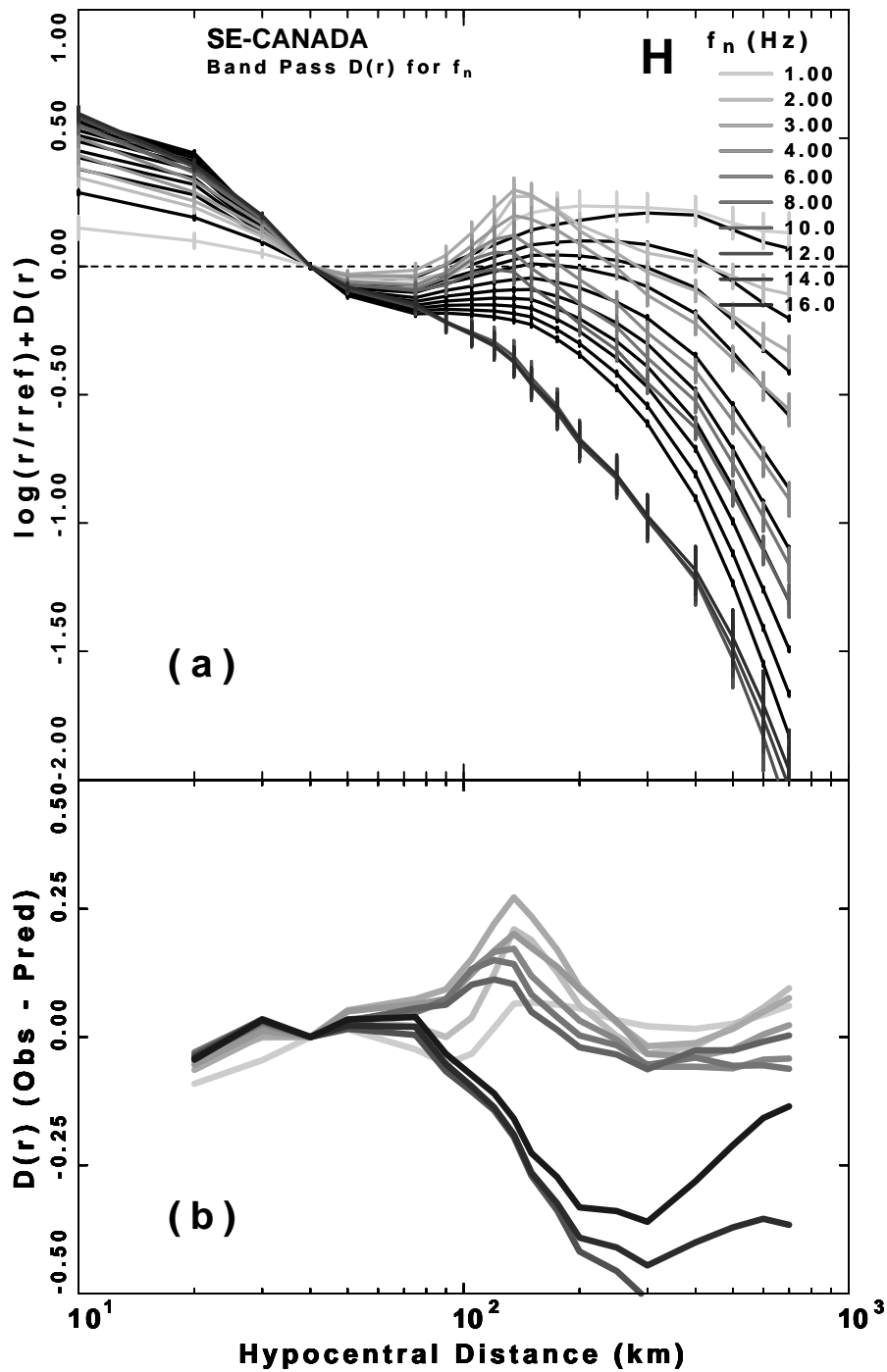


Figure 3.19: (a) Horizontal component reduced attenuation functional  $D(r, f)$  from bandpass-filtered velocities of 1.0, 2.0, 3.0, 4.0, 6.0, 8.0, 10.0, 12.0, 14.0, and 16.0 Hz for southeastern Canada; (b) The residuals of the model fit to the band pass  $D(r, f)$ .

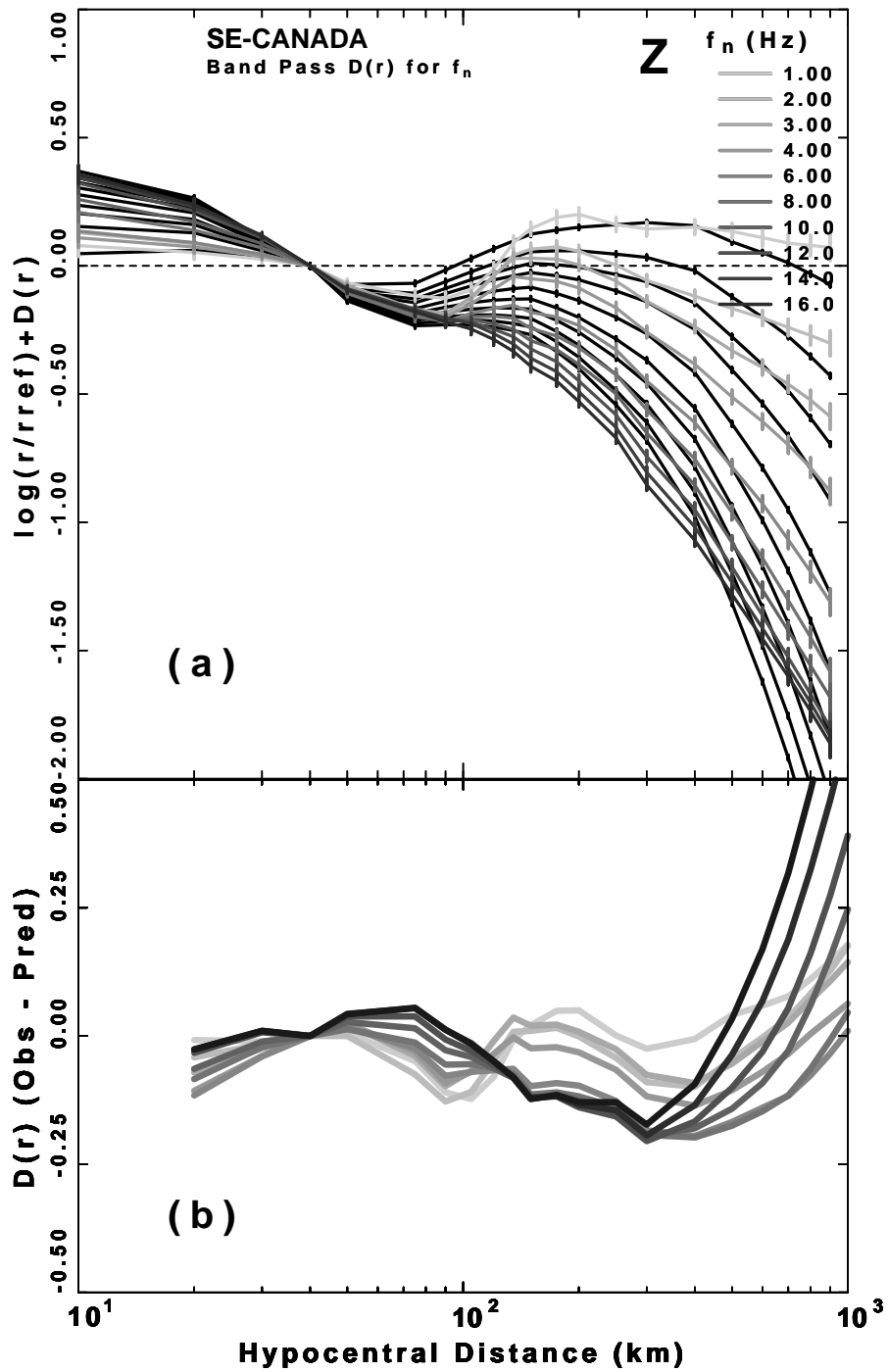


Figure 3.20: (a) Vertical component reduced attenuation functional  $D(r, f)$  obtained from the regression on the bandpass-filtered velocities of 1.0, 2.0, 3.0, 4.0, 6.0, 8.0, 10.0, 12.0, 14.0, and 16.0 Hz for southeastern Canada; (b) The residuals of the model fit to the band pass  $D(r, f)$  for the frequency range of 1 - 16 Hz.

### 3.3.5 Wave propagation comparisons: Atkinson and Boore (1995) model

Figure 3.21a compares three component distance scaling of the peak filtered velocity  $D(r, f)$  term for southeastern Canada and the theoretical  $D(r, f)$  of Atkinson and Boore's model (1995). The regression results are plotted in gray shades and the theoretical predictions as solid black curves. Figure 3.21b shows the differences between the observations and predictions. The residuals of fit are low out to 600 km. Table 3.13 lists the model parameters of Atkinson and Boore and this study (three component data set) for southeastern Canada.

Figure 3.22a shows horizontal component distance scaling of the  $D(r, f)$  terms of the peak filtered velocities on southeastern Canada and theoretical  $D(r, f)$  of the Atkinson and Boore (1995) model. The residuals of fit (Figure 3.22b) are high at 14 and 16 Hz because the data window used at larger distances does not include  $L_g$  waves.

Figure 3.23a shows vertical component distance scaling of the  $D(r, f)$  terms for the regression on southeastern Canada. The residuals of fit are similar to that of Figure 3.21b in overall distance range. The comparisons of  $g(r)$  at a short distance range is not applicable because Atkinson and Boore (1995) model does not have data less than 30 km in distance range. Overall, the Atkinson and Boore (1995) model predicts the  $D(r, f)$  well for the entire distance range (30 - 600 km), while this study has the advantage of having more observations at short (less than 30 km) and longer (600 - 1000 km) distance range.

Recently, Atkinson (2004) studied empirical attenuation of ground motions

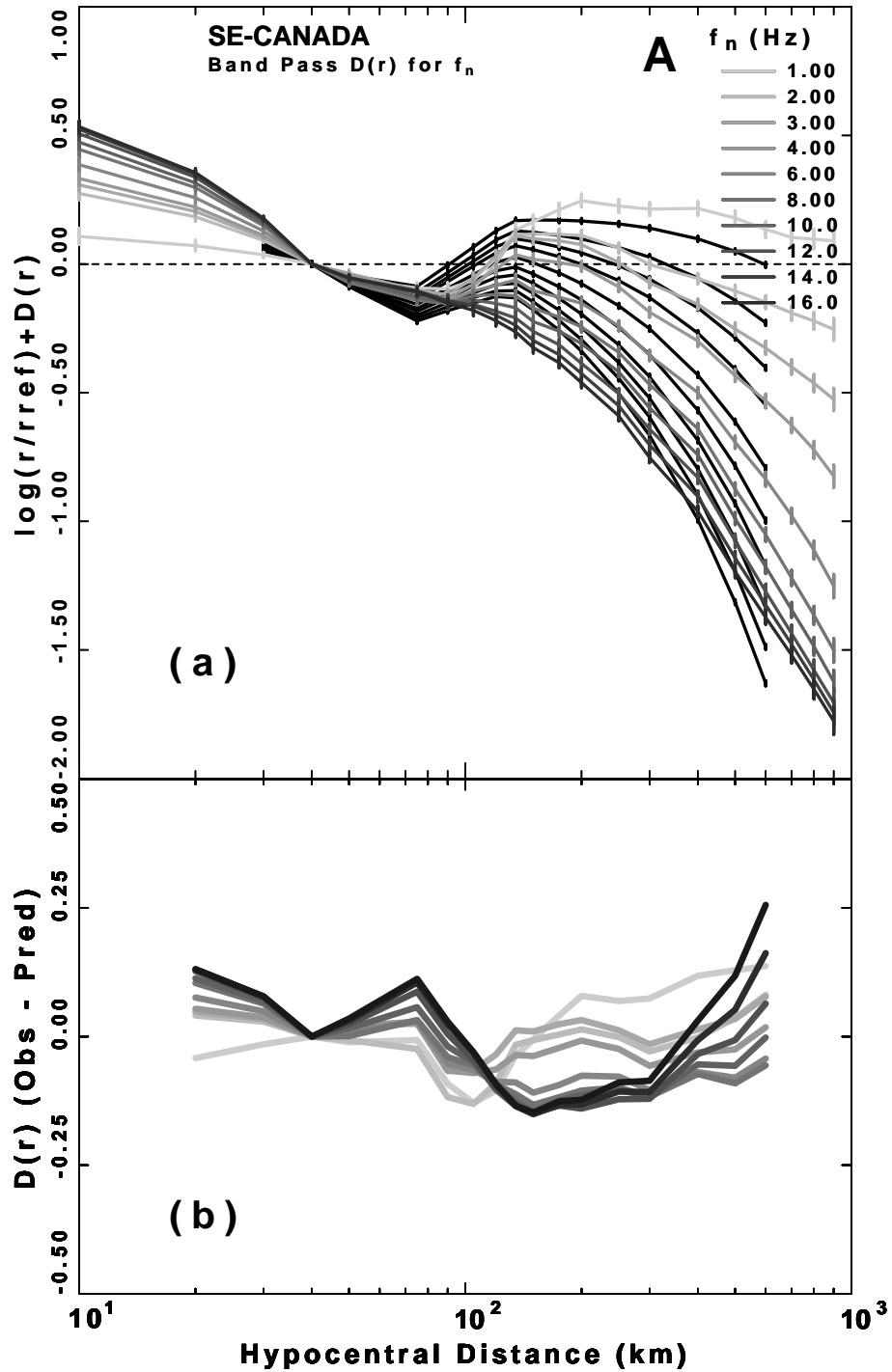


Figure 3.21: (a) The  $D(r, f)$  obtained from the regression on the bandpass-filtered velocities for southeastern Canada. The black lines in the background are the theoretical  $D(r, f)$  of Atkinson and Boore (1995) model parameters; (b) The residuals of the model fit to the band pass  $D(r, f)$  from 1 to 16 Hz.

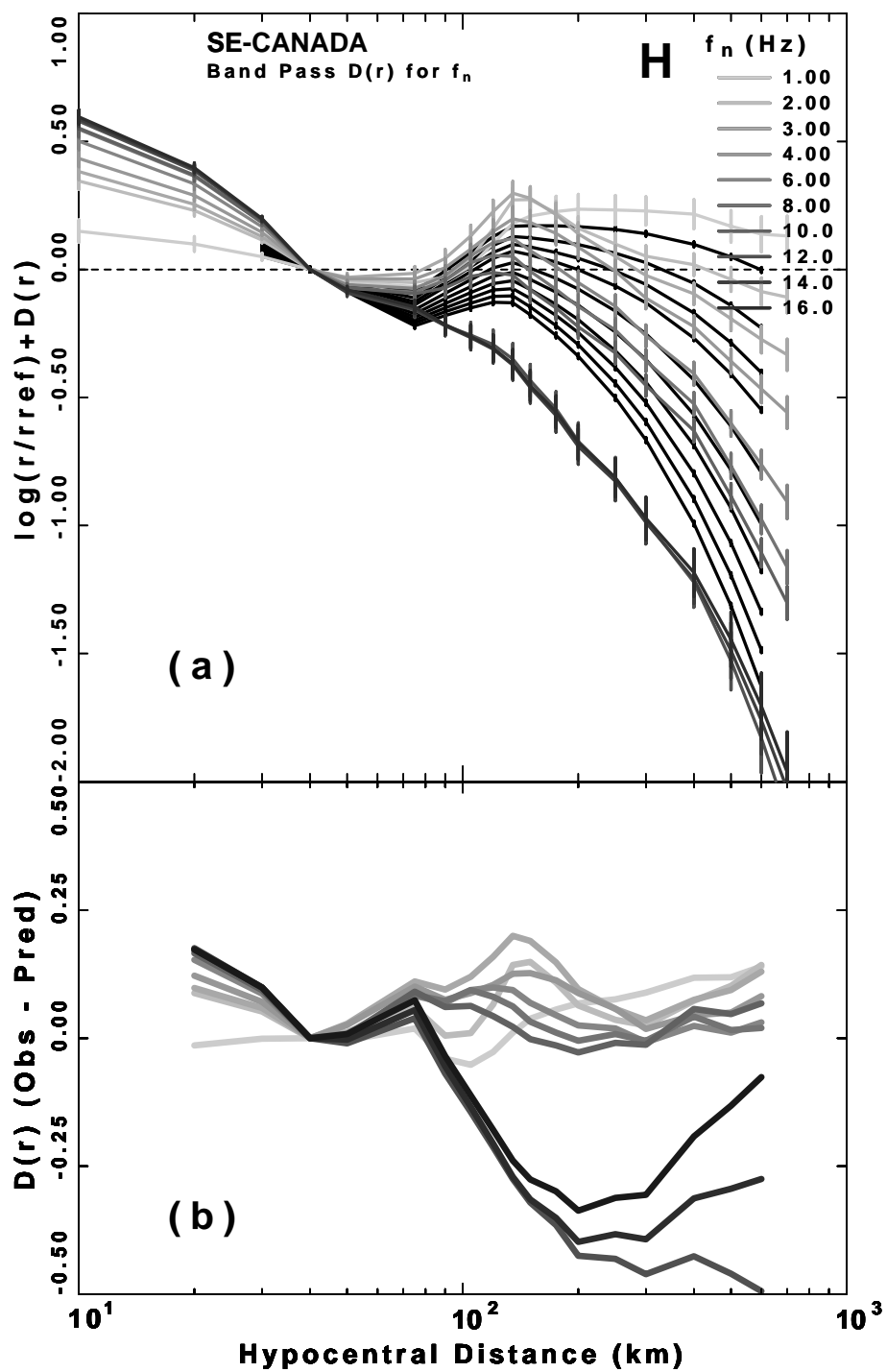


Figure 3.22: (a) Horizontal component  $D(r, f)$  of the bandpassed filtered velocities on southeastern Canada and theoretical  $D(r, f)$  of Atkinson and Boore (1995) model (black lines in the background); (b) The residuals of the model fit to the band pass  $D(r, f)$  from 1 to 16 Hz.

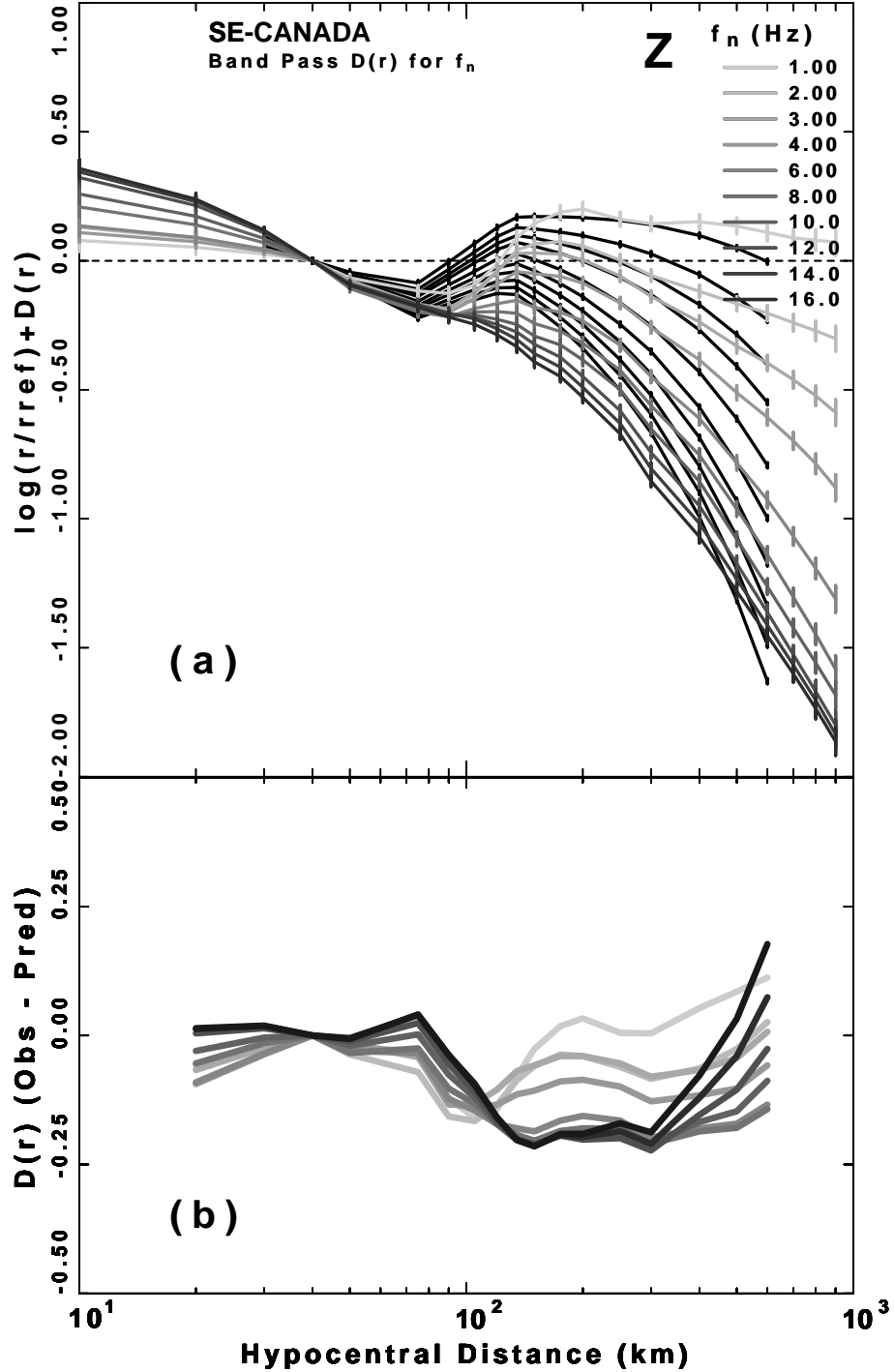


Figure 3.23: (a) Vertical component  $D(r, f)$  of the bandpass-filtered velocities for southeastern Canada. Atkinson and Boore (1995) model parameters used for theoretical  $D(r, f)$ ; (b) The residuals of the model fit to the band pass  $D(r, f)$  from 1 to 16 Hz.

Atkinson and Boore (1995)			This study	
$Q(f)$	$670f^{0.33}$		$650f^{0.33}$	
$g(r)$	$r^{-1.1}$	$0 < r \leq 70 \text{ km}$	$r^{-1.3}$	$0 < r \leq 40 \text{ km}$
	$r^{0.0}$	$70 \leq r \leq 130 \text{ km}$	$r^{-1.0}$	$40 \leq r \leq 60 \text{ km}$
	$r^{-0.5}$	$130 \leq r \leq 600 \text{ km}$	$r^{0.0}$	$60 \leq r \leq 80 \text{ km}$
			$r^{-0.2}$	$80 \leq r \leq 400 \text{ km}$
			$r^{-0.5}$	$r \geq 400 \text{ km}$
$T(r)$	0.0 sec	r = 0.0 km	0.0 sec	r = 0.0 km
	11.2 sec	r = 70.0 km	8.2 sec	r = 60.0 km
	7.4 sec	r = 130.0 km	9.6 sec	r = 150.0 km
	26.6 sec	r = 600.0 km	41.8 sec	r = 1000 km

Table 3.13

spectral amplitudes in *ENA* and re-evaluated model parameters for Southeastern Canada and Northeastern United States because the database for *ENA* has been grown significantly. The commonly used empirical models for *ENA* are Atkinson and Boore (1995), Toro et al. (1997), Frankel et al. (1996, 1999), and Campbell (2003). All of which are based upon the Atkinson and Mereu (1992) attenuation model derived from about 1000 digital short period vertical component seismogram recorded from 1980 to 1990 on the Eastern Canada Telemetered Network (ECTN). The new model parameters for Fourier spectra of earthquakes are based upon 1700 digital seismograms from 1990 to 2003 occurring in *ENA*. The old model parameters were derived using data from 1 to 10 Hz, while the new model uses 0.2 to 20 Hz including horizontal component ground motions. The Brune model and stress drops of 100 to 200 bars are used for spectral model parameters. Fourier spectral amplitudes decay as  $g(r) = -1.3$  less than 70 km,  $g(r) = +0.2$  from 70 to 140 km, and  $g(r) = -0.5$  beyond 140

km with the associated  $Q(f) = 893f^{0.32}$  (Atkinson, 2004).

### 3.4 Site

The estimation of site amplification is also important for simulating earthquake ground motions such as stochastic model (e. g., Boore, 1996). It is parameterized by the  $\exp(-\pi\kappa f)$ . The high frequency spectral decay parameter which is related to attenuation is converted to  $\kappa$ , the value of the slope, to quantify the trends of Fourier amplitude spectrum of acceleration (or velocity). It represent a gradual diminution of spectral amplitudes with increasing frequencies near-source distances where anelastic attenuation is negligible (Atkinson and Boore, 1998).

$\kappa$  tends toward a finite value as epicentral distance approaches zero; This finite value interpreted as a characteristic of the subsurface geological structures near the station because it is a weak function of distance. Dobrin (1960) referred to terminology "subsurface geological structures" as the conditions below and near the site within distances from a few hundred meters to several kilometers.  $\kappa$  values scatter with the effect of different subsurface geological structures.  $\kappa$  values seem to be smaller on rock sites than on sites of less compact geology, soil or alluvium (Anderson and Hough, 1984).

The parameter  $\kappa$  in the exponential filter can be related to a  $f_{max}$ , cut off frequency. For some small to moderate earthquakes, if the exponential form be reduced to  $1/e$  at  $f = f_{max}$ , this will leads to  $\kappa = 1/\pi f_{max}$ . For larger earthquakes,  $\kappa = 1/2\pi f_{max}$  is required.  $f_{max}$  is generally large enough that the choice of the

high-cut filter makes little difference on the frequency range of interest, normally, less than 10Hz (Boore and Atkinson, 1987).  $f_{max}$  has been interpreted as a source or a site parameter (Hanks, 1982; Papageorgiou and Aki, 1983) and its effects can be represented by a single-valued cut-off frequency. Normally, 15 Hz for the rock sites in the Western United States (Hanks, 1982) and 50 Hz for ENA hard-rock sites (Atkinson, 1984) are used.

Figure 3.24 shows the site terms for the southeastern Canada for the peak filtered velocity regression. The individual site terms agree well for the three components (top panel: a, b) and vertical component (lower right panel: d), but there is much deviation in the horizontal component (lower left panel: c). The constraint of  $\sum S_Z(f) = 0$  is used for site amplifications on the left panels (a, c) while the constraint of  $\sum S_H(f) = 0$  is used for site amplifications on the right panels (b, d).

### 3.5 Excitation

The theoretical Fourier velocity spectra at a distance of  $r = 1 \text{ km}$  used in equation (3.4) is

$$S(f, M_{\mathbf{W}}) = \frac{C M_0 2\pi f}{(1 + (f/f_c)^2)} \quad (3.9)$$

where the seismic moment in dyne-cm is a function of moment magnitude  $M_{\mathbf{W}}$  and  $f_c$  is the source corner frequency (equation (4), Boore, 2003) defined in terms of  $S$ -wave velocity  $\beta$  (in  $\text{km/sec}$ ),  $M_0$  and a stress propagation parameter  $\Delta\sigma$ . The constant  $C$  is

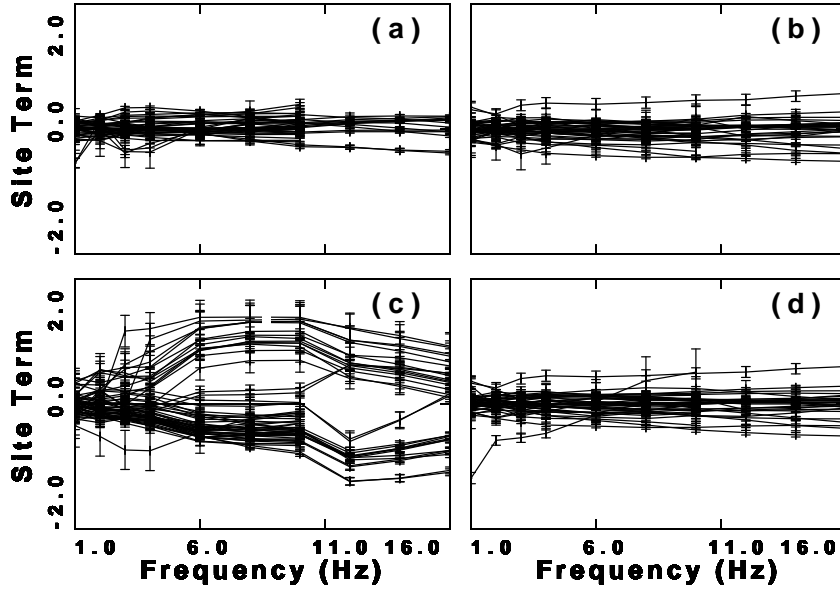


Figure 3.24: Inverted site amplifications of southeastern Canada in peak amplitudes. a and b are Z and H component site terms of ground motion while c and d are H and Z component site terms of ground motion.

$$C = \frac{R_{\Theta \Phi} F V}{10^{20} R_0 4 \pi \rho \beta^3}. \quad (3.10)$$

Here  $R_{\Theta \Phi}$  is the radiation pattern averaged over a suitable range of azimuths and takeoff angles,  $F$  represents the amplification at the free surface,  $V$  denotes the reduction factor that accounts for the partitioning of energy into two horizontal components,  $R_0$  refers a reference distance set equal to 1 km,  $\rho$  is the density (in  $g/cm^3$ ) at the source and  $10^{20}$  converts kilometers to centimeters so that  $M_0$  has units of dyne-cm and  $S(f, M_W)$  has units of cm-sec. I use  $R_{\Theta \Phi} = 0.55$ ,  $F = 2.0$ ,  $V = 0.707$  following Boore (2003).

Source parameters such as strain energy release, fault offset, fault area, rise time and duration of fault, stress drop, source dimension, moment and radiated seismic energy can be related each others, but their relationship requires a

spectral description of the seismic source. Such a description demands either stress release mechanism or a complete time and space history of the faulting (Kanamori and Anderson, 1975). Among these parameters, stress drop  $\Delta\sigma$  has been subject of discussion by seismologists as to its meaning, measurement, and scaling with magnitude. It was first presented as a static measure of final fault slip,  $\Delta\mu/r$ , where  $\mu$  is the rigidity and  $r$  is the radius of fault and was estimated from direct measurements or inferences of geological parameters. It is defined as the ratio of fault slip to fault dimensions and may be calculated from seismic moment and the source duration. The definition of stress drop is

$$\Delta\sigma = C\mu(\bar{D}/\tilde{L}) \quad (3.11)$$

where  $C$  is a non-dimensional shape factor, and  $\bar{D}/\tilde{L} \equiv \Delta\tilde{\epsilon}$  is the representative strain change, or strain drop. The stress drop may be depends on the earthquake size and is generally assumed to be constant for smaller earthquakes. The stress drop values derived from data are dependent on the specific model which is used to derive them. They are subject to a large degree of uncertainty caused by uncertainties between model parameters. This uncertainty may be due to estimates of source duration and even the relation used to extrapolate observations at distance back to the source. Stress drop has been used in engineering seismology as a formal parameter controlling the strength of high frequency radiation. The Brune (1970, 1971) omega-squared point source model has the average (over all azimuths) high frequency spectral level proportional

to the stress drop.

Figure 3.25 compares the predicted excitations at 40 kilometers to those obtained from the regressions on the band passed filtered velocity spectra (black lines). Thick dark gray lines each mark the  $M_W$  for 2.0, 2.5, 3.0, 3.5, 4.0, 4.5, 5.0, and 5.5 from the lowest line. I found that a  $\kappa_{eff} = 0.01$  sec is required to fit the time domain excitation terms for the smallest earthquakes and that  $\Delta\sigma = 300$  bars by Brune's point source model for source spectra fits the observed  $E(r, f)$  over the moment magnitude range less than 4. The lack of fit by theoretical excitation level for  $M_W = 4.5, 5.0, 5.5$  in Figure 3.25 in the low frequency range is also noted by Atkinson and Boore (1995). The theoretical excitation level of  $M_W = 4.5$  matches source excitation level of the thick short-dashed line ( $M_W = 5.0$ ) indicating that either the observed source excitation level is higher or the theoretical excitation level is lower, while the source excitations of the thick long-dashed lines ( $M_W = 4.3, 4.4,$  and  $4.5$ ) plot between the predicted  $M_W$  4.0 and 4.5 indicating that the theoretical excitation levels are appropriate. I also put the thick light gray lines ( $M_W = 3.4, 3.5, 3.6,$  and  $3.7$ ) for reference. The standard errors on the excitation terms are normally less than  $0.2 \log_{10}$  units, but high as much as  $0.3 \log_{10}$  units in a few events depends on the number of trace used for regressions.

### 3.5.1 Source model parameters of Atkinson and Boore

The earthquake that occurred near Au Sable Forks, New York on 20 April 2002 is the first earthquake recorded in *ENA* since the modern broadband

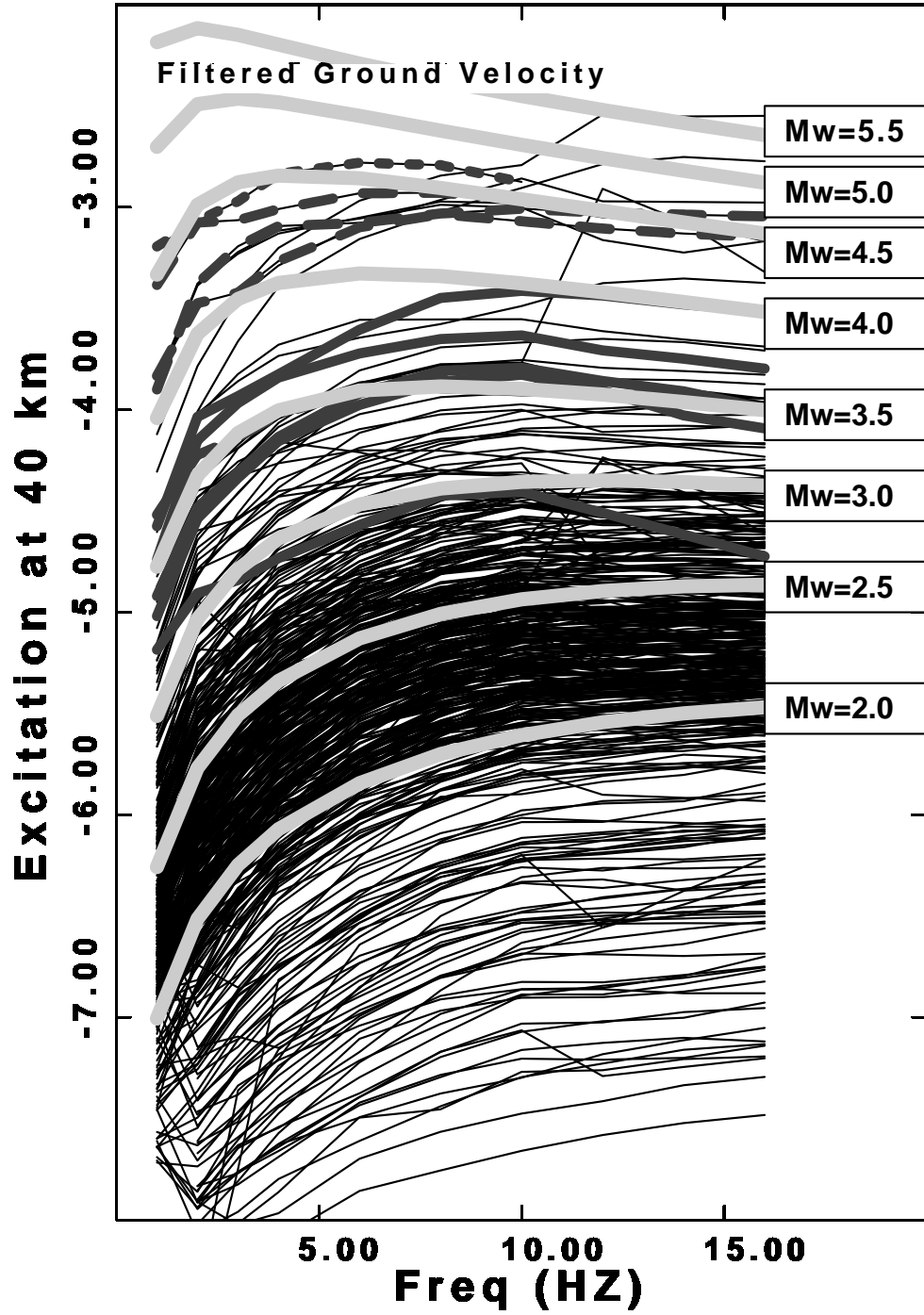


Figure 3.25: Inverted filtered ground velocity excitation terms for the earthquake events recorded by three-component velocity seismograms plotted on a linear frequency scale. Thin black lines are the inverted excitation and thick gray lines are model based prediction for southeastern Canada.

seismic network were installed (Atkinson and Sonley, 2003). This event is important because of its moderate size  $M_W = 5.0$  and data fidelity for source and propagation studies of *ENA* earthquakes. The Saguenay earthquake which raised many questions occurred in 1988 before modern high dynamic range digital instruments installed . The Au Sable Forks earthquake is very useful to review the source parameters of the last decade's work and check if they are well defined. A sag near 2 Hz (intermediate frequencies) is observed and its source spectrum matches the two corner model of Atkinson and Boore (1995) rather than Brune's point source model. The complexity of source sag can be explained as the result of finite-fault effects (Beresnev and Atkinson, 2002).

Figure 3.26 shows the excitations obtained from band passed filtered velocity spectra (black lines) and theoretical excitations of Atkinson and Boore (1995) model parameters (two corner model) in southeastern Canada. Thick dark gray lines each mark the  $M_W$  from 2.0 to 5.5. The theoretical excitation level of  $M_W = 5.0$  matches the Au Sable Forks earthquake's source excitation level (thick short dash line) while the source excitations of thick long dash lines ( $M_W = 4.3, 4.4, \text{ and } 4.5$ ) are overestimated. I also put the thick light gray lines ( $M_W = 3.4, 3.5, 3.6, \text{ and } 3.7$ ) for reference. The two corner model fits better at lower frequency range compared to that of Figure 3.25. However the excitation levels of some events (thick lines) are not well matched by the theoretical.

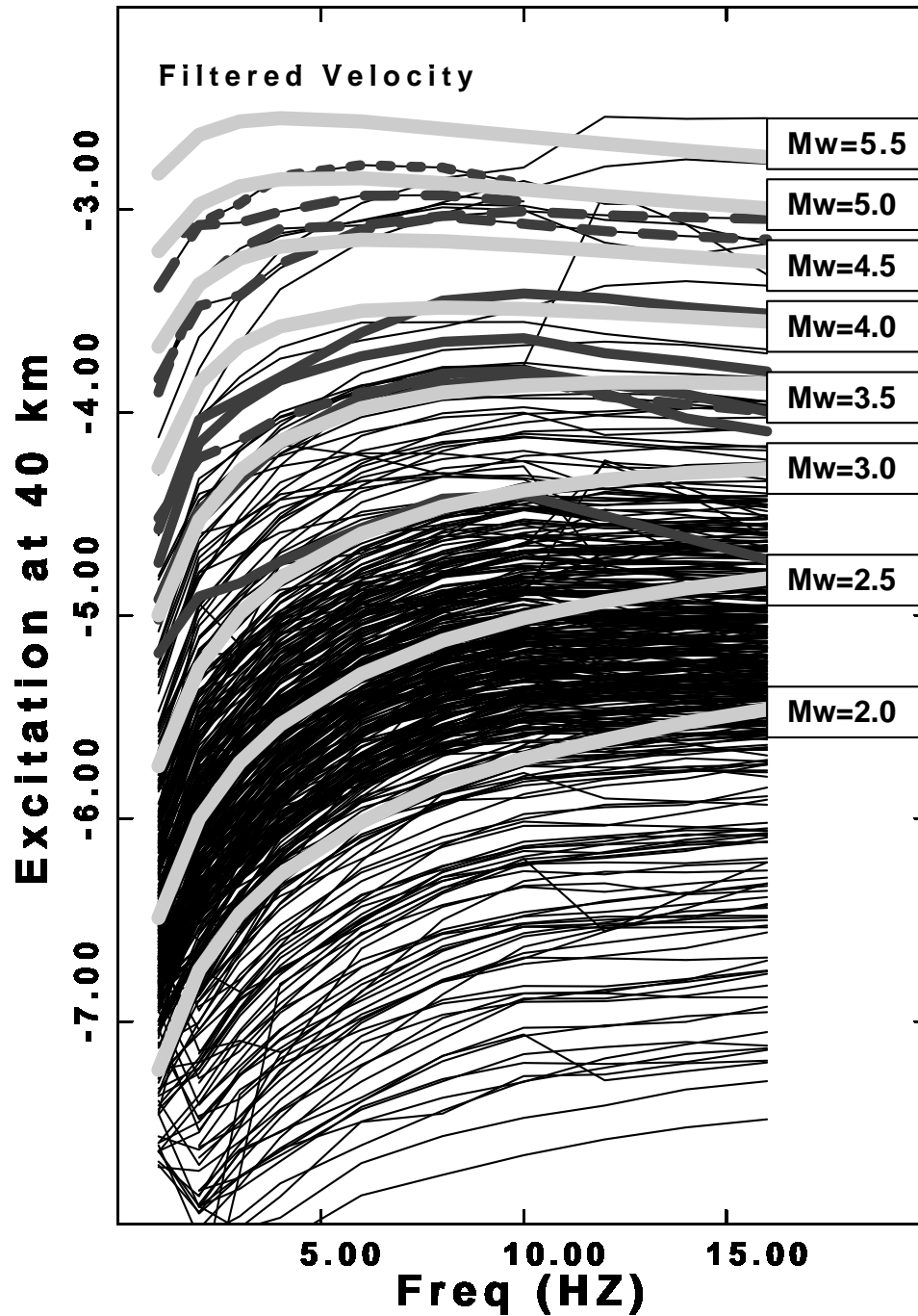


Figure 3.26: Band passed filtered velocity excitation (thin black lines) and model based prediction (thick gray lines) for the southeastern Canada. The thin black line linked by thin long-dashed line is the observed excitation of Au Sable Forks earthquake and the thin black lines linked by thick short-dashed lines are the excitations of  $M_w = 4.3$ ,  $4.4$ , and  $4.5$  events.

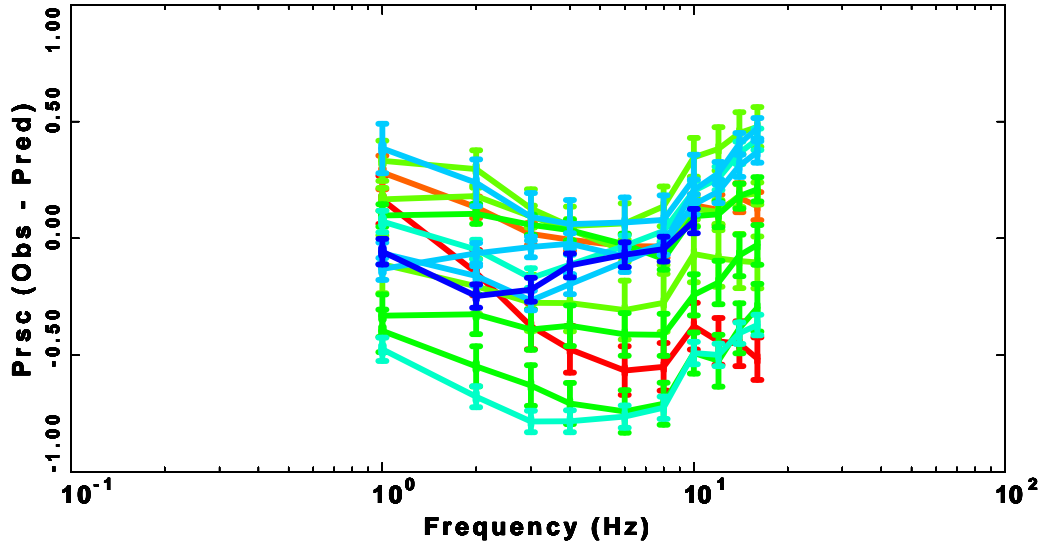


Figure 3.27: The residuals of the model fit to the band pass  $E(f)$  for the stochastic point source model as a function of frequency range from 1 to 16 Hz for southeastern Canada.

### 3.5.2 Source excitation comparisons

Figure 3.27 shows the  $E(f)$  residuals, the deviation between observed and predicted  $E(f)$  for southeastern Canada's events with known moment magnitude. The purpose of this is to define absolute scaling of ground motion and to check if the  $g(r)$  chosen is valid. The residuals of fit are high at lower and higher frequency ranges. Low frequency residuals may be related with the sag of using Brune's source model and high frequency deviations are typical characteristics of southeastern Canada.

Figure 3.28 shows the reduced residuals of  $E(f)$  modified by changing stress drops in a single corner Brune model. This step is important because if I can reduce the residuals dramatically, then it indicates that the parameterization should be revisited. I tried several kappa values to reduce the high frequency

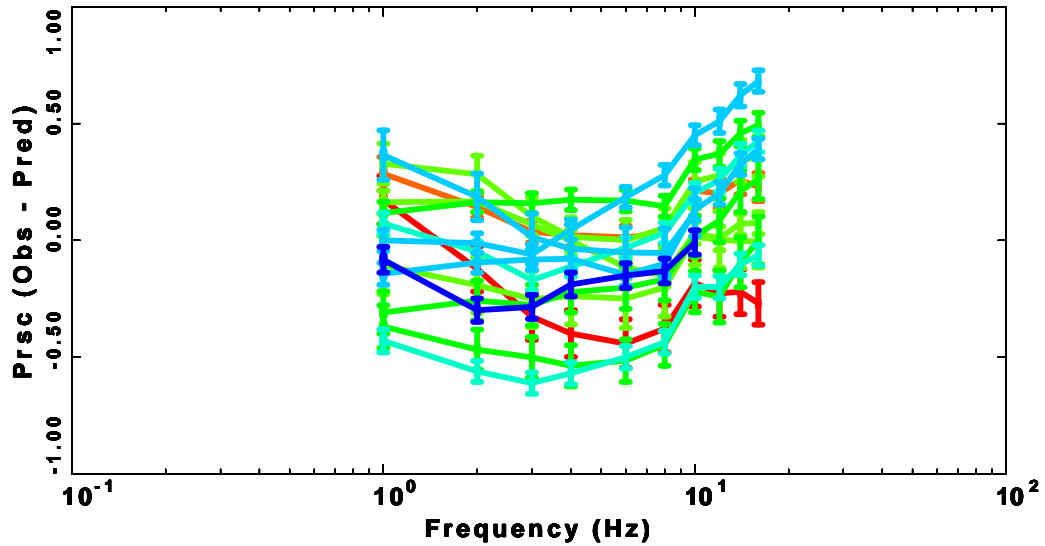


Figure 3.28: Modified residuals of the model fit to the band pass  $E(f)$  for the stochastic point source model as a function of frequency range from 1 to 16 Hz for southeastern Canada. Individual stress drops (100, 200, 300, 400, and 500 bars) are applied to stochastic model to reduce the residuals.

residuals and varied the stress drops to find the absolute value of source scaling relations. But, even if I can reduce the residuals in some frequency range, I could not find the model parameters that can reduce the residuals over the entire frequency ranges. This may indicate that different stress drops for each event are required to explain the southeastern Canada's source characteristics. Atkinson (2004) also used independent stress drops to fit the source spectra for earthquakes in southeastern Canada.

The spectral parameters for southeastern Canada used for Figures 3.26 and 3.27 are

### Focal mechanism parameters for ENA

Lat <sup>†</sup> (N <sup>0</sup> )	Lon <sup>‡</sup> (W <sup>0</sup> )	Depth (km)	Strike ( <sup>0</sup> )	Dip ( <sup>0</sup> )	Rake ( <sup>0</sup> )	M <sub>w</sub>	Date yy/mm/dd
44.2600	71.4100	7.0	144	60	93	3.4	96/08/21
44.5800	73.7300	18.0	-	-	-	3.55	02/04/20
41.9300	80.7200	5.0	-	-	-	4.03	01/01/26
50.0300	63.3500	18.0	-	-	-	3.92	01/03/24
52.8900	74.4100	5.0	-	-	-	3.84	02/06/05
43.9500	74.2500	8.0	150	54	120	3.6	00/04/20
44.3300	72.0400	6.0	95	50	40	3.7	95/06/16
45.9200	74.4000	18.0	136	36	98	3.7	96/03/14
47.6700	69.9100	5.0	27	66	111	4.3	97/10/28
49.6100	66.3200	18.0	30	63	93	4.4	99/03/16
46.8000	71.4200	22.0	39	63	87	4.5	97/11/06
41.5200	80.5300	2.0	9	69	144	4.5	98/09/25
44.5300	73.7300	12.0	-	-	-	5.0	02/04/20

---

Lat<sup>†</sup> and Lon<sup>‡</sup> denote latitude and longitude. Details on the determination of the source parameters are at Du et al. (2003) and Atkinson (2004).

---

Table 3.14

$$\left\{ \begin{array}{l} \Delta\sigma = 200 \text{ bars} \\ \kappa_{eff} = 0.01 \text{ sec} \\ \rho = 2.8 \text{ g/cm}^3 \\ \beta = 3.5 \text{ km/sec} \\ f_c = 4.9 \times 10^6 \beta (\Delta\sigma/M_0)^{1/3} \text{ Hz} \\ M_0 = 10^{1.5M_w+16.05} \end{array} \right.$$

Table 3.14 summarizes the results of focal mechanism studies used to obtain the seismic moments. I used these results to check the absolute ground motions.

### 3.6 Summary

I parameterized the ground motion attenuation relationships for bandpass filtered time series with modern digital data set in southeastern Canada. The

results obtained in this chapter are compared with previous study results of Atkinson and Boore (1995) and Atkinson (2004). Comparing my result with that of Atkinson and Boore (1995) indicates that more rapid  $g(r)$  is required at short distance ranges for all and horizontal component propagation terms while similar  $g(r)$  is required at short distance ranges for vertical component propagation terms. Another difference exists at mid distance ranges where Atkinson and Boore (1995) use simple  $g(r)$  while I split that range into three segments, but I used more to provide a better fit. The attenuation term of  $Q_0 = 670$ , and  $\eta = 0.33$  (Atkinson and Boore, 1995) is almost the same with that of my study. My study has the advantage of more data set at larger distances. The recent attenuation model of Atkinson (2004) indicate more rapid geometrical spreading at short distance range and higher  $Q$ ,  $Q(f) = 893 f^{0.32}$ . The geometrical spreading of Atkinson (2004) is

$$g(r) = \begin{cases} r^{-1.3} & r < 70 \text{ km} \\ r^{-0.0} & 70 < r < 140 \text{ km} \\ r^{-0.5} & r > 140 \text{ km}. \end{cases}$$

Different geometrical spreading used for same distance ranges is evidence of the different scaling of individual component.

In the paper of Atkinson (2004), she mentioned that the steeper than  $r^{-1.0}$  at near distance range may be the consequence of directivity. Burger et al. (1987) and Ou and Herrmann (1990) indicated on their wave propagation studies that the expected shape of amplitude decay for simple model layered crustal model is complex and layering in the crust causes direct-wave amplitudes to decay

more rapidly than  $r^{-1.0}$ .

I divided the data set into horizontal and vertical components and performed separate regressions. The geometrical spreading function for each component shows same values at mid- to long- distance ranges, while there are some deviations at shorter distance ranges. The combined and horizontal components of  $g(r)$  show very rapid fall off of geometrical spreading compared to the vertical component distance ranges less than 40 km. The model of Atkinson and Boore (1995) does not fit my observed  $D(r, f)$  at the mid distance range of 100 - 200 km. Their model does not provide the data at short distance range less than 30 km and distances greater than 600 km. The work of Atkinson (2004) is not directly comparable here because the result does not provide duration estimated. The measured durations do not show much variations among the durations from all, horizontal, and vertical components. The duration from combined component of horizontal and vertical data set shows not much variation compared to that of Atkinson and Boore (1995).

The spectral parameters of  $\kappa_{eff} = 0.01$  sec, and  $\Delta\sigma = 200$  bars are selected to predict the theoretical excitation spectra of southeastern Canada. Unlike to California where a Brune source model with a stress parameters of 100 bars matches well at all magnitude ranges, the stochastic method which uses one stress drop controlling the spectral level and corner frequency does not fit events with moment magnitudes greater than 4. Some events require a stress drop greater than 200 bars, while other events require lower stress drop such as 100 bars. In general, for events of  $M_W > 4$ , low frequency spectra (less

than about 4 Hz) shows a better fit for a lower stress drop (less than 100 bars), while the source excitation spectra are more nearly matched by a Brune stress parameter of 200 bars or more higher stress drop at higher frequencies (about 4 - 16 Hz). For the Fourier acceleration spectra for a given  $M_W$ , the high-frequency level varies with respect to  $\Delta\sigma$ . Normally,  $M_W$  greater than 4, the spectral level increases with  $\Delta\sigma$  and the corner frequency is lowered proportion to increasing  $M_W$ .

Previous studies of *ENA* earthquakes showed stress drops significantly different than the typical 100 bars used for *WNA*. For example, the 1990  $M_W$  4.7 Mont Laurier, Quebec earthquake, was modeled by a stress drop of 500 bars based on the average amplitude of the Fourier spectrum at high frequencies and 25 bars based on the radius of the aftershock zone. The 1988  $M_W$  5.8 Saguenay earthquake yielded the stress drop estimated from 70 bars to 600 bars. Those two results indicate that the static source characteristics are not robust predictors of high frequency ground motion for complex ruptures (Atkinson and Beresnev, 1997).

The two-corner model of Atkinson (1993a) shows better fit at intermediate frequencies at higher moment magnitude events, but may not fit all individual events given, especially at high frequency. Atkinson (2004) indicated that the stress drop increase with moment magnitude for events less than 4.3, while relatively constant level in the range of 100 to 200 bars is applied for larger events (less than  $M_W < 5$ ). Therefore, I may speculate the earthquakes population may have a distribution of stress drops rather than a single universal

value for this region.

## Chapter 4

# Ground motion scaling in Korea

### 4.1 Data set

#### 4.1.1 Korean network

The KMA seismic network data are the result of Kinemetrics-Quanterra data loggers, STS-2, STS-1, and Episensor sensors, and the Antelope analysis system. Tables 4.1 and 4.2 give the station names and sensors used for Korean study. Table 4.3 lists the response information for each sensor system used.

#### 4.1.2 Study area

The study area ranges from  $33^{\circ}$  to  $43^{\circ}$  in latitude and from  $124^{\circ}$  to  $131^{\circ}$  in longitude (degrees east). The data set consists of 158 earthquakes and 2701 waveforms recorded from 2000 to 2004. Figure 4.1 is the map of the epicenters of the events and stations of the KMA and KIGAM networks providing the waveform data set for Korean study. Figure 4.2 shows the map of the epicenters and stations used for the inland subset study to see if there is any bias in using off-shore events in the data set. Figure 4.3 shows the distance coverage for each station component used.

For this study, I used unclipped and high *signal/noise* ratio data having distinct P and S waves. The digital data series were corrected for instrument response to form ground velocity in units of *m/sec* using the deconvolution operation within SAC. The SAC pole-zero files of the instrument response were in

<b>KMA and KIGAM Digital Stations</b>				
STN code	Lat	Lon	Elev (m)	Sensor
AND	36.5687	128.7057	140.0	SS-1, Epi
BGD	34.1596	128.5553	0.0	STS-2
BRD	37.9677	124.6303	169.0	STS-2, Epi
BUS	35.2487	129.1125	91.0	STS-2, Epi
BUY	36.2683	126.9204	11.34	Epi
CHA	36.7727	127.1193	24.89	Epi
CHI	35.2032	128.1194	21.0	SS-1, Epi
CHC	37.7775	127.8145	245.0	STS-2, Epi
CHO	35.8178	127.1542	54.0	SS-1, Epi
CHJ	36.8730	127.9748	227.0	STS-2, Epi
CHY	36.9378	128.9167	321.52	Epi
CHU	37.8904	127.7308	125.0	STS-2
CHW	38.1404	127.3038	154.22	-
CPN	36.2168	127.9912	242.53	SS-1, Epi
CWO	38.0833	127.5167	351.00	SS-1, Epi
DAG	35.7685	128.8970	262.0	STS-2, Epi
DGY	37.6904	128.6742	791.0	STS-2, Epi
EUS	36.3519	128.6870	81.09	Epi
GKP1	35.8891	128.6056	0.0	STS-2
HAC	35.5572	128.1699	32.66	Epi
HDB	35.7307	129.4012	0.0	CMG-3TB
HUK	34.6873	125.4506	17.0	SS-1, Epi
IMS	35.6055	127.2859	246.85	Epi
ICN	37.2907	127.4167	164.00	SS-1, Epi
INJ	38.0543	128.1681	198.59	Epi
JEC	37.1538	128.1912	263.21	Epi
JEU	35.4935	126.9298	182.00	SS-1, Epi
JJU	33.4306	126.5463	542.0	SS-1, Epi
JOU	35.5561	126.8676	44.11	Epi
KAN	37.7425	128.8893	26.0	Epi
KMS	36.1016	127.4837	171.26	Epi
KOH	34.6090	127.2733	53.27	Epi
KSA	38.5953	128.3512	0.0	Epi
KUC	35.6675	127.9079	220.88	SS-1, Epi
KUJ	34.8843	128.6041	45.26	Epi
KUM	36.1232	128.3202	47.86	Epi
KUS	36.0005	126.7848	209.83	SS-1, Epi
KWA	35.1731	126.8909	71.0	-
KWJ	35.1599	126.9909	0.0	SS-1, STS-2, Epi

Table 4.1: List of stations for the KMA and KIGAM Digital Stations. STN code represents the station code, Lat, Lon, and Elev each denote latitude, longitude, and elevation. Epi, SS-1, STS-1, and STS-2 each denote accelerometer, short period (1 Hz) velocity sensor, broadband sensor and broadband sensor.

<b>KMA and KIGAM Digital Stations</b>				
STN code	Lat	Log	Elev (m)	Sensor
MAS	35.1855	128.5670	3.31	Epi
MIY	35.4863	128.7410	12.59	Epi
MOP	34.8081	126.3765	37.88	SS-1, Epi
MUA	35.0876	126.2855	24.49	-
MUG	36.6213	128.1505	170.36	Epi
MUS	37.8881	126.7594	40.00	SS-1, Epi
NAW	35.4013	127.3343	89.70	Epi
POH	36.0329	129.3796	2.0	SS-1, Epi
POR	36.3211	126.5555	15.29	Epi
PUA	35.7225	126.7178	10.68	Epi
PUS	35.1010	129.0339	70.0	STS-2
SAC	35.4060	127.8754	138.56	Epi
SEO	37.4879	126.9188	34.0	STS-2, Epi
SES	36.7892	126.4531	0.0	STS-2, Epi
SGP	33.2587	126.4994	222.0	STS-2, Epi
SNU	37.4533	126.9538	0.0	STS-2
SOC	38.2421	128.5668	17.79	SS-1, Epi
SOG	33.2390	126.5671	51.0	STS-2
SOS	36.7770	126.4942	26.0	-
SUC	35.0696	127.2380	74.38	Epi
SWO	37.2669	126.9669	56.60	SS-1, Epi
TAB	37.1672	128.9883	713.44	Epi
TAG	35.8760	128.6194	58.0	STS-2
TEJ	36.3681	127.3712	68.0	STS-2, Epi
TJN	36.3805	127.3615	0.0	STS-2
TOH	37.5025	129.1225	39.60	Epi
ULC	36.9918	129.4133	49.0	-
ULL	37.4736	130.9008	221.0	STS-2, Epi
ULS	35.5542	129.3202	34.69	SS-1, Epi
ULJ	36.7020	129.4084	0.0	STS-2, Epi
WAN	34.3956	126.7017	34.0	SS-1, Epi
WON	37.3372	127.9470	149.0	SS-1, Epi
YAP	37.4846	127.4912	47.00	Epi
YOC	35.9713	128.9522	94.09	Epi
YOD	36.5248	129.4071	41.23	Epi
YOJ	36.8680	128.5181	210.21	Epi
YOS	34.7350	127.7388	66.05	SS-1, Epi
YOW	37.1736	128.4556	239.79	SS-1, Epi

Table 4.2: List of stations for the KMA and KIGAM Digital Stations. STN code represents the station code, Lat, Lon, and Elev each denote latitude, longitude, and elevation. Epi, SS-1, STS-1, and STS-2 each denote accelerometer, short period (1 Hz) velocity sensor, broadband sensor and broadband sensor.

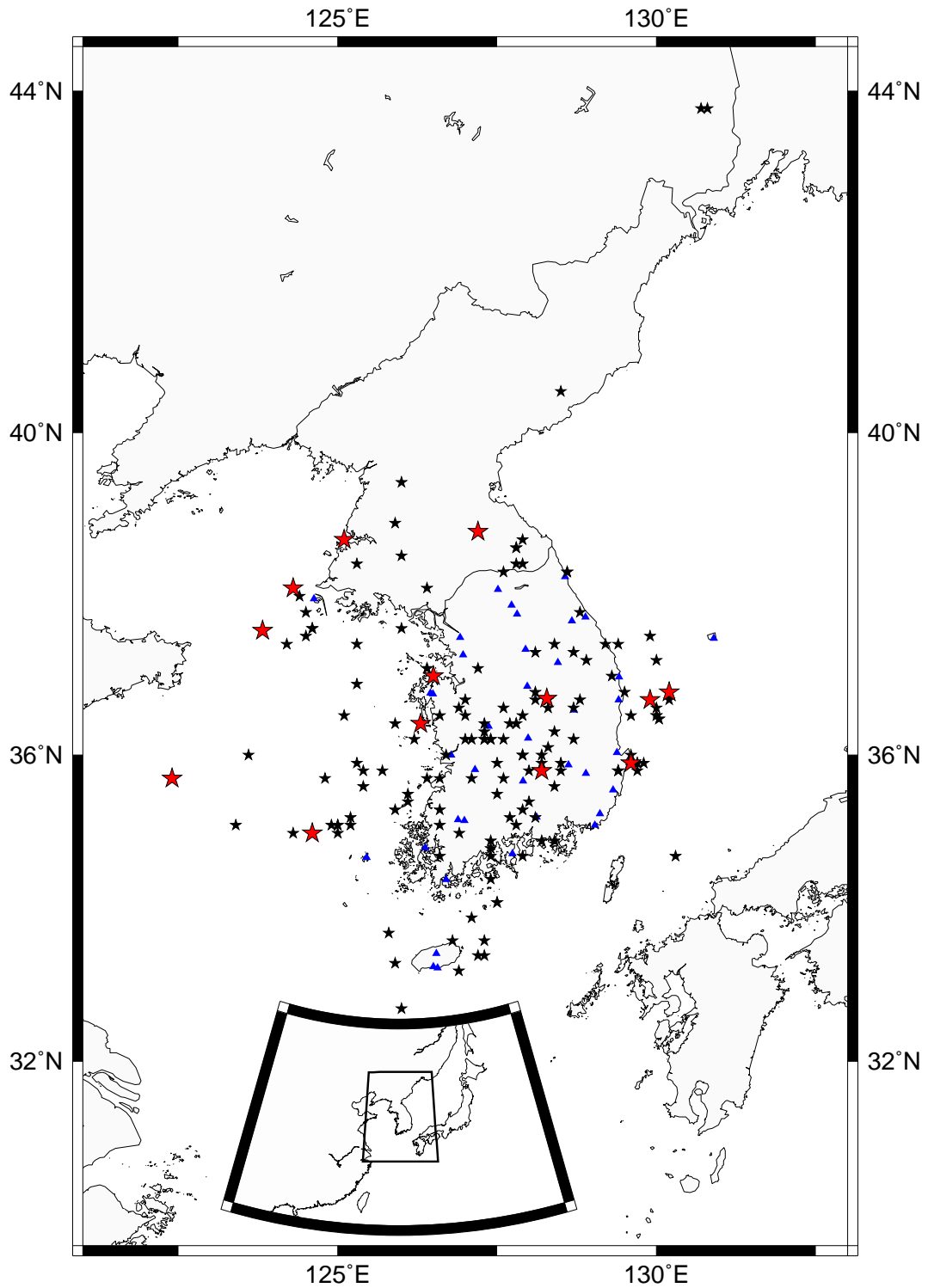


Figure 4.1: Map shows the epicenters and station locations for whole KMA and KIGAM data-set. The earthquake epicenters are marked by black stars, the big stars indicate the epicenters of known moment magnitudes, and stations are denoted by black triangles.

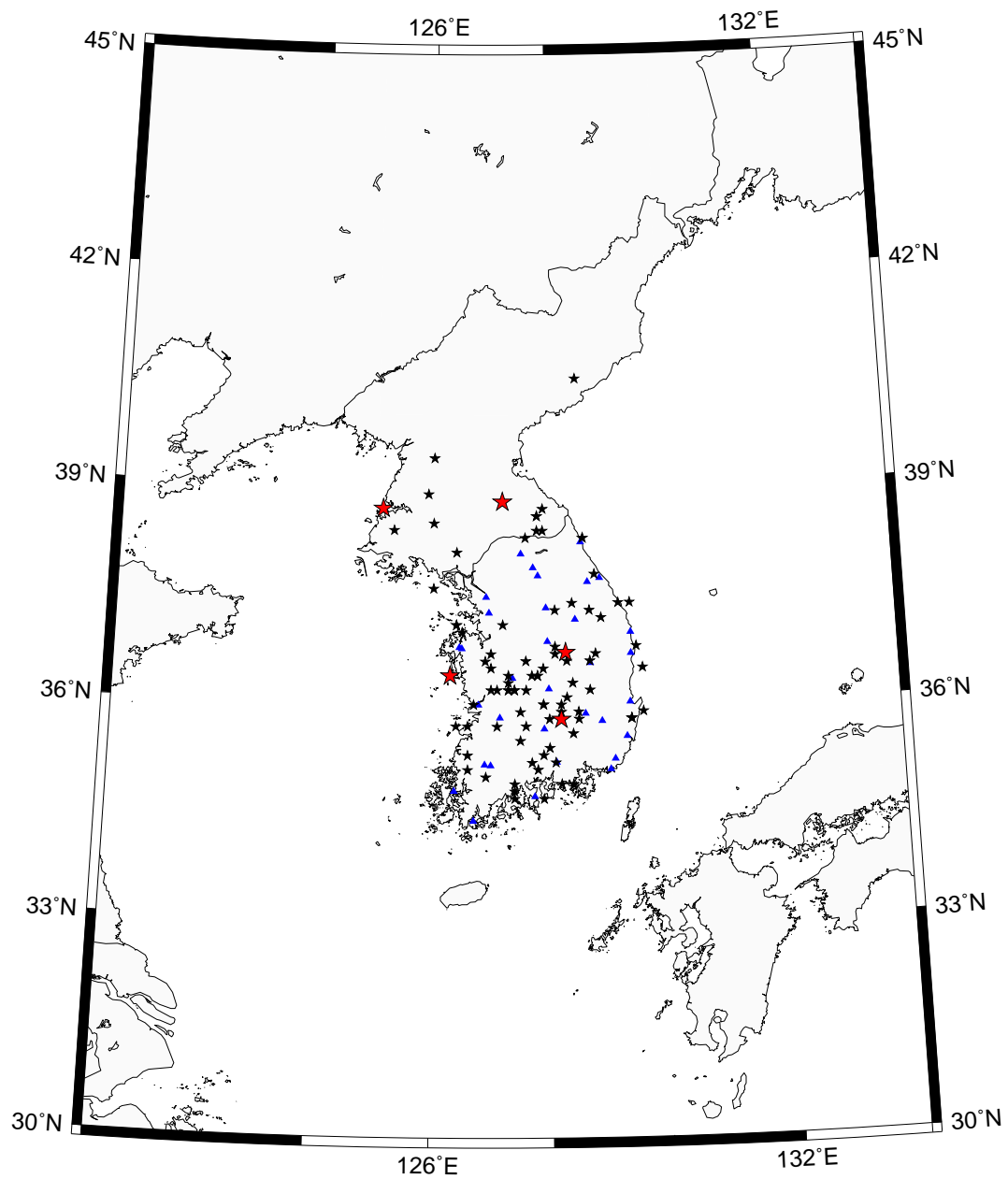


Figure 4.2: Map shows the epicenters and station locations for inland KMA and KIGAM data-set. The earthquake epicenters are marked by black stars, the big stars indicate the epicenters of known moment magnitudes, and stations are denoted by black triangles.

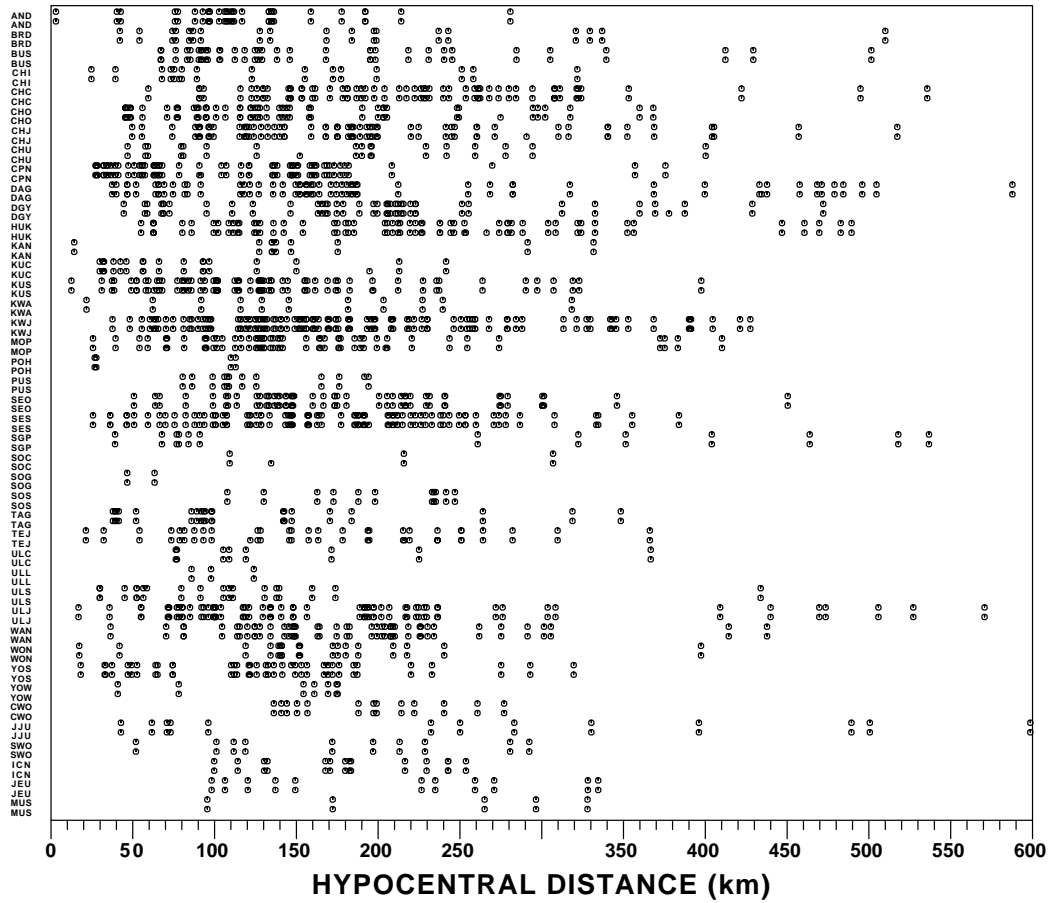


Figure 4.3: Distance coverage for KMA and KIGAM stations. The observation distances for each station that containing horizontal and vertical component should cover a wide distance range and overlap with other stations to reduce the tradeoff possibility between the excitation and propagation term.

<b>Sensors and instrument response</b>							
Sensor	Channel	Rate	Sensor output	Digitizer	Calibration gain	Poles and Zeros	constant
STS-2	HHZ BHZ LHZ	100 20 1	1500 V/m/sec	419460 counts/V	6.29190E+08 counts/m/s	-0.035647-0.036879i -0.035647+0.036879i -251.33+0.0i -131.04-467.29i -131.04+467.29i  0.0+0.0i 0.0+0.0i	3.75504E+16
SS-1	SLZ ELZ	100 20	150 V/m/sec	419460 counts/V	6.29190E+07 counts/m/s	-4.44+4.44i -4.44-4.44i  0.0+0.0i 0.0+0.0i	6.2919E+07
Epi	HGZ BGZ	100 20	40 V/g	419460 counts/V	1.713E+06 counts/m/s/s	-981+1009i -981-1009i -3290+1263i -3290-1263i  0.0+0.0i 0.0+0.0i	6.2919E+07

Table 4.3: KMA and KIGAM digital station sensors.

the form of displacement sensitivity in units of counts/micron. The result of deconvolution is a displacement time series in units of microns which is converted to velocity by differentiation, dividing by the factor 1000000 yields ground velocity in meters/sec. A bandpass filter used is required to ensure the stability of the deconvolution process. The width of the band is chosen not to interfere with the analysis of ground motions. Typically I used frequency band of 0.005 - 25 Hz.

### 4.1.3 Coda Shape

Figures 4.4 and 4.5 illustrate the decay shape of the normalized coda as a function of time. Every peak value is normalized to the value of the coda at a

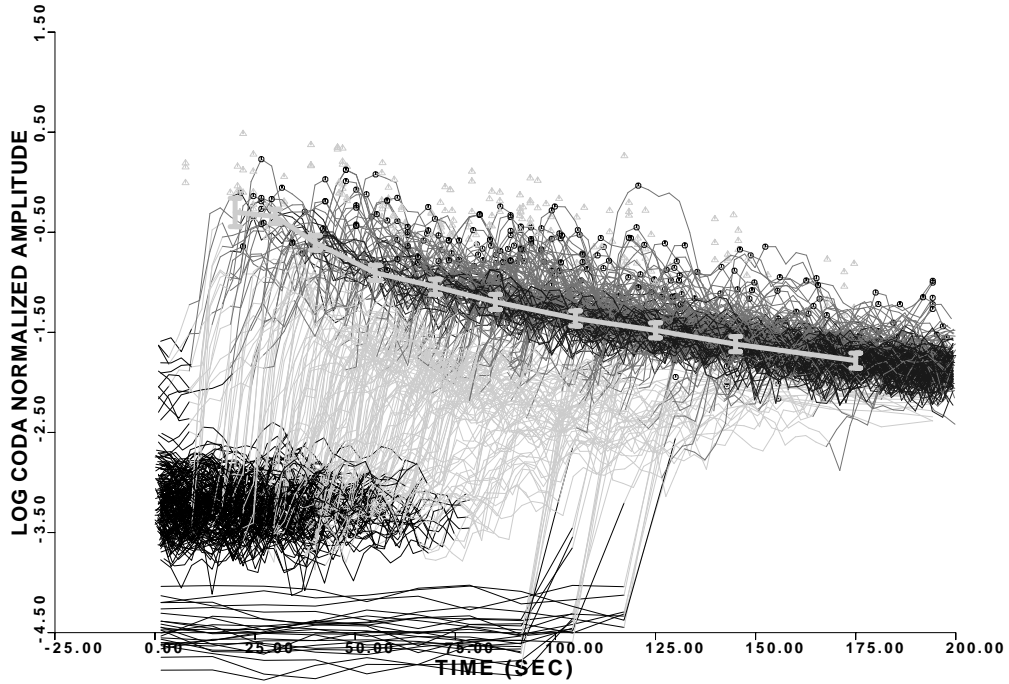


Figure 4.4: Shape of the 0.5 Hz normalized seismic coda as a function of lapse time from earthquake origin time. The black lines denote the initial part before the P-wave arrival, light gray lines are the signal between P and S-wave arrivals, gray lines are the *RMS* average between the S-wave arrival and the dark gray segment of the curves start at  $2t_s$ . Gray triangles represent the peak values and circles denote normalized peak amplitudes.

reference level. The black lines mark the initial part before the P-wave arrival, light gray lines are the signal between P and S-wave arrivals, gray lines denote the *RMS* average between the S-wave arrival and the stable coda, and dark gray lines are signal in the stable coda which start at  $2t_s$ . The heavy gray line is the empirically determined coda shape function. The symbols denote the peak amplitude (gray triangles) value and the normalized peak amplitude (circles) used to provide an initial estimate of  $D(r)$ . The distribution of the normalized amplitudes is well defined and show a consistent shape.

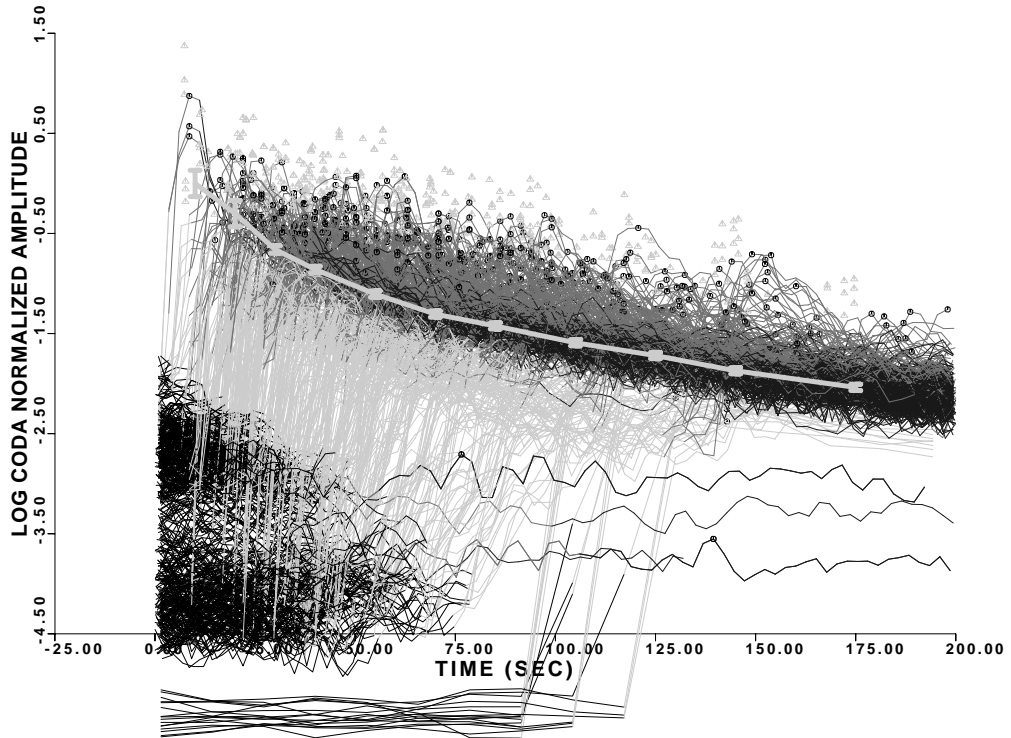


Figure 4.5: Shape of the 1.0 Hz normalized seismic coda as a function of lapse time from earthquake origin time. The black lines denote the initial part before the P-wave arrival, light gray lines are the signal between P and S-wave arrivals, gray lines are the *RMS* average between the S-wave arrival and the dark gray segment of the curves start at  $2t_s$ . Gray triangles represent the peak values and circles denote normalized peak amplitudes.

## 4.2 Regression and parameterization of Fourier velocity spectra

Figures 4.6 and 4.7 show typical examples of the regression analysis at filter frequencies of 1.0, 3.0, 4.0, and 10.0 Hz on the Fourier velocity spectra. Top panels also show the coda propagation term estimated by the coda normalization technique. The coda and regression propagation functionals in the mid-panels show good agreement for the Fourier velocity spectra data set at all distance ranges. The regression residual plots in the bottom panels indicate that the distance nodes were appropriate to determine  $D(r)$ . The estimates of the standard errors of the fit varies between 0.19 and 0.26  $\log_{10}$  units from 1 - 16 Hz. The residuals of lower frequencies are higher due to the limited numbers of waveforms used for regressions.

Since I had three-component data sets, I did three regressions on vertical, horizontal, and all component data sets. Figure 4.8a shows the three component distance scaling of the  $D(r)$  term at twelve different frequencies for regression on the Fourier velocity spectra. It is obtained from the regression of the combined vertical and horizontal component data sets. This figure is corrected for an  $r^{-1.0}$  trend to emphasize departure (scattering, deviation) of high frequency spectra with distance from  $r^{-1}$  spreading. The 0.25 and 0.5 Hz signals in the top panel show different propagation shapes compare to the rest of the  $D(r)$  frequency ranges because lesser data population used is affect that slope. The standard error of the  $D(r)$  is less than 0.1  $\log_{10}$  units for all

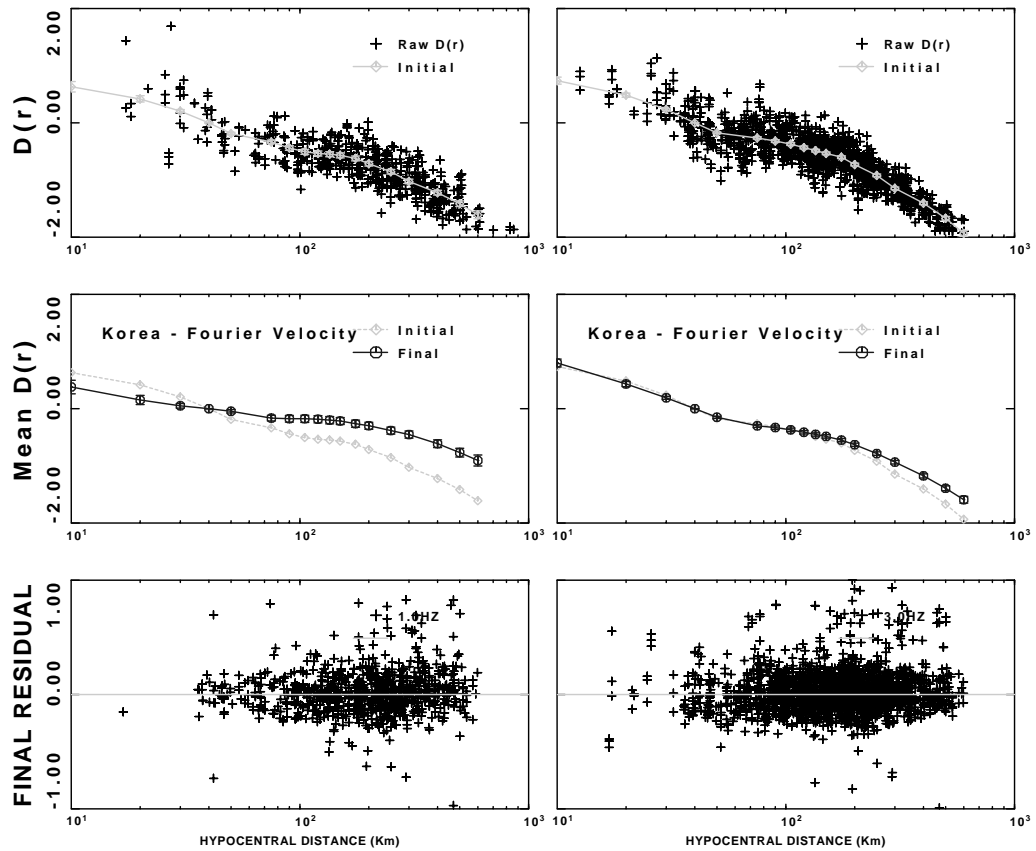


Figure 4.6: Regression analysis for 1.0 and 3.0 Hz. Top, coda estimate of  $D(r)$  using coda normalization technique. Middle, coda and regression propagation functionals (open circles linked by thin black lines). Bottom, final residuals of the regression analysis.

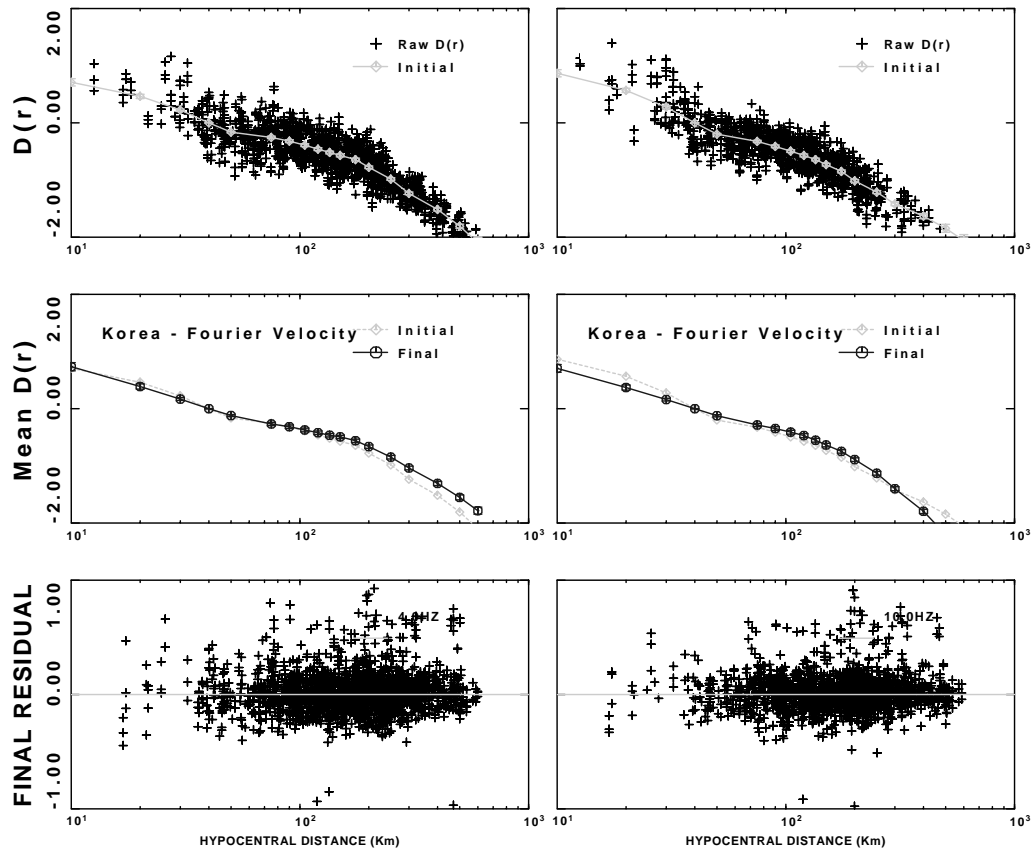


Figure 4.7: Regression analysis for 4.0 and 10.0 Hz. Top, coda estimate of  $D(r)$  using coda normalization technique. Middle, coda and regression propagation functionals (open circles linked by thin black lines). Bottom, final residuals of the regression analysis.

distances. I used  $Q_0 = 330$ ,  $\eta = 0.40$ , and geometrical spreading

$$g(r) = \begin{cases} r^{-1.1} & r < 60 \text{ km} \\ r^{-0.0} & 60 < r < 250 \text{ km} \\ r^{-0.5} & r > 250 \text{ km} \end{cases}$$

for parameterization. The residuals of fit (Figure 4.8b) are less than about 0.1 out to 200 km in the frequency range of (1 - 16 Hz) and increase consistently related to frequency dependence at larger distances, while the fit at lower frequency range (0.25 - 0.5 Hz) is not good at all distance ranges.

Figure 4.9 shows horizontal (top panel) and vertical (lower panel) component distance scaling of the  $D(r, f)$  terms for the separate regressions of the Fourier amplitudes for Korea. Both  $D(r, f)$  have an amplitude decay similar to the  $D(r, f)$  of Figure 4.8a. For vertical component  $D(r, f)$ ,  $Q_0 = 330$ ,  $\eta = 0.40$ , and

$$g(r) = \begin{cases} r^{-1.0} & r < 40 \text{ km} \\ r^{-1.3} & 40 < r < 60 \text{ km} \\ r^{-0.0} & 60 < r < 250 \text{ km} \\ r^{-0.5} & r > 250 \text{ km} \end{cases}$$

are used for parameterization while  $D(r, f)$  of horizontal component is  $Q_0 = 330$ ,  $\eta = 0.40$ , and

$$g(r) = \begin{cases} r^{-1.1} & r < 40 \text{ km} \\ r^{-1.0} & 40 < r < 60 \text{ km} \\ r^{-0.0} & 60 < r < 250 \text{ km} \\ r^{-0.5} & r > 250 \text{ km} \end{cases}$$

are used for parameterization.

Tables 4.4, 4.5 and 4.6 give the numerical results of the regression on the three component regional attenuation functional of Fourier Velocity spectra for

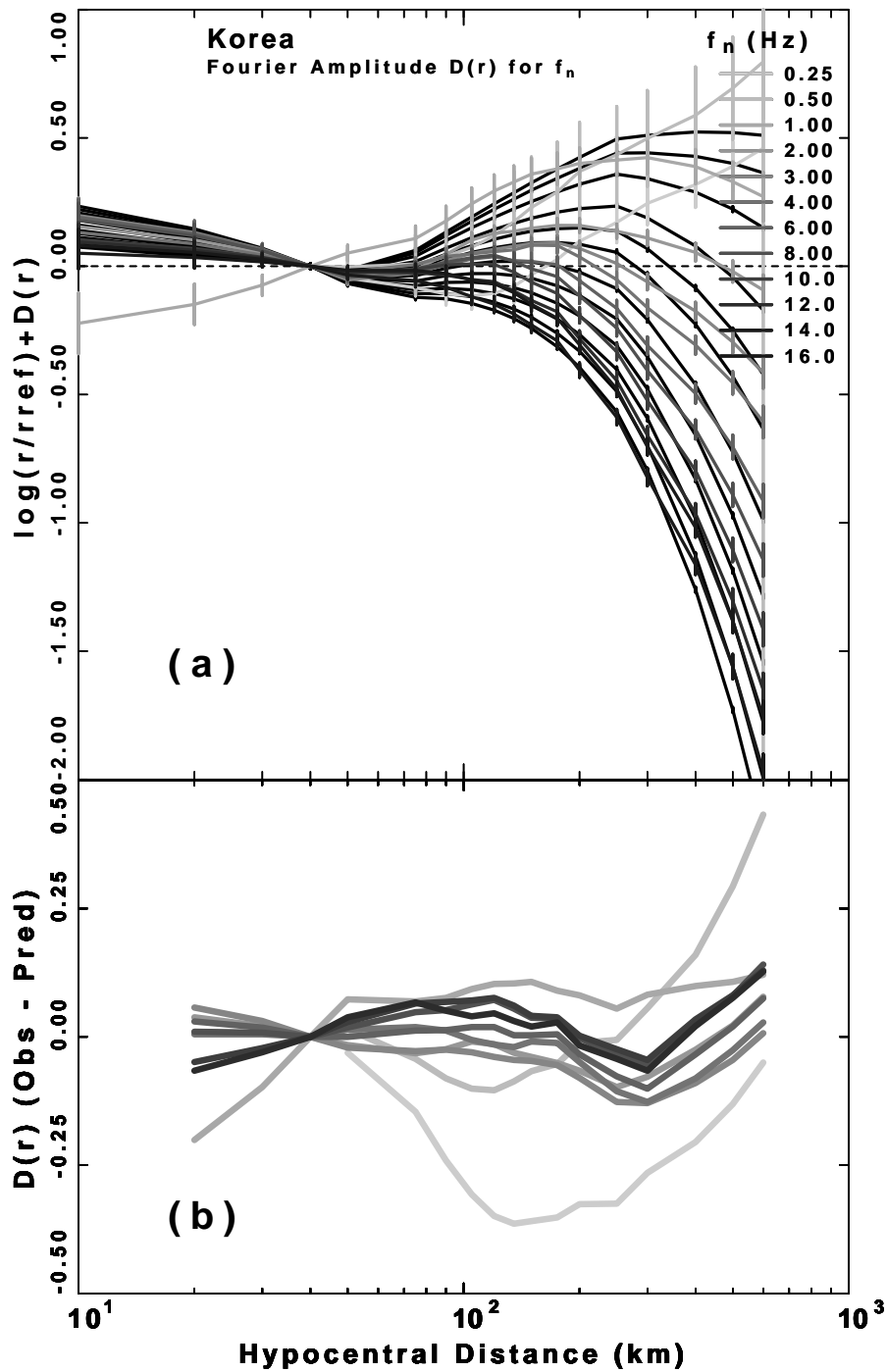


Figure 4.8: (a) Three component reduced attenuation functional  $D(r, f)$  obtained from the regression of the Fourier amplitudes at the frequencies of 0.25, 0.5, 1.0, 2.0, 3.0, 4.0, 6.0, 8.0, 10.0, 12.0, 14.0, and 16.0 Hz. The black lines at the background are the theoretical  $D(r, f)$ . (b) The residuals of the model fit to the Fourier velocity spectra  $D(r, f)$  for the frequency range of 0.25 - 16 Hz.

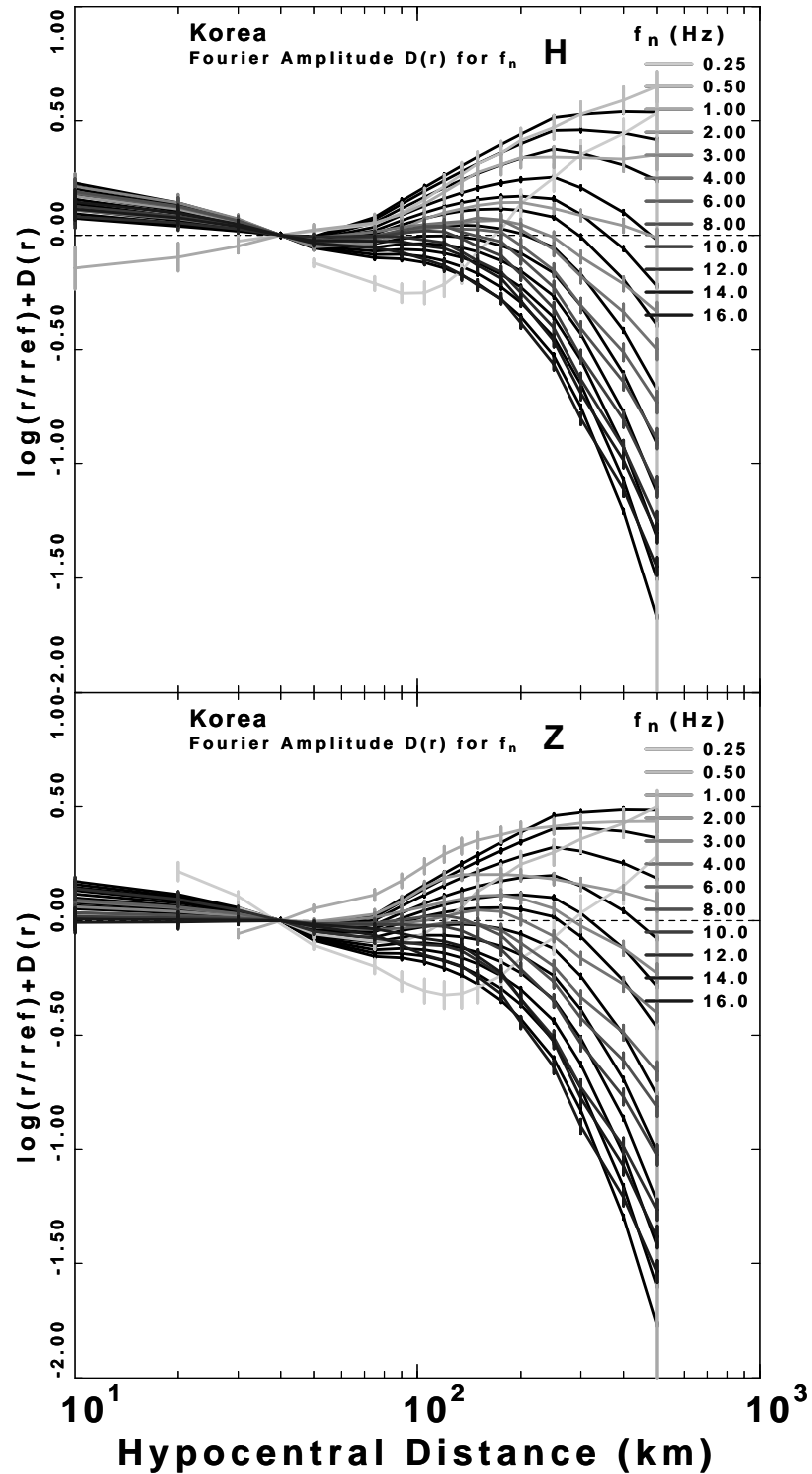


Figure 4.9: Horizontal component (top panel) and vertical component (bottom panel) reduced attenuation functional  $D(r, f)$  obtained from the regression on the Fourier amplitudes from 0.25 to 16.0 Hz for Korea. The black lines at the background are the theoretical  $D(r, f)$ . The presentation of this plot is to emphasize the departure from  $r^{-1}$  spreading.

Korea. Those tables describe the corresponding value  $D(r)$  for each frequency, distance, and  $\sigma$  as well as the number of observations available at the specific distance (within each distance bin). Table 4.7 gives the number of observations in regressions of time domain and Fourier domain for each frequency.

<b>Korea Fourier velocity spectra D(r)</b>									
f (Hz)	r (km)	$D(r, f)$	$\sigma$	Nobs	f (Hz)	r (km)	$D(r, f)$	$\sigma$	Nobs
0.25	40	0.000	0.364E-05	0.000	0.5	40	0.000	0.364E-05	1.610
0.25	50	-0.143	0.173E-01	0.910	0.5	50	-0.099	0.651E-01	3.020
0.25	75	-0.357	0.316E-01	2.710	0.5	75	-0.264	0.115E+00	7.370
0.25	90	-0.460	0.434E-01	1.820	0.5	90	-0.313	0.152E+00	10.46
0.25	105	-0.534	0.529E-01	1.350	0.5	105	-0.345	0.177E+00	9.230
0.25	120	-0.583	0.603E-01	1.080	0.5	120	-0.359	0.191E+00	6.650
0.25	135	-0.606	0.659E-01	2.690	0.5	135	-0.354	0.197E+00	11.17
0.25	150	-0.608	0.701E-01	5.970	0.5	150	-0.345	0.197E+00	9.660
0.25	175	-0.614	0.733E-01	6.340	0.5	175	-0.351	0.195E+00	17.11
0.25	200	-0.601	0.760E-01	6.930	0.5	200	-0.329	0.191E+00	29.84
0.25	250	-0.625	0.790E-01	6.950	0.5	250	-0.361	0.188E+00	32.40
0.25	300	-0.630	0.832E-01	11.24	0.5	300	-0.377	0.187E+00	39.36
0.25	400	-0.682	0.892E-01	11.34	0.5	400	-0.412	0.189E+00	20.15
0.25	500	-0.707	0.976E-01	5.700	0.5	500	-0.403	0.200E+00	13.44
0.25	600	-0.716	0.109E+00	0.880	0.5	600	-0.379	0.223E+00	2.460
1.0	10	0.380	0.119E+00	0.310	2.0	10	0.756	0.664E-01	1.720
1.0	20	0.153	0.793E-01	0.680	2.0	20	0.404	0.442E-01	11.32
1.0	30	0.051	0.397E-01	2.230	2.0	30	0.176	0.221E-01	11.62
1.0	40	0.000	0.280E-05	17.67	2.0	40	0.000	0.232E-05	47.94
1.0	50	-0.045	0.310E-01	28.82	2.0	50	-0.140	0.174E-01	83.62
1.0	75	-0.165	0.491E-01	36.11	2.0	75	-0.287	0.254E-01	129.6
1.0	90	-0.176	0.586E-01	34.29	2.0	90	-0.306	0.286E-01	128.8
1.0	105	-0.176	0.626E-01	40.90	2.0	105	-0.317	0.294E-01	112.6
1.0	120	-0.184	0.635E-01	46.00	2.0	120	-0.348	0.288E-01	139.8
1.0	135	-0.200	0.629E-01	52.74	2.0	135	-0.392	0.284E-01	129.3
1.0	150	-0.215	0.621E-01	49.45	2.0	150	-0.426	0.279E-01	145.3
1.0	175	-0.261	0.611E-01	65.50	2.0	175	-0.481	0.273E-01	186.9
1.0	200	-0.298	0.604E-01	109.9	2.0	200	-0.540	0.270E-01	264.3
1.0	250	-0.382	0.610E-01	127.1	2.0	250	-0.659	0.280E-01	258.2
1.0	300	-0.452	0.630E-01	109.8	2.0	300	-0.765	0.301E-01	189.6
1.0	400	-0.612	0.671E-01	79.93	2.0	400	-0.946	0.341E-01	122.3
1.0	500	-0.767	0.763E-01	42.39	2.0	500	-1.117	0.423E-01	60.22
1.0	600	-0.905	0.959E-01	7.090	2.0	600	-1.269	0.596E-01	10.73

Table 4.4: Attenuation functional at 0.25, 0.5, 1.0, and 2.0 Hz for Fourier velocity spectra. The columns give values of frequency (first and sixth columns), hypocentral distance (second and seventh columns), attenuation  $D(r, f)$  at a reference distance of 40 km (third and eighth columns), associated error bar (fourth and ninth columns) and number of observations (fifth and tenth columns).

<b>Korea Fourier velocity spectra <math>D(r)</math></b>									
f (Hz)	r (km)	$D(r, f)$	$\sigma$	Nobs	f (Hz)	r (km)	$D(r, f)$	$\sigma$	Nobs
3.0	10	0.800	0.692E-01	1.720	4.0	10	0.734	0.705E-01	1.720
3.0	20	0.433	0.462E-01	11.32	4.0	20	0.389	0.470E-01	12.19
3.0	30	0.191	0.231E-01	11.26	4.0	30	0.169	0.235E-01	11.58
3.0	40	0.000	0.244E-05	48.22	4.0	40	0.000	0.251E-05	46.03
3.0	50	-0.150	0.182E-01	78.85	4.0	50	-0.119	0.185E-01	72.98
3.0	75	-0.300	0.264E-01	120.5	4.0	75	-0.267	0.270E-01	118.7
3.0	90	-0.330	0.298E-01	138.5	4.0	90	-0.314	0.307E-01	129.8
3.0	105	-0.369	0.307E-01	112.0	4.0	105	-0.371	0.317E-01	127.2
3.0	120	-0.411	0.302E-01	137.6	4.0	120	-0.420	0.312E-01	141.2
3.0	135	-0.450	0.296E-01	132.5	4.0	135	-0.464	0.305E-01	137.5
3.0	150	-0.485	0.291E-01	155.8	4.0	150	-0.492	0.299E-01	155.1
3.0	175	-0.549	0.285E-01	188.0	4.0	175	-0.560	0.294E-01	185.1
3.0	200	-0.629	0.282E-01	288.0	4.0	200	-0.662	0.291E-01	281.8
3.0	250	-0.785	0.291E-01	270.2	4.0	250	-0.848	0.301E-01	266.3
3.0	300	-0.936	0.311E-01	201.8	4.0	300	-1.037	0.322E-01	199.8
3.0	400	-1.175	0.352E-01	120.0	4.0	400	-1.307	0.364E-01	121.5
3.0	500	-1.392	0.430E-01	65.12	4.0	500	-1.551	0.444E-01	67.36
3.0	600	-1.591	0.604E-01	10.79	4.0	600	-1.783	0.622E-01	11.10
6.0	10	0.793	0.699E-01	1.720	8.0	10	0.781	0.666E-01	1.720
6.0	20	0.428	0.466E-01	12.14	8.0	20	0.420	0.444E-01	11.31
6.0	30	0.189	0.233E-01	12.14	8.0	30	0.185	0.222E-01	11.57
6.0	40	0.000	0.251E-05	32.41	8.0	40	0.000	0.239E-05	30.25
6.0	50	-0.140	0.187E-01	63.48	8.0	50	-0.128	0.180E-01	58.53
6.0	75	-0.298	0.278E-01	115.9	8.0	75	-0.283	0.269E-01	106.0
6.0	90	-0.347	0.319E-01	123.5	8.0	90	-0.337	0.310E-01	120.3
6.0	105	-0.391	0.332E-01	109.1	8.0	105	-0.385	0.325E-01	104.7
6.0	120	-0.440	0.328E-01	134.4	8.0	120	-0.434	0.324E-01	119.4
6.0	135	-0.506	0.323E-01	134.4	8.0	135	-0.509	0.320E-01	113.9
6.0	150	-0.555	0.319E-01	144.7	8.0	150	-0.584	0.315E-01	132.0
6.0	175	-0.635	0.313E-01	187.4	8.0	175	-0.681	0.308E-01	176.5
6.0	200	-0.755	0.309E-01	267.6	8.0	200	-0.814	0.302E-01	263.0
6.0	250	-0.960	0.319E-01	242.1	8.0	250	-1.037	0.311E-01	241.8
6.0	300	-1.184	0.342E-01	177.4	8.0	300	-1.282	0.334E-01	178.7
6.0	400	-1.496	0.383E-01	115.5	8.0	400	-1.636	0.376E-01	104.9
6.0	500	-1.801	0.467E-01	62.58	8.0	500	-1.988	0.459E-01	62.08
6.0	600	-2.091	0.655E-01	8.700	8.0	600	-2.321	0.640E-01	8.510

Table 4.5: Attenuation functional at 3.0, 4.0, 6.0, and 8.0 Hz for Fourier velocity spectra. The columns give values of frequency (first and sixth columns), hypocentral distance (second and seventh columns), attenuation  $D(r, f)$  at a reference distance of 40 km (third and eighth columns), associated error bar (fourth and ninth columns) and number of observations (fifth and tenth columns).

<b>Korea Fourier velocity spectra <math>D(r)</math></b>									
f (Hz)	r (km)	$D(r, f)$	$\sigma$	Nobs	f (Hz)	r (km)	$D(r, f)$	$\sigma$	Nobs
10.0	10	0.706	0.677E-01	1.720	12.0	10	0.697	0.679E-01	1.100
10.0	20	0.371	0.452E-01	10.04	12.0	20	0.364	0.453E-01	8.690
10.0	30	0.160	0.226E-01	8.760	12.0	30	0.157	0.226E-01	8.670
10.0	40	0.000	0.236E-05	28.65	12.0	40	0.000	0.222E-05	22.87
10.0	50	-0.122	0.183E-01	62.80	12.0	50	-0.118	0.183E-01	55.66
10.0	75	-0.284	0.274E-01	108.6	12.0	75	-0.298	0.277E-01	101.5
10.0	90	-0.347	0.316E-01	124.5	12.0	90	-0.387	0.321E-01	116.8
10.0	105	-0.410	0.329E-01	113.8	12.0	105	-0.471	0.335E-01	104.6
10.0	120	-0.470	0.327E-01	128.5	12.0	120	-0.537	0.333E-01	118.4
10.0	135	-0.551	0.322E-01	113.5	12.0	135	-0.624	0.328E-01	110.4
10.0	150	-0.636	0.316E-01	136.0	12.0	150	-0.707	0.321E-01	134.8
10.0	175	-0.747	0.308E-01	183.0	12.0	175	-0.818	0.314E-01	180.8
10.0	200	-0.890	0.303E-01	262.0	12.0	200	-0.981	0.310E-01	245.4
10.0	250	-1.129	0.314E-01	225.7	12.0	250	-1.241	0.320E-01	215.4
10.0	300	-1.399	0.337E-01	158.8	12.0	300	-1.534	0.342E-01	148.3
10.0	400	-1.796	0.379E-01	96.75	12.0	400	-1.963	0.387E-01	94.14
10.0	500	-2.202	0.465E-01	55.87	12.0	500	-2.401	0.477E-01	44.59
10.0	600	-2.591	0.647E-01	8.080	12.0	600	-2.827	0.657E-01	6.830
14.0	10	0.683	0.632E-01	1.410	16.0	10	0.653	0.622E-01	1.410
14.0	20	0.355	0.421E-01	9.660	16.0	20	0.335	0.415E-01	9.290
14.0	30	0.152	0.211E-01	7.150	16.0	30	0.142	0.207E-01	9.050
14.0	40	0.000	0.210E-05	27.31	16.0	40	0.000	0.207E-05	25.86
14.0	50	-0.113	0.171E-01	58.22	16.0	50	-0.131	0.169E-01	57.67
14.0	75	-0.290	0.259E-01	97.92	16.0	75	-0.329	0.255E-01	98.29
14.0	90	-0.380	0.298E-01	122.3	16.0	90	-0.434	0.294E-01	121.8
14.0	105	-0.473	0.311E-01	114.9	16.0	105	-0.538	0.307E-01	114.8
14.0	120	-0.545	0.309E-01	126.0	16.0	120	-0.625	0.306E-01	124.9
14.0	135	-0.631	0.306E-01	97.30	16.0	135	-0.714	0.303E-01	100.0
14.0	150	-0.722	0.300E-01	128.6	16.0	150	-0.803	0.297E-01	130.6
14.0	175	-0.843	0.293E-01	173.9	16.0	175	-0.931	0.290E-01	165.8
14.0	200	-1.005	0.290E-01	236.9	16.0	200	-1.104	0.287E-01	237.0
14.0	250	-1.274	0.299E-01	220.2	16.0	250	-1.384	0.297E-01	205.8
14.0	300	-1.579	0.322E-01	144.0	16.0	300	-1.699	0.324E-01	136.4
14.0	400	-2.019	0.368E-01	87.03	16.0	400	-2.164	0.379E-01	71.11
14.0	500	-2.479	0.460E-01	38.75	16.0	500	-2.657	0.484E-01	31.01
14.0	600	-2.934	0.637E-01	6.430	16.0	600	-3.144	0.667E-01	6.320

Table 4.6: Attenuation functional at 10.0, 12.0, 14.0 and 16.0 Hz for Fourier velocity spectra. The columns give values of frequency (first and sixth columns), hypocentral distance (second and seventh columns), attenuation  $D(r, f)$  at a reference distance of 40 km (third and eighth columns), associated error bar (fourth and ninth columns) and number of observations (fifth and tenth columns).

<b>Number of observations</b>		
<b>Frequency</b>	<b>Fourier velocity</b>	<b>Peak velocity</b>
0.25	88	396
0.5	236	598
01	873	1605
02	2056	2640
03	2123	2671
04	2109	2701
06	1967	2554
08	1867	2543
10	1849	2525
12	1741	2497
14	1720	2463
16	1669	2427

Table 4.7: Number of observations in regression of filtered velocity and Fourier velocity.

### 4.3 Duration

Figures 4.10 and 4.11 show the measured durations of the combined data set at 0.5, 1.0, 2.0, 4.0, 6.0, 10.0, 12.0, and 14.0 Hz filter frequencies. Because lower frequencies (0.25, 0.5, and 1.0 Hz) do not have enough data set, significantly more scatter exists at lower frequencies compared to higher frequencies. The number of observations decreases rapidly at large distances and did not permit a reliable estimation of duration there. The durations (thick solid lines) increase with increasing hypocentral distance and decrease with increasing frequency range.

Table 4.8 lists frequency dependent duration functionals as a function of distance for vertical and horizontal data set for all frequency range. Table 4.9 lists frequency independent duration functionals as a function of distance determined for all, horizontal, and vertical components. These average durations

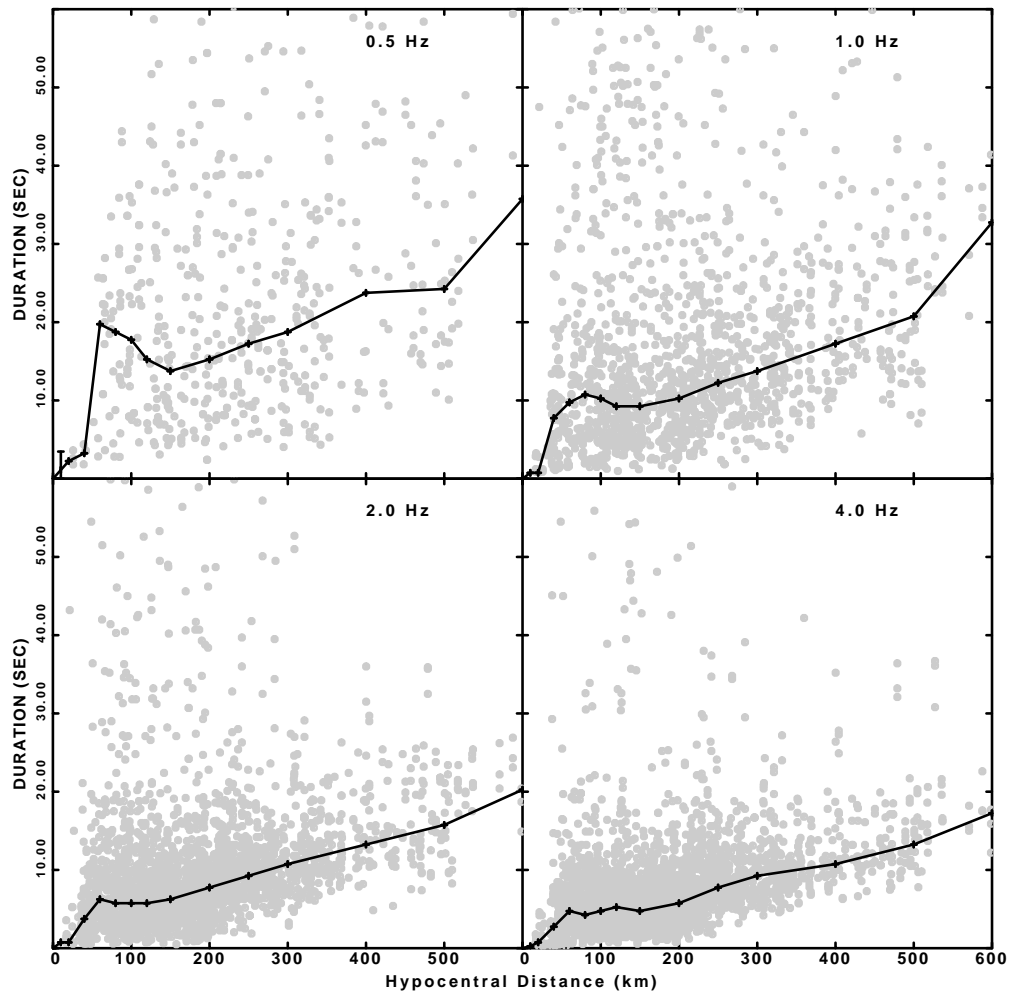


Figure 4.10: Durations at 0.5, 1.0, 2.0 and 4.0 Hz obtained for Korea. Rounded gray circles denote individual duration estimates. Thick solid lines represent the duration computed using a median value method.

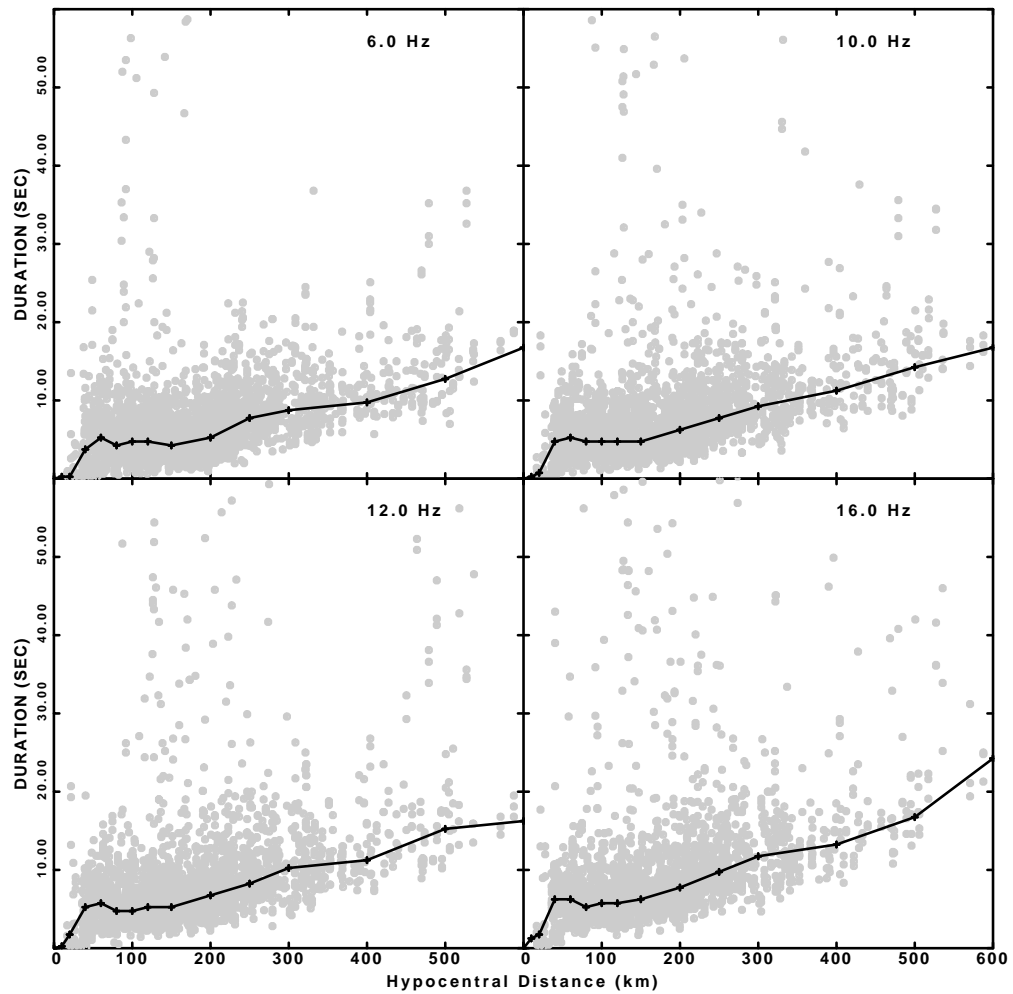


Figure 4.11: Durations at 6.0, 10.0, 12.0, and 16.0 Hz obtained for Korea. Rounded gray circles denote individual duration estimates. Thick solid lines represent the duration computed using a median value method.

were obtained from the frequency dependent durations by a weighted average. More weight was given to the higher frequency data.

#### **4.4 Regression and parameterization of peak filtered velocity**

Figures 4.12 and 4.13 are typical examples of the regression analysis results for the band pass filtered ground velocity at 1.0, 3.0, 4.0 and 10.0 Hz. The top panels illustrate the coda propagation term estimated from the coda normalization technique. The coda and regression propagation functional in the mid-panels show good agreement at higher frequencies. The regression residual plots on the bottom panels are used to see whether the distance nodes were appropriate to determine proper  $D(r)$ . The standard error of the regression ranges from 0.3 to 0.22  $\log_{10}$  units at the frequency range above 1 Hz. Fourier velocity spectra residuals also maintain the consistent distribution shape for the entire distance ranges, means that the residuals measured are well predicted for both data-sets. Band-pass filtered regression results have more data points than those of Fourier velocity spectra regressions.

For time domain parameterization, I started with the model parameters that fit the Fourier velocity spectra and the duration to fit the  $D(r, f)$  of Figure 4.14, 4.15 and 4.16. Figure 4.14a shows the three component data set distance scaling of the peak filtered velocity  $D(r, f)$  term at center frequency ranges of 0.25, 0.5, 1.0, 2.0, 3.0, 4.0, 6.0, 8.0, 10.0, 12.0, 14.0, and 16.0 Hz for Korea. The black curves in the background are the theoretical  $D(r, f)$ . The reference

<b>Durations for different frequencies</b>						
Distance (km)	0.25 (Hz) (sec)	0.5 (Hz) (sec)	1 (Hz) (sec)	2 (Hz) (sec)	3 (Hz) (sec)	4 (Hz) (sec)
0.000	0.000	0.000	0.000	0.000	0.000	0.000
10.000	2.267	1.129	0.750	0.750	0.750	0.250
20.000	3.750	2.250	0.750	0.750	0.750	0.750
40.000	3.251	3.251	7.750	3.750	2.750	2.750
60.000	21.749	19.749	9.750	6.250	5.250	4.750
80.000	12.250	18.750	10.750	5.750	5.250	4.250
100.000	9.250	17.750	10.250	5.750	4.750	4.750
120.000	14.750	15.250	9.250	5.750	5.250	5.250
150.000	12.750	13.750	9.250	6.250	5.250	4.750
200.000	13.750	15.250	10.250	7.750	6.250	5.750
250.000	16.750	17.250	12.250	9.250	8.750	7.750
300.000	19.250	18.750	13.750	10.750	9.750	9.250
400.000	20.250	23.750	17.250	13.250	11.250	10.750
500.000	29.250	24.250	20.750	15.750	14.750	13.250
600.000	37.750	35.750	32.750	20.250	16.250	17.250
Distance (km)	6 (Hz) (sec)	8 (Hz) (sec)	10 (Hz) (sec)	12 (Hz) (sec)	14 (Hz) (sec)	16 (Hz) (sec)
0.000	0.000	0.000	0.000	0.000	0.000	0.000
10.000	0.250	0.250	0.250	0.250	0.750	1.250
20.000	0.250	0.750	0.750	1.750	2.250	1.750
40.000	3.750	4.750	4.750	5.250	6.250	6.250
60.000	5.250	5.250	5.250	5.750	5.750	6.250
80.000	4.250	4.250	4.750	4.750	5.250	5.250
100.000	4.750	4.250	4.750	4.750	5.250	5.750
120.000	4.750	4.250	4.750	5.250	5.250	5.750
150.000	4.250	4.750	4.750	5.250	5.750	6.250
200.000	5.250	5.750	6.250	6.750	7.250	7.750
250.000	7.750	7.750	7.750	8.250	9.250	9.750
300.000	8.750	9.250	9.250	10.250	10.750	11.750
400.000	9.750	10.750	11.250	11.250	12.250	13.250
500.000	12.750	13.250	14.250	15.250	15.750	16.750
600.000	16.750	16.750	16.750	16.250	20.250	24.250

Table 4.8: Durations as a function of distance and frequencies from 0.25 to 16 Hz for the three component data set.

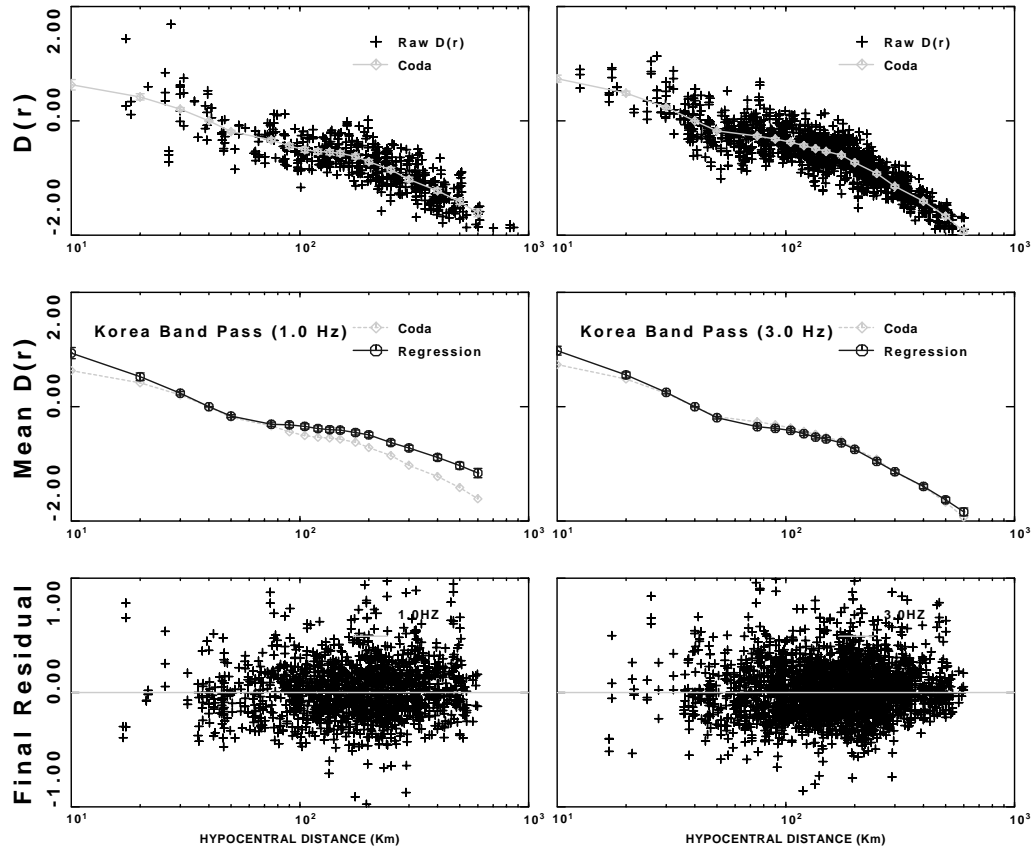


Figure 4.12: Regression analysis for 1.0 and 3.0 Hz. Top, coda estimate of  $D(r)$  using coda normalization technique. Middle, coda and regression propagation functionals (open circles linked by thin black lines). Bottom, final residuals of the regression analysis.

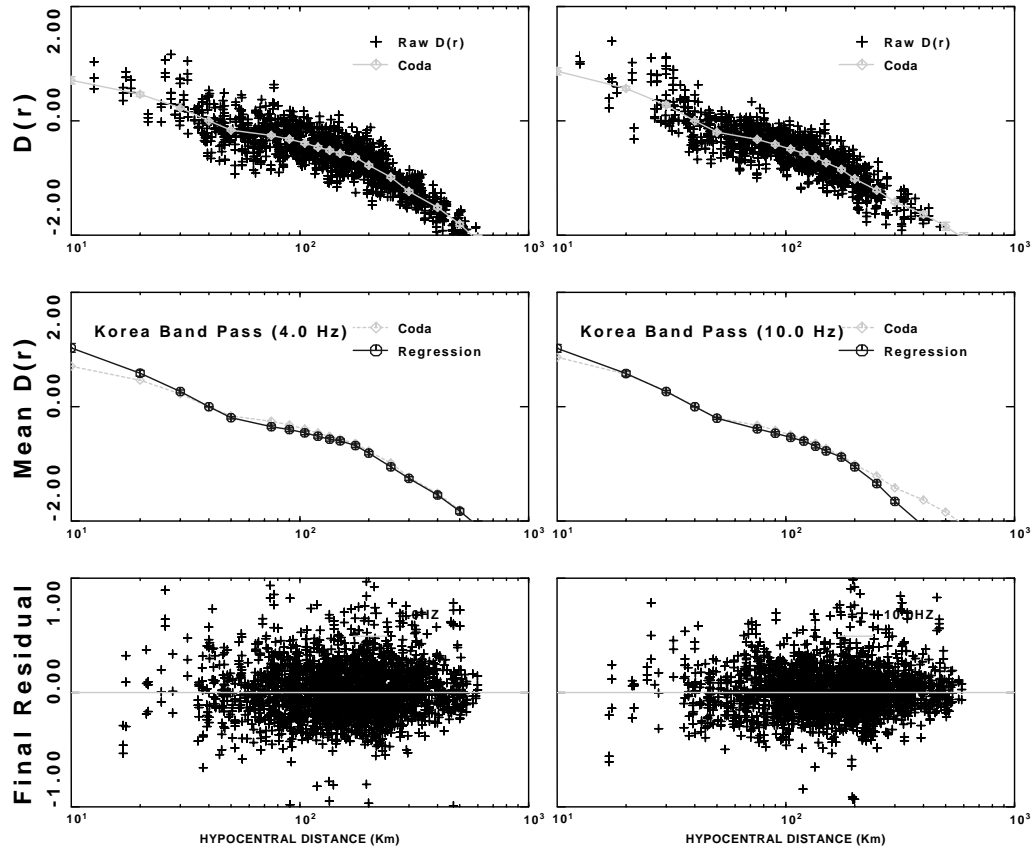


Figure 4.13: Regression analysis for 4.0 and 10.0 Hz. Top, coda estimate of  $D(r)$  using coda normalization technique. Middle, coda and regression propagation functionals (open circles linked by thin black lines). Bottom, final residuals of the regression analysis.

<b>Measured durations</b>			
Distance (km)	All (sec)	Hor (sec)	Ver (sec)
0.000	0.00	0.00	0.00
10.000	0.60	0.50	1.20
20.000	1.10	1.00	1.90
40.000	4.50	4.70	4.40
60.000	6.00	6.00	6.00
80.000	5.50	5.50	5.50
100.000	5.50	5.60	5.70
120.000	5.50	5.70	5.50
150.000	5.70	5.90	5.70
200.000	6.90	7.00	6.80
250.000	8.80	9.00	9.10
300.000	10.30	10.50	10.40
400.000	12.10	12.20	12.20
500.000	15.20	13.80	14.60
600.000	18.30	14.10	14.7

Table 4.9: Measured durations from band-passed filtered for Korea. Hor, Ver, and All are acronyms for horizontal, vertical, and combined data set.

distance at 40 km was used to normalize the  $D(r, f)$ . The theoretical attenuation modeling (black curves) is modeled by  $Q(f) = 330 f^{0.40}$ , and geometrical spreading

$$g(r) = \begin{cases} r^{-1.1} & r < 40 \text{ km} \\ r^{-1.2} & 40 < r < 60 \text{ km} \\ r^{-0.0} & 60 < r < 250 \text{ km} \\ r^{-0.5} & r > 250 \text{ km} \end{cases}$$

and duration of Table 4.9. Figure 4.14b shows the band pass filtered  $D(r)$  residuals, the deviation between observed and predicted  $D(r, f)$  as a function of distance. The residuals of fit are less than about 0.1  $\log_{10}$  units out to 200 km but increase at larger distances.

Figure 4.15a compares the horizontal data set distance scaling of the  $D(r, f)$  term for Korea at twelve different frequencies. The plot emphasizes the departure from  $r^{-1.0}$  spreading and required a geometrical spreading more rapid than  $r^{-1.0}$  in the 10 - 60 km distance range. Figure 4.15b shows the band pass

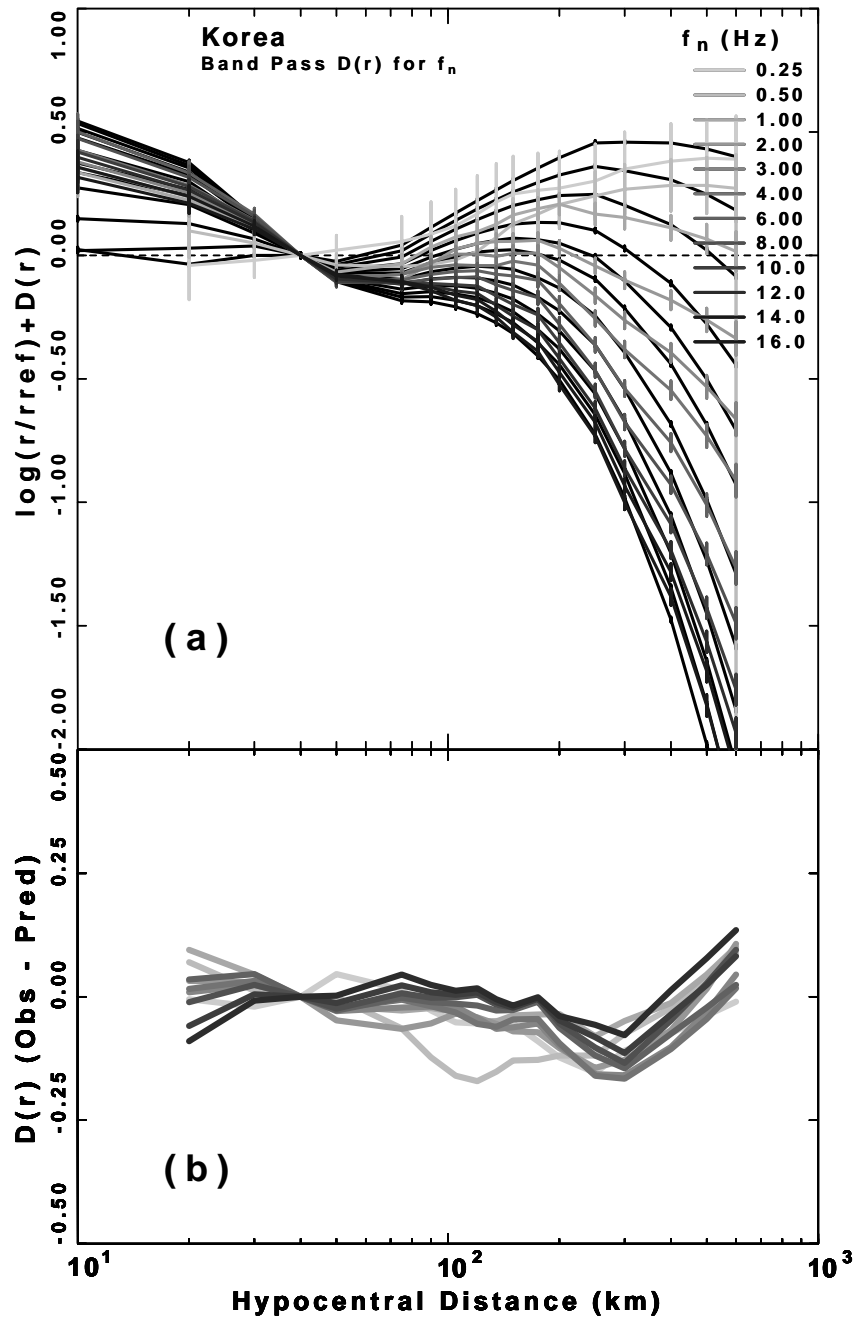


Figure 4.14: (a) Three component reduced attenuation functional  $D(r, f)$  obtained from the regression on the bandpass-filtered velocities from 0.25 to 16.0 Hz for Korea. The presentation of this plot is to emphasize the departure from  $r^{-1}$  spreading. The black lines in the background are the theoretical  $D(r, f)$ . The horizontal dashed line represents  $r^{-1}$  trend; (b) The residuals of the model fit to the band pass  $D(r, f)$  from 0.25 to 16 Hz.

filtered  $D(r)$  residuals, the deviation between observed and predicted  $D(r, f)$  of the distance range. The residuals of fit (Figure 4.15b) are less than about 0.1 out to 200 km, but increase in a manner that is not simply related to frequency dependence at larger distances. The theoretical attenuation modeling (black curves) is modeled by  $Q(f) = 330 f^{0.40}$ , and

$$g(r) = \begin{cases} r^{-1.0} & r < 40 \text{ km} \\ r^{-1.3} & 40 < r < 60 \text{ km} \\ r^{-0.1} & 60 < r < 250 \text{ km} \\ r^{-0.5} & r > 250 \text{ km}. \end{cases}$$

Figure 4.16a compares the vertical data set distance scaling of the  $D(r, f)$  term for Korea at twelve different frequencies. Figure 4.16b shows the band pass filtered  $D(r)$  residuals. The residuals of fit are less than about 0.1 out to 200 km, but increase consistently related to frequency dependence at larger distances. The theoretical attenuation is modeled by  $Q(f) = 330 f^{0.40}$ , and

$$g(r) = \begin{cases} r^{-1.0} & r < 40 \text{ km} \\ r^{-1.3} & 40 < r < 60 \text{ km} \\ r^{-0.0} & 60 < r < 250 \text{ km} \\ r^{-0.5} & r > 250 \text{ km}. \end{cases}$$

Tables 4.10 - 4.12 give the numerical results of the regression on the three component regional attenuation functional for Korea. They give the corresponding value of  $D(r)$  for each frequency, distance, and  $\sigma$  as well as the number of observations contributing to each node. The  $g(r)$  used here differ slightly from those used to model the frequency domain regression results. I recommend the use of these since the time domain data set is better than those of the frequency domain.

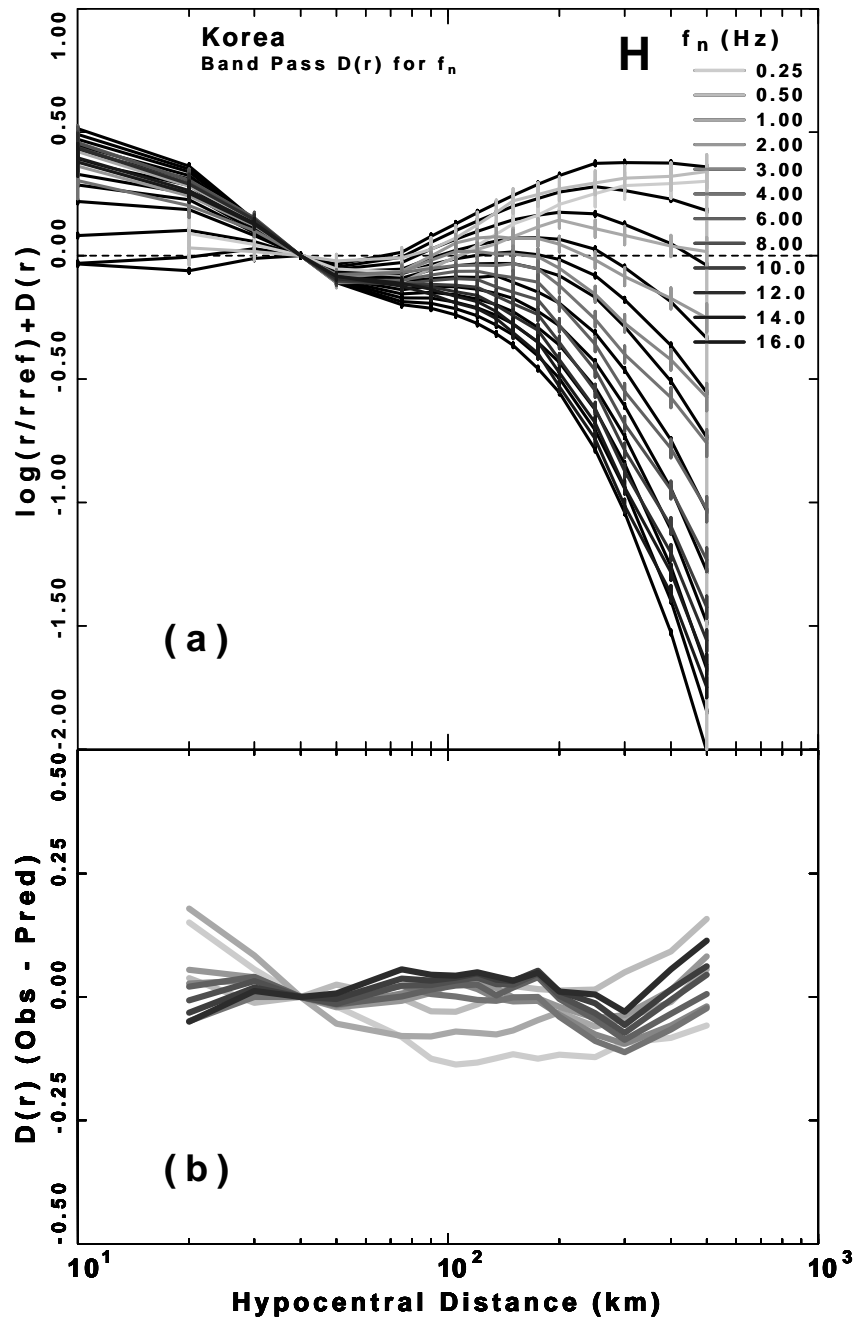


Figure 4.15: (a) Horizontal component reduced attenuation functional  $D(r, f)$  obtained from the regression on the bandpass-filtered velocities of 0.25, 0.5, 1.0, 2.0, 3.0, 4.0, 6.0, 8.0, 10.0, 12.0, 14.0, and 16.0 Hz for Korea. The reference distance at 40 km was used to normalize the  $D(r, f)$ ; (b) The residuals of the model fit to the band pass  $D(r, f)$  for the frequency range of 0.25 - 16 Hz.

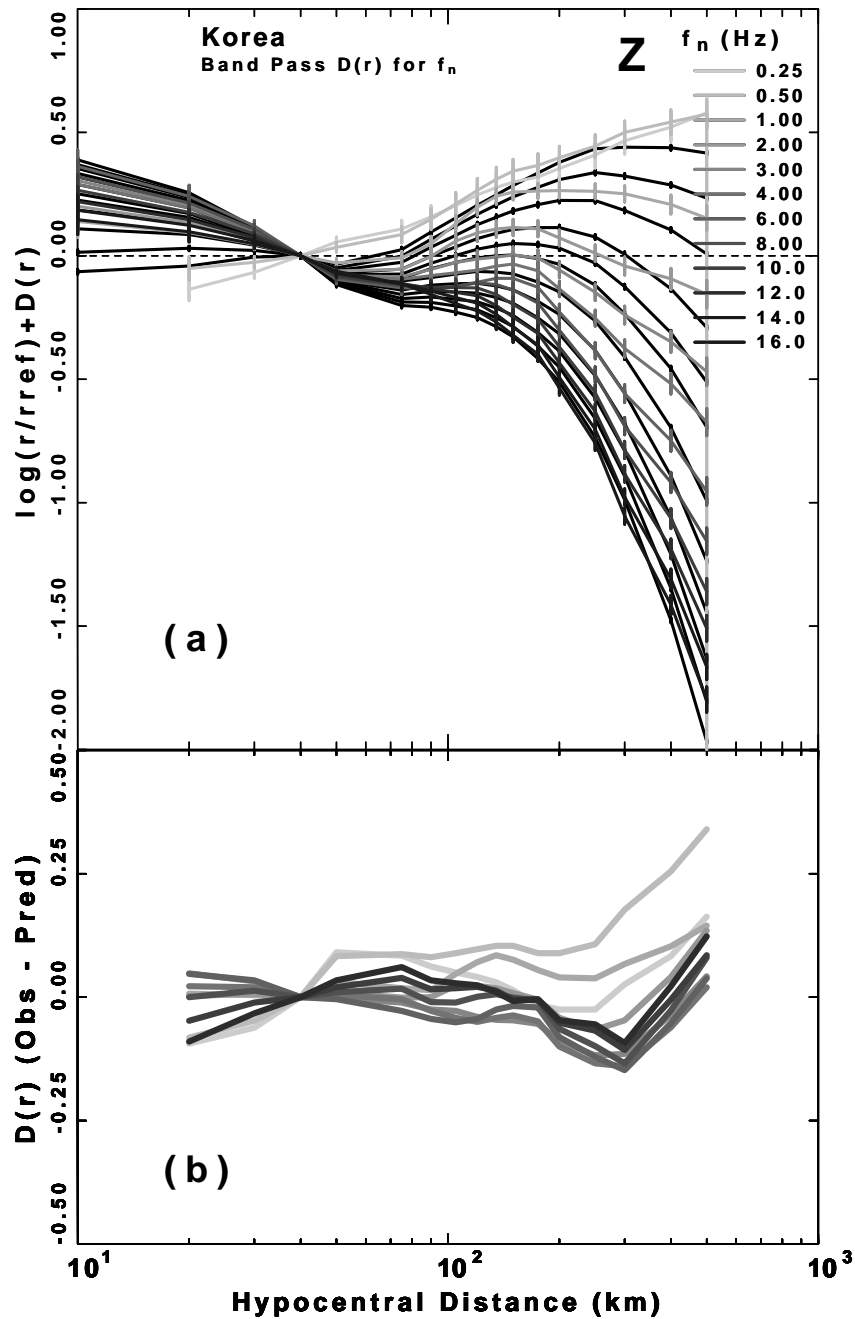


Figure 4.16: (a) Vertical component reduced attenuation functional  $D(r, f)$  obtained from the regression on the bandpass-filtered velocities of 0.25, 0.5, 1.0, 2.0, 3.0, 4.0, 6.0, 8.0, 10.0, 12.0, 14.0, and 16.0 Hz for Korea; (b) The residuals of the model fit to the band pass  $D(r, f)$  for the frequency range of 0.25 - 16 Hz.

Korea Filtered velocity spectra $D(r)$									
f (Hz)	r (km)	$D(r, f)$	$\sigma$	Nobs	f (Hz)	r (km)	$D(r, f)$	$\sigma$	Nobs
0.25	20	0.261	0.139E+00	0.420	0.5	20	0.401	0.108E+00	2.090
0.25	30	0.105	0.695E-01	0.570	0.5	30	0.175	0.538E-01	2.050
0.25	40	0.000	0.392E-05	2.690	0.5	40	0.000	0.364E-05	5.000
0.25	50	-0.075	0.594E-01	6.870	0.5	50	-0.135	0.449E-01	13.38
0.25	75	-0.217	0.102E+00	16.81	0.5	75	-0.318	0.751E-01	24.18
0.25	90	-0.266	0.131E+00	17.77	0.5	90	-0.388	0.943E-01	25.28
0.25	105	-0.299	0.148E+00	20.11	0.5	105	-0.437	0.104E+00	24.25
0.25	120	-0.309	0.155E+00	13.80	0.5	120	-0.460	0.107E+00	21.98
0.25	135	-0.312	0.156E+00	16.43	0.5	135	-0.455	0.105E+00	36.45
0.25	150	-0.325	0.153E+00	19.93	0.5	150	-0.446	0.102E+00	33.25
0.25	175	-0.377	0.151E+00	20.17	0.5	175	-0.473	0.995E-01	38.74
0.25	200	-0.426	0.150E+00	34.20	0.5	200	-0.492	0.979E-01	70.69
0.25	250	-0.494	0.150E+00	48.35	0.5	250	-0.554	0.984E-01	81.78
0.25	300	-0.525	0.150E+00	60.28	0.5	300	-0.607	0.101E+00	86.98
0.25	400	-0.618	0.152E+00	49.27	0.5	400	-0.716	0.105E+00	58.32
0.25	500	-0.703	0.157E+00	39.89	0.5	500	-0.813	0.114E+00	44.97
0.25	600	-0.786	0.175E+00	6.360	0.5	600	-0.904	0.136E+00	6.540
1.0	10	0.938	0.977E-01	1.410	2.0	10	0.959	0.787E-01	1.720
1.0	20	0.525	0.651E-01	9.060	2.0	20	0.539	0.525E-01	12.74
1.0	30	0.237	0.326E-01	9.130	2.0	30	0.244	0.262E-01	14.06
1.0	40	0.000	0.316E-05	39.25	2.0	40	0.000	0.293E-05	55.26
1.0	50	-0.164	0.257E-01	63.24	2.0	50	-0.204	0.206E-01	107.8
1.0	75	-0.307	0.384E-01	79.91	2.0	75	-0.372	0.295E-01	162.3
1.0	90	-0.318	0.439E-01	85.21	2.0	90	-0.386	0.326E-01	186.4
1.0	105	-0.344	0.455E-01	87.87	2.0	105	-0.393	0.332E-01	159.7
1.0	120	-0.381	0.452E-01	94.53	2.0	120	-0.429	0.325E-01	182.6
1.0	135	-0.402	0.444E-01	97.56	2.0	135	-0.472	0.320E-01	180.5
1.0	150	-0.410	0.438E-01	104.7	2.0	150	-0.517	0.316E-01	194.6
1.0	175	-0.451	0.434E-01	128.1	2.0	175	-0.579	0.310E-01	243.4
1.0	200	-0.491	0.433E-01	190.1	2.0	200	-0.670	0.307E-01	342.8
1.0	250	-0.628	0.445E-01	205.1	2.0	250	-0.838	0.318E-01	315.6
1.0	300	-0.721	0.467E-01	172.7	2.0	300	-0.975	0.343E-01	229.1
1.0	400	-0.888	0.506E-01	127.9	2.0	400	-1.181	0.388E-01	139.9
1.0	500	-1.030	0.593E-01	75.65	2.0	500	-1.358	0.476E-01	76.94
1.0	600	-1.160	0.804E-01	11.46	2.0	600	-1.512	0.681E-01	12.45

Table 4.10: Attenuation functional at 0.25, 0.5, 1.0, and 2.0 Hz for band passed filtered. The columns give values of frequency (first and sixth columns), hypocentral distance (second and seventh columns), attenuation  $D(r, f)$  at a reference distance of 40 km (third and eighth columns), associated error bar (fourth and ninth columns) and number of observations (fifth and tenth columns).

<b>Korea filtered velocity spectra <math>D(r)</math></b>									
f (Hz)	r (km)	$D(r, f)$	$\sigma$	Nobs	f (Hz)	r (km)	$D(r, f)$	$\sigma$	Nobs
3.0	10	0.981	0.775E-01	1.720	4.0	10	1.029	0.770E-01	1.720
3.0	20	0.554	0.517E-01	12.86	4.0	20	0.585	0.514E-01	12.86
3.0	30	0.251	0.258E-01	14.99	4.0	30	0.267	0.257E-01	14.99
3.0	40	0.000	0.289E-05	56.10	4.0	40	0.000	0.288E-05	56.21
3.0	50	-0.192	0.203E-01	108.8	4.0	50	-0.192	0.202E-01	111.0
3.0	75	-0.349	0.289E-01	165.7	4.0	75	-0.350	0.287E-01	171.3
3.0	90	-0.379	0.320E-01	187.5	4.0	90	-0.400	0.318E-01	191.5
3.0	105	-0.414	0.326E-01	165.5	4.0	105	-0.457	0.324E-01	166.6
3.0	120	-0.472	0.319E-01	188.1	4.0	120	-0.518	0.316E-01	193.1
3.0	135	-0.532	0.315E-01	186.8	4.0	135	-0.569	0.312E-01	190.5
3.0	150	-0.566	0.311E-01	198.7	4.0	150	-0.597	0.309E-01	200.2
3.0	175	-0.631	0.306E-01	239.3	4.0	175	-0.680	0.303E-01	245.0
3.0	200	-0.748	0.303E-01	344.2	4.0	200	-0.811	0.300E-01	344.3
3.0	250	-0.958	0.313E-01	319.2	4.0	250	-1.051	0.310E-01	320.1
3.0	300	-1.138	0.337E-01	230.8	4.0	300	-1.256	0.335E-01	231.8
3.0	400	-1.394	0.382E-01	139.2	4.0	400	-1.546	0.380E-01	138.3
3.0	500	-1.629	0.469E-01	76.94	4.0	500	-1.828	0.467E-01	76.94
3.0	600	-1.839	0.671E-01	12.45	4.0	600	-2.088	0.668E-01	12.45
6.0	10	1.103	0.724E-01	1.720	8.0	10	1.076	0.696E-01	1.720
6.0	20	0.635	0.483E-01	13.19	8.0	20	0.617	0.464E-01	13.52
6.0	30	0.292	0.241E-01	15.66	8.0	30	0.283	0.232E-01	16.33
6.0	40	0.000	0.271E-05	53.79	8.0	40	0.000	0.262E-05	53.79
6.0	50	-0.204	0.190E-01	110.3	8.0	50	-0.206	0.183E-01	110.3
6.0	75	-0.372	0.272E-01	165.7	8.0	75	-0.383	0.262E-01	165.4
6.0	90	-0.429	0.302E-01	185.3	8.0	90	-0.449	0.290E-01	185.6
6.0	105	-0.484	0.308E-01	158.6	8.0	105	-0.509	0.297E-01	158.6
6.0	120	-0.539	0.302E-01	185.1	8.0	120	-0.564	0.291E-01	184.4
6.0	135	-0.604	0.299E-01	176.7	8.0	135	-0.647	0.288E-01	176.4
6.0	150	-0.657	0.295E-01	184.9	8.0	150	-0.716	0.284E-01	184.5
6.0	175	-0.741	0.289E-01	238.8	8.0	175	-0.812	0.279E-01	237.4
6.0	200	-0.894	0.286E-01	329.5	8.0	200	-0.977	0.276E-01	327.1
6.0	250	-1.158	0.298E-01	293.7	8.0	250	-1.261	0.287E-01	292.9
6.0	300	-1.414	0.323E-01	205.9	8.0	300	-1.550	0.312E-01	204.6
6.0	400	-1.758	0.368E-01	129.3	8.0	400	-1.929	0.355E-01	125.7
6.0	500	-2.108	0.456E-01	74.42	8.0	500	-2.306	0.441E-01	73.31
6.0	600	-2.442	0.660E-01	9.490	8.0	600	-2.666	0.638E-01	9.470

Table 4.11: Attenuation functional at 3.0, 4.0, 6.0, and 8.0 Hz for bandpass filtered. The columns give values of frequency (first and sixth columns), hypocentral distance (second and seventh columns), attenuation  $D(r, f)$  at a reference distance of 40 km (third and eighth columns), associated error bar (fourth and ninth columns) and number of observations (fifth and tenth columns).

Korea filtered velocity spectra $D(r)$									
f (Hz)	r (km)	$D(r, f)$	$\sigma$	Nobs	f (Hz)	r (km)	$D(r, f)$	$\sigma$	Nobs
10.0	10	1.021	0.685E-01	1.720	12.0	10	1.000	0.667E-01	1.720
10.0	20	0.580	0.457E-01	13.19	12.0	20	0.566	0.445E-01	13.52
10.0	30	0.265	0.228E-01	15.45	12.0	30	0.258	0.222E-01	16.12
10.0	40	0.000	0.256E-05	52.90	12.0	40	0.000	0.250E-05	52.78
10.0	50	-0.201	0.180E-01	109.4	12.0	50	-0.192	0.176E-01	108.5
10.0	75	-0.387	0.258E-01	167.1	12.0	75	-0.383	0.251E-01	167.1
10.0	90	-0.466	0.286E-01	185.9	12.0	90	-0.475	0.279E-01	185.9
10.0	105	-0.538	0.292E-01	157.4	12.0	105	-0.563	0.285E-01	154.8
10.0	120	-0.601	0.287E-01	183.1	12.0	120	-0.631	0.280E-01	181.0
10.0	135	-0.692	0.283E-01	174.4	12.0	135	-0.730	0.277E-01	174.1
10.0	150	-0.773	0.280E-01	183.8	12.0	150	-0.820	0.273E-01	183.9
10.0	175	-0.882	0.274E-01	236.6	12.0	175	-0.942	0.268E-01	233.5
10.0	200	-1.052	0.271E-01	326.5	12.0	200	-1.116	0.265E-01	322.0
10.0	250	-1.345	0.282E-01	290.5	12.0	250	-1.414	0.276E-01	290.0
10.0	300	-1.658	0.307E-01	202.2	12.0	300	-1.737	0.301E-01	196.8
10.0	400	-2.089	0.350E-01	122.8	12.0	400	-2.193	0.345E-01	117.5
10.0	500	-2.524	0.435E-01	70.58	12.0	500	-2.662	0.432E-01	66.76
10.0	600	-2.935	0.629E-01	9.440	12.0	600	-3.111	0.624E-01	9.070
14.0	10	0.960	0.654E-01	1.720	16.0	10	0.919	0.634E-01	1.720
14.0	20	0.540	0.436E-01	13.85	16.0	20	0.513	0.423E-01	13.02
14.0	30	0.244	0.218E-01	17.00	16.0	30	0.231	0.211E-01	16.83
14.0	40	0.000	0.246E-05	53.79	16.0	40	0.000	0.238E-05	53.79
14.0	50	-0.180	0.172E-01	110.1	16.0	50	-0.173	0.167E-01	110.1
14.0	75	-0.378	0.247E-01	166.3	16.0	75	-0.382	0.239E-01	164.7
14.0	90	-0.481	0.274E-01	185.9	16.0	90	-0.495	0.265E-01	185.4
14.0	105	-0.580	0.280E-01	154.0	16.0	105	-0.601	0.272E-01	154.0
14.0	120	-0.656	0.275E-01	178.5	16.0	120	-0.680	0.267E-01	178.4
14.0	135	-0.755	0.272E-01	170.0	16.0	135	-0.778	0.264E-01	165.9
14.0	150	-0.855	0.268E-01	184.2	16.0	150	-0.885	0.260E-01	184.2
14.0	175	-0.989	0.263E-01	233.3	16.0	175	-1.029	0.255E-01	230.7
14.0	200	-1.172	0.261E-01	315.7	16.0	200	-1.222	0.253E-01	311.4
14.0	250	-1.472	0.272E-01	285.1	16.0	250	-1.528	0.264E-01	283.1
14.0	300	-1.808	0.297E-01	194.3	16.0	300	-1.876	0.289E-01	186.6
14.0	400	-2.283	0.343E-01	112.4	16.0	400	-2.383	0.338E-01	105.8
14.0	500	-2.781	0.436E-01	56.83	16.0	500	-2.920	0.436E-01	51.67
14.0	600	-3.273	0.633E-01	8.060	16.0	600	-3.447	0.634E-01	7.600

Table 4.12: Attenuation functional at 10.0, 12.0, 14.0, and 16.0 Hz for band-pass filtered. The columns give values of frequency (first and sixth columns), hypocentral distance (second and seventh columns), attenuation  $D(r, f)$  at a reference distance of 40 km (third and eighth columns), associated error bar (fourth and ninth columns) and number of observations (fifth and tenth columns).

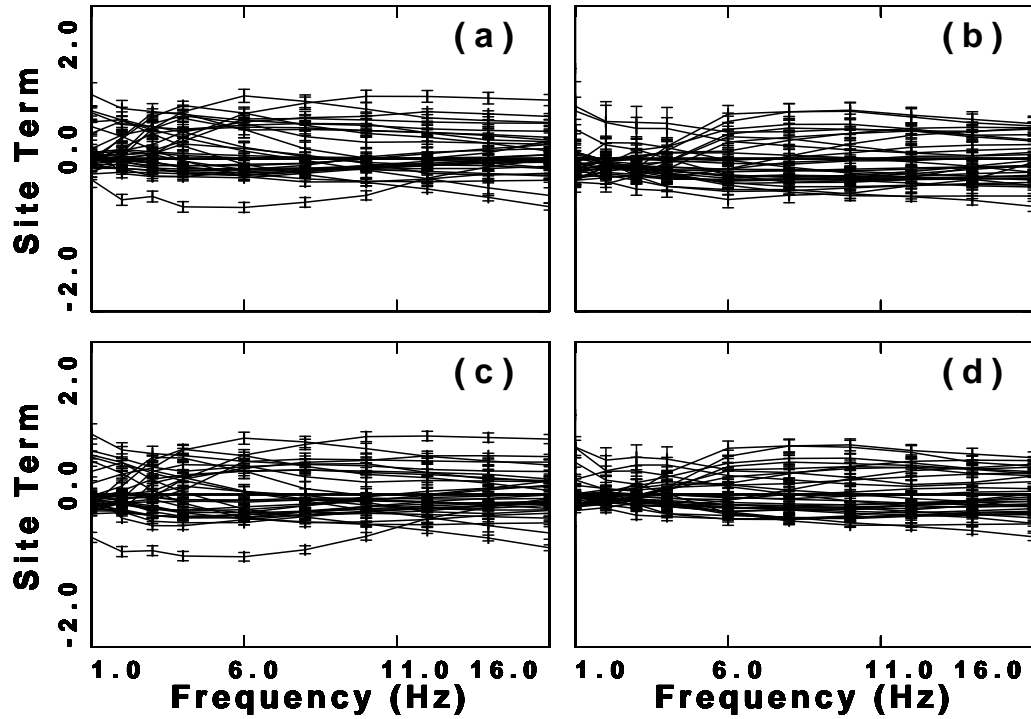


Figure 4.17: Inverted site amplifications of Korea. Each line denotes single stations. a and b are Z and H component site terms of ground motion while c and d are H and Z component site terms of ground motion.

#### 4.4.1 Site

Figure 4.17 show the site terms from the regression on the band-passed time domain data. There is little frequency variation in the site terms and each site term is parallel to other sites except at lower frequencies. The individual site terms agree well for the all component (top panel: a, b), horizontal component (lower left panel: c), and vertical component (lower right panel: d). Right panel shows vertical (Z) and left panels show horizontal (H) component site terms.  $\sum S_Z(f) = 0$  is used for site amplifications of right panel while the constraint of  $\sum S_H(f) = 0$  is used for site amplifications of left panel.

## 4.4.2 Excitation

Figure 4.18 compares the observed and predicted excitation of filtered velocity spectra obtained from Korea. The black lines indicate the regression results, while the thick gray lines denote the theoretical excitations. The thin black lines linked by thick short dash lines indicate the excitation spectra of  $M_W$  from 4.61 to 5.10. The thin black lines linked by thick long dash lines denote the excitation spectra of  $M_W$  from 3.63 to 4.06.  $M_W$  ranges from 2.5 to 5.5 is marked by gray lines from the lowest.  $\kappa_{eff} = 0.005$  and  $\Delta\sigma = 200$  bars are selected model parameters to fit the observed spectra. The theoretical excitation level of  $M_W = 4.5, 5.0,$  and  $5.5$  shows the sag in high frequency range compare with the thick short dash line. Even if I tried to fit the excitation spectra by changing the model parameters, I can not find appropriate spectral levels. The thick long dash lines shows good agreement with the theoretical spectra level of  $M_W = 3.5$  and  $4.0$  because the Brune's point source model works well for  $M_W < 4.0$ . The standard errors on the excitation terms are less than  $0.1 \log_{10}$  units, while that of individual events depend on the number of trace used for regressions.

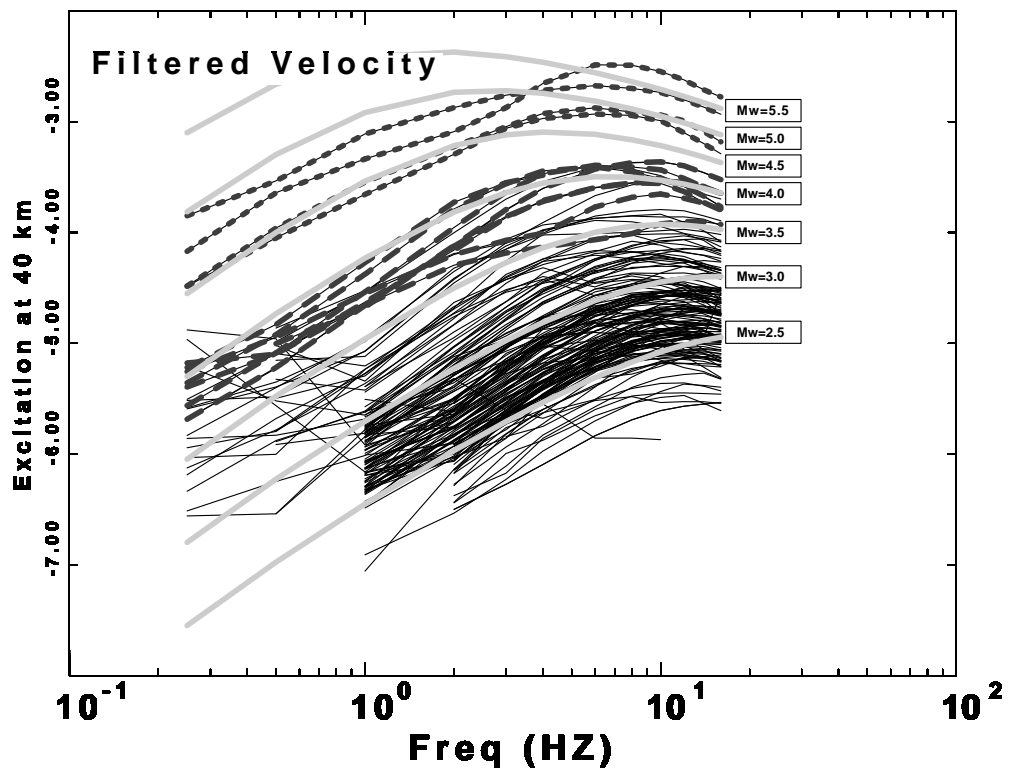


Figure 4.18: Inverted filtered ground velocity excitation terms for the earthquake events recorded by three-component velocity seismograms plotted on a log scale for Korea. The thin black lines linked by thick short and long dash lines are the excitations of known moment magnitudes.

## 4.5 Inland regression

The objective here was to study wave propagation solely on land to determine if there was any bias introduced by using events in the eastern and western seas.

### 4.5.1 Regression of peak filtered velocity

The data set consists of 94 earthquakes and 1478 waveforms recorded from 2000 to 2004 were used for analysis. Figure 4.19 is the map of the station distance distribution. Only data at distances less than 400 km are used.

Figures 4.20 and 4.21 illustrate the regression analysis results for the band pass filtered spectra data for 1.0, 3.0, 4.0, and 10.0 Hz. Top panels illustrate the coda propagation term estimated from the coda normalization technique. The coda and regression propagation functional in the mid-panels show good agreement for the band pass filtered spectra data set at that distance range.

Figure 4.22 shows the three component distance scaling of the peak filtered velocity  $D(r, f)$  term at the frequencies of 0.25, 0.5, 1.0, 2.0, 3.0, 4.0, 6.0, 8.0, 10.0, 12.0, 14.0, and 16.0 Hz for inland Korea. I used  $Q(f) = 330 f^{0.40}$ , and geometrical spreading

$$g(r) = \begin{cases} r^{-1.1} & r < 40 \text{ km} \\ r^{-1.3} & 40 < r < 60 \text{ km} \\ r^{-0.0} & 60 < r < 250 \text{ km} \\ r^{-0.5} & r > 250 \text{ km}. \end{cases}$$

The predicted  $D(r, f)$  fit regression results very well.

Figure 4.23 shows the horizontal (top) and vertical (bottom) component re-

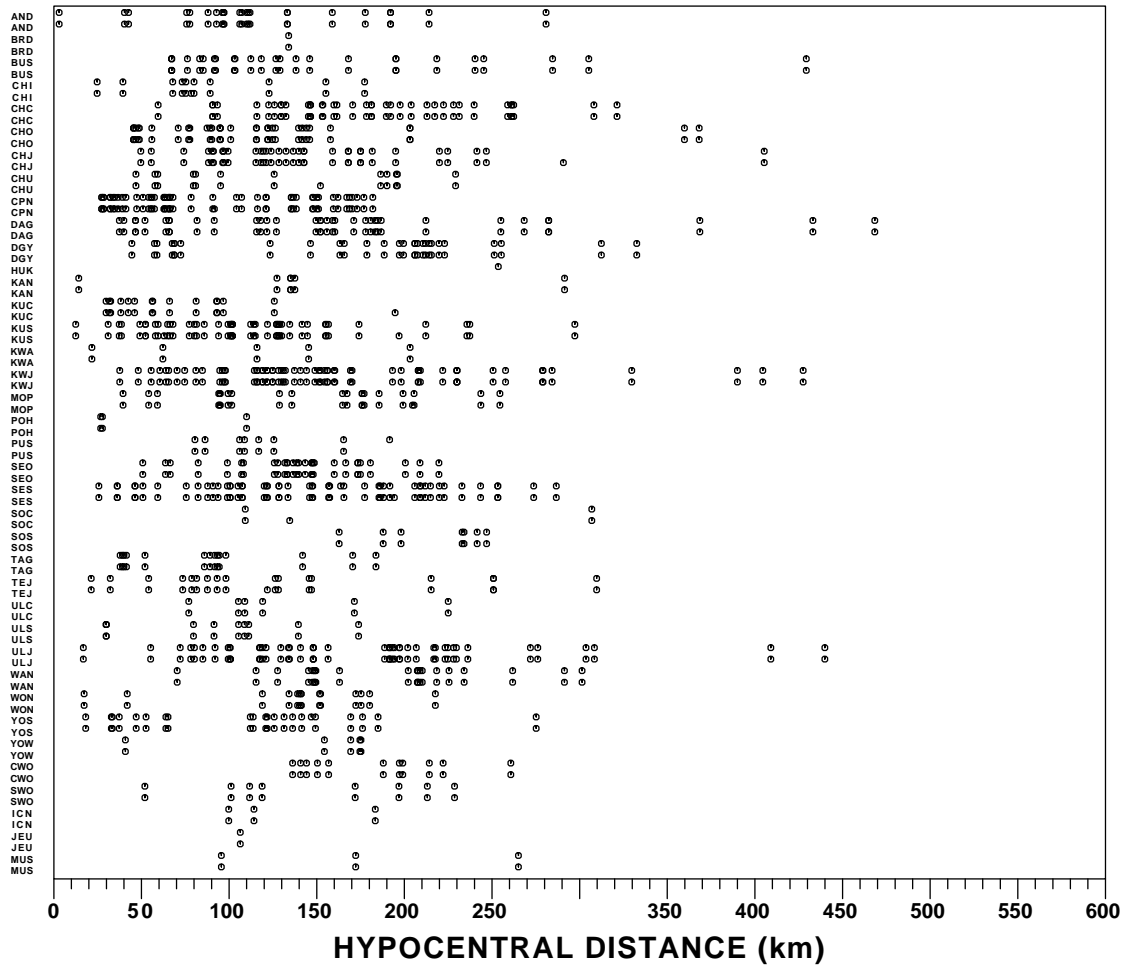


Figure 4.19: Source-receiver hypocentral distance distribution of observed stations for the data recorded along the seismic network.

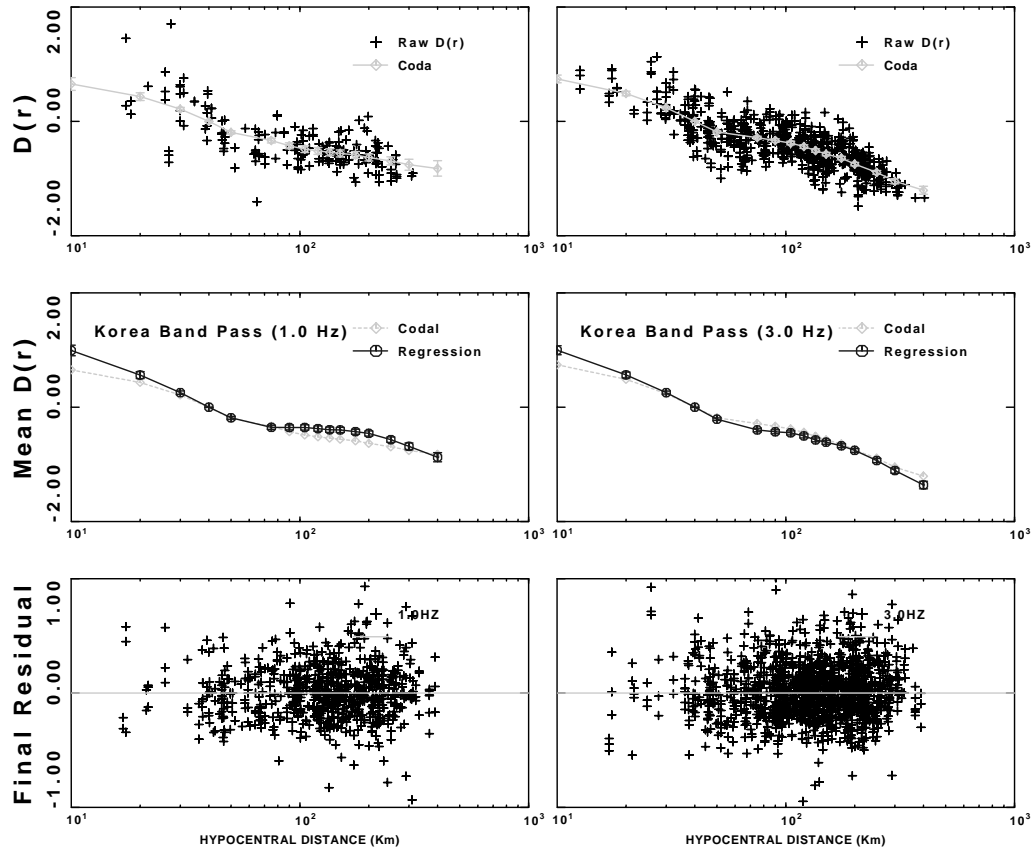


Figure 4.20: Regression analysis for 1.0 and 3.0 Hz. Top, coda estimate of  $D(r)$  using coda normalization technique. Middle, coda and regression propagation functionals. Bottom, final residuals of the regression analysis.

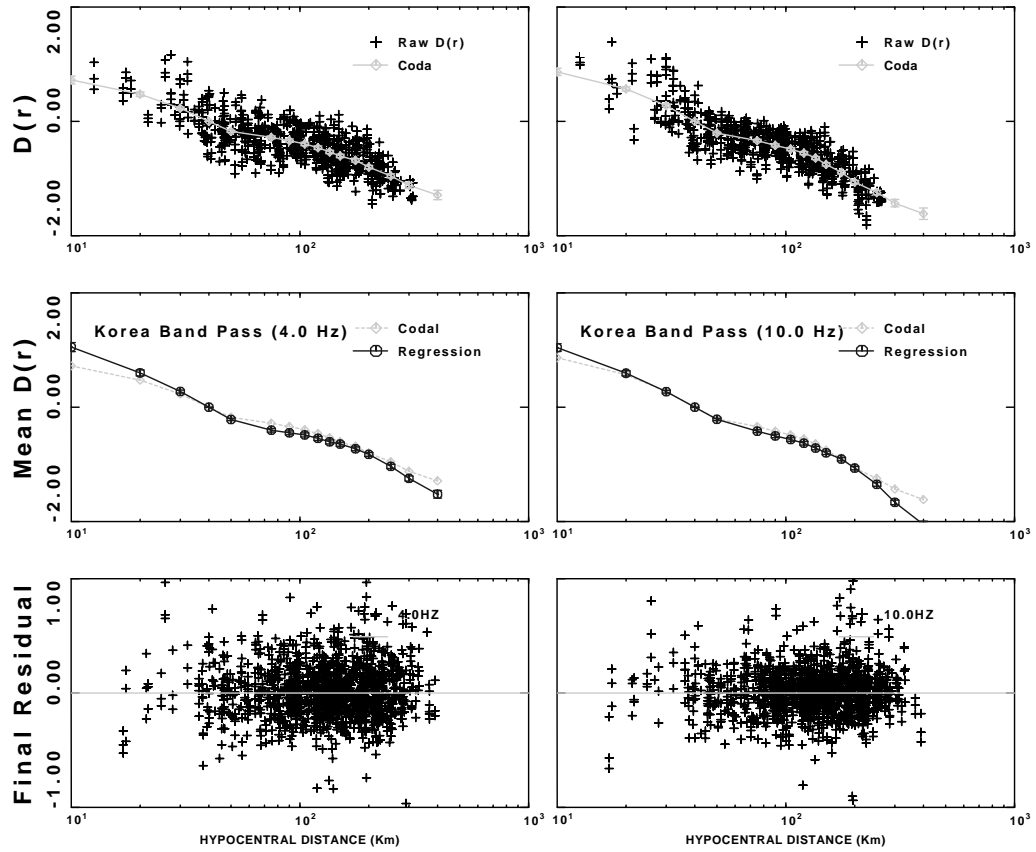


Figure 4.21: Regression analysis for 4.0 and 10.0 Hz. Top, coda estimate of  $D(r)$  using coda normalization technique. Middle, coda and regression propagation functionals. Bottom, final residuals of the regression analysis.

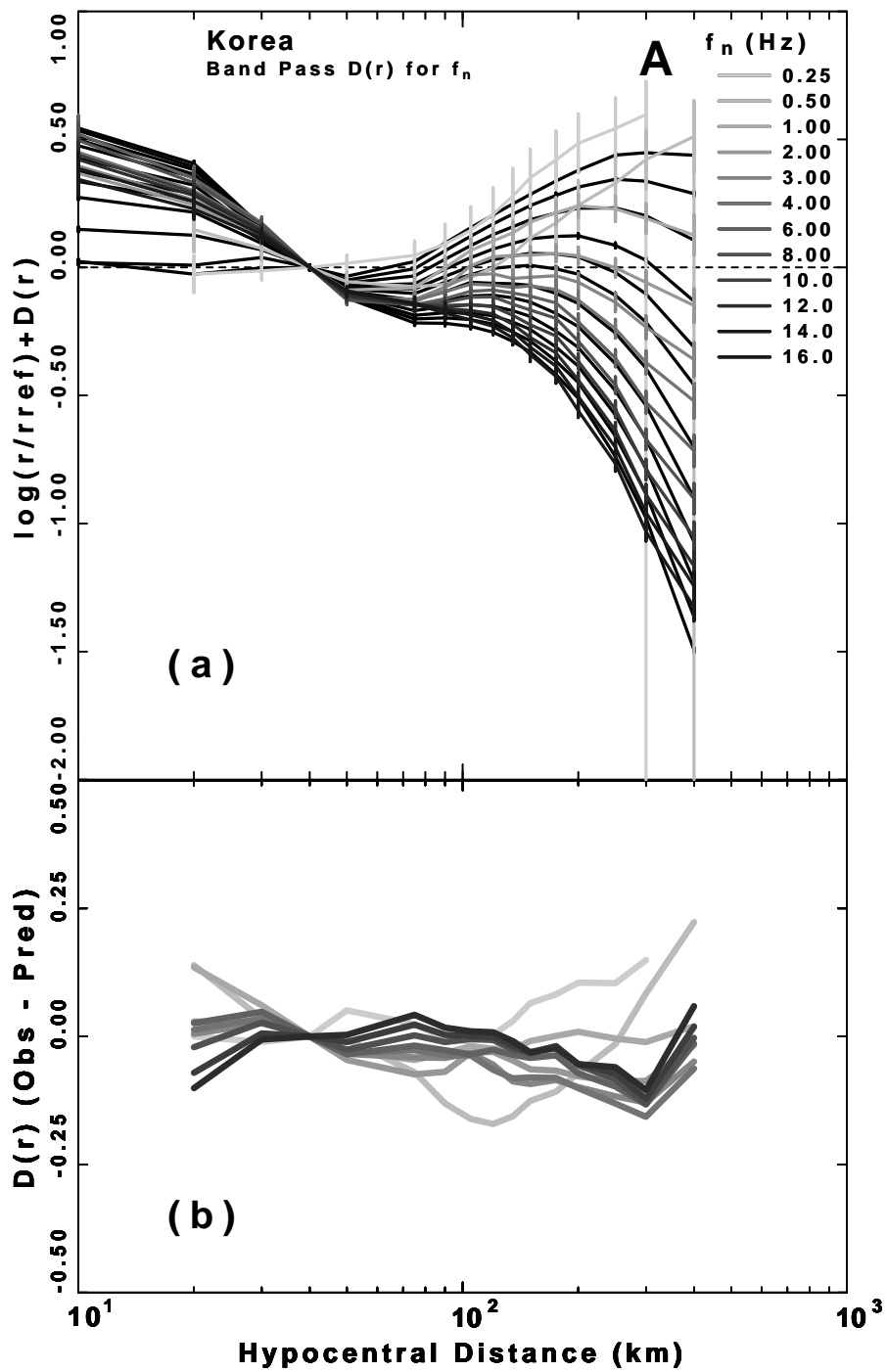


Figure 4.22: Three component reduced attenuation functional  $D(r, f)$  from band passed-filtered velocities at the frequencies from 0.25 to 16.0 Hz for inland Korea. The black lines in the background are the theoretical  $D(r, f)$ ; (b) The residuals of the model fit to the band passed  $D(r, f)$  for the frequency range of 0.25 - 16 Hz.

duced attenuation functional  $D(r, f)$  obtained from the regression on the band passed filtered spectra from 0.25 to 16 Hz. An  $r^{-1.0}$  is required to fit the distance range (10 - 40 km) for horizontal component and vertical component distance scaling. The geometrical spreading at short distance range (10 - 40 km) for different data sets identical each others in Korea.  $Q(f) = 330 f^{0.40}$ , and

$$g(r) = \begin{cases} r^{-1.0} & r < 40 \text{ km} \\ r^{-1.3} & 40 < r < 60 \text{ km} \\ r^{-0.0} & 60 < r < 250 \text{ km} \\ r^{-0.5} & r > 250 \text{ km} \end{cases}$$

are used for horizontal and vertical component theoretical  $D(r, f)$ .

The least squares fits are at Figure 4.24 showing the durations at 1.0, 3.0, 4.0, 8.0, 10.0, and 14.0 Hz. The individual duration estimates (gray circles) show much scatter at lower frequency ranges of 1.0 - 3.0 Hz, while it decreases at higher frequencies. Table 4.13 lists frequency independent duration functionals as a function of distance determined for all, horizontal, and vertical component of inland Korea.

Figure 4.25 shows the site terms for the inland Korea on the peak filtered velocity values. The individual site terms agree well each others after I removed islands stations. The individual site terms agree well for the all component (top panel: a, b), horizontal component (lower left panel: c), and vertical component (lower right panel: c). Right panel shows vertical (Z) and left panels show horizontal (H) component site terms.  $\sum S_Z(f) = 0$  is used for site amplifications of right panel while the constraint of  $\sum S_H(f) = 0$  is used for site amplifications of left panel.

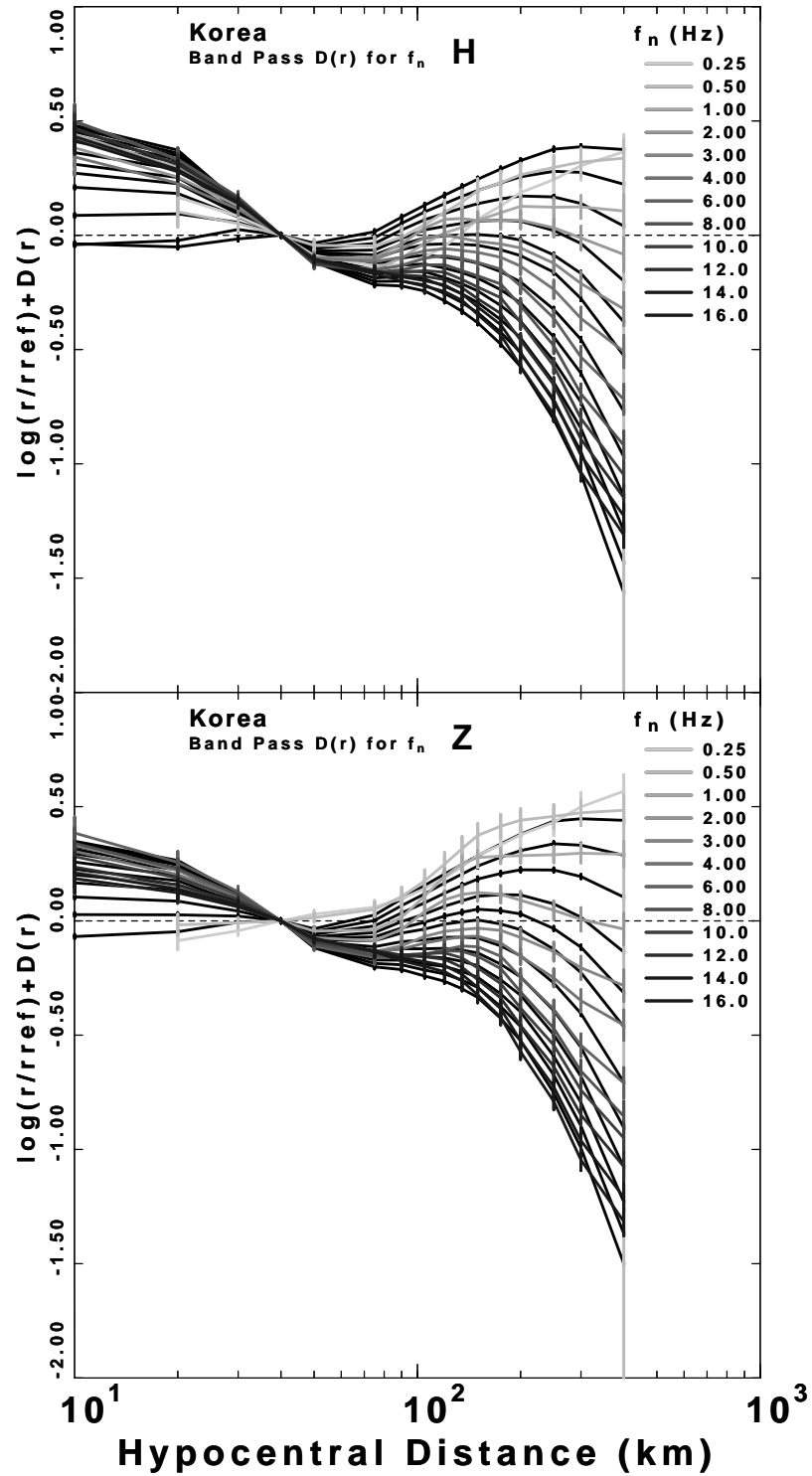


Figure 4.23: Horizontal component (top panel) and vertical component (bottom panel) reduced attenuation functional  $D(r, f)$  obtained from the regression on the band passed filtered spectra from 0.25 to 16.0 Hz for the inland Korea. The black lines in the background are the theoretical  $D(r, f)$ .

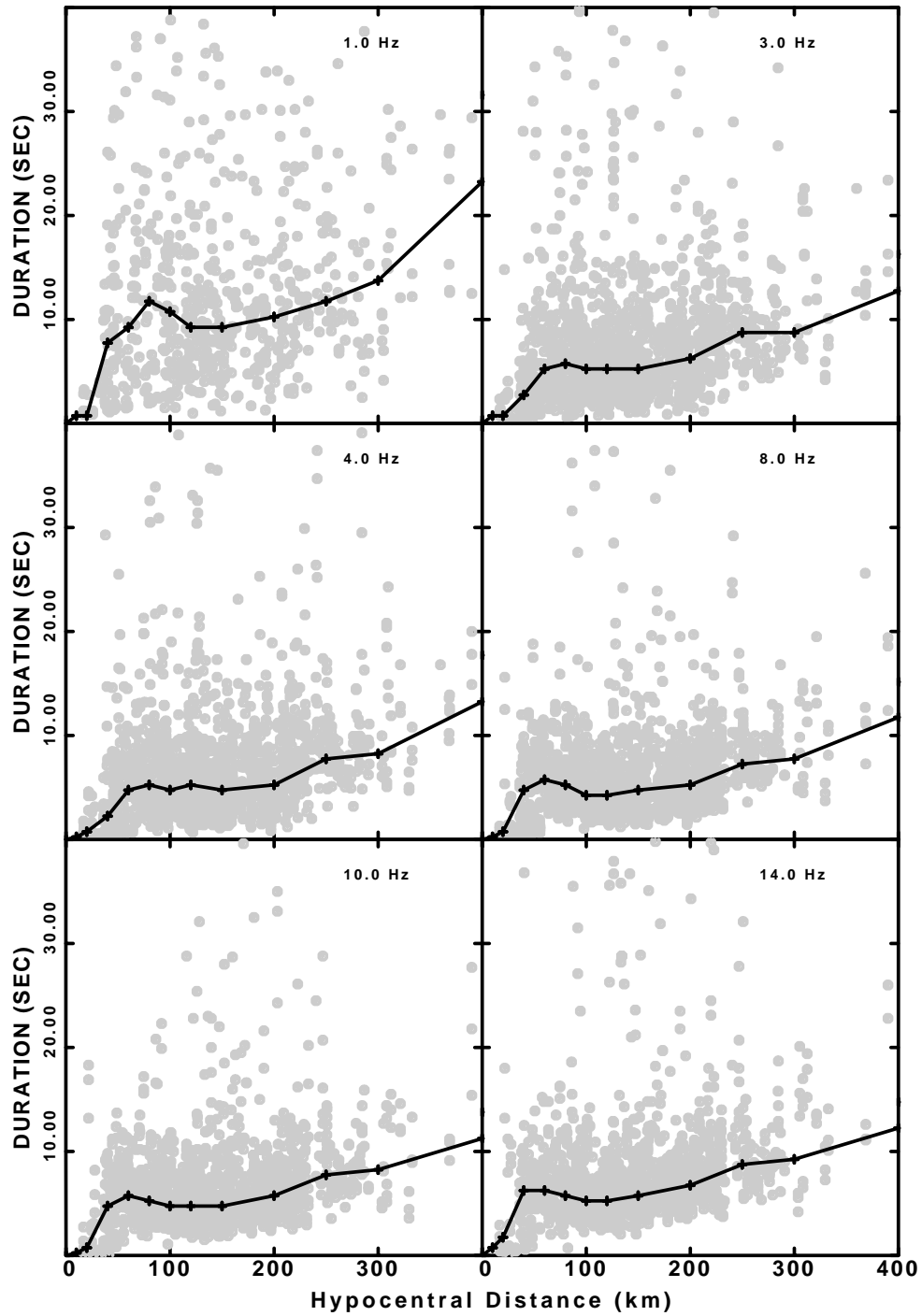


Figure 4.24: Durations at 1.0, 3.0, 4.0, 8.0, 10.0, and 14.0 Hz obtained for inland Korea. Rounded gray circles indicate individual duration estimates and thick solid lines is the duration measured using by a median value method.

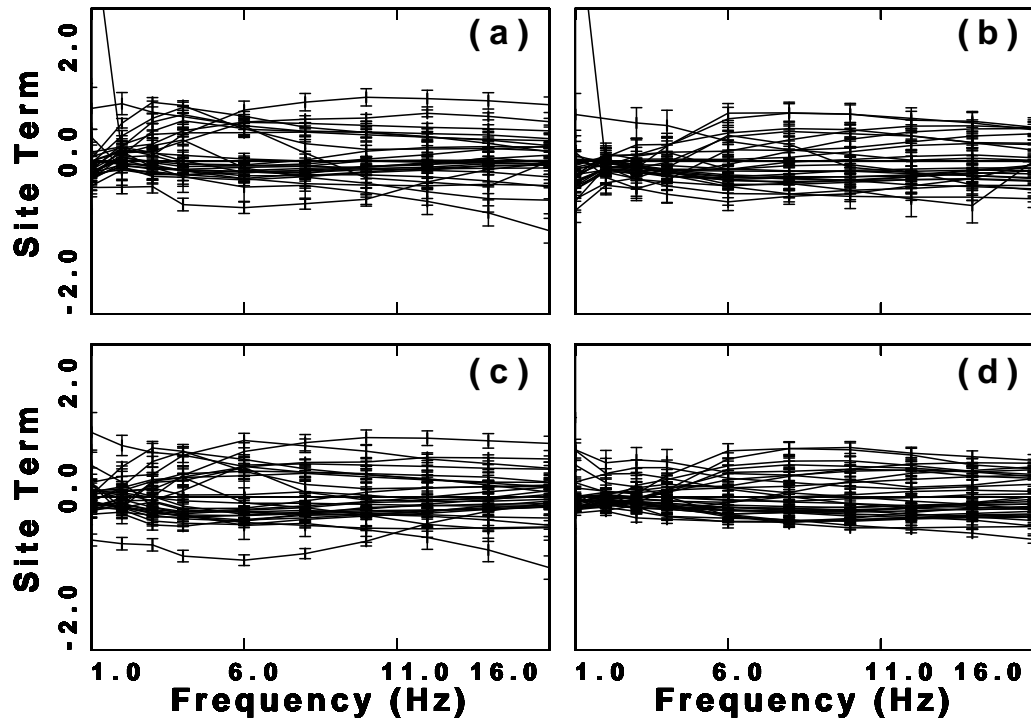


Figure 4.25: Inverted site amplifications of inland Korea in peak amplitudes. a and b are Z and H component site terms of ground motion while c and d are H and Z component site terms of ground motion.

<b>Measured durations</b>			
Distance (km)	All (sec)	Hor (sec)	Ver (sec)
0.000	0.00	0.00	0.00
10.000	0.60	0.60	1.50
20.000	0.90	0.90	1.80
40.000	4.50	4.40	4.30
60.000	6.20	5.90	5.80
80.000	6.10	5.60	5.20
100.000	5.70	5.10	5.80
120.000	5.50	5.50	5.60
150.000	5.60	5.90	5.50
200.000	6.50	6.80	6.70
250.000	8.60	8.70	9.00
300.000	9.20	9.10	9.50
400.000	12.20	12.40	12.00

Table 4.13: Measured durations from band-passed filtered for inland Korea.

Figure 4.26 show the excitations at 40 kilometer obtained from the regressions on the band passed filtered velocity spectra (black lines) and theoretical excitations computed (thick gray lines) in inland Korea.  $\kappa_{eff} = 0.005$  and  $\Delta\sigma = 300$  bars are used for parameterization. Thick gray lines each marks the  $M_W$  for 2.0, 2.5, 3.0, 3.5, and 4.0 from the lowest line. The source excitation levels match well with the observed spectra at overall  $M_W$  while higher frequencies for lower  $M_W$  requires higher  $\kappa_{eff}$ .

Figure 4.27 shows the deviations for Korean inland earthquakes with known moment. Even if the residuals are less, the events used have moment magnitudes typically less than 4, ranging from 3.25 to 4.06. Since the Brune's model successfully applied up to  $M_W = 4.0$ , I need earthquakes having greater  $M_W$  to test if the Brune's point source model can represent Korean events.

Figure 4.28 shows the modified residuals for Korea's oceanic events. The oceanic events having  $M_W$  ranges from 3.72 to 4.90. Because the shapes of residuals differ significantly from the residuals of Figure 4.27, I used the modified  $E(f)$  by changing stress drop to reduce the residuals of fit. I can't find the proper parameters to reduce the residuals of  $E(f)$ . Because the deviations are not fit well for the entire frequency ranges, the oceanic events may need different individual source model parameters or the Brune's model may not applicable to present the absolute source scaling at higher magnitude range in Korea and it's surrounding oceans.

The spectral parameters for Korea are

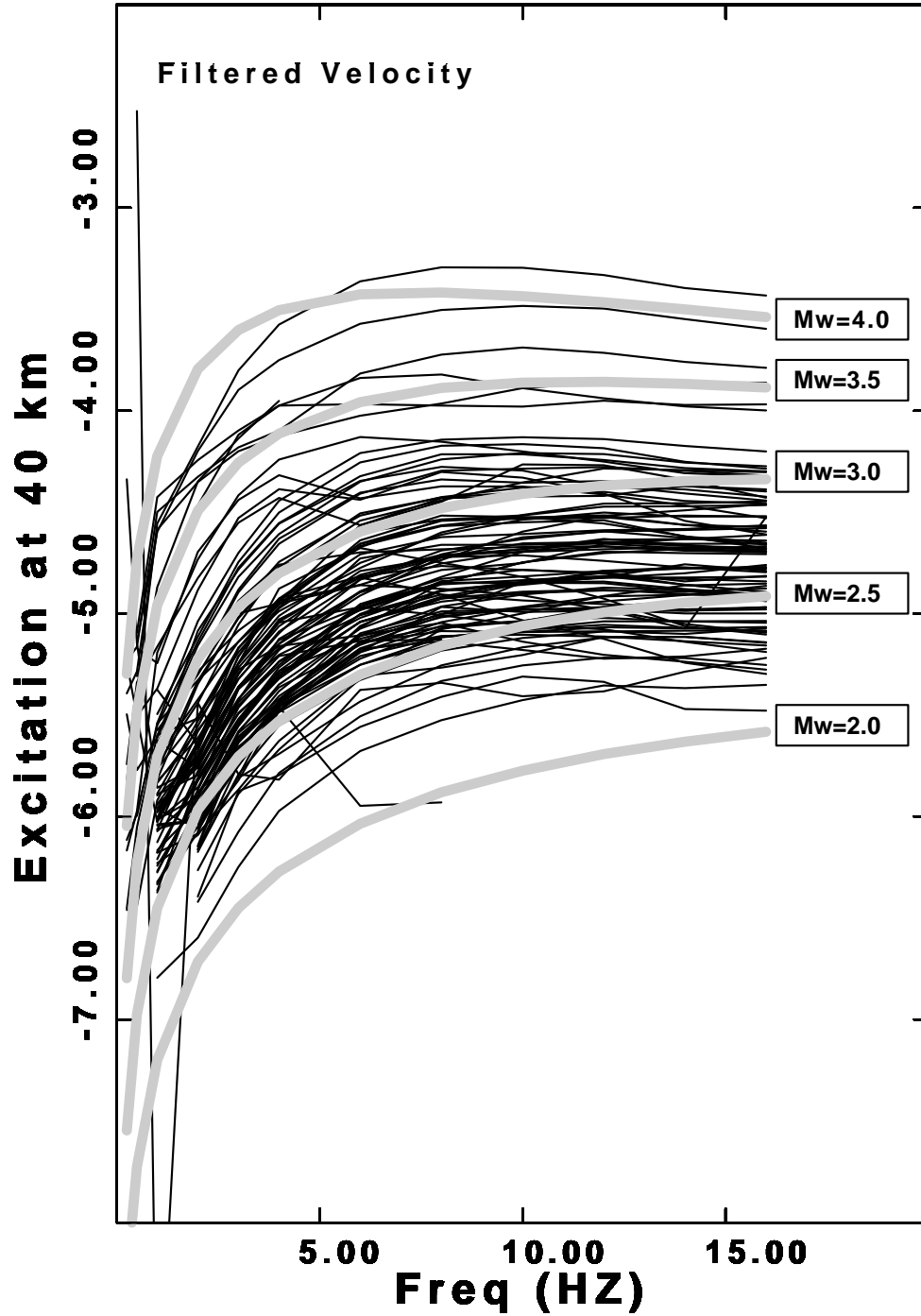


Figure 4.26: Inverted filtered ground velocity excitation terms for the earthquake events recorded by three-component velocity seismograms plotted on a linear frequency scale. Thin black lines are the inverted excitation and thick gray lines are model based prediction for inland Korea.

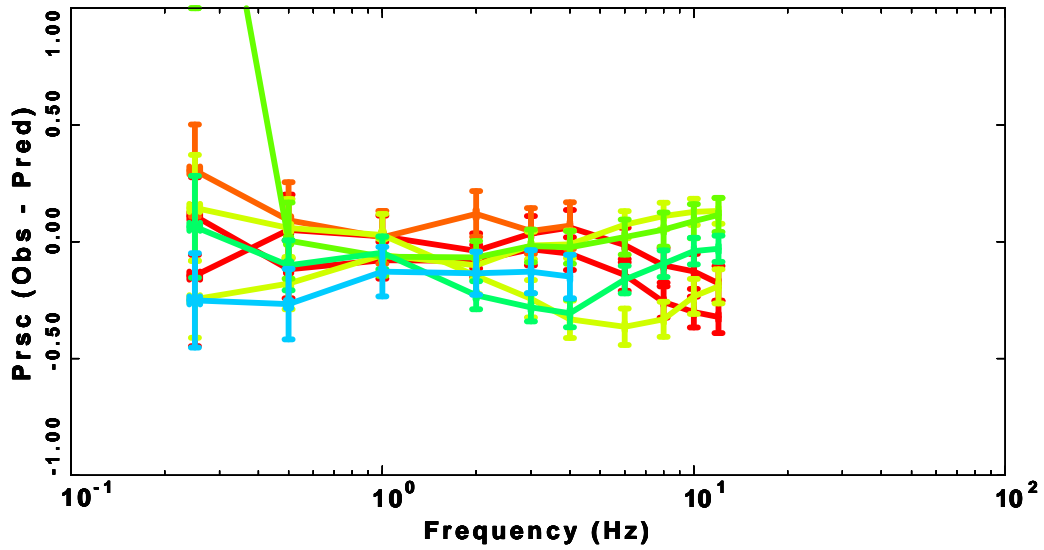


Figure 4.27: The residuals of the model fit to the band pass  $E(f)$  for the stochastic point source model as a function of frequency range of 1 - 16 Hz for inland events of Korea.

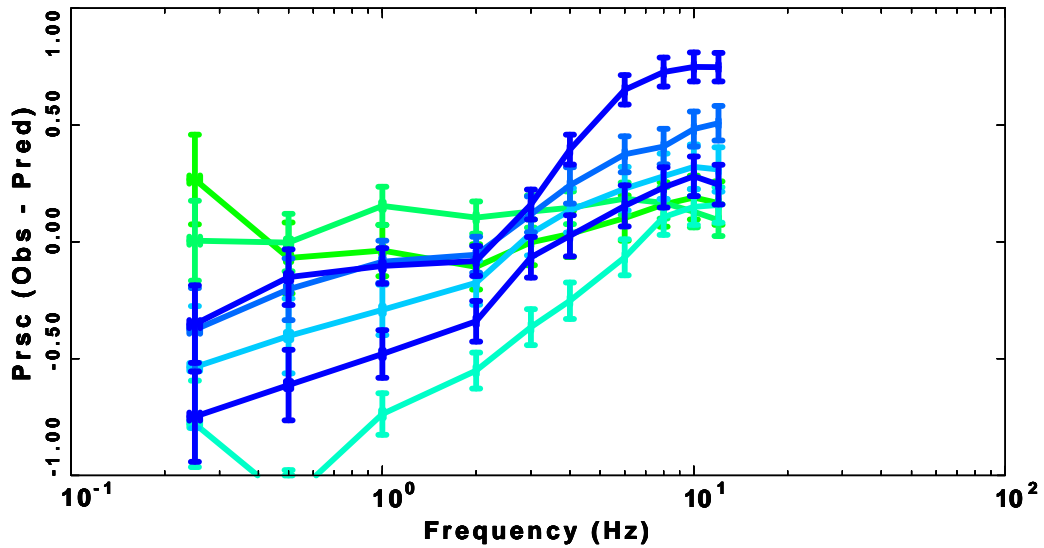


Figure 4.28: Modified residuals of the model fit to the band pass  $E(f)$  for the stochastic point source model as a function of frequency range of 1 - 16 Hz for oceanic events.

### Focal mechanism parameters for Korea

Lat <sup>†</sup> (N <sup>0</sup> )	Lon <sup>‡</sup> (E <sup>0</sup> )	Depth (km)	Strike ( <sup>0</sup> )	Dip ( <sup>0</sup> )	Rake ( <sup>0</sup> )	M <sub>W</sub>	Date yy/mm/dd
36.46	130.04	11.0	185	65	75	<b>4.06</b>	00/12/09
36.72	128.28	9.0	115	55	35	<b>3.44</b>	01/11/21
36.74	129.87	10.0	315	65	20	<b>3.79</b>	01/11/24
37.99	124.53	7.0	180	65	-120	<b>3.72</b>	02/03/17
35.85	129.76	11.0	125	75	10	<b>3.63</b>	02/07/08
35.57	122.18	19.0	120	70	25	<b>4.90</b>	02/07/23
38.86	127.26	6.0	295	90	-25	<b>3.69</b>	02/12/09
37.40	124.20	5.0	355	65	-170	<b>3.85</b>	03/01/09
34.96	124.39	14.0	30	80	-170	<b>4.83</b>	03/03/22
37.57	123.57	13.0	25	80	-155	<b>4.61</b>	03/03/30
36.95	126.51	9.0	25	75	-175	<b>3.80</b>	03/10/12
36.0	123.6	16.0	305	75	15	<b>3.98</b>	03/06/09
36.44	126.17	9.0	300	35	50	<b>3.30</b>	03/04/15
38.7	125.1	7.0	135	60	25	<b>3.25</b>	04/01/05
36.71	129.93	11.0	160	65	65	<b>5.10</b>	04/05/29

Table 4.14: Lat<sup>†</sup> and Lon<sup>‡</sup> denote latitude and longitude. Thick bold M<sub>W</sub> denotes inland events. Details of source parameters of Korea are at <http://www.eas.slu.edu/People/RBHerrmann/KOREA.2003>

$$\left\{ \begin{array}{l} \kappa_{eff} = 0.005sec \\ \Delta\sigma = 200bars(Korean\ peninsula) \\ \Delta\sigma = 300bars(Inland\ Korea) \\ \rho = 2.8\ g/cm^3 \\ \beta = 3.7\ km/sec \\ f_c = 4.9 \times 10^6 \beta (\Delta\sigma/M_0)^{1/3} Hz \\ M_0 = 10^{1.5M_W+16.05}. \end{array} \right.$$

Table 4.14 summarizes the results of focal mechanism that I used for Korea.

I used these results to check the absolute ground motions.

### 4.5.2 Proposed Korean model

The specific characteristics of Korean source study is that the high frequency content is higher at  $M_W$  greater than 4 than other studies, and that the

Brune's point source model may not be applicable to Korea. Then, one question that arises is "what is the appropriate source scaling model for Korea?" But this question is not completely answered here because Korea does not have strong motion earthquake data since the recent installation of the KMA and KIGAM digital networks. I used some events having moment magnitudes greater than 4 to define absolute source scaling models, but these events mostly originated from the west sea.

In this section, I started with the empirical two-corner model of Atkinson (1993a) for the source spectrum  $E(M_0, f)$  to fit the high frequency contents of Korea by slightly modifying their parameters:

$$E(M_0, f) = C (2\pi f)^2 M_0 \left[ \frac{1 - \epsilon}{1 + (f/f_A)^2} + \frac{\epsilon}{1 + (f/f_B)^2} \right], \quad (4.1)$$

where  $C = \frac{R_p F V}{4\pi \rho \beta^3 R}$ ,  $R = 1$  km,  $R_p = 0.55$ ,  $F = 2.0$ ,  $V = 0.71$ ,  $\rho = 2.8$  g/cm<sup>3</sup>, and  $\beta = 3.7$  km/sec.  $\epsilon$ ,  $f_A$ , and  $f_B$  are functions of seismic moment for  $4 \leq M \leq 7$  by

$$\log \epsilon = 2.52 - 0.580 M \quad (4.2)$$

$$\log f_A = 2.41 - 0.533 M \quad (4.3)$$

$$\log f_B = 1.80 - 0.265 M. \quad (4.4)$$

My model differs from theirs basically in equation 4.4.

Figure 4.29 compares the modified source spectrum model for seismic moment 4, 5, and 6 for Korea to that of Atkinson (1993a). Thin black lines shows the empirical two-corner model of Atkinson (1993a) and the thick short dashed lines indicate the proposed model from equations 4.1 - 4.4. To find the appropriate source model, I fixed the lower corner frequency ( $f_A$ ) and adjusted the  $\epsilon$  and upper corner frequency  $f_B$ . The major difference between two spectra for each seismic moment is the high frequency content.

For comparison, Figure 4.30 shows the stochastic single corner model of Boore (1983), (thick short dashed lines) the empirical two-corner model of Atkinson (1993a), (thin black lines) for seismic moments of 4, 5, 6, and 7. The Atkinson (1993a) model reduces at low to middle frequencies ( $\sim 0.1 - 2.0$  Hz) for earthquakes in Eastern North America. Overall, the proposed model for Korea (thick short dashed lines of Figure 4.29) has been changed at middle and high frequencies compared to single corner model of Boore (1983).

Figure 4.31 compares the predicted excitations (thick dark gray lines) of proposed model to the regressions on the band passed filtered velocity spectra (black lines). Thick dark gray lines each mark predictions for  $M_W$  of 2.0, 2.5, 3.0, 3.5, 4.0, 4.5, 5.0, and 5.5. I found that  $\kappa_{eff} = 0.01$  sec, and input parameters of equation 4.1 to 4.4 are required to fit the time domain excitation terms. If I compare Figure 4.31 with Figure 4.18, I can see that Figure 4.31 shows a better fit at higher frequencies. The linear frequency plot of Figure 4.32 demonstrates again that the proposed model shows the better fit to Korea data.

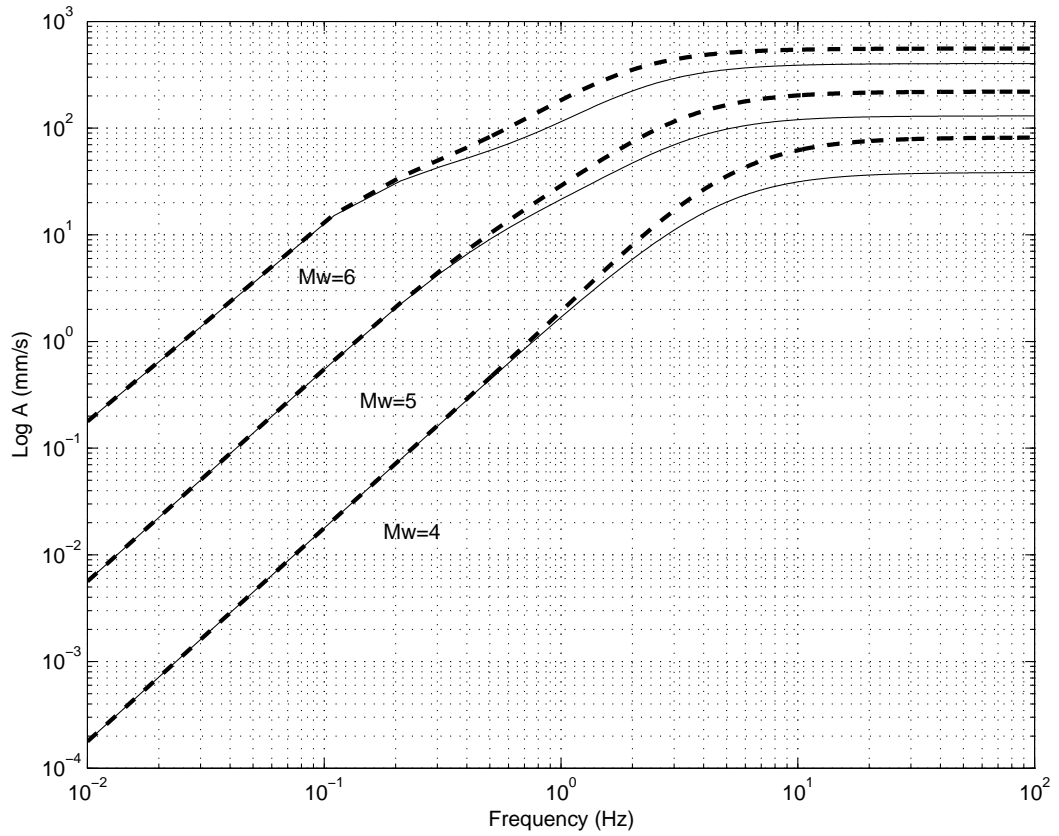


Figure 4.29: Proposed model for Korea source spectral amplitudes as a function of frequencies for seismic moments 4 - 6 (thick short dashed lines) compared with corresponding two-corner model of Atkinson (1993a) on a log scale (solid lines) .

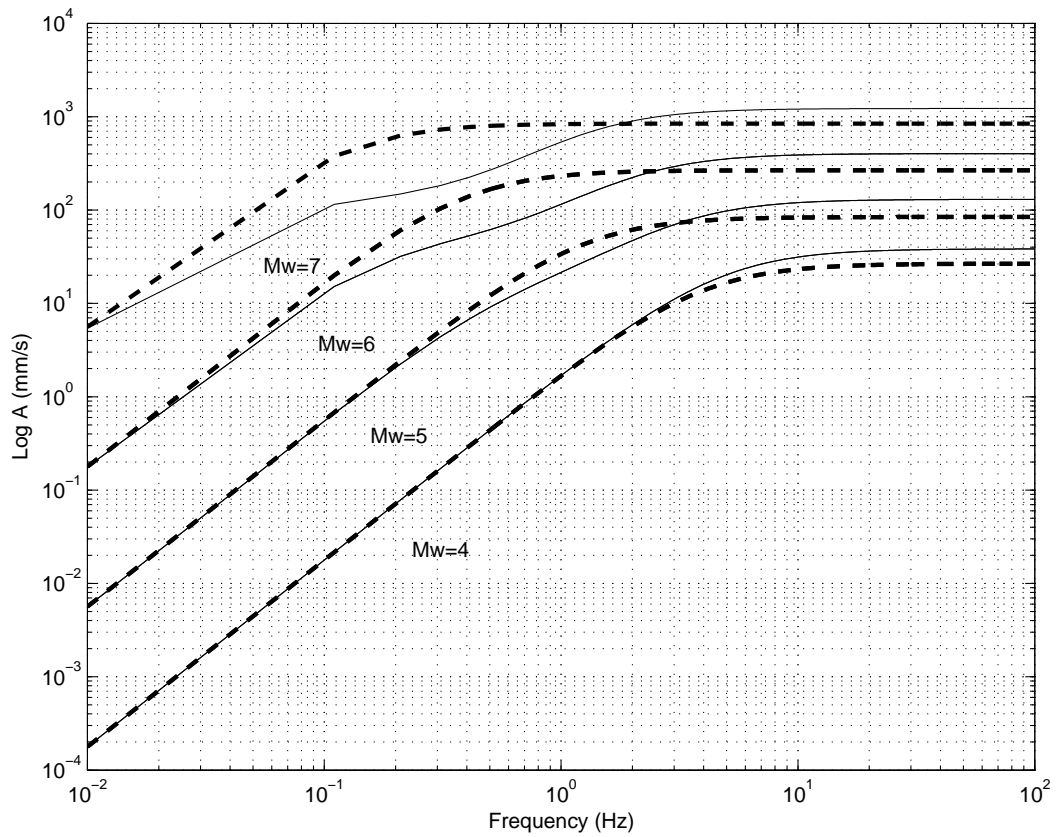


Figure 4.30: Comparison of the stochastic model of Boore (1983), thick short dashed lines, and empirical two-corner model of Atkinson (1993a) solid lines. Comparisons are made for seismic moments of 4, 5, 6, and 7.

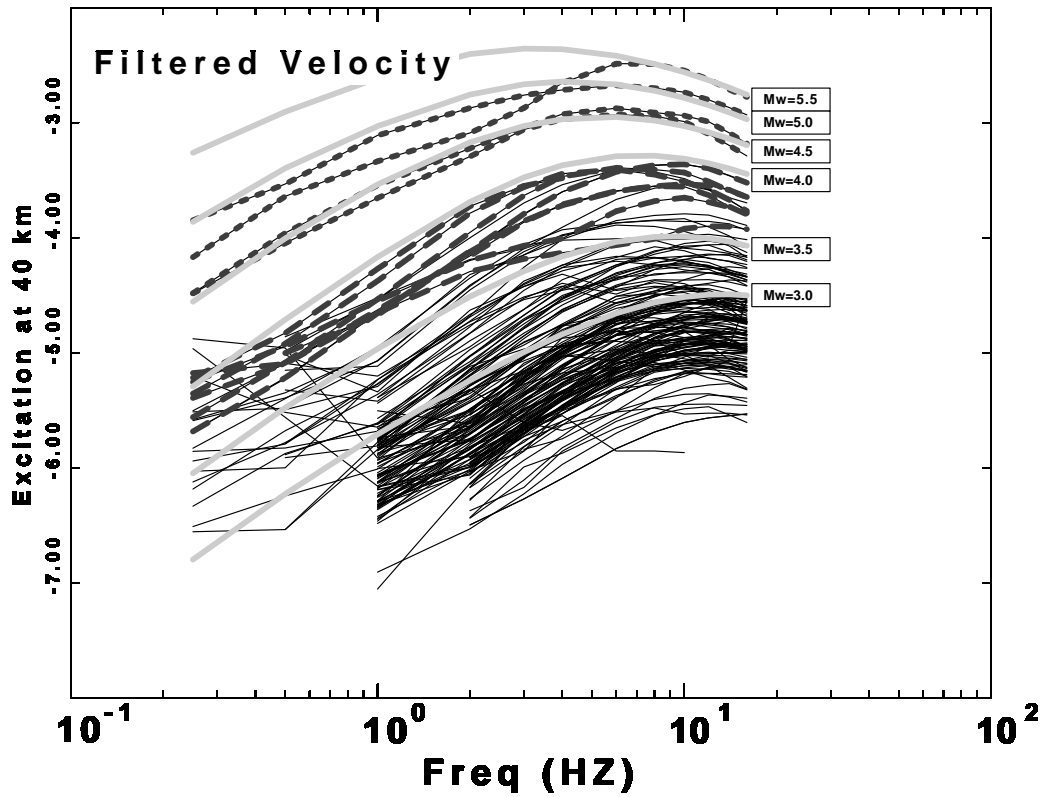


Figure 4.31: Inverted filtered ground velocity excitation terms for the earthquake events recorded by three-component velocity seismograms plotted on a log scale. The thin black lines linked by thick short and long dash lines are the excitations of known moment magnitudes.

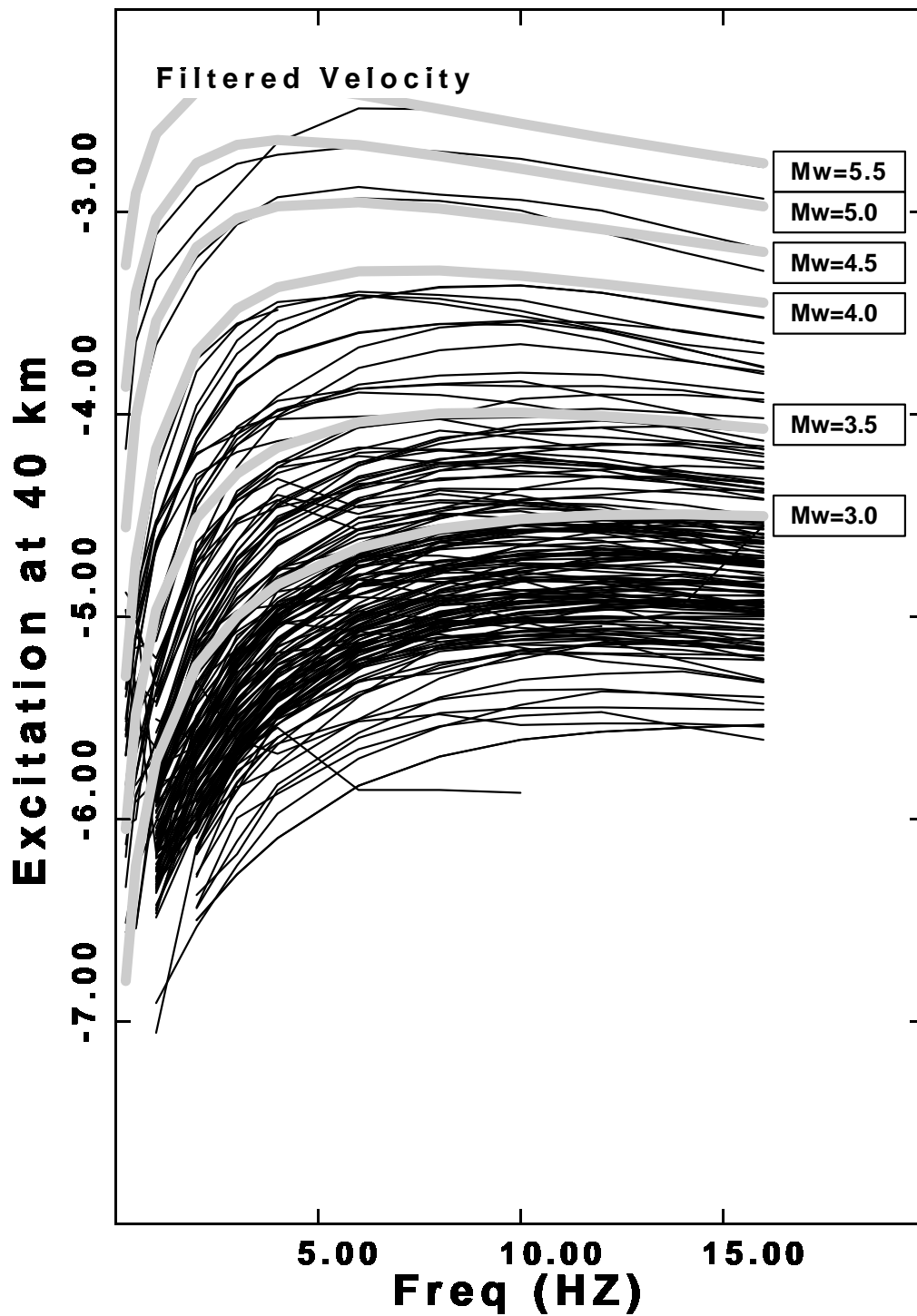


Figure 4.32: Excitation of peak filtered velocity for the combined vertical and horizontal data sets in linear scale of frequency range. Thin black lines are the inverted excitation and Thick gray curve is the prediction of suggested model.

### 4.5.3 F-test

Because the two corner model increases the number of free parameters and has a better fit at a certain frequency range, the residuals are decreased. But is the decrease statistically significant? Or is the decrease too large to be accounted for by random fluctuations of data? The  $F$  test quantifies the residuals between the observed data ( $Obs_i$ ) and predicted value ( $Pre_i$ ) and shows if the proposed model is really different from existing model. Suppose that the variance of the data  $Obs_i$  from the prediction error is estimated as

$$\sigma_d^2 = \sum_{i=1}^n \frac{(Obs_i - Pre_i)^2}{(N - M)} \quad (4.5)$$

where  $N$  is the number of observations and  $M$  is the number of model parameters. The ratio of the  $\sigma_{d_i}^2$  for the two models is given by

$$F = \frac{\sigma_{d1}^2}{\sigma_{d2}^2} \quad (4.6)$$

where  $\sigma_{d1}^2$  is the variance of the existing model and  $\sigma_{d2}^2$  is the variance of new model (Menke, 1989).

Table 4.15 shows the results of  $F$  test for Korea. An  $F$  ratio of 2.67 denotes the 90 % of probability that the estimates are derived from data sets with different true variances. An  $F$  ratio of 3.58 denotes the 95 % of the probability. In overall, 4 events ( $M_W = 3.85, 4.61, 4.89$ . and 5.10) indicate that new model reduces the fit significantly, while the events of  $M_W = 3.98$  and 4.90 do not show that the new one is better than the former one. It may be that the selected

Date	M <sub>w</sub>	$\sigma_{d1}^2$	$\sigma_{d2}^2$	F ratio	value
04/05/29	5.10	0.056025110	0.024429373	2.2934	75 - 90
02/07/23	4.90	0.159332380	0.218430758	0.7294	25 - 50
03/03/22	4.89	0.182408899	0.107079615	1.7035	75 - 90
03/03/30	4.61	0.040287651	0.009053476	4.4500	95 - 97.5
03/06/09	3.98	0.039261751	0.067431723	0.5822	25 - 50
03/01/09	3.85	0.534698188	0.096946766	5.5154	97.5 - 99

Table 4.15:  $F$  test results obtained from the variances (second and third column) of Korean events with known M<sub>w</sub>. Value at the sixth column denotes the range of percentiles of  $F$  distributions.

events are mostly from the western sea and have different source characteristics compared to that of inland events. Future study should contain events from the peninsula and the parameters of the two corner model should be validated again. Table 4.16 shows the results of  $F$  test from the events of southeastern Canada. Because the two corner model was initially developed for southeastern Canada by Atkinson (1993a), most of the  $F$  ratios greater than or equal to  $F$  occur only 10 % of the time. Especially, the  $F$  ratio of Au Sable Forks earthquake (M<sub>w</sub> = 5.0) indicates that the two corner model is appropriate in this region.

## 4.6 Summary

I determined the attenuation functional relationships for  $S$  waves at regional distance for the peak ground motion in Korean peninsula. Korea is characterized by an attenuation parameters of  $Q(f) = 330 f^{0.40}$  and combined with geometrical spreading for vertical and horizontal component data set:  $r^{-1.1}$  for

Date	M <sub>W</sub>	$\sigma_{d1}^2$	$\sigma_{d2}^2$	F ratio	value
02/04/20	5.0	0.087990165	0.004461680	19.7213	99.99
99/03/16	4.5	0.074976064	0.037601136	1.9940	75 - 90
97/11/06	4.5	0.074976064	0.037601136	1.9940	75 - 90
97/10/28	4.30	0.815264583	0.664384643	1.2271	50 - 75
01/01/26	4.03	0.712259293	0.597677708	1.1917	50 - 75

Table 4.16:  $F$  test results obtained from the variances of Southeastern Canada events with known  $M_W$ . Value at the sixth column denotes the range of percentiles of  $F$  distributions.

$r < 40$  km,  $r^{-1.2}$  for  $40 < r < 60$  km,  $r^{0.0}$  for  $60 < r < 250$  km and  $r^{-0.5}$  for  $r > 250$  km. The horizontal and vertical  $D(r, f)$  of Korea is similar with that of combined data set of vertical and horizontal component.

In this chapter, I performed another wave propagation study by separating the events from the surrounding seas. The purpose is to check if the wave propagation is biased by events in the eastern, western, and southern sea. The inland regressions yield almost identical results compared to the complete data set except for the  $r^{-1.3}$  at short ( $40 < r < 60$  km) distance ranges of the three-component data sets.

The Korean wave propagation study results indicate a more moderate near source amplitude decay at very short distance ranges (less than 40 km) than seen in southeastern Canada even if the distance range from 40 to 60 km indicates rapid fall off of  $r^{-1.3}$ . The attenuation term of  $Q(f) = 330 f^{0.40}$  is found for both Korean peninsula and inland Korea. The oceanic events do not introduce any bias in determining the wave propagation functional. Previous attenuation

study results of Chung and Sato (2001),  $Q_s = 250 f^{0.70}$ , and Kim et al. (2002),  $Q(f) = 383.3 f^{0.406}$ , are roughly similar but not directly comparable with my study results because of different study regions, different methods used, and a limited data set.

The spectral parameters of  $\kappa_{eff} = 0.005$  sec, and  $\Delta\sigma = 200$  bars are selected for Korean peninsula.  $\kappa_{eff} = 0.005$  sec, and  $\Delta\sigma = 300$  bars are used for inland parameterization. The  $\kappa_{eff}$  and  $\Delta\sigma$  applied are very similar to those of southeastern Canada for smaller events. The applied stochastic point source model of Brune (1970) showed the lack of fit at moderate size magnitude events similar to the result of southeastern Canada's excitation scaling relation. Because the fixed  $\Delta\sigma$  can not describe the complicate range of excitations, I modified the spectral model parameter of two-corner model of Atkinson (1993a) to fit the Korean observations. The simple modification of higher corner frequency,  $f_B$ , yields better fit at the desired frequency limits for both data-sets of Korea. But, systematic research is need to improve the absolute source scaling model for Korea.

This study of high frequency wave propagation of Korea has its importance in terms of originality by using modern digital seismic network, by suggesting a new source spectral scaling model, and for providing the foundation for developing seismic hazard maps of Korea. Because of the low seismic rate, especially for larger earthquakes, this study should be replaced as more data are acquired.

# Chapter 5

## Conclusions

### 5.1 Results

I studied regional ground motion scaling for southeastern Canada and Korea. I analyzed a data set consisting of 4646 three component seismograms from CNSN seismic network and 394 regional earthquakes in the range of 10 - 1000 km hypocentral distance for southeastern Canada and 2701 three component waveforms from KMA and KIGAM network in the range of 10 - 600 km hypocentral distance for Korea to measure and quantify the regional attenuation ground motion. In my study, I used a large number of velocity seismograms from the southeastern Canada and Korea and then separated the data sets into horizontal, vertical, and all component and performed the regressions in separate ways. The total numbers of horizontal and vertical component digital seismograms for southeastern Canada are 2164 and 2574 while those of Korea are 1694 and 917. The purpose of this step was to check if the wave propagations of three different components are different in their behaviors with distance ranges.

The distance scaling of Fourier velocity spectra and band-pass filtered time domain peak motion were obtained for frequency ranges between 1.0 and 16.0 Hz for southeastern Canada and between 0.25 - 16 Hz for Korea. The high frequency wave propagation and excitation spectra in this study has its advan-

tage because of the separate regressions over Fourier velocity spectra, peak filtered ground velocities, the determination of a distant dependent duration consistent with these two data sets, and the *RVT* prediction method.

During the process of collecting data sets and regression analysis, I realized that stable regression results require at least 2000 seismic recordings in the regional data sets. Figures 3.13 and 4.12 are the good examples of the stable inversion processes. In my study, southeastern Canada has greater hypocentral distance ranges and larger moment magnitude events compared to the Korean data sets. The two regions yield similar wave propagation scaling relations at short distances and require a two-corner model to describe the larger earthquakes.

In this study, I performed three regressions over Fourier velocity spectra and peak filtered ground velocities for southeastern Canada and Korea each. The crustal propagation terms for southeastern Canada and Korea of peak filtered ground velocities are described at Table 5.1.

In Korea, the inland regressions intended to identify the crustal propagation of inland crust nearly identical to the regression results of the complete data set except for the  $r^{-1.3}$  at short ( $40 < r < 60 \text{ km}$ ) distance ranges.

The spectral parameters of  $\kappa_{eff} = 0.01 \text{ sec}$ , and  $\Delta\sigma = 200 \text{ bars}$  are selected to predict the theoretical excitation spectra of southeastern Canada for smaller earthquakes. The stochastic method technique used for this study indicates that one stress drop model does not fit well for events with moment magnitude greater than 4 and the lack of predicting some moderate events in my study

	All component	<b>Southeastern Canada</b> Horizontal component	Vertical component
$Q(f)$		$Q_0 = 650f^{0.33}$	
$g(r)$	$r^{-1.3} \quad r \leq 40 \text{ km}$ $r^{-1.0} \quad 40 \leq r \leq 60 \text{ km}$ $r^{-0.0} \quad 60 \leq r \leq 80 \text{ km}$ $r^{-0.2} \quad 80 \leq r \leq 400 \text{ km}$ $r^{-0.5} \quad r \geq 400 \text{ km}$	$r^{-1.3} \quad r \leq 40 \text{ km}$ $r^{-1.2} \quad 40 \leq r \leq 60 \text{ km}$ $r^{-0.0} \quad 60 \leq r \leq 80 \text{ km}$ $r^{-0.2} \quad 80 \leq r \leq 400 \text{ km}$ $r^{-0.5} \quad r \geq 400 \text{ km}$	$r^{-1.0} \quad r \leq 40 \text{ km}$ $r^{-1.2} \quad 40 \leq r \leq 60 \text{ km}$ $r^{-0.0} \quad 60 \leq r \leq 80 \text{ km}$ $r^{-0.2} \quad 80 \leq r \leq 400 \text{ km}$ $r^{-0.5} \quad r \geq 400 \text{ km}$
	All component	<b>Korea</b> Horizontal component	Vertical component
$Q(f)$		$Q_0 = 330f^{0.40}$	
$g(r)$	$r^{-1.1} \quad r \leq 40 \text{ km}$ $r^{-1.2} \quad 40 \leq r \leq 60 \text{ km}$ $r^{-0.0} \quad 60 \leq r \leq 250 \text{ km}$ $r^{-0.5} \quad r \geq 250 \text{ km}$	$r^{-1.0} \quad r \leq 40 \text{ km}$ $r^{-1.3} \quad 40 \leq r \leq 60 \text{ km}$ $r^{-0.1} \quad 60 \leq r \leq 250 \text{ km}$ $r^{-0.5} \quad r \geq 250 \text{ km}$	$r^{-1.0} \quad r \leq 40 \text{ km}$ $r^{-1.3} \quad 40 \leq r \leq 60 \text{ km}$ $r^{-0.0} \quad 60 \leq r \leq 250 \text{ km}$ $r^{-0.5} \quad r \geq 250 \text{ km}$

Table 5.1: Propagation parameters of all, horizontal and vertical component for southeastern Canada and Korea.

and two-corner model of Atkinson and Boore (1995) shows better fit at higher moment magnitude events.

The spectral parameters of  $\kappa_{eff} = 0.005$  sec, and  $\Delta\sigma = 200$  bars are used for Korea.  $\kappa_{eff} = 0.005$  sec, and  $\Delta\sigma = 300$  bars are used for inland parameterization. The stochastic point source model of Brune (1970) shows the lack of fit at moderate size magnitude events. I modified the spectral model parameter of two- corner model of Atkinson (1993a) to fit the Korean source scaling model. The simple modification of source parameters yields better fit at the high frequency ranges.

## 5.2 Final remarks

In defining the ground motion model parameters, I realized that trade offs exist between the source model and the model of propagation parameters. The propagation parameters ( $Q_0$  and  $\eta$ ) trade off with geometrical spreading function due to the limited distance range. The source excitation model also show a strong sensitivity in defining  $E(f)$  from the  $g(r)$ ,  $\kappa_{eff}$ , and  $\Delta\sigma$ . Because  $g(r)$  used for the source excitation model are already predefined from propagation parameters, the source parameters of  $\kappa_{eff}$ , and  $\Delta\sigma$  will be affected if the predefined  $g(r)$  is not absolute. This concern arise since I never have data very close to the source.

My forward propagation model parameters are based upon a trial and error fit to the attenuation characteristics of the average shear wave which indicates that distance dependent scaling is only comparable with results obtained from

same analysis in other regions. But, I have to consider the trade off between  $Q(f)$  and  $g(r)$  due to the different distance range and precise calibration of seismic network to define absolute ground motion scaling models and compare with other regions.

A direct comparison of  $D(r, f)$  between southeastern Canada and Korea has not been performed here due to the difference in distance scaling, frequency content and duration results from the parameterization. Southeastern Canada events normally have higher durations compared to Korean events and a more rapid  $g(r)$  at short distance ranges. Propagation parameters are also not similar each others. However, by comparing the observed  $D(r, f)$  functionals, I can recognize that the crustal propagation in Southeastern Canada is more rapid in near hypocentral distance scaling but similar at mid- to larger distance ranges compared to the  $D(r, f)$  of Korea.

The study regions are characterized by an old history of crustal deformation, represented by a less severe crustal attenuation. The  $Q(f) = 650 f^{0.33}$  found for southeastern Canada is similar to that of Atkinson and Boore (1995) but different from the  $Q(f) = 893 f^{0.32}$  of Atkinson (2004). The results of Atkinson (2004) are based on more data compared to that of Atkinson and Boore (1995) and indicates a more rapid near source amplitude decay and higher  $Q$ . The  $Q(f) = 330 f^{0.40}$  of Korea also indicate more attenuation than southeastern Canada's. Shi et al. (1996) mentioned that the difference in attenuation results come from specific regions analyzed, different frequency ranges in their measurement, and different method used to determine  $Q$ .

The strike-slip mechanism of Herrmann and Malagnini (2004) shows that the vertical motion at short distance is lower than that of horizontal or three component motions while dip-slip or mixed mechanisms show that the opposite motions. Based upon the focal mechanism results, both southeastern Canada and Korea are dominated by strike slip motion, and thrust motion respectively. The  $D(r, f)$  of short distance range may be composed of all hypocentral distance and magnitude range, but the focal mechanism study is only available from moderate earthquake size, e.g., moment magnitude greater than 3.0.

The primary product of this study is that I have carefully constrained ground motion scaling models for two different regions. I also constrained the error inherent in ground motion predictions. Thus, this study will lead to a better understanding of ground motions, a fundamental component in defining regional seismic hazard.

## Bibliography

- Abrahamson, N., P. Somerville, and A. Cornell (1990). Uncertainty in numerical strong ground motion predictions. *Proceedings of the Fourth National Conference on Earthquake Engineering*, Palm Springs, California, Vol. 1, 407-416.
- Adams, J. and P. Basham (1989). The seismicity and seismotectonics of Canada east of the Cordillera, *Geosci. Can.* 14, 3-16.
- Aki, K. (1966). Generation and propagation of G waves from the Niigata earthquake of June 16, 1964. Part 2. Estimation of earthquake moment, released energy, and stress-strain drop from the G wave spectrum, *Bull. Earthq. Res. Inst.*, 44 73-88.
- Aki, K. (1967). Scaling law of seismic spectrum, *J. Geophys. Res.* 72, 1217-1231.
- Aki, K. (1969). Analysis of the seismic coda of local earthquakes as scattered waves, *J. Geophys. Res.* 74, 615-631.
- Aki, K. (1980). Attenuation of shear waves in the lithosphere for frequencies from 0.05 to 25 Hz, *Phys. Earth Planet. Inter.* 21, 50-60.
- Aki, K. and B. Chouet (1975). Origin of coda waves: Source, attenuation, and scattering effects, *J. Geophys. Res.* 80, 3322-3342.
- Anderson, J. G. and S. E. Hough (1984). A model for the shape of the Fourier amplitude spectrum of acceleration at high frequencies, *Bull. Seism. Soc. Am.* 74, 1969-1993.
- Anderson, J. G. and Y. Lei (1994). Nonparametric description of peak acceleration as a function of magnitude, distance, and site in Guerrero, Mexico, *Bull. Seism. Soc. Am.* 74, 1003-1017.
- Atkinson, G. (1984). Attenuation of strong ground motion in Canada from a random vibrations approach, *Bull. Seism. Soc. Am.* 74, 2629-2653.
- Atkinson, G. (1989). Attenuation of the  $L_g$  phase and site response for the Eastern Canada Telemetered Network, *Seism. Res. Lett.* 60, no. 2, 59-69.
- Atkinson, G. (1990). A comparison of eastern North America ground motion observations with theoretical predictions, *Seism. Res. Lett.* 61, 171-180.
- Atkinson, G. (1993a) Earthquake source spectra for in eastern North America, *Bull. Seism. Soc. Am.* 83, 1778-1798.
- Atkinson, G. (1993b). Notes on ground motion parameters for eastern North America: duration and H/V ratio, *Bull. Seism. Soc. Am.* 83, 587-596.

- Atkinson, G. (2004). Empirical attenuation of ground motion spectral amplitudes in southeastern Canada and Northeastern United States, *Bull. Seism. Soc. Am.* 94, 1079-1095.
- Atkinson, G. and D. Boore (1990). Recent trends in ground motion and spectral response relations for North America, *Earthquake Spectra*, 6, 15-36.
- Atkinson, G. and D. Boore (1995). Ground-motion relations for eastern North America, *Bull. Seism. Soc. Am.* 85, 17-30.
- Atkinson, G. and D. Boore (1997). Some comparisons of recent ground motion relations, *Seism. Res. Lett.* 68, 24-40.
- Atkinson, G. and D. Boore (1998). Evaluation of Models for earthquake source spectra in eastern North America, *Bull. Seism. Soc. Am.* 88, 917-934.
- Atkinson, G. and E. Sonley (2003). Ground motions from the 2002 Au Sable Forks, New York M 5.0 earthquake, *Seismological Research Letters* 74, 339-349.
- Atkinson, G. and I. A. Beresnev (1997). Don't call it stress drop, *Seism. Res. Lett.* 68, 3-4.
- Atkinson, G. and M. Mereu (1992). The shape of ground motion attenuation curves in southeastern Canada, *Bull. Seism. Soc. Am.* 82, 2014-2031.
- Atkinson, G. and P. Somerville (1994). Calibration of time history simulation methods, *Bull. Seism. Soc. Am.* 84, 400-414.
- Atkinson, G. and T. Hanks (1995). A high-frequency magnitude scale, *Bull. Seism. Soc. Am.* 85, 825-833.
- Atkinson, G. and W. Silva (1997). Empirical source spectra for California earthquakes, *Bull. Seism. Soc. Am.* 87, 97-113.
- Automated Data Request Manager (Auto DRM) home page (2004). [http://www.seismo.nrcan.gc.ca/nwfa/autodrm/index\\_e.php](http://www.seismo.nrcan.gc.ca/nwfa/autodrm/index_e.php) (last accessed August 2004).
- Beresnev, I. A. and G. Atkinson (1997). Modeling finite-fault radiation from the  $\omega^n$  spectrum, *Bull. Seism. Soc. Am.* 87, 67-84.
- Beresnev, I. A. and G. M. Atkinson (1998). FINSIM-a FORTRAN program for simulating stochastic acceleration time histories from finite faults, *Seism. Res. Lett.* 69, 27-32.
- Beresnev, I. A. and G. M. Atkinson (1999). Generic finite-fault model for ground motion prediction in Eastern North America, *Bull. Seism. Soc. Am.* 89, 608-625.

- Beresnev, I. A. and G. Atkinson (2002). Source parameters of earthquakes in eastern and western North America based on finite-fault modeling, *Bull. Seism. Soc. Am.* **92**, 695-710.
- Boatwright, J. (1988). The seismic radiation from composite models of faulting, *Bull. Seism. Soc. Am.* **78**, 489-508.
- Boatwright, J. and G. Choy (1992). Acceleration source spectra anticipated for large earthquakes in eastern North America, *Bull. Seism. Soc. Am.* **82**, 660-682.
- Boore, D. M. (1983). Stochastic simulation of high-frequency ground motion based on seismological models of the radiated spectra, *Bull. Seism. Soc. Am.* **73**, 1865-1894.
- Boore, D. M. (1996). SMISM-Fortran programs for simulating ground motions from earthquakes; version 1.0, *U. S. Geol. Surv. Open-File Rept.* 96-80-A, 96-80-B, 69 pp.
- Boore, D. M. (2003). Prediction of ground motion using the stochastic method, *Aki symposium, PAGEOPH.* **160**, 635-676.
- Boore, D. M. and G. M. Atkinson (1987). Stochastic prediction of ground motion and spectral response parameters at hard-rock sites in Eastern North America, *Bull. Seism. Soc. Am.* **77**, 440-467.
- Boore, D. M. and G. M. Atkinson (1992). Source spectra for the 1988 Saguenay, Quebec earthquakes, *Bull. Seism. Soc. Am.* **82**, 683-719.
- Boore, D. M. and J. Boatwright (1984). Average body-wave radiation coefficients, *Bull. Seism. Soc. Am.* **74**, 1615-1621.
- Boore, D. M. and W. B. Joyner (1984). A note on the use of random vibration theory to predict peak amplitudes of Transient signals, *Bull. Seism. Soc. Am.* **74**, 2035-2039.
- Boore, D. M., W. B. Joyner, and L. Wennerberg (1992). Fitting the stochastic  $\omega^{-2}$  source model to observed response spectra in western north America: trade-offs between  $\Delta\sigma$  and  $\kappa$ , *Bull. Seism. Soc. Am.* **82**, 1956-1963.
- Bowman, J. and B. Kennett (1991). Propagation of  $Lg$  waves in the North Australian craton: influence of crustal velocity gradients, *Bull. Seism. Soc. Am.* **81**, 592-610.
- Burger, R., P. Somerville, J. Barker, R. Herrmann, and D. Helmberger (1987). The effect of crustal structures on strong ground motion attenuation relations in eastern North America, *Bull. Seism. Soc. Am.* **77**, 420 - 439.
- Brune, J. (1970). Tectonic stress and the spectra of seismic shear waves from earthquakes, *J. Geophys. Res.* **75**, 4997-5009.

- Brune, J. (1971). Correction, *J. Geophys. Res.* 76, 5002.
- Campbell, K. (2003). Prediction of strong-ground motion using the hybrid-empirical method and its use in the development of ground-motion (attenuation) relations in eastern North America. *Bull. Seism. Soc. Am.* 93, 1012-1033.
- Cartwright, D. E. and M. S. Longuet-Higgins (1956). The statistical distribution of the maxima of a random function, *Proc. Roy. Soc. London, Ser. A* 237, 212-223.
- Chang, K. H. (1975). Cretaceous stratigraphy of southeast Korea, *J. Geol. Soc. Korea* 11, 1-23.
- Cho M., S. T. Kwon, J. H. Ree, and E. Nakamura (1995). High-pressure amphibolite of the Imjingang belt in the Yeoncheon-Cheongok area, *J. Petrol. Soc. Korea* 4, 1-19.
- Choi, H. I. (1985). Sedimentology and its implications for stratigraphic classification of the Cretaceous Gyeongsang Basin, *J. Geol. Soc. Korea* 21, 26-37.
- Chough, S. K., I. G. Hwang, and M. Y. Choe (1990). The Miocene Doumsan fan-delta, southeast Korea: a composite fan-delta system in back-arc margin, *J. Sediment. Petrol.*, 60, 445-455.
- Chung, T. W. and H. Sato (2001). Attenuation of high-frequency P and S waves in the crust of the southeastern Korea, *Bull. Seism. Soc. Am.* 91, 1867-1874.
- Chung, T. W. and K. Lee (2003). A study of high-frequency  $Q_{Lg}^{-1}$  in the crust of south Korea, *Bull. Seism. Soc. Am.* 93, 1401-1406.
- Dobrin, M. B. (1960). *Introduction to Geophysical Prospecting*, and ed., McGraw-Hill, New York, 446 pp.9
- Du, W. X., W. Y. Kim, and L. R. Sykes, (2003). Earthquake source parameters and state of stress for northeastern United states and southeastern Canada from analysis of regional seismograms, *Bull. Seism. Soc. Am.*, 93, 1633- 1648.
- EPRI (1993). *Guidelines for Determining Design Basis Ground Motions. Early Site Permit Demonstration Program*, Vol. 1, RP3302, Electric Power Research Institute, Palo Alto, California.
- Fehler, M. and H. Sato (2003). Coda, *PAGEOPH.* 160, 541-554.
- Fletcher, J., J. Boatwright, L. Haar, T. Hanks, and A. McGarr (1984). Source parameters for aftershocks of the Oroville, California, earthquake, *textit-Bull. Seism. Soc. Am.*, 74, 1101-1123.

- Frankel, A., C. Mueller, T. Barnhard, D. Perkins, E. Leyendecker, N. Dickman, S. Hanson, and M. Hopper (1996). National seismic hazard maps, June 1996, *U. S. Geol. Surv. Open-File Rept.* 96-532.
- Frankel, A., C. Mueller, T. Barnhard, D. Perkins, E. Leyendecker, N. Dickman, S. Hanson, and M. Hopper (1999). National seismic hazard mapping project. <http://geohazards.cr.usgs.gov>.
- Frankel, A., McGarr, A., Bicknell, J., Mori, J., Seeber, L., and Cranswick, E. (1990). Attenuation of high-frequency shear waves in the crust: Measurements from New York state, South Africa, and Southern California, *J. Geophys. Res.* 95, 17441-17457.
- Haddon, R. (1992). Waveform modeling of the strong-motion data for the Saguenay earthquake of 25 November 1988. *Bull. Seism. Soc. Am.* 82, 720-754.
- Haddon, R. (1996). Earthquake source spectra in eastern North America, *Bull. Seism. Soc. Am.* 86, 1300-1313.
- Hanks, T. C. (1982).  $f_{max}$ , *Bull. Seism. Soc. Am.* 72, 1867-1879.
- Hanks, T. and R. McGuire (1981). The character of high-frequency strong ground motion, *Bull. Seism. Soc. Am.* 71, 2071-2095.
- Harmsen, S. (1997). Estimating the diminution of shear-wave amplitude with distance: application to the Los Angeles, California, urban area, *Bull. Seism. Soc. Am.* 87, 888-903.
- Hartzell, S. H. (1978). Earthquake aftershocks as Green's functions, *Geophys. Res. Lett.* 5, 1-4.
- Herrmann, R. B. (1985). An extension of Random Vibration Theory estimates of strong ground motion to large earthquakes, *Bull. Seism. Soc. Am.* 75, 1447-1453.
- Herrmann, R. B. and L. Malagnini (2004). Interpretation of high frequency ground motion from regional seismic network observations, *Bull. Seism. Soc. Am.*, (In revision).
- Hough, S. E., K. Jacob, and P. Friberg (1989). The 11/25/88, M = 6 Saguenay earthquake near Chicoutimi, Quebec: evidence for anisotropic wave propagation in northeastern North America, *Geophys. Res. Lett.*, 16, 645-648.
- Johnston, A. C. and L. R. Kanter (1990). Earthquakes in stable continental crust, *Sci. Am.* 262, 68-75.
- Joyner, W. (1984). A scaling law for the spectra of large earthquakes, *Bull. Seism. Soc. Am.* 74, 1167-1188.

- Kanamori, H. and D. L. Anderson (1975). Theoretical basis of some empirical relations in seismology, *Bull. Seism. Soc. Am.* 65, 1073-1095.
- Kanamori, H. and C. Allen (1986). Earthquake repeat time and average stress drop, in *Earthquake Source Mechanics*, S. Das, J. Boatwright, and C. H. Scholz (Editors), American Geophysical Monograph 37, Washington, D. C.
- Kennett, B. (1986).  $L_g$  waves and structural boundaries, *Bull. Seism. Soc. Am.* 76, 1133-1141.
- Kim, S. K., M. S. Jun, and J. K. Kim (1999). Attenuation of P-waves in the Kyungsang Basin, Southeastern Korea, *J. Geol. Soc. Korea*, 35, 223-228 (in Korean).
- Kim, S. K., S. K. Kim, and H. C. Chi (2002). Attenuation of peak spectral amplitude of acceleration in the southern part of the Korean Peninsula, *J. Geol. Soc. Korea*, 38, 237-250.
- Kramer, S. (1996). Geotechnical earthquake engineering, Prentice Hall, *Upper Saddle River*, NJ, 07458, 653.
- Lawson, C. L. and R. J. Hanson (1974). Solving Least Squares Problems, *Prentice-Hall, Inc.*, Englewood Cliffs, N. J..
- Lay, T. and T. C. Wallace (1995). Modern global seismology, International Geophysics Series, Vol. 58, Academic Press.
- Lee, K. and H. O. Jung (1980). A study of instrumental earthquake data of Korean peninsula, *J. Geol. Soc. Korea*, 16, 32-45.
- Lee, K., N. S. Chung, and T. W. Chung (2003). Earthquakes in Korea from 1905 to 1945, *Bull. Seism. Soc. Am.* 93, 2131-2145.
- Malagnini, L. (1999). Ground motion scaling in Italy and Germany, *Ph. D. Dissertation*, Saint Louis University.
- Malagnini, L., R. B. Herrmann, and M. Di Bona (2000). Ground motion scaling in the Apennines (Italy), *Bull. Seism. Soc. Am.* 90, 1062-1081.
- McGuire, R. K. and T. C. Hanks (1980). RMS acceleration and spectral amplitudes of strong ground motion during the San Fernando, California, earthquake, *Bull. Seism. Soc. Am.* 70, 1907-1919.
- Menke, W. (1989). Geophysical data analysis: Discrete Inverse Theory, Academy Press, *San Diego*, CA, 92101, 289.
- Mitchell, B. J. (1981). Regional variation and frequency dependence of  $Q_\beta$  in the crust of the United States, *Bull. Seism. Soc. Am.* 71, 1531-1071.

- Mitchell, B. J. (1995). Anelastic structure and evolution of the continental crust and upper mantle from seismic surface wave attenuation, *Rev. Geophys.* **33**, 441-462.
- National earthquake hazards program (NEHP) home page, 2002,  
[http://www.seismo.nrcan.gc.ca/cnsn/can-list\\_e.php](http://www.seismo.nrcan.gc.ca/cnsn/can-list_e.php).
- National earthquake hazards program (NEHP) home page, 2002,  
[http://www.seismo.nrcan.gc.ca/cnsn/index\\_e.php](http://www.seismo.nrcan.gc.ca/cnsn/index_e.php).
- National earthquake hazards program (NEHP) home page, 2002,  
[http://www.seismo.nrcan.gc.ca/cnsn/seis-net\\_e.php](http://www.seismo.nrcan.gc.ca/cnsn/seis-net_e.php).
- National earthquake hazards program (NEHP) home page, 2002,  
[http://www.seismo.nrcan.gc.ca/cnsn/sm-net\\_e.php](http://www.seismo.nrcan.gc.ca/cnsn/sm-net_e.php).
- National earthquake hazards program (NEHP) home page, 2002,  
[http://www.seismo.nrcan.gc.ca/historic\\_eq/eastcan\\_e.html](http://www.seismo.nrcan.gc.ca/historic_eq/eastcan_e.html).
- National earthquake hazards program (NEHP) home page, 2002,  
[http://www.seismo.nrcan.gc.ca/nwfa/events/index\\_e.php](http://www.seismo.nrcan.gc.ca/nwfa/events/index_e.php).
- Ojo, S. and R. Mereu (1986). The effect of random velocity functions on the travel times and amplitudes of seismic waves, *Geophys. J. R. Astr. Soc.* **84**, 607-618.
- Ortega, R. (2000). High frequency ground motion in central Mexico: site, excitation and attenuation, *Ph. D. Dissertation*, Saint Louis University.
- Ou, G. and R. Herrmann (1990). A statistical model for ground motion produced by earthquakes at local and regional distances, *Bull. Seism. Soc. Am.* **80**, 1397-1417.
- Papageorgiou, A. S. and K. Aki (1983). A specific barrier model for the quantitative description of inhomogeneous faulting and the prediction of strong ground motion. Part 2. Applications of the model, *Bull. Seism. Soc. Am.* **73**, 953-978.
- Rautian, T. G. and V. I. Khalturin (1978). The use of the coda for determination of the earthquake source spectrum, *Bull. Seism. Soc. Am.* **68**, 923-948.
- Ree, J. H., M. Cho, S. T. Kwon, and E. Nakamura (1996). Possible eastward extension of Chinese collision belt in South Korea: the Imjingang belt. *Geology*, **24**, 1071-1074.
- Reiter, L. (1990). *Earthquake Hazard Analysis - Issues and Insights*, Columbia University Press, New York, 254 pp.

- Rhee, C. W., H. R. Jo, and S. K. Chough (1998). An allostratigraphic approach to a non-marine basin: the northwestern part of Cretaceous Kyongsang Basin, SE Korea, *Sedimentology*, 449-472.
- Saint Louis University earthquake center home page (2004). <http://www.eas.slu.edu/People/RBHerrmann/KOREA.2003/index.html> (last modified August 2004).
- Sbar, M. L. and L. R. Sykes (1973). Contemporary compressive stress and seismicity in eastern North America: an example of intra-plate tectonics, *Geol. Sol. Am. Bull.* 84, 1861-1882.
- Scherbaum, F. (1996). Of poles and zeros, fundamentals of digital seismology, *Kluwer academic publishers*, Dordercht/Boston/London.
- Schneider, J., W. Silva, and C. Stark (1993). Ground motion model for the 1989 M 6.9 Loma Prieta earthquake including effects of source, path and site, *Earthquake Spectra*, 9, 251-287.
- Shi, J., W. Y. Kim, and P. G. Richards (1996). Variability of crustal attenuation in the northeastern United States from *L<sub>g</sub>* waves. *J. Geophys. Res.* 101, 25231-25242.
- Shimazaki, K. (1984). Mid-plate, plate-margin, and plate-boundary earthquakes and stress transmission in far east, in *A Collection of Papers of the International Symposium on Continental Seismicity and Earthquake Prediction (ISCSEP)*, The Organizing Committee of ISCSEP, Seismological Press, Beijing.
- Shin, T. and R. Herrmann (1987). *L<sub>g</sub>* attenuation and source studies using 1982 Miramichi data, *Bull. Seism. Soc. Am.* 77, 384-397.
- Silva, W., R. Darragh, and I. Wong (1990). Engineering characterization of earthquake strong ground motions with applications to the Pacific Northwest, in Hays, W., ed., *Proceedings at the Third NEHRP Workshop on Earthquake hazards in the Puget Sound/Portland Region*, W. Hays Editor), *U. S. Geol. Surv. Open-File Rept.*
- Silva, W. and C. Stark (1992). Source, path, and site ground motion model for the 1989 M Loma Prieta earthquake, CDMG report.
- Singh, S. and R. B. Herrmann (1983). Regionalization of crustal Q in the continental United States, *J. Geophys. Res.* 88, 527-538.
- Somerville, P., J. McLaren, L. Lefevre. R. Burger, and D. Helmberger (1987). Comparison of source scaling relations of eastern and western North American earthquakes, *Bull. Seism. Soc. Am.* 77, 322-346.

- Song, S. and K. Lee (2001). Crustal structure of the Korean peninsula by travel time inversion of local earthquakes, *J. Korea Geophys. Soc.* 4, 21-33.
- Sykes, L. R. (1978). Intraplate seismicity, reactivation of pre-existing zones of weakness, alkaline magmatism, and other tectonism postdating continental fragmentation, *Rev. Geophys.* 16, 621-688.
- Toro, G., N. Abrahamson, and J. Schneider (1997.) Model of strong ground motions from earthquakes in eastern and central North America: best estimates and uncertainties, *Seism. Res. Lett.* 68, 41-57.
- Tsumura, K. (1967). Determination of earthquake magnitude from duration of oscillation, *Zisin* (in Japanese) 20, 30-40.
- Yazd, M. R. S. (1993). Ground motion studies in the Southern Great Basin of Nevada and California, Ph. D. thesis, Saint Louis University.
- Yoo, H. J. and K. Lee (2001). Crustal structure under the Taejon (TJN) station by receiver function methods, *J. Korea Geophys. Soc.* 4, 35-46.
- Yoon, S. H. and S. K. Chough (1995). Regional strike-slip in the eastern continental margin of Korea and its tectonic implications for the evolution of Ulleung Basin, East sea (Sea of Japan), *Geol. Soc. Am. Bull.* 107, 83-97.
- Zoback, M. L. (1992). First and second-order patterns of stress in the lithosphere: The World Stress Map project, *J. Geophys. Res.* 97, 11703-11728.
- Zoback, M. L., M. D. Zoback, J. Adams, M. Assumpcao, S. Bell, E. A. Bergman, P. Bluemling, N. R. Brereton, D. Denham, J. Ding, K. Fuchs, N. Gay, S. Gregersen, H. K. Gupta, A. Gvishiani, K. Jacob, R. Klein, P. Knoll, M. Magee, J. L. Mercier, B. C. Mueller, C. Paquin, K. Rajendran, O. Stephansson, G. Suarez, M. Suter, A. Udias, Z. H. Xu, and M. Zhizin (1989). Global patterns of tectonic stress, *Nature*, 341, 291-298.

## Vita Auctoris

Young-Soo Jeon was born in Seoul, Korea on September 27, 1968. He finished his elementary and secondary education in Seoul. After attending Sang-Ji University, he graduated with a B. E. degree in Mineral and Mining Engineering in February 1995. During that time, he joined the army because it was a basic obligation for young Korean males. He then enrolled at Yonsei University and graduated with an M. S. degree in Geophysics in February 1997.

After that, while he worked as a researcher at Natural Science Center at Yonsei University, one of his mentors who works at the KIGAM (Korea Institute of Geology, Mining and Materials) seismology branch encouraged him to start his future work in Seismology. Even though the topic was totally new for him, he decided to pursue that field and joined the Saint Louis University Department of Earth and Atmospheric Sciences in August 1998 to pursue the degree in geophysics.

There have been many changes in the last six years. Young-Soo got married last spring and found his lifelong friend. But, his grandmother passed away. Also his parents got older. For the overall changes, the one thing still remain unchanged is the love: the love his parents shows to him and the attention from people who know him.

Since he started his career here, Young-Soo thought that he would learn a profound knowledge in seismology. But, for the last six years, the most important thing he learned here is life, the way to live for the rest of his life.